



**HAL**  
open science

# Can graphene oxide be a suitable platform for the complexation with nucleic acids?

Ngoc Do Quyen Chau

► **To cite this version:**

Ngoc Do Quyen Chau. Can graphene oxide be a suitable platform for the complexation with nucleic acids?. Other. Université de Strasbourg, 2017. English. NNT : 2017STRAF059 . tel-03934608

**HAL Id: tel-03934608**

**<https://theses.hal.science/tel-03934608>**

Submitted on 11 Jan 2023

**HAL** is a multi-disciplinary open access archive for the deposit and dissemination of scientific research documents, whether they are published or not. The documents may come from teaching and research institutions in France or abroad, or from public or private research centers.

L'archive ouverte pluridisciplinaire **HAL**, est destinée au dépôt et à la diffusion de documents scientifiques de niveau recherche, publiés ou non, émanant des établissements d'enseignement et de recherche français ou étrangers, des laboratoires publics ou privés.

**ÉCOLE DOCTORALE DES SCIENCES CHIMIQUES**

**UPR 3572**

**THÈSE** présentée par :

**Ngoc Do Quyen CHAU**

soutenue le : **24 Novembre 2017**

pour obtenir le grade de : **Docteur de l'université de Strasbourg**

Discipline/ Spécialité : Chimie

**L'oxyde de graphène peut-il devenir  
une plateforme appropriée pour la  
complexation d'acides nucléiques ?**

**THÈSE dirigée par :**

**M. BIANCO Alberto**

Directeur de recherche, CNRS

**RAPPORTEURS :**

**M. PALERMO Vincenzo**

Senior Researcher, CNR, Italie

**M. CAMPIDELLI Stéphane**

Chercheur, CEA

---

**AUTRES MEMBRES DU JURY :**

**M. BAATI Rachid**

Directeur de recherche, CNRS



## ACKNOWLEDGEMENTS

I would like to express my sincere gratitude to my supervisor, Dr. Alberto BIANCO for his generous support, his guidance, and his enthusiastic encouragement in this Thesis. It has been my honor to have a chance of working in this group, a very dynamic and international environment. I am deeply grateful for the chance of doing research in Japan that he gave to me. During my three years of PhD under his kind and interactive supervision, I have learned many new things from him and gained more knowledge. Many thanks for spending his precious time during this project.

I wish to express my very great appreciation to Dr. Cécilia MENARD-MOYON for her advice, her patience, constructive suggestions and assistance since my first days in the laboratory. Her kindness and her enthusiasm in science contribute to create such an effective and enjoyable laboratory environment.

I am very grateful to Dr. Vincenzo PALERMO, Dr. Stéphane CAMPIDELLI, Dr. Rachid BAATI for accepting to be members of my defense commission, especially for their precious time of reading this manuscript.

I would like to thank also to Prof. Sylviane MULLER for welcome me to the department.

My special thanks are given to Prof. Yuta NISHINA for accepting me as a visiting researcher in his group in Okayama University. I also would like to thank to the HONDA Foundation for the valuable support for my internship in Japan.

My thanks also go to the collaborators in Graphene FLAGSHIP, especially to Prof. François BERGER and Dr. Graciane PETRE in Grenoble, Prof. Kostas KOSTALEROS and his group in Manchester for the fruitful discussions.

My grateful thanks and appreciation are dedicated to Dr. Giacomo REINA not only for his valuable excessive support but also for his willingness to spend time to explain different concepts in this research work. Thanks for always be patient, be calm to me and be crazy together with me and Diane. And a really special thank goes to Dr. Diane MURERA-UWANYIRIGIRA not only for her arrangement of time for performing all the biological tests but also for the cheerfulness wherever she is. Thanks to Dr. Bianco to give me a great chance to work with such funny and crazy “papa and mama”. Indeed, for all the time we have been together in the lab and beer-time outside of the lab, for all the up and down results of experiments with many discussions to solve the problems, all I can say is thank you. I am very lucky to have you, “la petite famille”, always being by my side.

I would like to thank all the people in the analytical platform of the University of Strasbourg, especially Maurice COPPE, Cathy ROYER, Noemie BOURGEOIS for their warm



help. Thanks to Jean-Daniel FAUNY, Jean-Baptiste MADINIER, Olivier CHALOIN, Maxime GRILLAUD for their helping in handling of the instruments at the beginning days of my work. I really appreciate the help provided by Dr. Jésus RAYA for the solid-state MAS NMR experiments and his time of discussion.

Thanks to all people in the unit for their welcome, help and also for the warm working environment in the laboratory. I have learned a lot from them during this research work and I also have had a happy time with them during the outgoing activities. My thanks also go to Isabelle, the secretary of our laboratory, for her continuous help with all the complicated administrative documents that in some cases take me a lot of time.

I want to warmly thank to all the members of our group: Rajendra for his sharing ideas, and encouragement, Cinzia for her support and sharing in the initial period of my Thesis before her leaving, Isabella for her sharing in XPS analysis and in graphene study, Adriano for creating a team-spirit, Laura, Gloria and Maxime for the funny things in the lab, Sowmya, Dinesh, Matteo, Chloé, Janina, Sophia, Matthieu, Farouk for their kindness.

I cannot forget to thank to my friends in Japan, especially Tanimoto-san, Chen-san and Soliman for the scientific support and discussions; Minh and her friends from outside of the lab for the warm welcome, sharing and taking care of my social life there. Thanks to all my friends in Strasbourg for making a nice period away from home happy.

Finally, I would like to send my special thanks to my big family, especially my parents and my little sister for their inspiration and staying by my side although the long distance in real life. Thanks to my grand-mother and my cousins for sharing with me from far away. Thanks to my dear, Nhan, for his support, understanding and sharing.

Thank you all. Merci.

Quyen

# ABSTRACT

Doctoral Thesis

By Ngoc Do Quyen CHAU

In the last decades, graphene oxide (GO) has been predicted as a wonderful nanomaterial in myriad applications for its unique and outstanding properties. Intensive research is ongoing to scrutinize its potential role as a prominent vector in gene delivery, especially in gene silencing. The main aim of my Thesis is to design a graphene-based hybrid material as a non-viral vector for delivery of small interfering RNA (siRNA). Hence, control of the oxygenated groups on the surface of GO can lead to different behavior in term functionalization ability and interaction with biomolecules. In this context, one of the first approach has been to develop various green and facile reduction and reepoxidation methods to obtain GO with different levels of oxygenated moieties. In the next step, the introduction of different amines and polymers on these prepared graphene materials *via* the epoxy ring opening reaction allowed to obtain a novel platform for better complexation with siRNA. I have figured out that the driving forces of the ability of complexing with siRNA are dependent on the functional groups conjugated to GO, either due to electrostatic interaction or to hydrogen bond interaction. on the other hand, several works demonstrated the ability of GO to efficiently adsorb siRNA on its surface and to transport it into the cells. However, studies whether and how siRNA interacts with GO are still inconclusive. For this reason, the interactions between GO and siRNA molecules have been then systematically investigated. I have found that the siRNA secondary structure is clearly altered by the interaction with GO flakes. Interestingly, GO functionalized with low molecular weight polyethyleneimine is able to protect siRNA from structural modifications and to improve the complexing with siRNA. Various techniques have been explored to characterize GO with various oxygen percentages, conjugation of cationic molecules with graphene materials, and the interaction of GO with siRNA. Besides, the preliminary biological tests proved the efficiency of our graphene derivatives as a vehicle for delivery of siRNA into the cells. I believed that this research effort will improve our understanding of the behavior of the GO/siRNA complexes, and thus facilitate the design of new appropriate and efficient gene silencing systems.



# INDEX

Acknowledgements.....	V
Abstract.....	VII
Index .....	IX
Acronyms and Abbreviations .....	XIII
Resumé de Thèse .....	XVII
<b>CHAPTER 1: INTRODUCTION.....</b>	<b>1</b>
1.1 Graphene oxide .....	1
1.2 Promise, facts and challenges of graphene oxide in biomedical applications .....	4
1.2.1 Non-covalent and covalent approaches .....	4
1.2.1.1 Non-covalent interactions and their driving forces.....	4
1.2.1.2 Covalent functionalization .....	6
1.2.2 Graphene oxide based therapy .....	8
1.2.2.1 Drug and gene delivery .....	8
1.2.2.2 Photothermal therapy and photodynamic therapy .....	12
1.2.2.3 Biomedical imaging .....	13
1.2.3 Biocompatibility and toxicity .....	16
1.3 Graphene oxide and nucleic acids interactions .....	18
1.3.1 Graphene oxide bio-interfacing with nucleic acids and biological effects of the graphene/nucleic acid complexes .....	18
1.3.2 Bioapplication in gene delivery .....	21
1.4 Future perspective of graphene oxide in cancer therapy .....	25

1.5 Thesis objectives and outline .....	26
1.6 Bibliography .....	28
<b>CHAPTER 2: SYNTHESIS OF REDUCED GRAPHENE OXIDE WITH VARIOUS OXYGEN PERCENTAGES .....</b>	<b>41</b>
2.1 Introduction.....	41
2.2 Objectives of this chapter.....	43
2.3 Results and discussions.....	43
2.3 Part A: Reactions on GO <sub>S</sub> .....	44
2.3 Part B: Reactions on GO <sub>L</sub> .....	54
2.4 Conclusion .....	62
2.5 Experimental part.....	62
2.6 Bibliography .....	67
<b>CHAPTER 3: FUNCTIONALIZATION OF GRAPHENE OXIDE WITH VARIOUS AMINES AND POLYMERS. STUDY THEIR COMPLEXATION WITH siRNA .....</b>	<b>71</b>
3.1 Introduction.....	71
3.2 Objectives of this chapter.....	71
3.3 Results and discussions.....	72
3.3 Part A: Functionalization of GO <sub>S</sub> and reduced GO <sub>S</sub> materials with the different cationic molecules.....	72
A1: Synthesis of cationic molecules and dendrons.....	72
A2: Functionalization of the GO <sub>S</sub> with linear and dendritic amines. Characterization and complexation with siRNA.....	74
A3: Preparation of PEI functionalized GO <sub>S</sub> materials. Characterization and complexation with siRNA.....	81

3.3 Part B: Functionalization of GO <sub>s</sub> and reduced GO <sub>s</sub> materials with the different cationic molecules.....	85
3.4 Conclusion .....	93
3.5 Experimental part.....	94
3.6 Bibliography .....	102
<b>CHAPTER 4: GRAPHENE OXIDE SIZE AND OXIDATION DEGREE GOVERN ITS SUPRAMOLECULAR INTERACTIONS WITH siRNA .....</b>	<b>105</b>
4.1 Introduction.....	105
4.2 Objectives of this chapter.....	105
4.3 Results and discussions.....	105
4.3 Part A: Investigations on the interaction of graphene materials with siRNA: complexation or denaturation?.....	106
A1: Complexation of starting GO materials with siRNA.....	106
A2: Spectroscopic investigations on the interaction of graphene materials with siRNA .....	108
4.3 Part B: Internalization and release of siRNA into HeLa cells .....	116
4.4 Conclusion .....	125
4.5 Experimental part.....	125
4.6 Bibliography .....	128
<b>CHAPTER 5: CONCLUSIONS AND PERSPECTIVES .....</b>	<b>131</b>
List of publications and communications .....	135



---

## ACRONYMS AND ABBREVIATIONS

5-FU	5- fluorouracil
6-FAM	6-carboxyfluorescein
A549 cells	human lung carcinoma cells
AA	siRNA with one strand labeled at 5' position with Alexa Fluor®546 (donor) and another strand labeled at 5' position with Alexa Fluor®647 (acceptor)
ADR	Adriamycin
AFM	atomic force microscopy
Boc <sub>2</sub> O	di-tert-butyl dicarbonate
BPEI	branched PEI
CC	siRNA with one strand labeled at 5' position with Cy®3 (donor) and another strand labeled at 3' position with Cy®5 (acceptor)
CD	circular dichroism
Ce6	chlorin e6
CMG	magnetic rGO
CNTs	carbon nanotubes
CS	chitosan
D <sub>1</sub>	dendron first generation
D <sub>2</sub>	dendron second generation
DAPI	fluorescent stain, 4',6-Diamidino-2-phenylindole
DCM	dichloromethane
DIEA	N,N-Diisopropylethylamine
DLS	dynamic light scattering
DMA/c	N, N-dimethylacetamide
DMDO	dimethyldioxirane
DMF	N,N-Dimethylformamide
DMSO	Dimethyl sulfoxide
DNA	deoxyribonucleic acid



DOX	doxorubicin
dsDNA	double strand DNA
dsRNA	double strand RNA
E	FRET efficiency
EDC	1-ethyl-3-(3-dimethylaminopropyl)-carbodiimide
FA	folic acid
FAM	fluorescein-based dye
FRET	fluorescence resonance energy transfer
FT-IR	Fourier-transform infrared spectroscopy
GFP	green fluorescent protein
GIC	Graphite intercalated compound
GO	Graphene oxide
GO <sub>L</sub>	large GO, commercial, size distribution 3±1 μm
GO <sub>M</sub>	medium GO, academic, size distribution 600±300 nm
GO <sub>S</sub>	small GO, academic, size distribution 300±200 nm
HA	hyaluronic acid
H-bonding	hydrogen bonding
HMW-PEI	high molecular weight PEI
HOBt	1-hydroxybenzotriazole hydrate
LMW	low molecular weight
MAS	magic angle spinning
mCPBA	m-chloroperbenzoic acid
MD	molecular dynamic
MMP-9	matrix metalloproteinase-9
MRI	magnetic resonance imaging
mRNA	messenger RNA
MUA	11-mercaptoundecanoic acid
MWCNTs	multi-walled carbon nanotubes

NA	nucleic acids
NHS	N-hydroxylsuccinimide
NIR	near-infrared
NMP	N-Methyl-2-pyrrolidone
PAMAM	polyamidoamine dendrimer
pDNA	plasmid DNA
PDT	photodynamic therapy
PEG	Polyethylene glycol
PEI	polyethylenimine
PLL-rGO	poly(L-lysine) conjugates with reduced GO
PNP	4-(1-pyrenylvinyl)-N-butylpyridinium
PPG	PEI conjugated on GO-PEG
PPG-FA	Folic acid conjugated with PPG
PS	photosensitizers
PTT	photothermal therapy
Q	quaternary amine
QD	quantum dots
R	FRET distance
RGD	arginine–glycine–aspartic acid
rGO	reduced graphene oxide
RISC	RNA induced silencing complex
RNA	ribonucleic acid
RNAi	RNA interference
ROS	reactive oxygen species
SEM	scanning electron microscopy
shRNA	short hairpin RNA
siRNA	small interfering RNA
SPIONs	Superparamagnetic Fe <sub>3</sub> O <sub>4</sub> nanoparticles

ssDNA	single strand DNA
ssNMR	solid-state nuclear magnetic resonance spectroscopy
ssRNA	single strand RNA
SWCNTs	single-walled carbon nanotubes
T1	spin-lattice (longitudinal) relaxation time
T2	spin–spin (transversal) relaxation time
TEG	2,2'-ethylenedioxybisethylamine
TEM	transmission electron microscopy
TFA	trifluoroacetic acid
TGA	thermogravimetric analysis
UV-Vis	ultraviolet–visible spectroscopy
XPS	X-ray photoelectron spectroscopy
XRD	X-ray diffraction
YY	Yakima yellow dye
ζ potential	zeta potential

## RESUME DE THESE

### 1) Introduction

Depuis son isolement en 2004, le graphène est apparu comme un nanomatériau fascinant avec des propriétés physiques uniques.<sup>1</sup> Des recherches intensives sont en cours pour étudier les applications potentielles du graphène et de son dérivé, l'oxyde de graphène (GO), dans de nombreux domaines, y compris la biomédecine et la nanomédecine.<sup>2-7</sup> Néanmoins, la faible dispersabilité du graphène dans des solutions aqueuses gêne l'exploitation complète de ses propriétés. Pour surmonter ce problème, une chimie de fonctionnalisation rationnelle est nécessaire afin d'améliorer la processabilité et transmettre au graphène de nouvelles propriétés.

Dans ce contexte, le GO est une plateforme utile pour la conception de matériaux hybrides à base de graphène (Figure 1).<sup>8</sup> Le GO est composé d'une seule couche d'oxyde de graphène et il est habituellement produit par oxydation du graphite à l'aide de solutions d'acides forts.<sup>9,10</sup> Les groupes fonctionnels contenant de l'oxygène (i.e. hydroxyles, époxydes, carboxylates, cétones, etc...) le rendent hautement hydrophile, entraînant une bonne dispersion dans l'eau et de nombreux autres solvants. En outre, la dérivatisation de ces fonctions oxygénées est une méthode polyvalente et efficace pour fonctionnaliser chimiquement le graphène pour une large gamme d'applications.<sup>9</sup>

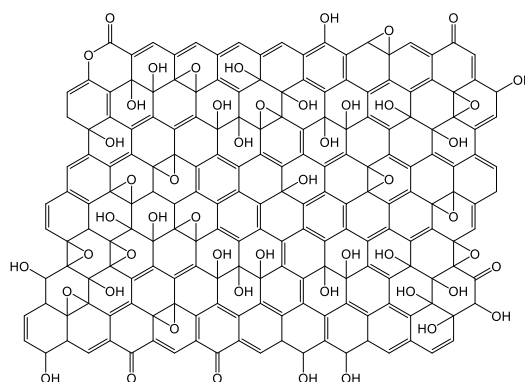


**Figure 1** : Modèle structurel du GO.

La thérapie génique a suscité un intérêt considérable en tant que méthode prometteuse pour le traitement de dysfonctions liés aux gènes et d'autres maladies comme le cancer.<sup>11,12</sup> À ce jour, parmi de nombreux types de nanomatériaux, ceux à base de carbone, notamment le graphène et ses dérivés, ont été largement développés, permettant leur exploitation en biomédecine, en

particulier pour l'administration de gènes, grâce à leurs propriétés intrinsèques uniques. En effet, en raison de sa grande surface, sa haute biocompatibilité, sa chimie de surface ajustable, et sa dispersabilité élevée dans l'eau, le GO est un candidat potentiel vis-à-vis d'autres nano-vecteurs en termes d'interaction avec des biomolécules telles que l'ADN, les peptides ou les protéines.<sup>13,14</sup>

## 2) Objectifs de la Thèse

L'objectif principal de ma thèse était de fonctionnaliser de manière covalente le GO avec des amines. Cette approche m'a permis de développer une nouvelle plateforme complexant des molécules biologiquement actives pour la délivrance de gènes, en particulier pour l'inhibition de gènes spécifiques à l'aide de petits ARN interférents (siRNA) (Figure 2).

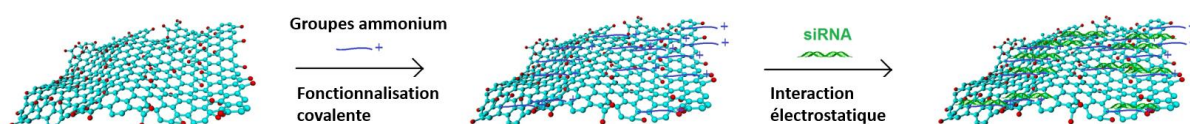


**Figure 2** : Fonctionnalisation covalente du GO avec des groupes ammonium et complexation du GO fonctionnalisé avec du siRNA.

En particulier, nous nous sommes concentrés d'abord sur la conception, la synthèse et l'étude d'échantillons de GO avec différents degrés d'oxydation en utilisant des protocoles divers. Afin d'augmenter la quantité de groupes ammonium qui conduisent à une meilleure complexation du siRNA, une ré-époxydation du GO, ayant subi une réduction préalable, a été réalisée suivie d'une ouverture du cycle époxy avec des dérivés aminés. Ensuite, une série d'amines a été synthétisée pour la fonctionnalisation covalente du GO. Enfin, la capacité de chaque GO fonctionnalisé et non-fonctionnalisé à interagir avec le siRNA a été étudiée par différentes techniques comme la spectroscopie UV-Vis, le gel d'électrophorèse, le dichroïsme circulaire et le transfert d'énergie par résonance de type Förster (FRET). Grâce à ces nouvelles méthodes et à la caractérisation précise de la surface, nous avons pu mieux comprendre l'interaction du siRNA avec le GO initial et fonctionnalisé. Finalement, les expériences biologiques ont été effectuées pour évaluer la capacité du GO comme plateforme pour la délivrance de siRNA dans les cellules. Dans les paragraphes suivants, les résultats sont présentés en détail.

### 3) Résultats et discussion

#### 3.1 Synthèse des GO réduits avec des pourcentages d'oxygène divers

Des propriétés très prometteuses et potentiellement applicables du GO lui permettent d'être exploré dans une grande variété de domaines. Il est bien connu que le GO a plusieurs groupements oxygénés chimiquement réactifs à sa surface, qui permettent de contrôler sa fonctionnalisation.<sup>15</sup> Le comportement de ces fonctions oxygénées vis-à-vis de l'interaction du GO avec des acides nucléiques n'a pas encore été étudié de manière systématique. Par conséquent, dans mon étude, la première étape a consisté à obtenir des GO avec un pourcentage d'oxygène variable selon l'utilisation de différents procédés de réduction faciles et « verts ». Nous avons initialement testé et adapté différentes conditions de réduction sur mes échantillons d'oxyde de graphène en utilisant deux GO avec des tailles différentes: l'un provenant d'une source commerciale de petite taille, nommé GO<sub>S</sub> et l'autre d'une source académique de grande taille, nommé GO<sub>L</sub> (Figure 3).

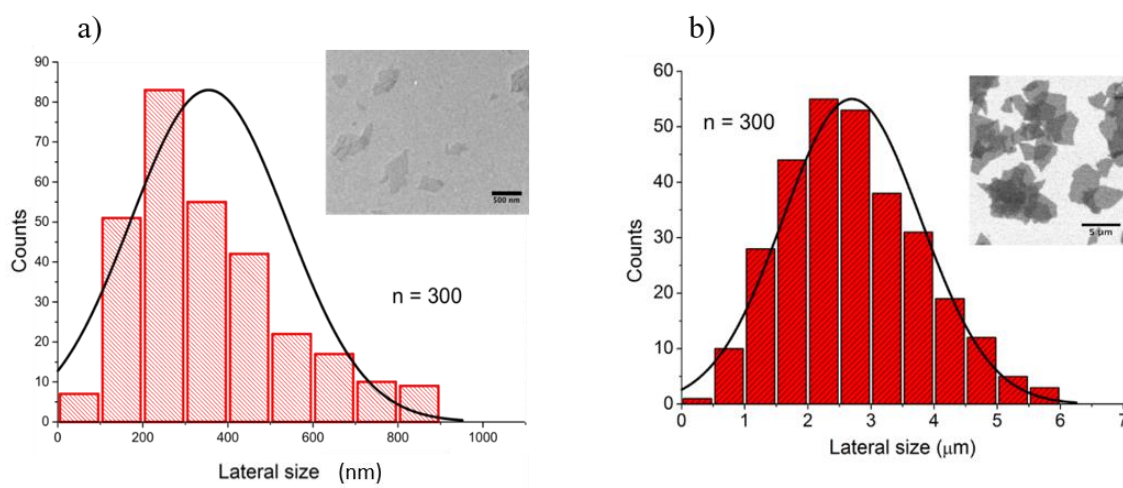


**Figure 3 :** a) Distribution de la taille latérale du GO<sub>S</sub>. Dans l'encart: image MET (microscopie électronique à transmission) du GO<sub>S</sub>, la barre d'échelle correspond à 500 nm. B) Distribution de la taille latérale du GO<sub>L</sub>. Dans l'encart: image MEB (microscopie électronique à balayage) de GO<sub>L</sub>, la barre d'échelle correspond à 5 μm.

Diverses conditions et plusieurs agents réducteurs ont été évalués tels que la désoxygénation hydrothermique et solvothermique (conditions douces dans l'eau et le DMSO, respectivement), l'utilisation des micro-ondes (conditions plus fortes), et la vitamine C qui a été employée comme alternative verte à l'hydrazine. Le but de la réduction du GO était

d'éliminer une fraction des groupes oxygénés (qui peuvent entraver la complexation des siRNA), tout en conservant les cycles époxydes afin de permettre l'introduction de charges positives par l'ouverture des époxydes avec différents dérivés d'amines. En outre, j'ai exploré la ré-époxydation du GO réduit en utilisant l'ozone. La réduction et la re-époxydation ont été réalisées d'abord sur le GO commercial avant de traiter le GO d'origine académique dans des conditions appropriées. Ces nanomatériaux ont été caractérisés par des techniques analytiques complémentaires telles que la spectroscopie photoélectronique par rayons X (XPS) (Figure 4), l'analyse thermogravimétrique (ATG), la spectroscopie FT-IR, et la spectroscopie RMN du solide.

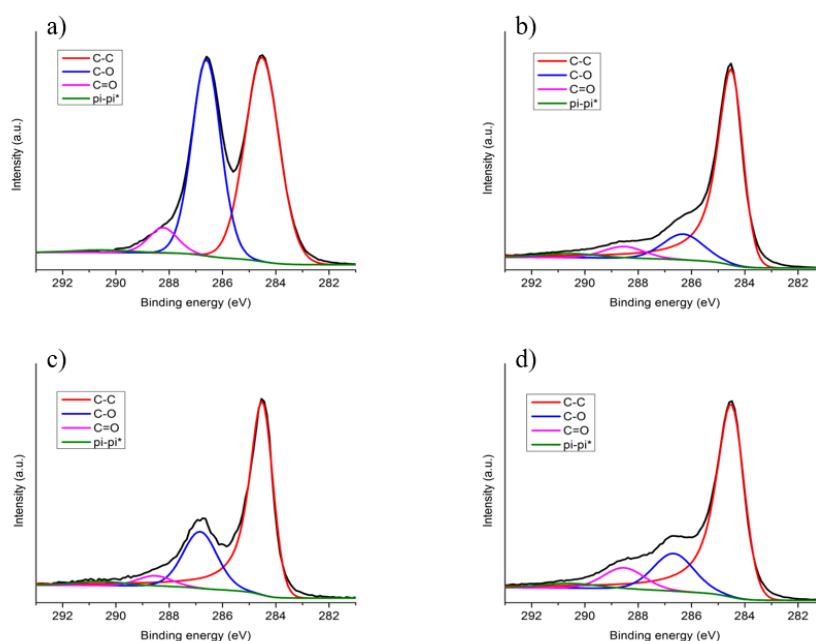


**Figure 4** : Déconvolution du pic C (1s) des GO<sub>L</sub> avec des pourcentages d'oxygène différents (liaisons C-O, C=O): GO<sub>L</sub> (a), GO réduit par désoxygénation hydrothermique (b), GO réduit par la vitamine C (c) et GO réduit traité par ré-époxydation via un traitement à l'ozone (d).

### 3.2 Fonctionnalisation des GOs avec divers amines et polymères. Étude de leur complexation avec du siRNA

J'ai tout d'abord effectué la synthèse de dérivés d'amines ramifiées et la fonctionnalisation du GOs et GOs réduit (rGOs) avec ces différentes amines. Dans le but d'accroître la capacité du GO à complexer le siRNA, une série de multiamines (amines commerciales et amines synthétiques) de faible poids moléculaire ont été utilisées telles que la triéthylène glycol (TEG) diamine ainsi que des dendrimères de plus haut poids moléculaire allant jusqu'à 800

kDa comme la polyéthylèneimine (PEI). Les réactions ont été réalisées dans des conditions douces, à température ambiante. Aucune addition de catalyseur n'a été nécessaire car les époxydes sont très réactifs vis-à-vis des amines. La fonctionnalisation du GO avec les amines est présentée dans le Schéma 1.

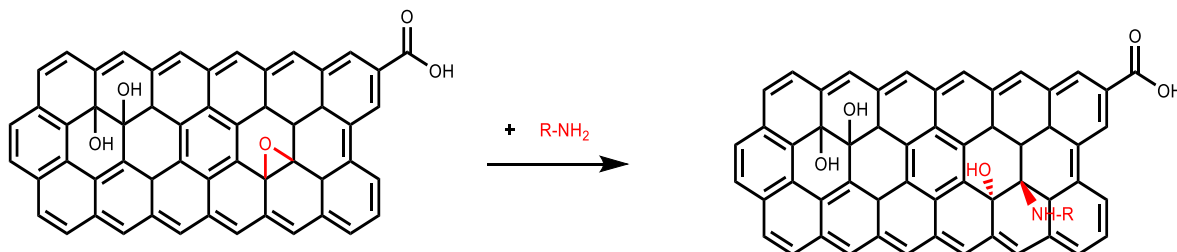


**Schéma 1** : Amino-fonctionnalisation du GO via l'ouverture nucléophile du cycle époxy. Pour des raisons de clarté, seul un groupe époxyde est représenté.

Les GO fonctionnalisés ont été caractérisés par des techniques analytiques complémentaires (i.e. XPS, ATG, RMN et potentiel zeta). J'ai observé la présence d'azote par XPS, ce qui est indicatif du succès de la conjugaison des amines sur les échantillons de GO. Par la suite, les meilleures stratégies trouvées ont aussi été appliquées aux GO<sub>L</sub> et GO<sub>L</sub> réduits (rGO<sub>L</sub>). Parmi les amines, nous avons choisi la TEG diamine et le PEI pour la fonctionnalisation des GO<sub>L</sub> et rGO<sub>L</sub>. Le pourcentage atomique d'azote pour les quatre échantillons de GO<sub>L</sub> fonctionnalisés avec la TEG diamine et le PEI sont montrés dans le Tableau 1: GO<sub>L</sub>, GO<sub>L</sub> réduit par désoxygénation hydrothermique (rGO<sub>L</sub>-5d), GO réduit par la vitamine C (rGO<sub>L</sub>-C), et GO réduit traité par ré-époxydation via un traitement à l'ozone (rGO<sub>S</sub>-5d-O<sub>3</sub>), .

**Tableau 1.** N% atomique des différents GO<sub>L</sub> fonctionnalisés avec la TEG diamine et le PEI calculés à partir des pics XPS à 400 eV.

Echantillons	TEG	PEI
GO <sub>L</sub>	2.1±0.5	5.8±0.1
rGO <sub>L</sub> -5d	1.9±0.1	5.3±0.1
rGO <sub>L</sub> -C	2.1±0.1	6.3±0.2
rGO <sub>L</sub> -5d-O <sub>3</sub>	2.1±0.1	9.5±0.2

Les spectres XPS de la série des échantillons de GO<sub>L</sub> après fonctionnalisation avec la TEG diamine et le PEI sont présentés dans la Figure 5.



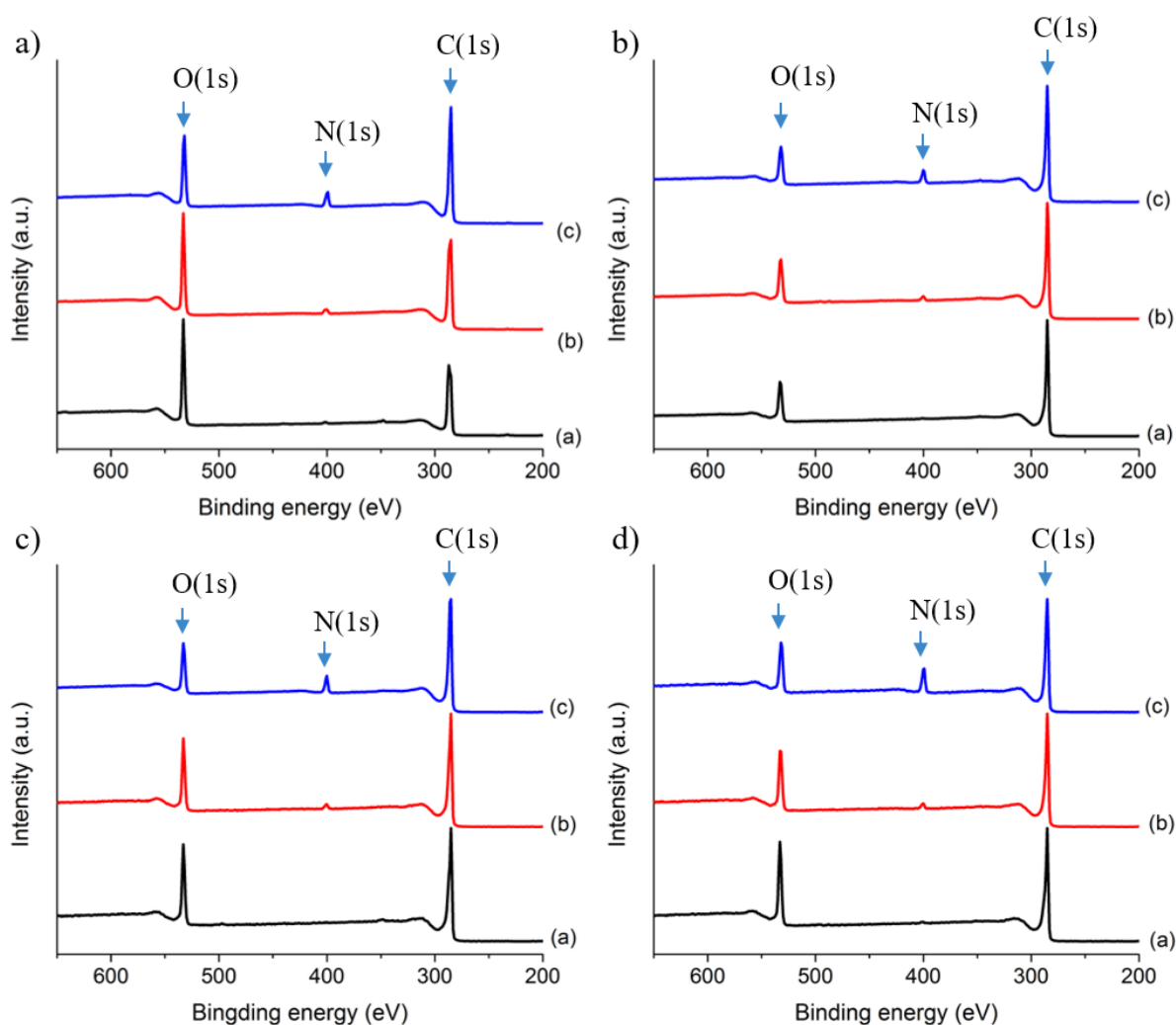


**Figure 5** : Spectres XPS des  $GO_L$  fonctionnalisés avec les amines: a)  $GO_L$  en noir (a),  $GO_L$ -TEG en rouge (b),  $GO_L$ -PEI en bleu (c); b)  $rGO_L$ -5d en noir (a),  $rGO_L$ -5d-TEG en rouge (b),  $rGO_L$ -5d-PEI en bleu (c); c)  $rGO_L$ -C en noir (a),  $rGO_L$ -C-TEG en rouge (b),  $rGO_L$ -C-PEI en bleu (c); d)  $rGO_L$ -5d- $O_3$  en noir (a),  $rGO_L$ -5d- $O_3$ -TEG en rouge (b),  $rGO_L$ -5d- $O_3$ -PEI en bleu (c). L'énergie de liaison du pic C (1s) a été fixée à  $284,5 \pm 0,2$  eV et utilisée comme référence pour calibrer les positions des autres pics.

Le but final de cette étude a été d'évaluer la capacité des différents GO à interagir et à complexer le siRNA. J'ai évalué la capacité de complexation du GO, ainsi que des différents échantillons de GO fonctionnalisés, avec du siRNA. Pour cela, j'ai utilisé un siRNA double brin (petite séquence de 19 bases nucléiques) dont un brin est marqué par la sonde fluorescente Yakima Yellow. La complexation a été effectuée en milieu aqueux sans addition de sels qui pourrait affecter les siRNA. Dans chaque expérience, les différents GOs ont été mélangés dans l'eau avec le siRNA à différents rapports de masse GO/siRNA. J'ai analysé les

interactions supramoléculaires entre la surface des différents GO et le siRNA par gel d'électrophorèse. Le gel d'électrophorèse a permis de comparer les signaux du siRNA avant et après l'interaction avec les GO (Figure 6).

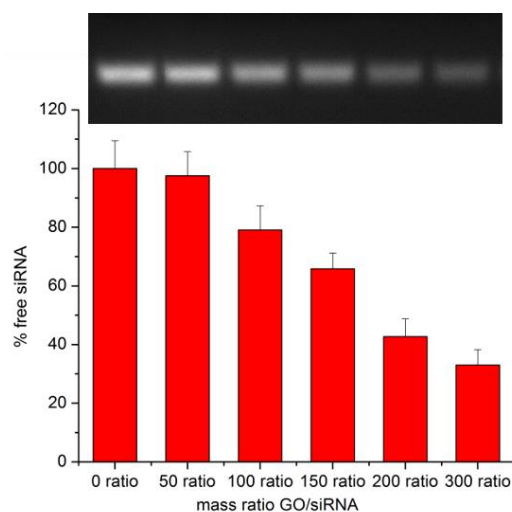


**Figure 6** : Complexation du GO<sub>L</sub>-TEG avec du siRNA. En haut : image obtenue après gel d'électrophorèse, en bas : histogramme représentant le % de siRNA libre pour différents rapports de masse (GO/siRNA).

### 3.3 Investigation des facteurs qui peuvent affecter les interactions des GOs avec le siRNA

Comme nous le savons, le GO a une absorbance élevée en dessous de 300 nm dans les spectres UV-Vis.<sup>16</sup> Ainsi, après avoir effectué l'incubation du siRNA avec le GO, nous avons filtré le complexe GO-siRNA et collecté les molécules de siRNA libres. Plus précisément, j'ai étudié les modifications conformationnelles des siRNA libres après avoir éliminé le GO de la solution. Initialement, j'ai optimisé les conditions afin d'éviter le passage des matériaux à base de graphène non-fonctionnalisés et fonctionnalisés à travers les filtres, ce qui a été confirmé par la non-absorbance à 230 nm due au GO dans le spectre UV-Vis. Pour étudier si nos matériaux à base de GO étaient capables d'induire l'appariement des bases nucléiques, j'ai utilisé un siRNA marqué avec le colorant Yakima Yellow (YY), qui absorbe à 522 nm. L'absorbance de YY est proportionnelle à la concentration réelle des molécules de siRNA en solution tandis que l'absorbance des siRNA à 260 nm peut être affectée par l'appariement des bases.<sup>17</sup>

Parmi les différents GO fonctionnalisés, celui qui contient le PEI a montré une augmentation significative de la complexation avec le siRNA. Le PEI est connu pour interagir efficacement avec des oligonucléotides. Ce polymère, contenant un grand nombre d'amines protonables, interagit de manière efficace avec des siRNA via des interactions électrostatiques. Par ailleurs, par spectroscopie UV-Vis nous avons observé une complexation à un rapport de masse plus faible par rapport au gel d'électrophorèse (Figure 7).

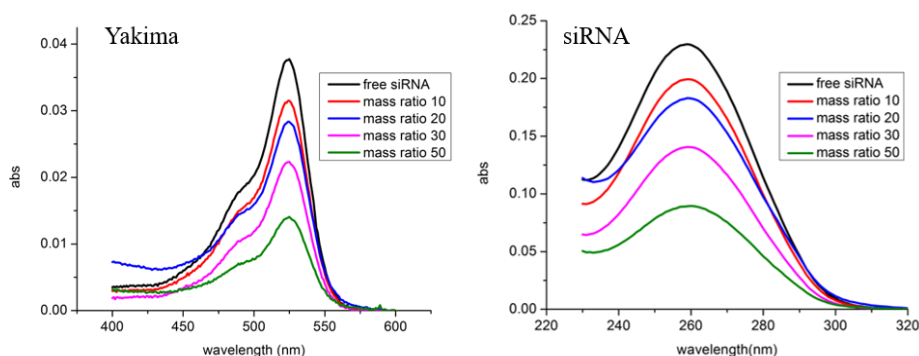


**Figure 7 :** Complexation du rGO<sub>L</sub>-5d-O<sub>3</sub> fonctionnalisé avec le PEI suivie par spectroscopie UV-Vis : absorption de la sonde Yakima Yellow (gauche) et du siRNA (droite) à des rapports de masse GO/siRNA.

Nous nous sommes aussi posés la question de la dénaturation du siRNA après interaction avec le GO. J'ai en effet observé une hyperchromicité du siRNA avec augmentation de l'absorbance dans l'UV-Vis de la bande à 260 nm (Figure 8). L'hyperchromicité a été calculée en considérant le pourcentage d'augmentation de l'absorbance du siRNA à 260 nm après contact avec le GO et l'absorbance du siRNA, à la même concentration, estimée à partir de la courbe d'étalonnage YY. Cet effet hyperchrome est lié à la dénaturation du siRNA.

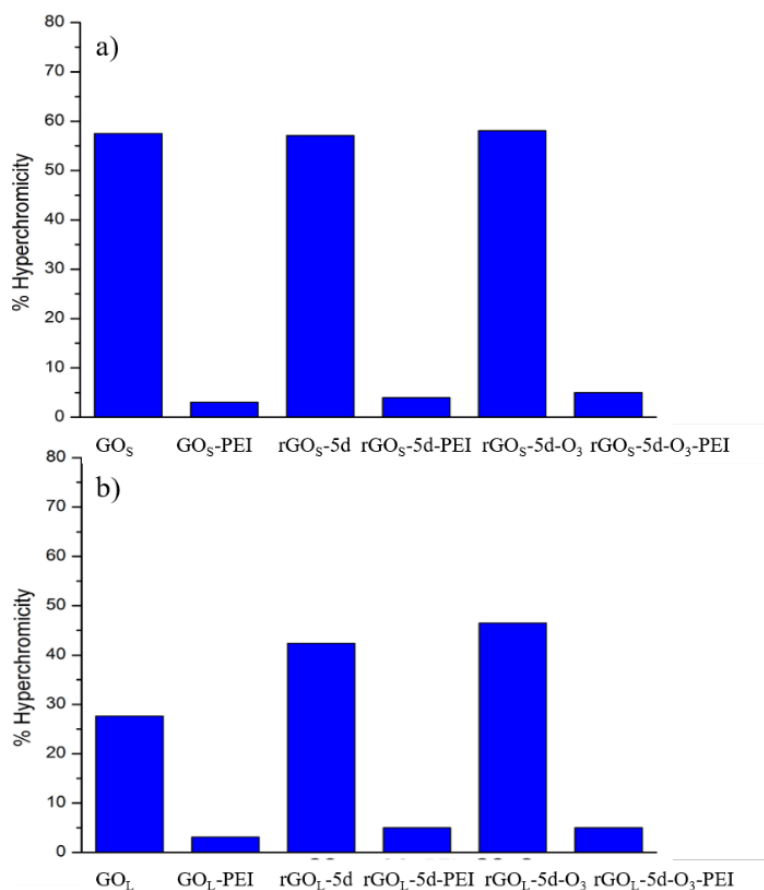


**Figure 8 :** Valeurs d'hyperchromicité des siRNA à 260 nm après incubation avec les différents conjugués GO et PEI. Les données rapportées sont obtenues à partir de deux ensembles de mesures.

Il est intéressant que les échantillons de GO fonctionnalisés avec le PEI montrent un pourcentage d'hyperchromicité inférieur à 5%. Cet effet est probablement dû à l'interaction directe des chaînes PEI qui protègent le déplacement des deux brins du siRNA.<sup>18</sup>

J'ai ensuite utilisé d'autres techniques pour mieux comprendre l'interaction entre le GO et le siRNA. Le dichroïsme circulaire a permis de détecter un changement de conformation du siRNA.<sup>19,20</sup> La technique de FRET a été utilisée pour savoir comment la dénaturation du siRNA s'est produite. Pour cela, nous avons utilisé deux sondes fluorescentes attachées sur les deux brins du siRNA, l'une ayant le rôle du donneur et l'autre d'accepteur pour créer un système de FRET. Les résultats ont montré que les différents échantillons de GO ont non seulement la capacité de complexer le siRNA, mais ils peuvent aussi les dénaturer partiellement. Cette étude a permis une compréhension profonde de l'interaction entre le siRNA à double brin et le GO ainsi que différents GO fonctionnalisés.

En combinant les résultats de l'hyperchromicité, du FRET et de CD, on peut conclure que les molécules de siRNA présentent des modifications structurales évidentes après l'interaction avec GO<sub>S</sub> et GO<sub>L</sub>. Il y a probablement une grande intercalation de GO<sub>S</sub> conduisant à une forte dissociation qui provoque un déplacement modéré des deux brins et induit la transition partielle de l'hélice A. De plus, l'altération de la structure secondaire du siRNA induite par GO<sub>L</sub> est médiée par des interactions non polaires comme les interactions  $\pi-\pi$  (Figure 9).

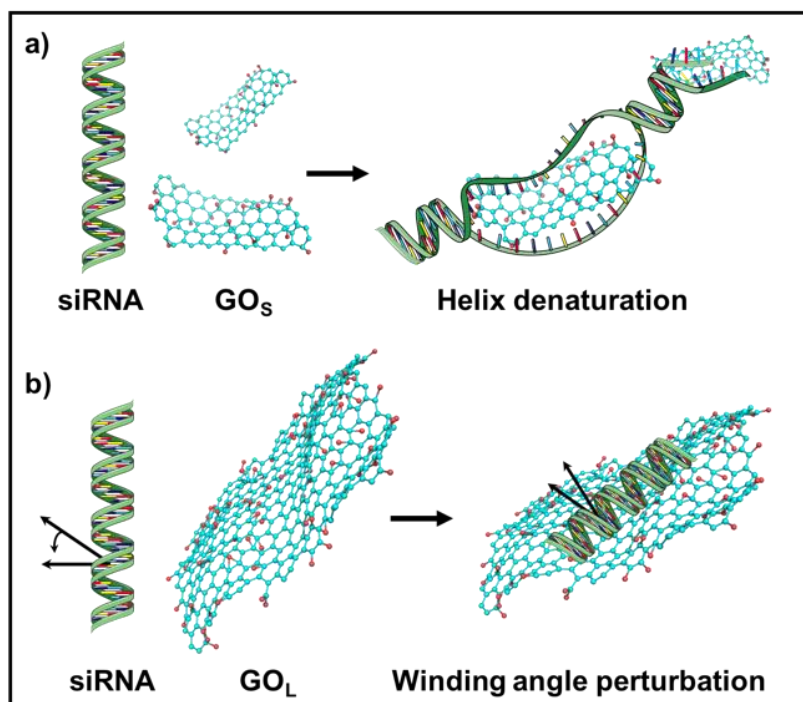


**Figure 9:** Illustration des interactions possibles et des changements conformationnels des molécules de siRNA en contact avec a) GO<sub>S</sub> et b) GO<sub>L</sub>.

En particulier, les échantillons de GO fonctionnalisés avec le PEI n'entraînent pas de changements significatifs sur la structure du siRNA.

Enfin, l'évaluation de l'efficacité de GO et du GO fonctionnalisé pour la délivrance de siRNA a été effectuée dans les cellules HeLa. En effet, nous avons réussi à développer une plate-forme de délivrance des molécules de siRNA qui sont libérées dans les cellules HeLa. Plus intéressant encore, les molécules de siRNA sont bien distribuées dans le cytoplasme cellulaire.

#### 4) Conclusion générale et perspectives

En conclusion, cette thèse a visé à explorer l'interaction de siRNA avec une série de nanomatériaux à base d'oxyde de graphène non-fonctionnalisés et fonctionnalisés de manière covalente avec différentes amines. J'ai conçu et testé diverses approches vertes afin d'obtenir des GOs avec des pourcentages d'oxygène variables par réduction suivie d'une ré-époxydation. J'ai fonctionnalisé ces GOs avec diverses amines grâce à l'ouverture des cycles époxydes. J'ai confirmé que l'azote a été introduit avec succès à la surface de ces nanomatériaux. Cette stratégie pourrait être étendue à d'autres molécules bioactives contenant des groupements amines plus complexes.

De plus, la complexation du siRNA avec les différents échantillons de GO non-fonctionnalisé et les GO aminés ont fait l'objet d'une étude approfondie. Enfin, j'ai évalué l'impact du GO seul sur la conformation du siRNA. En particulier, les échantillons de GO fonctionnalisés avec le PEI peuvent non seulement protéger de cette dénaturation mais aussi favoriser la complexation avec le siRNA. Nous pensons que l'identification et l'optimisation des interactions supramoléculaires qui affectent la complexation sont des points clé pour permettre de préparer des nano-vecteurs à base de GO plus efficaces. Finalement, nous avons réussi à déterminer que les matériaux de graphène sont une plate-forme appropriée pour la vectorisation du siRNA dans les cellules, avec une très bonne distribution de l'oligonucléotide dans le cytoplasme des cellules. Le mécanisme d'internalisation et de libération du siRNA et la capacité à inhiber l'expression des gènes doivent être étudiés attentivement dans le futur.

---

#### 4) Bibliographie

- 1 K. S. Novoselov, A. K. Geim, S. V. Morozov, D. Jiang, Y. Zhang, S. V. Dubonos, I. V. Grigorieva and A. A. Firsov, *Science*, 2004, **306**, 666–669.
- 2 C. Chung, Y. K. Kim, D. Shin, S. R. Ryoo, B. H. Hong and D. H. Min, *Acc. Chem. Res.*, 2013, **46**, 2211–2224.
- 3 H. Y. Mao, S. Laurent, W. Chen, O. Akhavan, M. Imani, A. A. Ashkarran and M. Mahmoudi, *Chem. Rev.*, 2013, **113**, 3407–3424.
- 4 G. Reina, J. M. González-Domínguez, A. Criado, E. Vázquez, A. Bianco and M. Prato, *Chem. Soc. Rev.*, 2017, 4400–4416.
- 5 M. Nurunnabi, K. Parvez, V. Revuri, H. A. Khan, X. Feng and Y. Lee, *RSC Adv.*, 2015, **5**, 42141–42161.
- 6 M. Vincent, I. De Lázaro and K. Kostarelos, *Gene Ther.*, 2016, **24**, 123–13279.
- 7 K. V. Krishna, C. Ménard-Moyon, S. Verma and A. Bianco, *Nanomedicine*, 2013, **8**, 1669–1688.
- 8 D. Chen, H. Feng and J. Li, *Chem. Rev.*, 2004, **112**, 6027–6053.
- 9 D. R. Dreyer, S. Park, C. W. Bielawski, R. S. Ruoff, J. M. Tour, K. Müllen, A. Ivaska, R. G.-S. Goh, R. H. Friend, A. T. S. Wee, P. K.-H. Ho, D. Chen and R. S. Ruoff, *Chem. Soc. Rev.*, 2010, **39**, 228–240.
- 10 N. Morimoto, H. Suzuki, Y. Takeuchi, S. Kawaguchi, M. Kunisu, C. W. Bielawski and Y. Nishina, *Chem. Mater.*, 2017, **29**, 2150–2156.
- 11 K. A. Whitehead, R. Langer and D. G. Anderson, *Nat. Rev. Drug Discov.*, 2009, **8**, 129–138.
- 12 Z. R. Yang, H. F. Wang, J. Zhao, Y. Y. Peng, J. Wang, B.-A. Guinn and L. Q. Huang, *Cancer Gene Ther.*, 2007, **14**, 599–615.
- 13 K. Yang, L. Feng, X. Shi and Z. Liu, *Chem. Soc. Rev.*, 2013, **42**, 530–547.
- 14 Z. E. Hughes and T. R. Walsh, *J. Mater. Chem. B*, 2015, **3**, 3211–3221.
- 15 S. Kim, Y. Yoo, H. Kim, E. Lee and J. Y. Lee, *Nanotechnology*, 2015, **26**, 405602.
- 16 J. Shang, L. Ma, J. Li, W. Ai, T. Yu and G. G. Gurzadyan, *Sci. Rep.*, 2012, **2**, 792.
- 17 D. E. Draper, Y. Xing and L. G. Laing, *J. Mol. Biol.*, 1995, **249**, 231–238.
- 18 N. D. Q. Chau, G. Reina, J. Raya, I. A. Vacchi, C. Ménard-Moyon, Y. Nishina and A. Bianco, *Carbon*, 2017, **122**, 643–652.
- 19 D. J. Phillips and A. M. Bobst, *Biochem. Biophys. Res. Commun.*, 1972, **47**, 150–156.
- 20 J. Kypr, I. Kejnovská, D. Renciuik and M. Vorlíčková, *Nucleic Acids Res.*, 2009, **37**, 1713–25.

## CHAPTER 1: INTRODUCTION

### 1.1 Graphene Oxide

Since its isolation in 2004 by Geim and Novoselov, graphene has emerged as a fascinating nanomaterial with unique structure and physical properties.<sup>1</sup> The potential applications of graphene family have gained an intensive interest in many fields including biology and nanomedicine.<sup>2</sup> However, one of the big disadvantages of graphene into these fields is its low dispersibility that hampers full exploitation of its properties.

In this context, one of the graphene family materials that is playing a crucial role in the bioapplication is graphene oxide (GO).<sup>3</sup> GO is a useful platform for the design of graphene-based hybrid materials.<sup>4</sup> It consists of a single layer of graphite oxide and it is usually produced by oxidation of graphite using strong acid solutions. In comparison to its graphene parent that is composed of only  $sp^2$  hybridized C, GO contains a substantial degree of  $sp^3$  hybridized C with the presence of various oxygenated groups (i.e. hydroxyls, epoxides, carbonyl, etc.) on its surface. Such range of polar oxygen-containing functional groups introduce a profound impact on the properties of GO, especially on a good dispersity in water and many other polar solvents. In addition, the derivatization of these oxygenated functions is a versatile and effective method to prepare chemically functionalized graphene oxide as a remarkable material for a wide range of applications.<sup>5</sup>

#### Preparation protocols of GO

Large-scale production of GO is based on top-down approaches using strong acids and oxidants to chemically oxidize graphite under different conditions (through Hummers method,<sup>6</sup> modified Hummers methods,<sup>7</sup> Brodie method,<sup>8</sup> Staudenmaier method<sup>9</sup> or by electrochemical oxidation<sup>10</sup>) followed by exfoliation. In the common modified Hummers methods, graphite is treated with potassium permanganate and various additives in sulfuric acid. Then, by graphite oxide exfoliation, single layer of GO was obtained with a high negative surface charge, composed of a variety of oxygen groups on the sheets and on the edges.<sup>11</sup> However, the mechanism of the oxidation process forming GO remains unclear, thus challenging the production of large amounts of GO with a high batch-to-batch reproducibility.<sup>12</sup> Overall, the first step in Hummers modified oxidation method is the conversion of graphite into graphite intercalated compound (GIC),<sup>13</sup> followed by the formation of graphite oxide and graphene



oxide as the last step (Figure 1.1). Depending on how the GO is prepared and the source of graphite precursor, the stoichiometry of GO's oxygenated groups can be different, leading to different materials with different behaviors.<sup>5,14</sup>

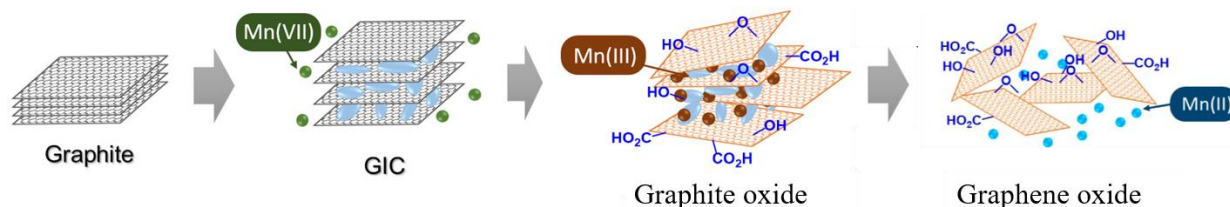


**Figure 1.1:** Preparation of graphene oxide, adapted from ref [12].

### Structure and properties of GO

The exact structure of GO has been a contradictory subject over the years: identifying and quantifying the oxygen groups on the surface of GO are still ambiguous and are considered as an important challenge. Various structural models (Hofmann, Ruess, Scholz-Boehm, Nakajima-Matsuo)<sup>5</sup> have been proposed. Lerf-Klinowski<sup>15</sup> has been the most widely accepted structural model of GO, which defined two regions on the surface of GO: one of highly oxidized predominately  $sp^3$  C and second of slightly oxygenated, predominately  $sp^2$  C like graphene (Figure 1.2). According to this model, the hydroxyl and epoxy groups are on the basal plane, while as the carboxylic groups are located on the edges of the GO sheets. These polar oxygen-containing functional groups render GO highly hydrophilic, leading to a good dispersibility in water and other solvents. In addition, the derivatization of these oxygenated functions is a versatile and effective strategy to prepare chemically functionalized GO for a wide range of applications. In particular, the great affinity for biomolecules and the large surface area ( $\sim 736.6 \text{ m}^2/\text{g}$ )<sup>16</sup> makes GO a good candidate as nanocarrier for drug-delivery. Moreover, GO possesses hydrophobic graphenic domains like graphene and a hydrophilic area. Therefore, the GO amphiphilic characteristic gives it the ability of loading water-insoluble drug for delivery. In summary, due to its unique morphology and structure as well as its favorable physicochemical properties and remarkable features, GO has shown a great potential in biomedical applications and has become a suitable carrier for a variety of bioactive molecules, for cancer therapy, molecular imaging, and drug and gene delivery.<sup>2,5,17</sup>

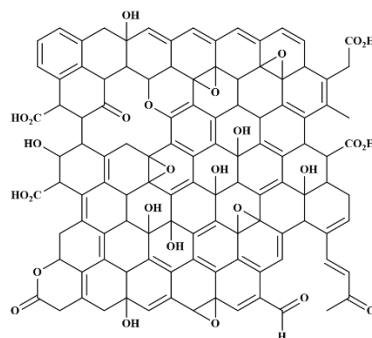


**Figure 1.2:** Lerf-Klinowski structural model of GO, adapted from ref [14].

### Characterization methods

In general, the characterization of GO is performed for two main purposes: one is to assess its stoichiometry in terms of the functionalized groups, and one is to describe its physical morphology (size, surface area, lattice defects, number of layers, etc.). For the chemical functionality, various well-known techniques have been used such as X-ray photoelectron spectroscopy (XPS),<sup>18</sup> which allows to identify chemical composition, or the identity and the ratio of the elements and of the functional groups present on the surface; Fourier-transform infrared spectroscopy (FT-IR),<sup>19</sup> which identifies the presence of functional groups; solid-state nuclear magnetic resonance spectroscopy (ssNMR),<sup>20</sup> which also give information on functional groups; different electrochemical methods<sup>21</sup> and various chemical reactivity tests<sup>15,22</sup>. For the morphology, various microscopy techniques have been used including atomic force microscopy (AFM),<sup>23</sup> which reveals the thickness and the number of layers; transmission electron microscopy (TEM),<sup>24</sup> which shows shape and also gives information on the thickness; scanning electron microscopy (SEM),<sup>25</sup> which shows size and shape. Moreover, other techniques have been used such as powder X-ray diffraction (XRD)<sup>26</sup> to determine the interlayer distance in GO, Raman spectroscopy to evidence the defects present on the lattice as well as the stacking layers, etc. In addition to these methods that provide basic physicochemical properties of GO, more specialized techniques have been used depending on its application. For instance, in drug and gene delivery, most of the used characterization are: cellular viability assays for determining GO's biocompatibility, ultraviolet–visible spectroscopy (UV-Vis) for the interaction of GO with other molecules, zeta ( $\zeta$ ) potential for measuring the changing of surface charge after loading polymers and drugs, dynamic light scattering (DLS) for additional

information on size variation after each modification, and fluorescence for detecting the quenching effect as well as the interaction of GO with others fluorescent molecules.

## **1.2 Promise, facts and challenges of graphene oxide in biomedical applications**

Although GO disperses well in water, it may aggregates in cell culture media (buffers) in the presence of salt due to the charge screening effect.<sup>27</sup> Therefore, the surface modification of GO becomes a key factor in creating a delivery platform with good biocompatibility and controlled behavior in biological systems. Depending on the purpose of application, two main roads for modification of GO's surface have been explored and established using either non-covalent or covalent approaches.

### **1.2.1 Non-covalent and covalent approaches**

#### **1.2.1.1 Non-covalent interactions and their driving forces**

GO and reduced graphene oxide (rGO), are characterized by a basal plane composed by two domains consisting on a low-polar area that resembles the graphene surface and a polar defected surface characterized by oxygenated group functions. Due to these features, besides the physisorption driven by the  $\pi$ - $\pi$  interactions that likely occur as in the case of graphene, other interactions can contribute to the anchoring of external molecules on GO surface like hydrogen bonding (H-bonding) with the epoxides, alcohols, ethers, and carboxylic groups. Therefore, non-covalent functionalization of GO with biomolecules, polymers or drugs involves the  $\pi$ - $\pi$  stacking, electrostatic interaction, and H-bonding. Here in, we introduce a brief discussion regarding the driving forces of these non-covalent functionalization. In contrast to covalent conjugation that can introduce surface defects and affect the electronic properties, the non-covalent functionalization does not alter the structure nor the rehybridization of the carbon atoms. In addition, adsorption of varies molecules appears on both sides of the basal plane with the existence of the  $\pi$ - $\pi$  system, thus leading to a very high loading of specific compounds.

Normally, the van der Waals forces are occurring between GO and organic molecules or polymers with high hydrophobic character, while as  $\pi$ - $\pi$  interactions are common between GO and planar molecules with extended  $\pi$  system, like pyrenes derivatives. In fact, the  $\pi$ - $\pi$  interactions require both the existence of a  $\pi$  system and the geometry of the complementary component. It is necessary that the two components have a strong interaction based on their overlap that are usually favored by their planarity. For example, organic molecules with pyrene

terminated chains were used to functionalize rGO *via*  $\pi$ - $\pi$  stacking.<sup>28,29</sup> Yang et al.<sup>30</sup> assembled folic acid-modified  $\beta$ -cyclodextrin on GO, after being non-covalent functionalized with adamantane-grafted porphyrine *via*  $\pi$ - $\pi$  stacking. A common drug like doxorubicin (DOX) was also attached onto GO *via*  $\pi$ - $\pi$  stacking, followed by the encapsulation of GO with folic acid (FA) conjugated chitosan (CS) to improve the complex stability.<sup>31</sup>

In some cases, the intrinsic optical characteristics of GO can interfere with most of the optical spectroscopies such as UV-Vis or photoluminescence. One of the most common strategies of GO-based biosensor depends on its high efficiency on fluorescence energy transfer from a dye to GO.<sup>32</sup> In this case, adsorption of a target fluorescent molecule can be monitored following its emission quenching due to the GO proximity. A classic example regards its interaction with nucleic acids. For instance, *via*  $\pi$ - $\pi$  interaction and H-bonding, fluorescently-labeled single strand DNA (ssDNA) can strongly adsorb onto GO, thus causing the dye emission quenching. The signal of the fluorescent dye could be recovered once the probe forms a duplex with a complementary DNA sequence, indicating the release of the probe from GO. Lu et al.<sup>33</sup> used this technique for the case of detection ssDNA labeled with FAM (a fluorescein-based dye) onto GO (Figure 1.3). In another example based on the fluorescence quenching property of GO, Janardhan et al.<sup>34</sup> developed a fluorescent quenched charge transfer complex of positive charge 4-(1-pyrenylvinyl)-N-butylpyridinium (PNP) onto GO, named PNP+GO-. Because the ionic attraction of DNA for PNP<sup>+</sup> is greater than the one of GO, DNA-pyrene is released from the GO surface, turning on the fluorescence of pyrene derivative.

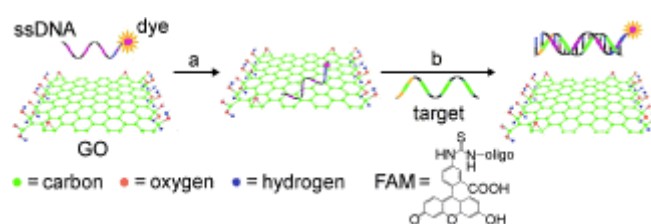


**Figure 1.3:** Schematic representation of the target induced fluorescence change of the ssDNA FAM/GO complex. Adapted from ref [33].

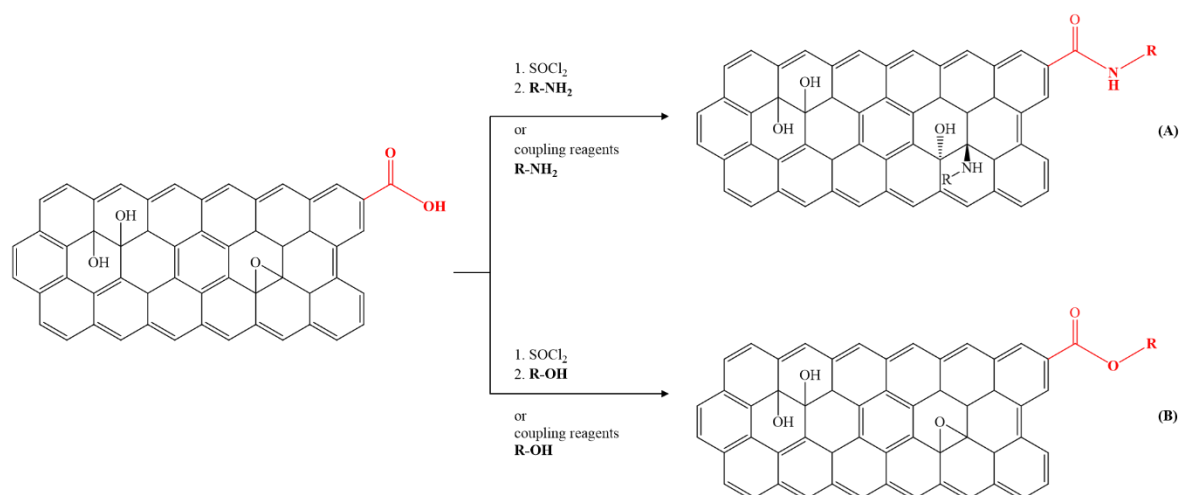
Generally, the binding between GO and ssDNA or single strand RNA (ssRNA) is ascribed either to the  $\pi$ - $\pi$  stacking involving both purine and pyrimidine bases of DNA or the hydrogen bonding and van der Waals forces.<sup>35</sup> Furthermore, ionic interaction between amphiphilic molecules and GO and rGO was also investigated to improve the dispersibility of GO and rGO

in organic solvents. For example, Liang et al.<sup>36</sup> showed that GO and rGO can be functionalized with quaternary ammonium salts such as didodecyldimethylammonium bromide to transfer GO and rGO from water phase to chloroform phase. The hydrophilic and positive “heads” of the surfactants adsorb on graphene sheet through electrostatic interactions, while the aliphatic chains of the surfactants provide necessary lipophilicity and stability of GO and rGO in chloroform.

### 1.2.1.2 Covalent functionalization

As mentioned before, GO has many reactive oxygen functionalities with hydroxyl functions and epoxide groups on the basal plane, and carboxyl, carbonyl, phenol, lactone, and quinone groups at the edges.<sup>37–39</sup> Therefore, the presence of reactive oxygenated groups on the surface of GO allows a covalent functionalization exploiting different types of reactions like nucleophilic substitution, electrophilic addition, condensation and radical addition. The functionalization of GO can be divided into two main categories: one is the peripheral conjugation to carboxylic acids on the edges and one is the basal plane conjugation to epoxy and hydroxyl groups.

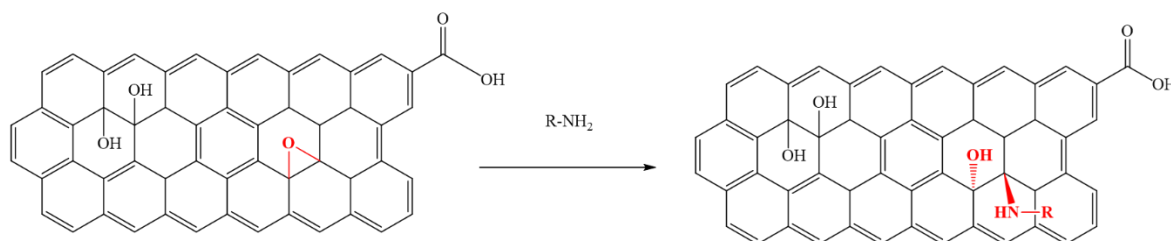
Carboxylic group functionalization is generally performed with the acylation reaction (esterification or amidation). Indeed, carboxylic acids can easily be activated by  $\text{SOCl}_2$  or through coupling agents such as N-hydroxysuccinimide (NHS), 1-hydroxybenzotriazole hydrate (HOBt) or 1-ethyl-3-(3-dimethylaminopropyl)-carbodiimide (EDC), then subsequently reacted with many nucleophiles (i.e. amines or alcohols) that lead to the formation of ester and amide bonds, respectively (Scheme 1.1). These routes can be applied not only to small molecules,<sup>40</sup> but also to antibodies,<sup>41,42</sup> CS,<sup>43</sup> and other polymeric compounds<sup>44,45</sup>. In all these cases, one major issue should be considered: that multiple reactions occur simultaneously. For example, epoxy ring opening is happening during the amidation as shown in Scheme 1.1A.



**Scheme 1.1:** Covalent functionalization of GO by amidation (A) and esterification (B). For the sake of clarity, a simplified model of GO with only one functional moiety is shown.

Similar to carboxylic acids, the hydroxyl groups can undergo a carbodiimide coupling. In this case, the hydroxyl groups serve as a nucleophile to condense with the activated carboxylic acids. Another reaction route of hydroxyl groups is the condensation with isocyanates *via* formation of carbamate esters.<sup>46</sup> Alternatively, the hydroxyl groups can react with trialkoxysilanes to afford Si-O-C bond.<sup>47,48</sup> In a comparative study, due to a higher amount of hydroxyl groups than carboxylic acid functions on GO sheets, the efficiency of silanization on hydroxyl groups is much higher than that of amidation on carboxylic groups of GO.<sup>49</sup>

Moreover, the epoxy groups easily react with amino functionalities (-NH<sub>2</sub>) *via* a nucleophilic ring opening reaction (Scheme 1.2).<sup>50</sup> This is a simple reaction that can be performed at room temperature in an aqueous medium, without adding any other catalysts. As a consequence it can be considered a promising method for large-scale modification with all type of molecules from aliphatic or aromatic amines to amine-terminated biomolecules or polymers, etc.<sup>5,51,52</sup> This amine-functionalized GO has been applied in different areas, such as biodevices,<sup>53</sup> polymer composites,<sup>54</sup> optoelectronics,<sup>55</sup> and drug delivery<sup>44</sup>. For instance, Bourlinos et al.<sup>56</sup> have covalently attached onto GO a range of alkyl-amines from two to eighteen carbon atoms and amino acids.



**Scheme 1.2:** Amino functionalization of GO via nucleophilic epoxy ring opening. For the sake of clarity, a simplified model of GO with only one functional moiety is shown.

Besides, thanks to its classical C  $sp^2$ , a variety of typical reactions can be performed onto GO, such as 1,3-dipolar additions, radical reactions, Diels–Alder reactions, etc.

Furthermore, due to the presence of aromatic domains and multiple oxygen functional groups, it is easy to perform both covalent and non-covalent functionalization chemistry on GO sheets to make it become more interesting for potential applications in biological systems.<sup>57–59</sup>

### 1.2.2 Graphene oxide based therapy

Among many types of nanomaterials, carbon based nanomaterials, especially graphene family materials, have been extensively explored, opening their exploitation in biomedicine.<sup>60–62</sup> Indeed, owing to large surface area, good biocompatibility, tunable surface chemistry, high water dispersibility and low-cost scalable production, GO has become a potential candidate over other nanocarriers in term of interaction with biomolecules such as DNA, peptides, and proteins.<sup>63–66</sup> In particular, the study of the interactions of GO with nucleic acids have been substantially enhanced over the past few years for the application in biosensing, diagnostics and biomedicine.<sup>2,67</sup> Moreover, its optical absorption in the near-infrared (NIR) region makes GO as a powerful photothermal agent, while its intrinsic photoluminescence is useful in cell imaging. Herein, we will resume in detail the potential applications of GO in biomedical field including drug and gene delivery, phototherapy, and biomedical imaging.

#### 1.2.2.1 Drug and gene delivery

The most challenge in building a versatile drug and gene carrier concerns the search of a system with the capacity of a high loading of therapeutics, and an efficient specific targeting delivery without harmful effects on the other tissues and organs. GO was widely reported as an efficient non-viral carrier of various therapeutics, including anticancer drugs, poorly soluble drugs, antibodies, antibiotics, DNA, RNA, etc.<sup>68–70</sup>



One of the first examples in non-targeting drug delivery described the direct immobilization of DOX onto GO large surface (DOX loading of 2.35 mg per mg of GO).<sup>71</sup> The H-bonding between the carboxylic groups of GO and the amino groups of DOX was confirmed *via* the pH loading dependence and release of DOX from GO, while as the existence of strong  $\pi$ - $\pi$  interaction between the aromatic rings of DOX and GO was proved by fluorescent and electrochemical characterization.

Based on the characteristic of GO, a combination of both covalent and non-covalent chemistry can be applied. GO lends also to multifunctionalization as it has been widely demonstrated. In general, molecules like dispersants or targeting ligands are first covalently attached to GO while as drugs, which are mainly lyophilic, are then adsorbed onto GO surface *via* low polar interaction such as  $\pi$ - $\pi$  stacking. This simple and versatile strategy helps to enhance the dispersibility of the platform in cellular culture, to reduce the cytotoxicity and to increase the drug efficacy. For example, functionalization with polymers can prevent GO aggregation in cell culture medium<sup>72</sup> and can also enhance circulation times of GO *in vivo*.<sup>70</sup> Polyethylene glycol (PEG), a biocompatible hydrophilic polymer with high stability in serum,<sup>73</sup> has been widely used for covalent conjugation with GO via amide bond formation. Subsequently, the GO-PEG has been functionalized with insoluble drug such as analogue of camptothecin,<sup>44</sup> paclitaxel,<sup>74</sup> etc. The platform of GO-PEG complexing drugs prolonged drug blood circulation time by avoiding opsonization leading to a high efficiency in tumor-targeting and suppressing.<sup>75</sup> Other polymers such as hydrophilic polyacrylic acid,<sup>76</sup> polycationic natural polymer like CS<sup>43</sup> have been also tested.

In term of non-targeting drug and gene delivery, Zhang et al.<sup>77</sup> developed a polyethylenimine (PEI) conjugated GO system for co-delivery of small interfering RNA (siRNA) and DOX *in vitro*. PEI(25K) was first covalently attached to GO *via* formation of amide bond using EDC, then siRNA and DOX were simultaneously loaded by electrostatic interaction and  $\pi$ - $\pi$  stacking, respectively. Interestingly, sequential delivery of siRNA and DOX in Hela cells displayed a strong synergistic effect. In fact, Hela cells were first incubated with Bcl2-targeted siRNA, followed by PEI-GO/DOX. The results reported a decreasing of IC<sub>50</sub> value (concentration of a drug that kills 50% of cells) from 1.3  $\mu$ g/ml for the control PEI-GO/scrambled siRNA/DOX to 0.52  $\mu$ g/ml for PEI-GO/Bcl2-targeted siRNA/DOX, thus affording an enhanced chemotherapy efficacy.



Although there have many carriers, such as inorganic nanoparticles, polymer-based systems, lipid-based systems, that improve the drug solubilization and blood circulation half-life; low targeting accumulation and low conjugation efficiency remain a constrain in the therapeutic efficiency at the tumor sites. Nevertheless, the side-effects of non-specific accumulation in normal tissues as well as the insufficiency of cellular uptake require a novel and intelligent design of carriers. Therefore, to enhance the cellular uptake, to control the drug release and to selectively deliver genes and drugs on specific tumor sites, different tumor targeting moieties (i.e. antibodies,<sup>78</sup> peptides,<sup>79</sup> folic acid,<sup>80</sup> aptamer,<sup>81</sup> etc) have been introduced onto GO surface to recognize the corresponding "molecular signature" on cellular surface. These active targeting moieties on GO favor the accumulation of the platform at the desired tissues, thus enhancing the therapeutic effects while decreasing the side effects of the drug.

In term of targeting delivery, a dual carrier for delivering DOX and siRNA to overcome drug-resistant MCF-7/ADR cancer cells was reported by Zeng et al.<sup>82</sup> (Figure 1.4). First, PEG-NH<sub>2</sub> was covalently attached on GO *via* ring-opening epoxide reaction in the presence of KOH at 80°C,<sup>83</sup> then PEI(10K) was linked to the carboxylic group of PEG-GO using EDC /NHS coupling to form PPG. Then, FA, recognized by folate receptors overexpressed on cancer cell surface, was conjugated with PPG (PPG-FA) *via* amide bond formation between carboxylic group of FA and the amino groups of PPG. PPG-FA was loaded with siRNA *via* electrostatic interaction and DOX *via*  $\pi$ - $\pi$  stacking. The results showed that the PPG-FA/siRNA/DOX exhibits a significant cellular uptake, an increased DOX penetration into the nuclei, and an enhanced DOX cytotoxicity on the MCF-7/ADR cells in comparison to free DOX, or PPG-FA/DOX devoid of PEG. Interestingly, the authors also proved that the combination treatment of chemotherapy with photothermal treatment showed synergistic effects compared with only chemotherapy effect alone.

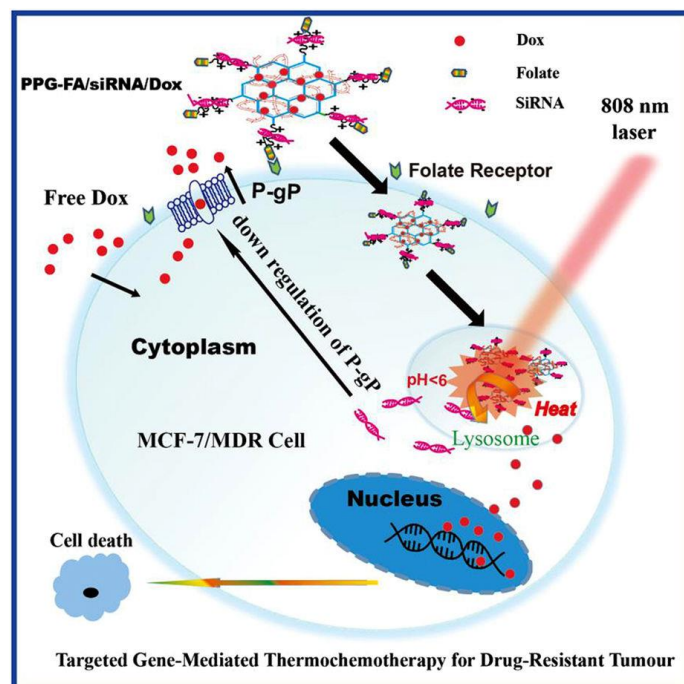


**Figure 1.4:** Targeted gene-mediated thermo-chemotherapy for drug-resistant tumor adapted from ref [82].

Generally, drug controlled release is based on the change of the environment between the extracellular matrix and the cytoplasm. Up to date, several physiological approaches such as body temperature, pH, specific chemical reactivity or external methods such as magnetic or electric field, ultrasound have been applied in controlling drug release. For example, one of the first reports in using superparamagnetic GO/Fe<sub>3</sub>O<sub>4</sub> nanoparticle hybrids loading DOX to control targeted drug delivery was proposed by Yang et al<sup>84</sup>. This hybrid, with or without DOX, aggregated under acidic conditions, reversibly re-dispersed under basic conditions. More interestingly, after aggregating at low pH, the GO/Fe<sub>3</sub>O<sub>4</sub> hybrid could be dragged by applying an external magnetic field. Thus, the transfer efficiency of drug vectors was greatly improved by magnetic field targeting. This also indicated that at acidic pH, some functional groups on the GO, such as carboxylic acid groups, even after loading with a large amount of Fe<sub>3</sub>O<sub>4</sub> and DOX were still free for efficient formation of H-bonding, making this hybrid a promising pH-triggered targeting carrier. Due to its pH-triggered magnetically controlled capabilities, this hybrid was functionalized with different biomolecules or drugs such as FA<sup>85,86</sup> and 5-fluorouracil (5-FU),<sup>87</sup> for specific multi-targeting or multidrug loading and delivery. At acidic conditions, protonation of the amine group of DOX could break the hydrogen bonding between DOX and GO, leading to a quick release of the drug. Hence, the multifunctionalized GO was

able to first transport the drugs to the targeted tumor cells by the force of an external magnetic field localized at the site of the tumor, and then the drug-loaded carriers were taken up by the tumor cells.<sup>88</sup>

In addition, to visualize whether the drugs and genes were delivered, GO was also functionalized with organic dyes, luminescent particles or radioactive compounds with the attention on the ability of luminescence quenching of GO.<sup>89</sup>

### 1.2.2.2 Photothermal therapy and photodynamic therapy

Chemotherapy plays a crucial role in the therapeutic modalities for the treatment of cancer diseases. However, nonspecific delivery of the chemotherapeutics and the radiotherapeutics reduces the efficiency on cancer cell ablation, and leads to undesired side effects to normal tissues and organs. Nowadays, the trend of combination of different therapeutic approaches in cancer treatment is widely increased. Compared with chemotherapy alone, a combined therapy would decrease the dosage of drugs that needed to treat patients and thus may result in lower side effects during treatment.<sup>90</sup>

Phototherapies, including photothermal therapy (PTT) and photodynamic therapy (PDT), can destruct cancer cells *via* specific light irradiation.<sup>60</sup> With the help of nanotechnology, phototherapeutic nano-agents can specifically address cancer *via* either passive or active tumor targeting. Furthermore, the advantage of phototherapies is their selectivity on only the harmful tumors, which exposed to light irradiation, can be killed by phototherapy, without severe damage to normal organs. Therefore, phototherapies exhibit remarkable advantages in terms of enhancing cancer killing specificity and reducing side effects, in comparison to conventional cancer therapies. In the past few years, phototherapies based on the unique optical and chemical properties of graphene-based materials have aroused increasing interest.

The principle of PTT is based on using of optical-absorbing materials to generate heat under light irradiation, thus generating heat sufficient to promote the destruction of cancer cells.<sup>91</sup> The NIR light (700-1100 nm) has become attractive for this induction of hyperthermia because organs and tissues are transparent in NIR region. As mentioned above, GO has gained attention in this field due to its strong NIR absorption. Graphene-based materials have shown great promise in photothermal treatment of cancer.<sup>92,93</sup>

Zhang et al.<sup>92</sup> developed a DOX-loaded PEGylated GO (GO-PEG-DOX) to facilitate the combined chemotherapy and photothermal treatment in one system. Both *in vitro* and *in vivo* tests on murine mammary tumor line EMT6 revealed that the designed system can deliver both the heat and drug to the tumorigenic region. Moreover, the combined therapy demonstrated a synergistic effect, resulting in higher efficacy than chemotherapy or photothermal therapy alone. Alternatively, reduced GO has become widely used in PTT for its remarkable enhancement of optical absorbance in the NIR region compared to GO. Robinson et al.<sup>94</sup> reported that ultra-small rGO, which was prepared by initial PEGylation of GO, reduction of the obtained GO-PEG, and further coating with additional PEGylated phospholipid afforded a ~7-fold increase in NIR absorption capacity at 808 nm. Then, rGO was conjugated with an arginine-glycine-aspartic acid (RGD) peptide, and acted as a highly efficient targeted photothermal agent for *in vitro* selective U87MG cancer cell ablation. Kim et al.<sup>95</sup> reported a pH-dependent contrast agent for cancer cell specific fluorescent imaging and photothermal therapy using NIR active dye IR825, conjugated with poly(ethylene glycol)-g-poly(dimethylaminoethyl methacrylate) (PEG-g-PDMA, PgP), and hyaluronic acid (HA) anchored to rGO. The rGO complex, owing a pH dependent fluorescence emission and an excellent NIR irradiation on cancer cells, exhibited the potential in controlling fluorescence quenching for regulation of the triggered photothermal heat.

The principle of PDT is based on reactive oxygen species (ROS) or free radicals that are produced from the irradiation of photosensitizers (PS) under suitable light, leading to cancer cells death.<sup>96</sup> The use of graphene oxide as carriers of PS is a promising method in clinical applications.<sup>97</sup> Huang et al.<sup>98</sup> reported that FA-conjugated GO was able to load PS molecule chlorin e6 (Ce6) *via* hydrophobic and  $\pi$ - $\pi$  stacking. The prepared nanocarrier could significantly increase the accumulation of Ce6 into tumor cells and achieved a significant photodynamic efficacy on MGC803 cells using a 633 nm He-Ne laser irradiation. These results suggest that PS-based GO complexes have great potential as effective drug delivery systems in targeting PDT.

### 1.2.2.3 Biomedical imaging

To observe the characteristics or behavior of targeted biomolecules *in vitro* and *in vivo*, and to reveal where they are exactly localized and where they have delivered the drug or have accumulated into the cells and into living subjects, biomedical imaging has gained a profound

interest.<sup>99</sup> Due to its versatile surface functionalization and high surface area, GO can be conjugated with different compounds for various molecular imaging modalities including optical imaging using fluorescent molecules, radionuclide-based imaging, magnetic resonance imaging (MRI). It should be noticed that each imaging modality has its own advantages and disadvantages that should be considered when a platform of bioimaging is developed. For instance, the fluorescence imaging, which is based on the photons emitted from fluorescent probes, should afford quantitative results while there are sometimes interferences from the fluorescence quenching effect of GO. Although the radionuclide imaging can overcome the quantitative concerns of optical imaging by measuring the radioisotope concentration especially *in vivo*, this technique faces the challenge in its poor spatial resolution. This low resolution is also the disadvantage of MRI in imaging single cells.

Based on the intrinsic photoluminescence of GO, Sun et al.<sup>45</sup> have studied for the first time the NIR photoluminescence of GO-PEG for cell imaging. In this study, the anti-CD20-antibody Rituxan was covalently conjugated to GO-PEG for B cell specific imaging using an InGaAs detector under 658 nm laser excitation. However, the low quantum yield of GO-PEG fluorescence limited its imaging efficiency *in vivo*. Therefore, GO functionalized with fluorescent dyes have been used as an imaging probe with the attention on the natural ability of quenching of GO that required to guarantee optimized distances of these dyes from GO surface.<sup>100,101</sup> Besides conjugation with fluorescent dyes,<sup>102,103</sup> graphene-based materials have been loaded with inorganic nanomaterials like quantum dots (QD) for fluorescence imaging. Hu et al.<sup>104</sup> introduced a low toxicity, multifunctional rGO-QD based on electrostatic interaction of poly(L-lysine)-rGO (PLL-rGO) and 11-mercaptopundecanoic acid (MUA) capped CdSe/ZnS QDs. QD-rGO was used as an imaging agent in the visible region and as photothermal agent in the NIR region. One of the advantages of this system is that the fluorescence quenching effect of GO was drastically reduced *via* the introduction of PLL and MUA as spacers between QD and rGO (Figure 1.5).

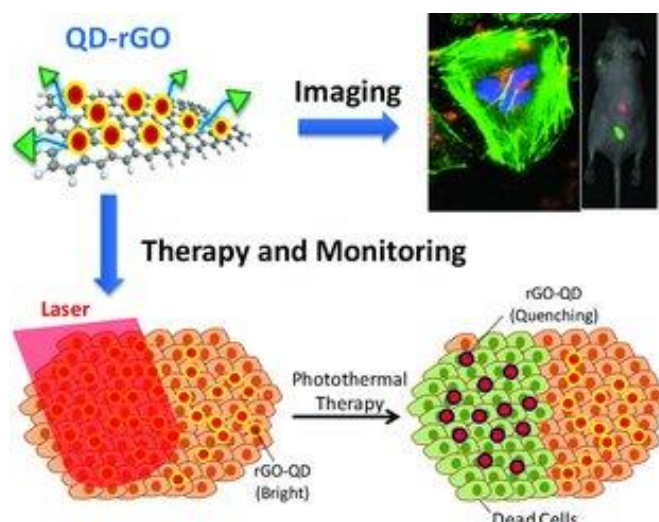


**Figure 1.5:** Quantum dot targeted rGO for bright fluorescence bioimaging and photothermal therapy, adapted from ref [104].

One of the powerful *in vivo* non-invasive imaging method that has been widely used in clinical practice is based on the magnetic resonance to observe tissues. However, because the spin-lattice (longitudinal) relaxation time (T1) and the spin-spin (transversal) relaxation time (T2) of water proton's, MRI contrast agents have been actively explored to enhance the relativity to overcome its low sensitivity and long signal acquisition time. T1 agents provide brighter images, whereas T2 agents produce darker contrast. Superparamagnetic Fe<sub>3</sub>O<sub>4</sub> nanoparticles (SPIONs) has been widely used for grafting onto GO, as T2 contrast agents in MRI because they can shorten T2 relaxation time. For instance, Chen et al.<sup>105</sup> conjugated the aminodextran on Fe<sub>3</sub>O<sub>4</sub>, then anchored onto GO to obtain a platform that can induce efficient T2 responses. Compared to isolated Fe<sub>3</sub>O<sub>4</sub>, the Fe<sub>3</sub>O<sub>4</sub>-GO exhibited significantly enhanced cellular MRI signals.

In another study, CS functionalized magnetic rGO (CMG) was used as platform for simultaneous targeted cancer chemotherapy, gene therapy and enhanced MRI.<sup>106</sup> The CMG was loaded with SPIONs for evaluating contrast enhancement and targeting ability of CMG in tumors. DOX-loaded CMG resulted more effective in killing A549 lung cancer cells than free DOX. Moreover, to evaluate the potential for simultaneous drug and nucleic acid delivery of CMG, DOX-CMG was encapsulated with plasmid DNA (pDNA) encoding green fluorescent protein (GFP). The results showed that DOX-CMG-GFP-pDNA exhibited both GFP expression and DOX accumulation at the tumor site 48 h after administration, but no GFP expression was observed in other organs. The toxicity of DOX-CMG was also investigated by

monitoring the body weight changes of mice after a single intravenous administration. No loss in the body weight was measured for the animal treated with DOX-CMG, compared to the loss of 14% in two weeks in case of mice receiving free DOX.

DOX was loaded onto superparamagnetic iron oxide GO hybrid functionalized with PEG (GO-SPIONs-PEG-DOX).<sup>107</sup> This conjugate was used for magnetically targeted drug delivery and PTT due to the strong optical absorbance of GO. The PTT treatment resulted in the selective killing of cancer cells in highly localized regions. The T2 contrast agent properties of the SPIONPs were exploited for MRI in tumor-bearing mice. In another work, a multifunctional theranostic platform incorporating Fe<sub>3</sub>O<sub>4</sub> magnetic nanoparticles for enhanced magnetic targeting and MRI has been also synthesized.<sup>108</sup> The targeting peptide-modified magnetic graphene-based mesoporous silica nanoparticles demonstrated the potential of this complex for MRI, dual targeting recognition (magnetic targeting and receptor-mediated active targeting), and chemo-photothermal therapy into a single system for visualized-synergistic therapy of glioma.<sup>88</sup>

Overall, GO plays various key roles in biomedical imaging: i) as carriers for its high loading of drugs, dyes, photosensitizers, inorganic compounds thanks to its large specific surface area, ii) as fluorescent quencher because of its C sp<sup>2</sup> structure, iii) as wrapping or encapsulating materials due to its amphiphilic and flexible structure, and iv) as building block for its high surface area and versatile conjugation surface.

### 1.2.3 Biocompatibility and toxicity

According to American heritage dictionary, biocompatibility is the property of being biologically compatible without producing a toxic, injurious, or immunologic response in living tissue. Therefore, the increased bioapplications of graphene-based materials require stringent toxicological assessment.<sup>109</sup> In fact, the first screening studies addressing the impact of new materials in living systems is generally performed at the cellular level, thus leading to the *in vitro* assessment of potential cytotoxic effects. The discovery of the biodegradability of GO is one of the positive factors to assess the safe use of graphene-based materials.<sup>110,111</sup>

Recent studies demonstrated that the modulation of toxicity of graphene-based materials could be achieved by the surface chemical modifications of GO, as it has been also studied for carbon nanotubes (CNTs).<sup>60</sup> This is an essential point that needs to be considered when platform based on GO for nanomedicine are developed.<sup>109,112</sup> Some studies indicated that the cytotoxicity of



GO at different concentrations (10-400 $\mu$ /ml) depended on the type of cells and the cell culture conditions.<sup>113-115</sup>

Once graphene-based materials get in contact with cells, what can happen? GO can be internalized by different mechanisms if the sheets have the suitable dimension. Once inside the cells, besides the ability of being degraded by oxidative enzymes, GO sheets can also escape from subcellular compartments and travel within the cytoplasm. GO and its derivatives have found to display a certain degree of cytotoxicity.<sup>116</sup> The following examples illustrate the biological effects of GO and the undesired effects.

The influence of GO on the morphology, viability, mortality, and membrane integrity of human lung carcinoma (A549) cells was studied using GO sheets of different sizes (160, 430 and 780 nm) by Chang et al.<sup>113</sup> The results suggest no cellular uptake and no obvious cytotoxicity of GO in A549 cells. However, a slight loss of viability at high concentrations of GO as well as a dose-dependent oxidative stress in cells were detected. In a similar study, Yue et al.<sup>117</sup> systematically investigated the effects of GO lateral dimension (2  $\mu$ m and 350 nm) on a series of cellular responses including the cellular uptake, internalization mechanisms, intracellular trafficking, and inflammation response. Among six cell lines cultured with the two different GO, only two phagocytic cells were able to internalize GO. The authors observed a size-independent uptake behavior in macrophages. However, considering the intracellular event and cytokine profiles, the lateral dimensions played a significant role in the biological responses: the GO in micro-size induced much stronger inflammation responses while the smaller GO sheets showed better biocompatibility.

As in the case of the *in vitro* impact, it is necessary to carefully consider many parameters, such as the morphological and physicochemical characteristics of each type and quality of samples, the surface modifications, the size, etc..., also for testing the toxicity of GO *in vivo*. Zhang et al.<sup>118</sup> studied the biodistribution and biocompatibility of single layer GO sheets of 10–800 nm in Kunming mice after intravenous administration at a dose of 1 mg/kg or 10 mg/kg. The results showed that GO exhibited a good biocompatibility on red blood cell with a long blood circulation time (half-time 5.3 $\pm$ 1.2 h), and low uptake in the organs of the reticuloendothelial system. No pathological alterations were observed with a dose of 1mg/kg after 14 days post-injection. However, at the high dosage of 10 mg/kg, GO slow clearance caused granulomatous lesions, pulmonary edema, inflammation and fibrosis. In another example, Wang et al.<sup>119</sup>



intravenously administered low, medium and high doses of GO (0.1 mg, 0.25 mg, and 0.4 mg) in Kunming mice. The report showed that low and medium exposure of animals did not give signs of toxicity, whereas the highest dose exhibited chronic toxicity with severe side-effects that triggered an inflammatory response in the lung and the formation of granulomas and lesions.

In summary, several factors can affect the tests on cytotoxicity of GO: the variability of the materials, the surface area, the type of cells *in vitro*, the correlation of the impact on cells with their physicochemical characteristic, the doses as well as the routes of administration *in vivo*. Furthermore, it is important to consider the chemical surface modifications and to reduce the oxygen reactive species which mediate apoptosis through protein (i.e. caspase-3) activation,<sup>120</sup> and improve the biocompatibility *via* conjugated with various suitable polymers.

### 1.3 Graphene oxide and nucleic acids interactions

#### 1.3.1 Graphene oxide bio-interfacing with nucleic acids and biological effects of the graphene/nucleic acid complexes

Nucleic acids (NA) are polymeric biomolecules, which are made of monomers called nucleotides. Each nucleotide is composed of three components: a phosphate group, a ribose or a deoxyribose, and a purine or pyrimidine base. Depending on the sugar, we obtain DNA (deoxyribonucleic acid) or RNA (ribonucleic acid), respectively. Due to their base-pairing and double helix structure, various advanced design, fabrication and control of nucleic acid-mediated assembled structures have been studied. Research on interaction between nanomaterials and nucleic acids has been profoundly investigated to yield interesting nanostructures with synergistic properties and functions.<sup>121–123</sup> In this context, graphene oxide with its high cargo loading capacity of both hydrophilic and hydrophobic molecules has gained rapidly lot of interest.<sup>5</sup> The study of the interactions of GO with nucleic acids through either non-covalent adsorption or covalent binding have substantially enhanced over the past few years for the application in biosensing, diagnostics and biomedicine.<sup>2,67</sup>

Generally, the binding between GO and ssDNA is ascribed either to the  $\pi$ - $\pi$  stacking or the hydrogen bonding and van der Waals forces.<sup>124</sup> In term of ssDNA, it was found that the adsorption was stabilized mainly by the H-bonding formed between the graphene surface oxygen groups and the polar groups of the oligonucleotide strand,<sup>85,86</sup> the  $\pi$ - $\pi$  stacking between the hexagonal aromatic rings of GO and the ring structure of the nucleobases<sup>125,126</sup>. For

example, Zhang et al.<sup>127</sup> designed a novel fluorescence-sensing system for the detection of biotin based on the interaction of GO and biotinylated ssDNA binding streptavidin. In this platform, the streptavidin was conjugated with ssDNA, which was modified before with biotin at the 3'-end and the 6-carboxyfluorescein (6-FAM) at the 5'-end, to protect the DNA from hydrolysis by exonuclease I. When streptavidin-DNA was adsorbed onto GO *via*  $\pi$ - $\pi$  stacking, the fluorescence of 6-FAM was quenched. When free biotin was added, it competed with the labeled biotin for the binding sites of streptavidin and then exonuclease I could digest the unbound DNA sequence, thus releasing the fluorophore from the oligonucleotide. Because of the weak affinity between the fluorophore and graphene oxide, the fluorescence was recovered. This study presented a unique platform for fluorescence sensing of small biomolecules. However, in another work, Xue et al.<sup>128</sup> proved that the interaction between GO and ssDNA was mainly due to the H-bonding formation rather than a  $\pi$ - $\pi$  stacking or hydrophobic contact. Indeed, surface plasmon resonance was used to directly investigate DNA/GO binding upon combination of GO and gold nanoparticles. The study not only demonstrated the ability of the system in ultra-sensitive detection of ssDNA, but also showed that the binding tendency of double strand DNA (dsDNA) was weaker than ssDNA presumably due to competition between the interstrand binding in dsDNA and the binding with the GO. In fact, the double strand structure of dsDNA infers a more rigid conformation to the genetic material and this likely changes its interactions with GO surface.

Up to date, there are still controversies in term of driving force on the interaction between GO and double strand DNA or double strand RNA. Some studies illustrated that the hydrophilic external surface of dsDNA can prevent the hydrophobic interactions of their bases with GO,<sup>129</sup> while as others confirmed that there was sufficient between the oxygenated groups of GO and DNA bases<sup>130</sup>. Moreover, the preferable binding of ssDNA to dsDNA was further studied. Wu et al.<sup>131</sup> reported that the hydrophobic forces were much higher than the electrostatic repulsion, especially in the presence of other ionic charges or low pH, where GO charge was reduced by protonation, thus diminishing the repulsion. In dsDNA, where the bases are inside the helical structure and the phosphate groups are exposed, there is a lower affinity on GO surface. Lei et al.<sup>132</sup> have figured out that dsDNA can bind to GO to form a dsDNA/GO complex in the presence of a high concentration of salts *via* electrostatic interactions. Liu et al.<sup>133</sup> also reported the salt-controlled assembly of graphene sheets as a capture of dsDNA in high salt concentration. In contrast, Tang *et al.*,<sup>35</sup> by measuring the quenching effect between a

fluorescently-labeled dsDNA and GO, proved that there was no effect of salt on fluorescence changes, thus excluding influence of the electrostatic interactions as major driving forces for dsDNA on the surface of GO. Moreover, the same study explored for the first time the partial denaturation of dsDNA incubated with GO. The deformation of dsDNA driven by hydrophobic  $\pi$ - $\pi$  stacking was also confirmed in a previous study by molecular dynamic (MD) simulation.<sup>130</sup> On the other hand, Ren *et al.*<sup>134</sup> suggested that GO could intercalate efficiently with DNA molecules and enhance the DNA cleavage activity of copper ions *via* a mechanism based on an oxidative and hydrolytic effect (Figure 1.6). The DNA cleavage behavior of GO and rGO in the presence of  $\text{Cu}^{2+}$  was triggered by  $\pi$ - $\pi$  interaction of GO with DNA.<sup>135</sup>

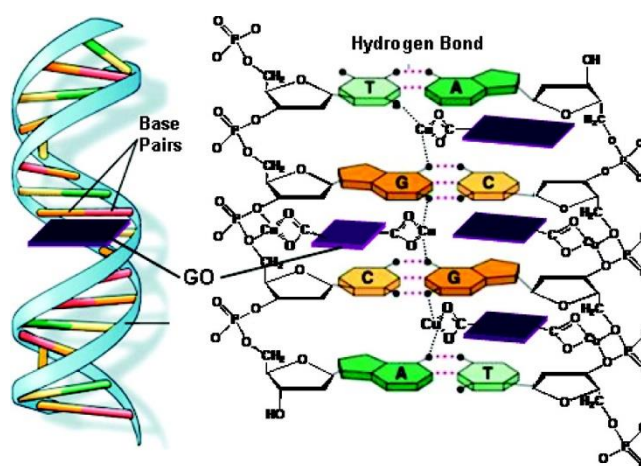


**Figure 1.6:** Proposed DNA cleavage mechanism by the GO/ $\text{Cu}^{2+}$  system, adapted from ref [134].

In term of ssRNA, there are very few study on its interaction with GO because of its instability. Zhang *et al.*<sup>136</sup> explored the stronger  $\pi$ - $\pi$  interaction of ssRNA with PEG-rGO than with PEG-GO, leading to superior ssRNA loading and delivery efficiency. Consistent with the experiments, MD simulation revealed that the attractive van der Waals interaction energy of ssRNA-rGO was more negative than that of ssRNA-GO. The computational method also evidenced a higher stacking number between the bases of ssRNA and the  $\text{sp}^2$  domain, indicating the increasing of  $\pi$ - $\pi$  interaction with the number of aromatic domains on graphene sheet.

Overall, the interaction of GO and double strand RNA (dsRNA), in particular siRNA, has not been deeply studied yet. How the conformation of double strand siRNA is affected by GO remains still unclear. Most of the reports on the main interactions of functionalized GO with

siRNA were based on the electrostatic interaction between the negatively charged siRNA and the positively charged functionalized GO.<sup>77,137,138</sup> The comprehension of the mechanism of interaction between GO/functionalized GO and siRNA is crucial for their clinical future application in gene silencing.

### 1.3.2 Bioapplication in gene delivery

Nucleic acids have considerable potential as therapeutic agents, either as gene expression systems for gene therapy (pDNA or messenger RNA-mRNA), or for knocking down gene expression (siRNA). Gene delivery methods can be mechanical (e.g. microinjection, electroporation or biolistics), chemical (e.g. lipid or nanoparticle carriers) or biological (e.g. viral or bacterial vectors). Gene therapy has gained a significant interest as a promising method for treating gene related disorders and other diseases like cancer.<sup>139,140</sup>

Generally, transfection is the introduction of genetic materials (DNA and RNA) into cells to obtain genetically modified cells and to induce gene expression and the consequent production of defected proteins. Depending on the nature of genomes, there are two main diverse ways of transfection: i) stable transfection, and ii) transient transfection. In the case of the stable transfection, foreign DNA (normally pDNA), which is delivered to nucleus after traverse through cell and nucleus membrane, is integrated into the host genome and express constantly even after the mitosis of the host cells. In contrast, for the transient transfection, foreign DNA is delivered into the nucleus but does not interact with the genome, while as mRNA is delivered into the cytosol where it is translated and lead to protein expression. In this case, gene expression has a limited period of time depending on the cell divisions and environment. The stable transfection requires a complex and long process while as the transient process can afford extremely rapid responses.

Differently from gene transfection, gene knockdown or gene silencing is the switching off of gene (which induce the disease) by the introduction of an antisense RNA that can harm the translation of mRNA. Among different strategies, RNA interference (RNAi) in gene silencing has been rapidly recognized as one of the most revolutionary approaches in the specific knockdown of the target gene because of its simple and rapid mechanism.<sup>141,142</sup> Indeed, the induction of RNAi is mediated by siRNA, a class of dsRNA composed of 19-25 base pairs. Once siRNA enters into the cytoplasm, upon the incorporation into the RNA-induced silencing complex, it can bind the complementary RNA, which triggers the target mRNA degradation,

subsequently inhibiting the specific protein expression.<sup>143,144</sup> In fact, small RNA is preferred instead of long dsRNA because Dicer enzyme (one of the component of the complex involving mRNA translation) is not required for activation; so siRNA can start the gene downregulation pathway as long as it is released into the cytoplasm<sup>139</sup>.

Unfortunately, the “naked” siRNA faces rapid degradation in the extracellular environment *via* endogenous enzymes and it is not efficiently internalized into cells because it is too negative charge to cross the cellular membranes.<sup>145</sup> Therefore, the challenge in the use of nucleic acids is to overcome the struggle in delivering these anionic macromolecules to reach the targeted sites. For example, the mammalian pDNA are well known to express genes in cell culture. However, it is necessary to protect the DNA from oxidative enzymes, and then propose appropriate mechanisms to overcome the biological barriers to effectively deliver pDNA to the nucleus of a mammalian cell *in vivo*. Less challenges are required in term of delivery of mRNA for gene expression or siRNA for knockdown because these molecules need to be delivered only to the cytoplasm. Thus, gene therapy requires a vector that protects the guest genetic material from nuclease degradation and facilitates its cellular uptake with high transfection efficiency, targeted tissue distribution and intracellular trafficking.<sup>146</sup> The major issue is the lack of efficient and safe gene vector.<sup>122</sup>

The first investigations in gene delivery focused on the use of viral vectors due to their strong transgene expression.<sup>147</sup> However, the fundamental problems using capsids, related to toxicity,<sup>148</sup> immunogenicity,<sup>149</sup> carcinogenesis,<sup>150</sup> and lack of scalability, oriented the research towards the generation of safer and more efficient delivery vectors<sup>151</sup>. With the blooming of nanotechnology, the non-viral systems based on nanoparticles and nanomaterials have been explored to address these concerns.<sup>27</sup> In this context, graphene and its derivatives have been exploited as a novel platform because of their ability in protection the nucleic acids from enzymatic digestion.<sup>153,154</sup> For example, Tang et al.<sup>155</sup> reported that ssDNA adsorbed onto GO surfaces can be effectively protected from enzymatic cleavage by deoxyribonuclease (DNaseI, a common enzyme that promotes DNA degradation). Other groups have also observed similar results.<sup>156–158</sup> In comparison, it was evidenced that the protective effect of GO on ssDNA and dsDNA can be freely tuned by adjusting the salt concentration.<sup>132</sup> Furthermore, because the binding affinity of nucleic acids onto GO is affected by experimental conditions,<sup>59,159</sup> to create an ideal GO-protected nucleic acid system, it is needed to optimize certain experimental

conditions such as buffer solution, incubation time, concentration of nucleic acid and presence of nucleases.

In fact, different approaches to enhance the genetic material protection mechanisms are still under exploration. First, the interaction between the nucleic acid and graphene may cause a conformational change of the nucleic acid,<sup>136</sup> rendering it unrecognizable by enzyme binding pockets and thus protecting it from cleavage. Second, the change in local ion concentration induced by graphene can inhibit the enzyme activity. Third, the most interesting perspective is the steric hindrance protection, which prevents nuclease from approaching nucleic acids to initiate enzymatic hydrolysis. Likewise, nucleic acid adsorption onto graphene can result in steric hindrance, change in local ion concentration, or change in probe conformation, thereby protecting nucleic acids from nuclease digestion.<sup>35</sup> Indeed, Lu et al.<sup>160</sup> showed that graphene could protect oligonucleotides from enzymatic cleavage and was able to deliver ssDNA into cells. The exact mechanism of how nucleic acid complexes pass through the cell membrane is still under investigation, but the endocytosis and phagocytosis are believed to be the most involved in this process.

Nowadays, among polycationic polymers used in gene delivery, PEI has been considered as a suitable polymer.<sup>161,162</sup> Indeed, the ability of GO functionalized with high molecular weight PEI (HMW-PEI) in condensing and delivering pDNA into cells was demonstrated.<sup>163</sup> Tripathi et al.<sup>164</sup> have also reported the capability of linear PEI grafted to GO to transfer nucleic acids into mammalian cells. A HMW-PEI was also used to doubly functionalize the hydrothermally treated rGO modified with PEG to deliver a functional plasmid, proving a remarkable enhancement of gene transfection efficiency under near infrared irradiation compared to non-hydrothermally reduced GO-PEG-PEI.<sup>165</sup> Interests have recently shifted toward the conjugation of GO with low molecular weight (LMW) PEI, which was proved to exhibit less cytotoxicity,<sup>166</sup> enhanced cellular uptake and transfection. Feng et al.<sup>65</sup> have successfully performed the functionalization of GO with PEI of different molecular weights (i.e. 1.2 kDa and 10 kDa) as a non-toxic nanovehicle for efficient gene transfection of pDNA. The authors concluded that the GOPEI-10 kDa had similar transfection efficiency but lower toxicity compared to PEI-10 kDa alone. Kim et al.<sup>137</sup> also prepared LMW (1.8 kDa) branched PEI (BPEI) conjugated to GO (BPEI-GO) with high pDNA binding and observed transfection capacity comparable to that of HMW-PEI (Figure 1.7).



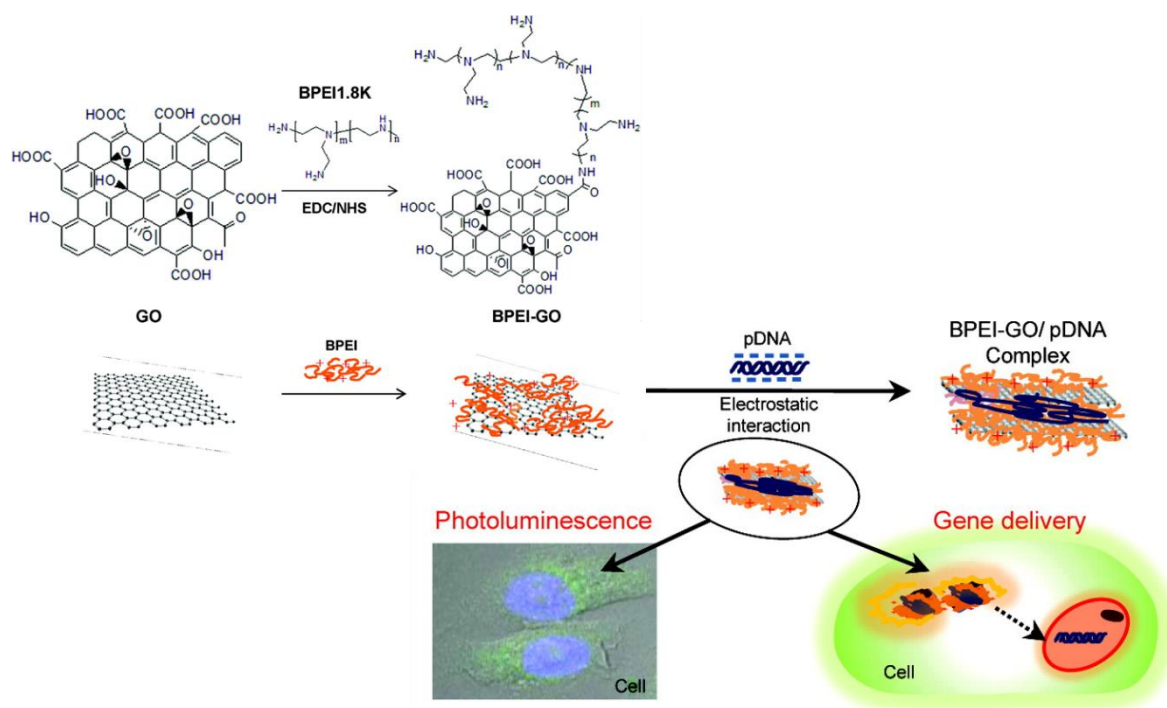


**Figure 1.7:** Synthetic scheme of BPEI-GO via EDC/NHS and its application in gene delivery and bioimaging, adapted from ref [137].

Considering the delivery of siRNA, Imani et al.<sup>138</sup> reported a novel rGO functionalized with a phospholipid-based amphiphilic polymer (PL-PEG) and the cell penetrating peptide octaarginine (R8). This rGO-carrier remained stable in biological solution and did not affect cell viability. Moreover, with the high positive charge surface provided by R8, siRNA was easily complexed and taken up by the cells. The transfection efficiency on MCF-7 cells of a FITC-labeled siRNA loaded onto rGON-PL-PEG-R8 was comparable to the commercial reagent HiPerFect.

Recently, Gu et al.<sup>167</sup> conjugated GO with polyamidoamine dendrimer (PAMAM) via EDC/NHS coupling for the co-delivery of DOX and matrix metalloproteinase-9 short hairpin RNA (MMP-9 shRNA) plasmid for breast cancer therapy. The results showed that GO-PAMAM exhibits a pH controlled drug release *in vitro*, and could mediate a significant reduction of MMP-9 protein in MCF-7 cells. Moreover, cell survival rate of co-delivered GO-PAMAM/DOX/MMP-9 was lower than that of DOX or MMP-9 shRNA separately. In addition, the co-delivery of DOX and siRNA using GO-PEI has been reported to overcome multidrug resistance of breast cancer cells.<sup>168</sup> In this case, Zhi et al.<sup>168</sup> assembled a branched HMW-PEI (25kDa) and poly(sodium 4-styrenesulfonates) via a layer-by-layer assembly

method onto GO, named PPG. Drug Adriamycin (ADR) was loaded onto PPG *via* physical adsorption, then anti-micro RNA (anti-miR-21) was complexed *via* electrostatic interaction. In ADR-resistant breast cancer cells (MCF-7/ADR), the complex significantly enhanced the accumulation of ADR and exhibited higher cytotoxicity in comparison to free ADR. Moreover, this enhanced therapeutic efficiency was correlated to the effective silencing of miR-21.

In another study, by co-loading PEI and PEG onto GO, Feng et al.<sup>169</sup> were able to photothermally enhance gene delivery. The transfection efficiency of pDNA coding for green fluorescent protein in HeLa cell and siRNA-mediated knockdown of mRNA for the target polo-like kinase 1 in MDA-MB-435s cells were improved using NIR irradiation at 808 nm. This synergistic effect in siRNA delivery was explained by the increase in cell membrane permeability which were caused by a photothermal effect.

In summary, when the siRNA is introduced into the cytoplasm of a cell, it can interact with the intracellular RNases that lead to its degradation. In addition, because of the extracellular degradation by enzymes located in serum and tissues, the siRNA delivery is extremely challenging. Indeed siRNA has a short life time in serum ranging from few minutes to one hour<sup>170</sup> before reaching the target site to trigger the gene silencing. Another issue in gene silencing is the off-target silencing of siRNA, which is caused by the homology with six to seven nucleotides in the seed region of siRNA sequence.<sup>171</sup> This off-target silencing leads to the suppression of noninterest genes, inducing dangerous mutation of other genes. Moreover, an immune response can be triggered by siRNA once the interferon responses are activated, leading to cell dead.<sup>172</sup> Because this immune response differs from each cell to another, it is necessary to carefully predict the *in vivo* behaviors.

#### **1.4 Future perspective of graphene oxide in cancer therapy**

Nanotechnology has become more and more a field of interdisciplinary research. In this perspective, the considerable aqueous dispersibility and colloidal stability of both single- or few-layered GO as well as the remarkable and tunable surface functionalization and biological properties have reinforced the reasons that GO is a highly promising candidate in biomedicine. In fact, GO as a carrier for drug and gene delivery, or for imaging has been deeply and widely investigated with the aim of understanding all factors, from the internal impacts of GO itself to various external interactions between GO and molecules, that can affect and guide their adaptable clinical applications.



Therefore, one of the first issue that needs to be considered is the understanding and the control of the oxygen function roles and the covalent functionalization of GO, particularly for the application in gene therapy. Moreover, the interaction of nucleic acids with GO and its conjugates is one of the key point to design a novel platform in gene silencing. The role of GO as a good carrier to deliver the genomic materials into cellular, subcellular compartments *in vitro* and in small animal *in vivo* demand a precise functionalization. The comprehension of pharmacokinetics and pharmacodynamics of GO, its long-term cytotoxicity, and its biodegradability are also crucial for clinical tests. The hope toward clinical applications of GO in cancer therapy should be highlighted and strongly investigated for its enormous benefits it can give.

In summary, GO and its derivatives have been studied as potential nanocarriers in cancer treatment. In this context, it will take a long time to address carefully several issues related to safety including the homogeneity of GO, the presence of trace of impurities after the synthesis and purification process, the amount and nature of oxygenated species in term of chemical point of view, the lateral size effect, etc. Every journey needs a little first step to start and the science community is ongoing to provide a fascinating progress on the road to obtain a “real suitable” platform of GO for treatment of cancer on human.

### **1.5 Thesis objectives and outline**

The research described in this Thesis aims to explore the interaction of GO with nucleic acids, especially siRNA, and to develop a novel platform complexing biologically active molecules for gene delivery study, specifically for silencing specific genes.

To this purpose, I first focused on the design, synthesis and study of GO samples with different degrees of oxidation using various protocols. In order to increase the quantity of ammonium groups which lead to a better complexation of the siRNA, a re-epoxidation of the GO, which has undergone a prior reduction, was carried out followed by an opening of the epoxy ring with amine derivatives. Moreover, because different examples of conjugation GO with various structures of PEI at different molecular weight have been reported, it is crucial to understand the relationship among the structure of amines/polymer, the complexation ability and the delivery efficiency. Therefore, a series of amines and a low molecular weight PEI were covalently conjugated to GO to obtain a functionalized GO with different types of positively charged groups. Finally, to evaluate the interaction of each functionalized and non-

functionalized GO with siRNA, various techniques have been applied including UV-Vis spectroscopy, gel electrophoresis, circular dichroism and fluorescence resonance energy transfer (FRET). Thanks to these methods and to the precise characterization of the surface, we were able to better understand the interaction of siRNA with pristine and functionalized GO. The question of the ability of GO and its functionalization in delivering siRNA into cells will also be discussed.

The Thesis is composed of five Chapters, as outlined:

**Chapter 1** gives an overview on the main characteristics of graphene oxide, its preparation, characterization, and applications in biomedical field, with a main focus on its interaction with nucleic acids for gene delivery.

**Chapter 2** describes the synthesis of reduced graphene oxide with various degree of oxygenated functions.

**Chapter 3** discusses the synthesis of cationic molecules and the functionalization of graphene materials with these amines and polymers. The study of their complexation with siRNA is also introduced.

**Chapter 4** focuses on the interaction and complexation of non-functionalized and functionalized graphene oxide with siRNA as well as on preliminary biological results

**Chapter 5** reports the conclusive remarks and perspective of this research.

Each chapter is followed by its own list of references and its own experimental part.

## 1.6 Bibliography

- (1) Novoselov, K. S.; Geim, A. K.; Morozov, S. V.; Jiang, D.; Zhang, Y.; Dubonos, S. V.; Grigorieva, I. V.; Firsov, A. A. Electric Field Effect in Atomically Thin Carbon Films. *Science* **2004**, *306*, 666–669.
- (2) Krishna, K. V.; Ménard-Moyon, C.; Verma, S.; Bianco, A. Graphene-Based Nanomaterials for Nanobiotechnology and Biomedical Applications. *Nanomedicine* **2013**, *8*, 1669–1688.
- (3) Chung, C.; Kim, Y. K.; Shin, D.; Ryoo, S. R.; Hong, B. H.; Min, D. H. Biomedical Applications of Graphene and Graphene Oxide. *Acc. Chem. Res.* **2013**, *46*, 2211–2224.
- (4) Chen, D.; Feng, H.; Li, J. Graphene Oxide: Preparation, Functionalization, and Electrochemical Applications. *Chem. Rev.* **2004**, *112*, 6027–6053.
- (5) Dreyer, D. R.; Park, S.; Bielawski, C. W.; Ruoff, R. S.; Tour, J. M.; Müllen, K.; Ivaska, A.; Goh, R. G.-S.; Friend, R. H.; Wee, A. T. S.; *et al.* The Chemistry of Graphene Oxide. *Chem. Soc. Rev.* **2010**, *39*, 228–240.
- (6) Hummers, W. S.; Offeman, R. E. Preparation of Graphitic Oxide. *J. Am. Chem. Soc.* **1958**, *80*, 1339–1339.
- (7) Cote, L. J.; Cruz-Silva, R.; Huang, J. Flash Reduction and Patterning of Graphite Oxide and Its Polymer Composite. *J. Am. Chem. Soc.* **2009**, *131*, 11027–11032.
- (8) Brodie, B. C. On the Atomic Weight of Graphite. *Philos. Trans. R. Soc. London* **1859**, *149*, 249–259.
- (9) Staudenmaier, L. Verfahren Zur Darstellung Der Graphitsäure. *Berichte der Dtsch. Chem. Gesellschaft* **1898**, *31*, 1481–1487.
- (10) Hudson, M. J.; Hunter-Fujita, F. R.; Peckett, J. W.; Smith, P. M.; Bekkum, H. van. Electrochemically Prepared Colloidal, Oxidised Graphite. *J. Mater. Chem.* **1997**, *7*, 301–305.
- (11) Gao, W.; Alemany, L. B.; Ci, L.; Ajayan, P. M. New Insights into the Structure and Reduction of Graphite Oxide. *Nat. Chem.* **2009**, *1*, 403–408.
- (12) Morimoto, N.; Suzuki, H.; Takeuchi, Y.; Kawaguchi, S.; Kunisu, M.; Bielawski, C. W.; Nishina, Y. Real-Time, in Situ Monitoring of the Oxidation of Graphite: Lessons Learned. *Chem. Mater.* **2017**, *29*, 2150–2156.
- (13) Dimiev, A. M.; Tour, J. M. Mechanism of Graphene Oxide Formation. **2014**, *8*, 3060–3068.
- (14) Dreyer, D. R.; Todd, A. D.; Bielawski, C. W. Harnessing the Chemistry of Graphene Oxide. *Chem. Soc. Rev.* **2014**, *43*, 5288–5301.
- (15) Lerf, A.; He, H.; Forster, M.; Klinowski, J. Structure of Graphite Oxide Revisited. *J. Phys. Chem. B* **1998**, *102*, 4477–4482.
- (16) Peigney, A.; Laurent, C.; Flahaut, E.; Bacsa, R. R.; Rousset, A. Specific Surface Area of Carbon Nanotubes and Bundles of Carbon Nanotubes. *Carbon* **2001**, *39*, 507–514.
- (17) Hung, A. H.; Holbrook, R. J.; Rotz, M. W.; Glasscock, C. J.; Mansukhani, N. D.; MacRenaris,

- K. W.; Manus, L. M.; Duch, M. C.; Dam, K. T.; Hersam, M. C.; *et al.* Graphene Oxide Enhances Cellular Delivery of Hydrophilic Small Molecules by Co-Incubation. *ACS Nano* **2014**, *8*, 10168–10177.
- (18) Yang, D.; Velamakanni, A.; Bozoklu, G.; Park, S.; Stoller, M.; Piner, R. D.; Stankovich, S.; Jung, I.; Field, D. A.; Ventrice, C. A.; *et al.* Chemical Analysis of Graphene Oxide Films after Heat and Chemical Treatments by X-Ray Photoelectron and Micro-Raman Spectroscopy. *Carbon* **2009**, *47*, 145–152.
- (19) Acik, M.; Lee, G.; Mattevi, C.; Pirkle, A.; Wallace, R. M.; Chhowalla, M.; Cho, K.; Chabal, Y. The Role of Oxygen during Thermal Reduction of Graphene Oxide Studied by Infrared Absorption Spectroscopy. *J. Phys. Chem. C* **2011**, *115*, 19761–19781.
- (20) Casabianca, L. B.; Shaibat, M. A.; Cai, W. W.; Park, S.; Piner, R.; Ruoff, R. S.; Ishii, Y. NMR-Based Structural Modeling of Graphite Oxide Using Multidimensional <sup>13</sup>C Solid-State NMR and Ab Initio Chemical Shift Calculations. *J. Am. Chem. Soc.* **2010**, *132*, 5672–5676.
- (21) Chua, C. K.; Sofer, Z.; Pumera, M. Graphite Oxides: Effects of Permanganate and Chlorate Oxidants on the Oxygen Composition. *Chem. A Eur. J.* **2012**, *18*, 13453–13459.
- (22) He, H.; Klinowski, J.; Forster, M.; Lerf, A. A New Structural Model for Graphite Oxide. *Chem. Phys. Lett.* **1998**, *287*, 53–56.
- (23) Lu, G.; Zhou, X.; Li, H.; Yin, Z.; Li, B.; Huang, L.; Boey, F.; Zhang, H. Nanolithography of Single-Layer Graphene Oxide Films by Atomic Force Microscopy. *Langmuir* **2010**, *26*, 6164–6166.
- (24) Mao, Y.; Wen, S.; Chen, Y.; Zhang, F.; Panine, P.; Chan, T. W.; Zhang, L.; Liang, Y.; Liu, L. High Performance Graphene Oxide Based Rubber Composites. *Sci. Rep.* **2013**, *3*, 2508.
- (25) Zhao, J.; Pei, S.; Ren, W.; Gao, L.; Cheng, H.-M. Efficient Preparation of Large-Area Graphene Oxide Sheets for Transparent Conductive Films. *ACS Nano* **2010**, *4*, 5245–5252.
- (26) Stobinski, L.; Lesiak, B.; Malolepszy, A.; Mazurkiewicz, M.; Mierzwa, B.; Zemek, J.; Jiricek, P.; Bieloshapka, I. Graphene Oxide and Reduced Graphene Oxide Studied by the XRD, TEM and Electron Spectroscopy Methods. *J. Electron Spectrosc. Relat. Phenom.* **2014**, *195*, 145–154.
- (27) Lay, E.; Chng, K.; Pumera, M. Toxicity of Graphene Related Materials and Transition Metal Dichalcogenides. *RSC Adv.* **2015**, *5*, 3074–3080.
- (28) Liu, J.; Yang, W.; Tao, L.; Li, D.; Boyer, C.; Davis, T. P. Thermosensitive Graphene Nanocomposites Formed Using Pyrene-Terminal Polymers Made by RAFT Polymerization. *J. Polym. Sci. Part A Polym. Chem.* **2010**, *48*, 425–433.
- (29) Liu, J.; Tao, L.; Yang, W.; Li, D.; Boyer, C.; Wuhrer, R.; Braet, F.; Davis, T. P. Synthesis, Characterization, and Multilayer Assembly of pH Sensitive Graphene–Polymer Nanocomposites. *Langmuir* **2010**, *26*, 10068–10075.
- (30) Yang, Y.; Zhang, Y.-M.; Chen, Y.; Zhao, D.; Chen, J.-T.; Liu, Y. Construction of a Graphene Oxide Based Noncovalent Multiple Nanosupramolecular Assembly as a Scaffold for Drug Delivery. *Chem. A Eur. J.* **2012**, *18*, 4208–4215.

- (31) Depan, D.; Shah, J.; Misra, R. D. K. Controlled Release of Drug from Folate-Decorated and Graphene Mediated Drug Delivery System: Synthesis, Loading Efficiency, and Drug Release Response. *Mater. Sci. Eng. C* **2011**, *31*, 1305–1312.
- (32) Lee, J.; Kim, J.; Kim, S.; Min, D.-H. Biosensors Based on Graphene Oxide and Its Biomedical Application. *Adv. Drug Deliv. Rev.* **2016**, *105*, 275–287.
- (33) Lu, C. H.; Yang, H. H.; Zhu, C. L.; Chen, X.; Chen, G. N. A Graphene Platform for Sensing Biomolecules. *Angew. Chem. Int. Ed.* **2009**, *48*, 4785–4787.
- (34) Balapanuru, J.; Yang, J.-X. X.; Xiao, S.; Bao, Q.; Jahan, M.; Polavarapu, L.; Wei, J.; Xu, Q.-H. H.; Loh, K. P. P. A Graphene Oxide-Organic Dye Ionic Complex with DNA-Sensing and Optical-Limiting Properties. *Angew. Chem. Int. Ed.* **2010**, *49*, 6549–6553.
- (35) Tang, L.; Chang, H.; Liu, Y.; Li, J. Duplex DNA/graphene Oxide Biointerface: From Fundamental Understanding to Specific Enzymatic Effects. *Adv. Funct. Mater.* **2012**, *22*, 3083–3088.
- (36) Liang, B. Y.; Wu, D.; Feng, X.; Mu, K. Dispersion of Graphene Sheets in Organic Solvent Supported by Ionic Interactions. **2009**, 1679–1683.
- (37) Liu, J.; Fu, S.; Yuan, B.; Li, Y.; Deng, Z. Toward a Universal “Adhesive Nanosheet” for the Assembly of Multiple Nanoparticles Based on a Protein-Induced Reduction/Decoration of Graphene Oxide. *J. Am. Chem. Soc.* **2010**, *132*, 7279–7281.
- (38) Gao, J.; Liu, F.; Liu, Y.; Ma, N.; Wang, Z.; Zhang, X. Environment-Friendly Method To Produce Graphene That Employs Vitamin C and Amino Acid. *Chem. Mater.* **2010**, *22*, 2213–2218.
- (39) Peng, C.; Hu, W.; Zhou, Y.; Fan, C.; Huang, Q. Intracellular Imaging with a Graphene-Based Fluorescent Probe. *Small* **2010**, *6*, 1686–1692.
- (40) Bonanni, A.; Ambrosi, A.; Pumera, M. Nucleic Acid Functionalized Graphene for Biosensing. *Chem. A Eur. J.* **2012**, *18*, 1668–1673.
- (41) Jung, J. H.; Cheon, D. S.; Liu, F.; Lee, K. B.; Seo, T. S. A Graphene Oxide Based Immuno-Biosensor for Pathogen Detection. *Angew. Chem. Int. Ed.* **2010**, *49*, 5708–5711.
- (42) Lee, J. S.; Joung, H.-A.; Kim, M.-G.; Park, C. B. Graphene-Based Chemiluminescence Resonance Energy Transfer for Homogeneous Immunoassay. *ACS Nano* **2012**, *6*, 2978–2983.
- (43) Bao, H.; Pan, Y.; Ping, Y.; Sahoo, N. G.; Wu, T.; Li, L.; Li, J.; Gan, L. H. Chitosan-Functionalized Graphene Oxide as a Nanocarrier for Drug and Gene Delivery. *Small* **2011**, *7*, 1569–1578.
- (44) Liu, Z.; Robinson, J. T.; Sun, X.; Dai, H. PEGylated Nanographene Oxide for Delivery of Water-Insoluble Cancer Drugs. *J. Am. Chem. Soc.* **2008**, *130*, 10876–10877.
- (45) Sun, X.; Liu, Z.; Welsher, K.; Robinson, J. T.; Goodwin, A.; Zaric, S.; Dai, H. Nano-Graphene Oxide for Cellular Imaging and Drug Delivery. *Nano Res.* **2008**, *1*, 203–212.
- (46) Stankovich, S.; Piner, R. D.; Nguyen, S. T.; Ruoff, R. S. Synthesis and Exfoliation of Isocyanate-Treated Graphene Oxide Nanoplatelets. *Carbon* **2006**, *44*, 3342–3347.

- 
- (47) Hou, S.; Su, S.; Kasner, M. L.; Shah, P.; Patel, K.; Madarang, C. J. Formation of Highly Stable Dispersions of Silane-Functionalized Reduced Graphene Oxide. *Chem. Phys. Lett.* **2010**, *501*, 68–74.
- (48) Ou, X.; Jiang, L.; Chen, P.; Zhu, M.; Hu, W.; Liu, M.; Zhu, J.; Ju, H. Highly Stable Graphene-Based Multilayer Films Immobilized via Covalent Bonds and Their Applications in Organic Field-Effect Transistors. *Adv. Funct. Mater.* **2013**, *23*, 2422–2435.
- (49) Meng, D.; Sun, J.; Jiang, S.; Zeng, Y.; Li, Y.; Yan, S.; Geng, J.; Huang, Y.; Guldi, D. M.; C. A. Ventrice, J.; *et al.* Grafting P3HT Brushes on GO Sheets: Distinctive Properties of the GO/P3HT Composites due to Different Grafting Approaches. *J. Mater. Chem.* **2012**, *22*, 21583–21591.
- (50) Vacchi, I. A.; Spinato, C.; Raya, J.; Bianco, A.; Ménard-Moyon, C. Chemical Reactivity of Graphene Oxide towards Amines Elucidated by Solid-State NMR. *Nanoscale* **2016**, *8*, 13714–13721.
- (51) Loh, K. P.; Bao, Q.; Ang, P. K.; Yang, J.; Tan, C. K.; Sow, C.-H.; Loh, K. P.; Cabello, N.; Basanta, M. A.; Ortega, J.; *et al.* The Chemistry of Graphene. *J. Mater. Chem.* **2010**, *20*, 2277–2289.
- (52) Dikin, D. A.; Stankovich, S.; Zimney, E. J.; Piner, R. D.; Dommett, G. H. B.; Evmenenko, G.; Nguyen, S. T.; Ruoff, R. S. Preparation and Characterization of Graphene Oxide Paper. *Nature* **2007**, *448*, 457–460.
- (53) Mohanty, N.; Berry, V. Graphene-Based Single-Bacterium Resolution Biodevice and DNA Transistor: Interfacing Graphene Derivatives with Nanoscale and Microscale Biocomponents. *Nano Lett.* **2008**, *8*, 4469–4476.
- (54) Veca, L. M.; Lu, F.; Meziani, M. J.; Cao, L.; Zhang, P.; Qi, G.; Qu, L.; Shrestha, M.; Sun, Y.-P.; Smalley, R. E.; *et al.* Polymer Functionalization and Solubilization of Carbon Nanosheets. *Chem. Commun.* **2009**, *17*, 2565–2567.
- (55) Xu, Y.; Liu, Z.; Zhang, X.; Wang, Y.; Tian, J.; Huang, Y.; Ma, Y.; Zhang, X.; Chen, Y. A Graphene Hybrid Material Covalently Functionalized with Porphyrin: Synthesis and Optical Limiting Property. *Adv. Mater.* **2009**, *21*, 1275–1279.
- (56) Bourlinos, A. B.; Gournis, D.; Petridis, D.; Szabó, T.; Szeri, A.; Dékány, I. Graphite Oxide: Chemical Reduction to Graphite and Surface Modification with Primary Aliphatic Amines and Amino Acids. *Langmuir* **2003**, *19*, 6050–6055.
- (57) He, A.; Lei, B.; Cheng, C. (Sage); Li, S.; Ma, L.; Sun, S.; Zhao, C.; Zhao, C.; Cho, S.-W.; Hersam, M. C.; *et al.* Toward Safe, Efficient and Multifunctional 3D Blood-Contact Adsorbents Engineered by Biopolymers/graphene Oxide Gels. *RSC Adv.* **2013**, *3*, 22120–22129.
- (58) Hu, K.; Liu, J.; Chen, J.; Huang, Y.; Zhao, S.; Tian, J.; Zhang, G. An Amplified Graphene Oxide-Based Fluorescence Aptasensor Based on Target-Triggered Aptamer Hairpin Switch and Strand-Displacement Polymerization Recycling For bioassays. *Biosens. Bioelectron.* **2013**, *42*, 598–602.
- (59) Park, J. S.; Baek, A.; Park, I.-S.; Jun, B.-H.; Kim, D.-E.; Leslie, M. D.; Schafer, E.; Marchand, B.; Adedeji, A.; Michailidis, E.; *et al.* A Graphene Oxide-Based Platform for the Assay of RNA
-

- Synthesis by RNA Polymerase Using a Fluorescent Peptide Nucleic Acid Probe. *Chem. Commun.* **2013**, 49, 9203.
- (60) Yang, K.; Feng, L.; Shi, X.; Liu, Z. Nano-Graphene in Biomedicine: Theranostic Applications. *Chem. Soc. Rev.* **2013**, 42, 530–547.
- (61) Jana, B.; Biswas, A.; Mohapatra, S.; Saha, A.; Ghosh, S.; Speranza, G.; Manitto, P.; Sironi, M.; Chen, C.; Theuer, C. P.; *et al.* Single Functionalized Graphene Oxide Reconstitutes Kinesin Mediated Intracellular Cargo Transport and Delivers Multiple Cytoskeleton Proteins and Therapeutic Molecules into the Cell. *Chem. Commun.* **2014**, 50, 11595–11598.
- (62) Jana, B.; Mondal, G.; Biswas, A.; Chakraborty, I.; Saha, A.; Kurkute, P.; Ghosh, S. Dual Functionalized Graphene Oxide Serves as a Carrier for Delivering Oligohistidine- and Biotin-Tagged Biomolecules into Cells. *Macromol. Biosci.* **2013**, 13, 1478–1484.
- (63) Cui, L.; Song, Y.; Ke, G.; Guan, Z.; Zhang, H.; Lin, Y.; Huang, Y.; Zhu, Z.; Yang, C. J. Graphene Oxide Protected Nucleic Acid Probes for Bioanalysis and Biomedicine. *Chem. Eur. J.* **2013**, 19, 10442–10451.
- (64) Hughes, Z. E.; Walsh, T. R. What Makes a Good Graphene-Binding Peptide? Adsorption of Amino Acids and Peptides at Aqueous Graphene Interfaces. *J. Mater. Chem. B* **2015**, 3, 3211–3221.
- (65) Feng, L.; Zhang, S.; Liu, Z.; Ma, Y. F.; Huang, Y.; Chen, Y.; Bai, Y. B.; Li, T. J.; Fang, H. P.; Fan, C. H.; *et al.* Graphene Based Gene Transfection. *Nanoscale* **2011**, 3, 1252–1257.
- (66) Theodosopoulos, G. V.; Bilalis, P.; Sakellariou, G. Polymer Functionalized Graphene Oxide: A Versatile Nanoplatforrm for Drug/Gene Delivery. *Curr. Org. Chem.* **2015**, 19, 1828–1837.
- (67) Lee, J.; Yim, Y.; Kim, S.; Choi, M.-H. H.; Choi, B.-S. S.; Lee, Y.; Min, D.-H. H. In-Depth Investigation of the Interaction between DNA and Nano-Sized Graphene Oxide. *Carbon* **2016**, 97, 92–98.
- (68) Shim, G.; Kim, M.-G.; Park, J. Y. Graphene-Based Nanosheets for Delivery of Chemotherapeutics and Biological Drugs. *Adv. Drug Deliv. Rev.* **2016**, 105, 205–227.
- (69) Li, D.; Zhang, W.; Yu, X.; Wang, Z.; Su, Z.; Wei, G. When Biomolecules Meet Graphene: From Molecular Level Interactions to Material Design and Applications. *Nanoscale* **2016**, 8, 19491–19509.
- (70) Nurunnabi, M.; Parvez, K.; Revuri, V.; Khan, H. A.; Feng, X.; Lee, Y. Bioapplication of Graphene Oxide Derivatives: Drug / Gene Delivery, Imaging, Polymeric Modification, Toxicology, Therapeutics and Challenges. *RSC Adv.* **2015**, 5, 42141–42161.
- (71) Xiaoying Yang Zunfeng Liu, Yanfeng Ma, Yi Huang, and, X. Z.; Chen, Y. High-Efficiency Loading and Controlled Release of Doxorubicin Hydrochloride on Graphene Oxide. *J Phys Chem C* **2008**, 112, 17554–17558.
- (72) Wojtoniszak, M.; Urbas, K.; Perużyńska, M.; Kurzawski, M.; Drożdżik, M.; Mijowska, E. Covalent Conjugation of Graphene Oxide with Methotrexate and Its Antitumor Activity. *Chem. Phys. Lett.* **2013**, 568–569, 151–156.



- 
- (73) Li, Y.; Feng, L.; Shi, X.; Wang, X.; Yang, Y.; Yang, K.; Liu, T.; Yang, G.; Liu, Z. Surface Coating-Dependent Cytotoxicity and Degradation of Graphene Derivatives: Towards the Design of Non-Toxic, Degradable Nano-Graphene. *Small* **2014**, *10*, 1544–1554.
- (74) Xu, Z.; Wang, S.; Li, Y.; Wang, M.; Shi, P.; Huang, X. Covalent Functionalization of Graphene Oxide with Biocompatible Poly(ethylene Glycol) for Delivery of Paclitaxel. *ACS Appl. Mater. Interfaces* **2014**, *6*, 17268–17276.
- (75) Xu, H.; Fan, M.; Elhissi, A. M.; Zhang, Z.; Wan, K. W.; Ahmed, W.; Phoenix, D. A.; Sun, X. PEGylated Graphene Oxide for Tumor-Targeted Delivery of Paclitaxel. *Nanomedicine (Lond)* **2015**, *10*, 1247–1262.
- (76) Chen, Y.; Qi, Y.; Liu, B. Polyacrylic Acid Functionalized Nanographene as a Nanocarrier for Loading and Controlled Release of Doxorubicin Hydrochloride. *J. Nanomater.* **2013**, *2013*, 1–8.
- (77) Zhang, L.; Lu, Z.; Zhao, Q.; Huang, J.; Shen, H.; Zhang, Z. Enhanced Chemotherapy Efficacy by Sequential Delivery of siRNA and Anticancer Drugs Using PEI-Grafted Graphene Oxide. *Small* **2011**, *7*, 460–464.
- (78) Dinauer, N.; Balthasar, S.; Weber, C.; Kreuter, J.; Langer, K.; von Briesen, H. Selective Targeting of Antibody-Conjugated Nanoparticles to Leukemic Cells and Primary T-Lymphocytes. *Biomaterials* **2005**, *26*, 5898–5906.
- (79) Guo, Y.; Xu, H.; Li, Y.; Wu, F.; Li, Y.; Bao, Y.; Yan, X.; Huang, Z.; Xu, P. Hyaluronic Acid and Arg-Gly-Asp Peptide Modified Graphene Oxide with Dual Receptor-Targeting Function for Cancer Therapy. *J. Biomater. Appl.* **2017**, *32*, 54–65.
- (80) Zhang, L.; Xia, J.; Zhao, Q.; Liu, L.; Zhang, Z. Functional Graphene Oxide as a Nanocarrier for Controlled Loading and Targeted Delivery of Mixed Anticancer Drugs. *Small* **2010**, *6*, 537–544.
- (81) Alibolandi, M.; Mohammadi, M.; Taghdisi, S. M.; Ramezani, M.; Abnous, K. Fabrication of Aptamer Decorated Dextran Coated Nano-Graphene Oxide for Targeted Drug Delivery. *Carbohydr. Polym.* **2017**, *155*, 218–229.
- (82) Zeng, Y.; Yang, Z.; Li, H.; Hao, Y.; Liu, C.; Zhu, L.; Liu, J.; Lu, B.; Li, R. Multifunctional Nanographene Oxide for Targeted Gene-Mediated Thermochemotherapy of Drug-Resistant Tumour. *Sci. Rep.* **2017**, *7*, 43506.
- (83) Zeng, Y.; Yang, Z.; Luo, S.; Li, H.; Liu, C.; Hao, Y.; Liu, J.; Wang, W.; Li, R. Fast and Facile Preparation of PEGylated Graphene from Graphene Oxide by Lysosome Targeting Delivery of Photosensitizer to Efficiently Enhance Photodynamic Therapy. *RSC Adv.* **2015**, *5*, 57725–57734.
- (84) Yang, X.; Zhang, X.; Ma, Y.; Huang, Y.; Wang, Y.; Chen, Y.; Zhang, F.; Sun, S.; Zhong, C. J.; Suh, J. S.; *et al.* Superparamagnetic Graphene oxide–Fe<sub>3</sub>O<sub>4</sub> Nanoparticles Hybrid for Controlled Targeted Drug Carriers. *J. Mater. Chem.* **2009**, *19*, 2710–2714.
- (85) Yang, X.; Wang, Y.; Huang, X.; Ma, Y.; Huang, Y.; Yang, R.; Duan, H.; Chen, Y.; Lubbe, A. S. Multi-Functionalized Graphene Oxide Based Anticancer Drug-Carrier with Dual-Targeting Function and pH-Sensitivity. *J. Mater. Chem.* **2011**, *21*, 3448.
-



- 
- (86) Wang, Z.; Zhou, C.; Xia, J.; Via, B.; Xia, Y.; Zhang, F.; Li, Y.; Xia, L. Fabrication and Characterization of a Triple Functionalization of Graphene Oxide with Fe<sub>3</sub>O<sub>4</sub>, Folic Acid and Doxorubicin as Dual-Targeted Drug Nanocarrier. *Colloids Surfaces B Biointerfaces* **2013**, *106*, 60–65.
- (87) Fan, X.; Jiao, G.; Zhao, W.; Jin, P.; Li, X. Magnetic Fe<sub>3</sub>O<sub>4</sub>-Graphene Composites as Targeted Drug Nanocarriers for pH-Activated Release. *Nanoscale* **2013**, *5*, 1143–1152.
- (88) Chau, N. D. Q.; Ménard-Moyon, C.; Kostarelos, K.; Bianco, A. Multifunctional Carbon Nanomaterial Hybrids for Magnetic Manipulation and Targeting. *Biochem. Biophys. Res. Commun.* **2015**, *468*, 454–462.
- (89) Reina, G.; González-Domínguez, J. M.; Criado, A.; Vázquez, E.; Bianco, A.; Prato, M. Promises, Facts and Challenges for Graphene in Biomedical Applications. *Chem. Soc. Rev.* **2017**, 4400–4416.
- (90) Scheinberg, D. A.; Villa, C. H.; Escorcía, F. E.; McDevitt, M. R. Conscripts of the Infinite Armada: Systemic Cancer Therapy Using Nanomaterials. *Nat. Rev. Clin. Oncol.* **2010**, *7*, 266–276.
- (91) Li, M.; Yang, X.; Ren, J.; Qu, K.; Qu, X. Using Graphene Oxide High Near-Infrared Absorbance for Photothermal Treatment of Alzheimer’s Disease. *Adv. Mater.* **2012**, *24*, 1722–1728.
- (92) Zhang, W.; Guo, Z.; Huang, D.; Liu, Z.; Guo, X.; Zhong, H. Synergistic Effect of Chemo-Photothermal Therapy Using PEGylated Graphene Oxide. *Biomaterials* **2011**, *32*, 8555–8561.
- (93) Markovic, Z. M.; Harhaji-Trajkovic, L. M.; Todorovic-Markovic, B. M.; Kepić, D. P.; Arsikin, K. M.; Jovanović, S. P.; Pantovic, A. C.; Dramićanin, M. D.; Trajkovic, V. S. In Vitro Comparison of the Photothermal Anticancer Activity of Graphene Nanoparticles and Carbon Nanotubes. *Biomaterials* **2011**, *32*, 1121–1129.
- (94) Robinson, J. T.; Tabakman, S. M.; Liang, Y.; Wang, H.; Sanchez Casalongue, H.; Vinh, D.; Dai, H. Ultrasmall Reduced Graphene Oxide with High near-Infrared Absorbance for Photothermal Therapy. *J. Am. Chem. Soc.* **2011**, *133*, 6825–6831.
- (95) Han Kim, S.; Eun Lee, J.; Md Sharker, S.; Hoon Jeong, J.; In, I.; Young Park, S. In Vitro and In Vivo Tumor Targeted Photothermal Cancer Therapy Using Functionalized Graphene Nanoparticles. *Biomacromoleculase* **2015**, *16*, 3519–3529.
- (96) Dolmans, D. E. J. G. J.; Fukumura, D.; Jain, R. K. TIMELINE: Photodynamic Therapy for Cancer. *Nat. Rev. Cancer* **2003**, *3*, 380–387.
- (97) Kalluru, P.; Vankayala, R.; Chiang, C.-S.; Hwang, K. C. Nano-Graphene Oxide-Mediated In Vivo Fluorescence Imaging and Bimodal Photodynamic and Photothermal Destruction of Tumors. *Biomaterials* **2016**, *95*, 1–10.
- (98) Huang, P.; Xu, C.; Lin, J.; Wang, C.; Wang, X.; Zhang, C.; Zhou, X.; Guo, S.; Cui, D. Folic Acid-Conjugated Graphene Oxide Loaded with Photosensitizers for Targeting Photodynamic Therapy. *Theranostics* **2011**, *1*, 240–250.
- (99) Shen, H.; Zhang, L.; Liu, M.; Zhang, Z. Biomedical Applications of Graphene. *Theranostics* **2012**, *2*, 283–294.
-

- 
- (100) Kim, J.; Cote, L. J.; Kim, F.; Huang, J. Visualizing Graphene Based Sheets by Fluorescence Quenching Microscopy. *J. Am. Chem. Soc.* **2010**, *132*, 260–267.
- (101) Swathi, R. S.; Sebastian, K. L. Long Range Resonance Energy Transfer from a Dye Molecule to Graphene Has Dependence. *J. Chem. Phys. J. Chem. Phys. Appl. Phys. Lett.* **2009**, *130*, 86101–111909.
- (102) Yi, M.; Yang, S.; Peng, Z.; Liu, C.; Li, J.; Zhong, W.; Yang, R.; Tan, W. Two-Photon Graphene Oxide/Aptamer Nanosensing Conjugate for *In Vitro* or *In Vivo* Molecular Probing. *Anal. Chem.* **2014**, *86*, 3548–3554.
- (103) Yang, K.; Zhang, S.; Zhang, G.; Sun, X.; Lee, S. T.; Liu, Z. Graphene in Mice: Ultrahigh *In Vivo* Tumor Uptake and Efficient Photothermal Therapy. *Nano Lett.* **2010**, *10*, 3318–3323.
- (104) Hu, S. H.; Chen, Y. W.; Hung, W. T.; Chen, I. W.; Chen, S. Y. Quantum-Dot-Tagged Reduced Graphene Oxide Nanocomposites for Bright Fluorescence Bioimaging and Photothermal Therapy Monitored *In Situ*. *Adv. Mater.* **2012**, *24*, 1748–1754.
- (105) Chen, W.; Yi, P.; Zhang, Y.; Zhang, L.; Deng, Z.; Zhang, Z. Composites of Aminodextran-Coated Fe<sub>3</sub>O<sub>4</sub> Nanoparticles and Graphene Oxide for Cellular Magnetic Resonance Imaging. *ACS Appl. Mater. Interfaces* **2011**, *3*, 4085–4091.
- (106) Wang, C.; Ravi, S.; Garapati, U. S.; Das, M.; Howell, M.; Mallela, J.; Alwarappan, S.; Mohapatra, S. S.; Mohapatra, S. S.; Nakanishi, K.; *et al.* Multifunctional Chitosan Magnetic-Graphene (CMG) Nanoparticles: A Theranostic Platform for Tumor-Targeted Co-Delivery of Drugs, Genes and MRI Contrast Agents. *J. Mater. Chem. B* **2013**, *1*, 4396–4405.
- (107) Ma, X.; Tao, H.; Yang, K.; Feng, L.; Cheng, L.; Shi, X.; Li, Y.; Guo, L.; Liu, Z. A Functionalized Graphene Oxide-Iron Oxide Nanocomposite for Magnetically Targeted Drug Delivery, Photothermal Therapy, and Magnetic Resonance Imaging. *Nano Res.* **2012**, *5*, 199–212.
- (108) Wang, Y.; Huang, R.; Liang, G.; Zhang, Z.; Zhang, P.; Yu, S.; Kong, J. MRI-Visualized, Dual-Targeting, Combined Tumor Therapy Using Magnetic Graphene-Based Mesoporous Silica. *Small* **2014**, *10*, 109–116.
- (109) Bianco, A. Graphene: Safe or Toxic? The Two Faces of the Medal. *Angew. Chem. Int. Ed.* **2013**, *52*, 4986–4997.
- (110) Kotchey, G. P.; Allen, B. L.; Vedala, H.; Yanamala, N.; Kapralov, A. A.; Tyurina, Y. Y.; Klein-Seetharaman, J.; Kagan, V. E.; Star, A. The Enzymatic Oxidation of Graphene Oxide. *ACS Nano* **2011**, *5*, 2098–2108.
- (111) Kurapati, R.; Russier, J.; Squillaci, M. A.; Treossi, E.; Ménard-Moyon, C.; Del Rio-Castillo, A. E.; Vazquez, E.; Samorì, P.; Palermo, V.; Bianco, A. Dispersibility-Dependent Biodegradation of Graphene Oxide by Myeloperoxidase. *Small* **2015**, *11*, 3985–3994.
- (112) Tonelli, F. M.; Goulart, V. A.; Gomes, K. N.; Ladeira, M. S.; Santos, A. K.; Lorençon, E.; Ladeira, L. O.; Resende, R. R. Graphene-Based Nanomaterials: Biological and Medical Applications and Toxicity. *Nanomedicine* **2015**, *10*, 2423–2450.
- (113) Chang, Y.; Yang, S.-T.; Liu, J.-H.; Dong, E.; Wang, Y.; Cao, A.; Liu, Y.; Wang, H. *In Vitro* Toxicity Evaluation of Graphene Oxide on A549 Cells. *Toxicol. Lett.* **2011**, *200*, 201–210.
-

- (114) Lv, M.; Zhang, Y.; Liang, L.; Wei, M.; Hu, W.; Li, X.; Huang, Q.; Niidome, T.; Takada-Takatori, Y.; Akaike, A. Effect of Graphene Oxide on Undifferentiated and Retinoic Acid-Differentiated SH-SY5Y Cells Line. *Nanoscale* **2012**, *4*, 3861.
- (115) Chowdhury, S. M.; Lalwani, G.; Zhang, K.; Yang, J. Y.; Neville, K.; Sitharaman, B. Cell Specific Cytotoxicity and Uptake of Graphene Nanoribbons. *Biomaterials* **2013**, *34*, 283–293.
- (116) Bitounis, D.; Ali-Boucetta, H.; Hong, B. H.; Min, D. H.; Kostarelos, K. Prospects and Challenges of Graphene in Biomedical Applications. *Adv. Mater.* **2013**, *25*, 2258–2268.
- (117) Yue, H.; Wei, W.; Yue, Z.; Wang, B.; Luo, N.; Gao, Y.; Ma, D.; Ma, G.; Su, Z. The Role of the Lateral Dimension of Graphene Oxide in the Regulation of Cellular Responses. *Biomaterials* **2012**, *33*, 4013–4021.
- (118) Zhang, X.; Yin, J.; Peng, C.; Hu, W.; Zhu, Z.; Li, W.; Fan, C.; Huang, Q. Distribution and Biocompatibility Studies of Graphene Oxide in Mice after Intravenous Administration. *Carbon* **2011**, *49*, 986–995.
- (119) Wang, K.; Jing, R.; Song, H.; Zhang, J.; Yan, W.; Guo, S. Biocompatibility of Graphene Oxide. *Nanoscale Res Lett* **2010**, *6*, 1–8.
- (120) Sasidharan, A.; Panchakarla, L. S.; Chandran, P.; Menon, D.; Nair, S.; Rao, C. N. R.; Koyakutty, M.; Car, R.; Saville, D. A.; Aksay, I. A.; *et al.* Differential Nano-Bio Interactions and Toxicity Effects of Pristine versus Functionalized Graphene. *Nanoscale* **2011**, *3*, 2461.
- (121) Mu, Q.; Jiang, G.; Chen, L.; Zhou, H.; Fourches, D.; Tropsha, A.; Yan, B. Chemical Basis of Interactions Between Engineered Nanoparticles and Biological Systems. *Chem. Rev.* **2014**, *114*, 7740–7781.
- (122) Mintzer, M. A.; Simanek, E. E. Nonviral Vectors for Gene Delivery. *Chem. Rev.* **2009**, *109*, 259–302.
- (123) Stadler, A.; Chi, C.; van der Lelie, D.; Gang, O. DNA-Incorporating Nanomaterials in Biotechnological Applications. *Nanomedicine* **2010**, *5*, 319–334.
- (124) Tang, L.; Wang, Y.; Li, J. The Graphene/nucleic Acid Nanobiointerface. *Chem. Soc. Rev.* **2015**, *44*, 6954–6980.
- (125) Li, M.; Pan, Y.; Guo, X.; Liang, Y.; Wu, Y.; Wen, Y.; Yang, H.; Xia, Y.; Ruoff, R. S.; Lin, Y. H.; *et al.* Pt/single-Stranded DNA/graphene Nanocomposite with Improved Catalytic Activity and CO Tolerance. *J. Mater. Chem. A* **2015**, *3*, 10353–10359.
- (126) Banerjee, S.; Wilson, J.; Shim, J.; Shankla, M.; Corbin, E. A.; Aksimentiev, A.; Bashir, R. Slowing DNA Transport Using Graphene-DNA Interactions. *Adv. Funct. Mater.* **2015**, *25*, 936–946.
- (127) Zhang, H.; Li, Y.; Su, X. A Small-Molecule-Linked DNA–graphene Oxide-Based Fluorescence-Sensing System for Detection of Biotin. *Anal. Biochem.* **2013**, *442*, 172–177.
- (128) Xue, T.; Cui, X.; Guan, W.; Wang, Q.; Liu, C.; Wang, H.; Qi, K.; Singh, D. J.; Zheng, W. Surface Plasmon Resonance Technique for Directly Probing the Interaction of DNA and Graphene Oxide and Ultra-Sensitive Biosensing. *Biosens. Bioelectron.* **2014**, *58*, 374–379.

- (129) He, S.; Song, B.; Li, D.; Zhu, C.; Qi, W.; Wen, Y.; Wang, L.; Song, S.; Fang, H.; Fan, C. A Graphene Nanoprobe for Rapid, Sensitive, and Multicolor Fluorescent DNA Analysis. *Adv. Funct. Mater.* **2010**, *20*, 453–459.
- (130) Zhao, X. Self-Assembly of DNA Segments on Graphene and Carbon Nanotube Arrays in Aqueous Solution: A Molecular Simulation Study. *J. Phys. Chem. C* **2011**, *115*, 6181–6189.
- (131) Wu, M.; Kempaiah, R.; Huang, P. J. J.; Maheshwari, V.; Liu, J. Adsorption and Desorption of DNA on Graphene Oxide Studied by Fluorescently Labeled Oligonucleotides. *Langmuir* **2011**, *27*, 2731–2738.
- (132) Lei, H.; Mi, L.; Zhou, X.; Chen, J.; Hu, J.; Guo, S.; Zhang, Y. Adsorption of Double-Stranded DNA to Graphene Oxide Preventing Enzymatic Digestion. *Nanoscale* **2011**, *3*, 3888–3892.
- (133) Liu, M.; Zhao, H.; Chen, S.; Yu, H.; Quan, X. Capture of Double-Stranded DNA in Stacked-Graphene: Giving New Insight into the graphene/DNA Interaction. *Chem. Commun.* **2012**, *48*, 564–566.
- (134) Ren, H.; Wang, C.; Zhang, J. J.; Zhou, X.; Xu, D.; Zheng, J.; Guo, S.; Zhang, J. J. DNA Cleavage System of Nanosized Graphene Oxide Sheets and Copper Ions. *ACS Nano* **2010**, *4*, 7169–7174.
- (135) Zheng, B.; Wang, C.; Wu, C.; Zhou, X.; Lin, M.; Wu, X.; Xin, X.; Chen, X.; Xu, L.; Liu, H.; *et al.* Nuclease Activity and Cytotoxicity Enhancement of the DNA Intercalators via Graphene Oxide. *J. Phys. Chem. C* **2012**, *116*, 15839–15846.
- (136) Zhang, L.; Wang, Z.; Lu, Z.; Shen, H.; Huang, J.; Zhao, Q.; Liu, M.; He, N.; Zhang, Z. PEGylated Reduced Graphene Oxide as a Superior ssRNA Delivery System. *J. Mater. Chem. B* **2013**, *1*, 749–755.
- (137) Kim, H.; Namgung, R.; Singha, K.; Oh, I.-K.; Kim, W. J. Graphene Oxide–Polyethylenimine Nanoconstruct as a Gene Delivery Vector and Bioimaging Tool. *Bioconjugate Chem.* **2011**, *22*, 2558–2567.
- (138) Imani, R.; Shao, W.; Taherkhani, S.; Emami, S. H.; Prakash, S.; Faghihi, S. Dual-Functionalized Graphene Oxide for Enhanced siRNA Delivery to Breast Cancer Cells. *Colloids Surfaces B Biointerfaces* **2016**, *147*, 315–325.
- (139) Whitehead, K. A.; Langer, R.; Anderson, D. G. Knocking down Barriers: Advances in siRNA Delivery. *Nat. Rev. Drug Discov.* **2009**, *8*, 129–138.
- (140) Yang, Z. R.; Wang, H. F.; Zhao, J.; Peng, Y. Y.; Wang, J.; Guinn, B.-A.; Huang, L. Q. Recent Developments in the Use of Adenoviruses and Immunotoxins in Cancer Gene Therapy. *Cancer Gene Ther.* **2007**, *14*, 599–615.
- (141) Hannon, G. J. RNA Interference. *Nature* **2002**, *418*, 244–251.
- (142) Fire, A.; Xu, S.; Montgomery, M. K.; Kostas, S. A.; Driver, S. E.; Mello, C. C. Potent and Specific Genetic Interference by Double-Stranded RNA in *Caenorhabditis Elegans*. *Nature* **1998**, *391*, 806–811.
- (143) Dykxhoorn, D. M.; Palliser, D.; Lieberman, J. The Silent Treatment: siRNAs as Small Molecule Drugs. *Gene Ther.* **2006**, *13*, 541–552.

- 
- (144) Elbashir, S. M.; Harborth, J.; Lendeckel, W.; Yalcin, A.; Weber, K.; Tuschl, T. Duplexes of 21 ± Nucleotide RNAs Mediate RNA Interference in Cultured Mammalian Cells. *Nature* **2001**, *411*, 494–498.
- (145) Draz, M. S.; Fang, B. A.; Zhang, P.; Hu, Z.; Gu, S.; Weng, K. C.; Gray, J. W.; Chen, F. F. Nanoparticle-Mediated Systemic Delivery of siRNA for Treatment of Cancers and Viral Infections. *Theranostics* **2014**, *4*, 872–892.
- (146) Naldini, L.; Blömer, U.; Gallay, P.; Ory, D.; Mulligan, R.; Gage, F. H.; Verma, I. M.; Trono, D. In Vivo Gene Delivery and Stable Transduction of Nondividing Cells by a Lentiviral Vector. *Science* **1996**, *272*, 263–267.
- (147) Wong, H. H.; Lemoine, N. R.; Wang, Y. Oncolytic Viruses for Cancer Therapy: Overcoming the Obstacles. *Viruses* **2010**, *2*, 78–106.
- (148) Thomas, C. E.; Ehrhardt, A.; Kay, M. A. Progress and Problems with the Use of Viral Vectors for Gene Therapy. *Nat. Rev. Genet.* **2003**, *4*, 346–358.
- (149) Bessis, N.; Garciacozar, F.; Boissier, M.-C. Immune Responses to Gene Therapy Vectors: Influence on Vector Function and Effector Mechanisms. *Gene Ther.* **2004**, *11*, S10–S17.
- (150) Baum, C.; Kustikova, O.; Modlich, U.; Li, Z.; Fehse, B. Mutagenesis and Oncogenesis by Chromosomal Insertion of Gene Transfer Vectors. *Hum. Gene Ther.* **2006**, *17*, 253–263.
- (151) Takenobu, T.; Tomizawa, K.; Matsushita, M.; Li, S.-T.; Moriwaki, A.; Lu, Y.-F.; Matsui, H. Development of p53 Protein Transduction Therapy Using Membrane-Permeable Peptides and the Application to Oral Cancer Cells. *Mol. Cancer Ther.* **2002**, *1*, 1043–1049.
- (152) Yin, H.; Kanasty, R. L.; Eltoukhy, A. A.; Vegas, A. J.; Dorkin, J. R.; Anderson, D. G. Non-Viral Vectors for Gene-Based Therapy. *Nat Rev Genet* **2014**, *15*, 541–555.
- (153) Yang, T.; Guan, Q.; Guo, X.; Meng, L.; Du, M.; Jiao, K. Direct and Freely Switchable Detection of Target Genes Engineered by Reduced Graphene Oxide-Poly( *M* -Aminobenzenesulfonic Acid) Nanocomposite via Synchronous Pulse Electrosynthesis. *Anal. Chem.* **2013**, *85*, 1358–1366.
- (154) Dong, H.; Zhang, J.; Ju, H.; Lu, H.; Wang, S.; Jin, S.; Hao, K.; Du, H.; Zhang, X. Highly Sensitive Multiple microRNA Detection Based on Fluorescence Quenching of Graphene Oxide and Isothermal Strand-Displacement Polymerase Reaction. *Anal. Chem.* **2012**, *84*, 4587–4593.
- (155) Tang, Z.; Wu, H.; Cort, J. R.; Buchko, G. W.; Zhang, Y.; Shao, Y.; Aksay, I. A.; Liu, J.; Lin, Y. Constraint of DNA on Functionalized Graphene Improves Its Biostability and Specificity. *Small* **2010**, *6*, 1205–1209.
- (156) Lu, C.-H.; Li, J.; Qi, X.-J.; Song, X.-R.; Yang, H.-H.; Chen, X.; Chen, G.-N. Multiplex Detection of Nucleases by a Graphene-Based Platform. *J. Mater. Chem.* **2011**, *21*, 10915–10919.
- (157) Wang, Y.; Li, Z.; Weber, T. J.; Hu, D.; Lin, C.-T.; Li, J.; Lin, Y. In Situ Live Cell Sensing of Multiple Nucleotides Exploiting DNA/RNA Aptamers and Graphene Oxide Nanosheets. *Anal. Chem.* **2013**, *85*, 6775–6782.
- (158) Cui, L.; Lin, X.; Lin, N.; Song, Y.; Zhu, Z.; Chen, X.; Yang, C. J.; Kang, H.; Lin, Y. H.; Fan, C.
-

- H.; *et al.* Graphene Oxide-Protected DNA Probes for Multiplex microRNA Analysis in Complex Biological Samples Based on a Cyclic Enzymatic Amplification Method. *Chem. Commun.* **2012**, 48, 194–196.
- (159) Tang, L.; Wang, Y.; Liu, Y.; Li, J. DNA-Directed Self-Assembly of Graphene Oxide with Applications to Ultrasensitive Oligonucleotide Assay. *ACS Nano* **2011**, 5, 3817–3822.
- (160) Lu, C.-H.; Zhu, C.-L.; Li, J.; Liu, J.-J.; Chen, X.; Yang, H.-H.; Dai, H. J.; Medley, C. D.; Cao, Z. H.; Li, J.; *et al.* Using Graphene to Protect DNA from Cleavage during Cellular Delivery. *Chem. Commun.* **2010**, 46, 3116–3118.
- (161) Neu, M.; Kissel, T. Recent Advances in Rational Gene Transfer Vector Design Based on Poly ( Ethylene Imine ) and Its Derivatives. *J. Gene. Med* **2005**, 7, 992–1009.
- (162) Ren, T.; Li, L.; Cai, X.; Dong, H.; Liu, S.; Li, Y. Engineered Polyethylenimine/graphene Oxide Nanocomposite for Nuclear Localized Gene Delivery. *Polym. Chem.* **2012**, 3, 2561.
- (163) Chen, B.; Liu, M.; Zhang, L.; Huang, J.; Yao, J.; Zhang, Z. Polyethylenimine-Functionalized Graphene Oxide as an Efficient Gene Delivery Vector. *J. Mater. Chem.* **2011**, 21, 7736–7741.
- (164) Tripathi, S. K.; Goyal, R.; Gupta, K. C.; Kumar, P. Functionalized Graphene Oxide Mediated Nucleic Acid Delivery. *Carbon* **2013**, 51, 224–235.
- (165) Li, T.; Wu, L.; Zhang, J.; Xi, G.; Pang, Y.; Wang, X.; Chen, T. Hydrothermal Reduction of Polyethylenimine and Polyethylene Glycol Dual-Functionalized Nanographene Oxide for High-Efficiency Gene Delivery. *ACS Appl. Mater. Interfaces* **2016**, 8, 31311–31320.
- (166) Xiong, M. P.; Forrest, M. L.; Ton, G.; Zhao, A.; Davies, N. M.; Kwon, G. S. Poly(aspartate-G-PEI800), a Polyethylenimine Analogue of Low Toxicity and High Transfection Efficiency for Gene Delivery. *Biomaterials* **2007**, 28, 4889–4900.
- (167) Gu, Y.; Guo, Y.; Wang, C.; Xu, J.; Wu, J.; Kirk, T. B.; Ma, D.; Xue, W. A Polyamidoamine Dendrimer Functionalized Graphene Oxide for DOX and MMP-9 shRNA Plasmid Co-Delivery. *Mater. Sci. Eng. C* **2017**, 70, 572–585.
- (168) Zhi, F.; Dong, H.; Jia, X.; Guo, W.; Lu, H.; Yang, Y.; Ju, H.; Zhang, X.; Hu, Y. Functionalized Graphene Oxide Mediated Adriamycin Delivery and miR-21 Gene Silencing to Overcome Tumor Multidrug Resistance In Vitro. *PLoS One* **2013**, 8, e60034.
- (169) Feng, L.; Yang, X.; Shi, X.; Tan, X.; Peng, R.; Wang, J.; Liu, Z. Polyethylene Glycol and Polyethylenimine Dual-Functionalized Nano-Graphene Oxide for Photothermally Enhanced Gene Delivery. *Small* **2013**, 9, 1989–1997.
- (170) Behlke, M. A.; Kalinina, T. S.; Dygalo, N. N.; Agami, R.; Mobbs, C. V.; Malik, A. B. Progress towards in Vivo Use of siRNAs. *Mol. Ther.* **2006**, 13, 644–670.
- (171) Reynolds, A.; Anderson, E. M.; Vermeulen, A.; Fedorov, Y.; Robinson, K.; Leake, D.; Karpilow, J.; Marshall, W. S.; Khvorova, A. Induction of the Interferon Response by siRNA Is Cell Type- and Duplex Length-Dependent. *RNA* **2006**, 12, 988–993.
- (172) Gao, Y.; Liu, X.-L.; Li, X.-R. IJN-17040-Research-Progress-on-Sirna-Delivery-with-Non-Viral-Carriers. *Int. J. Nanomedicine* **2011**, 6, 1017–1025.





## CHAPTER 2: SYNTHESIS OF REDUCED GRAPHENE OXIDE WITH VARIOUS OXYGEN PERCENTAGES

### 2.1 Introduction

In term of large scale and low cost production of graphene, mechanical exfoliation of graphite suffers of sheet stacking and low yields,<sup>1</sup> meanwhile electrochemical or thermal reduction of graphene oxide stand out as most promising strategies.<sup>2</sup> Reduced graphene oxide (rGO), is receiving more and more interest in biomedical field. Chemically speaking, rGO is a carbon material with an intermediate oxidation state between graphene and GO, hence most of rGO characteristics are modulated by the amount of oxygenated species present on its surface. For instance, the rGO is more hydrophilic than graphene because oxygenated groups are still retained after the reduction process. Moreover, rGO possesses a higher presence of  $sp^2$  C in the hexagonal structure than GO, thus enhancing the affinity of rGO with hydrophobic molecules. There is a wide range of reducing methods that have been used to afford rGO at very high C/O ratio. Besides, for application in gene delivery, the control of the surface chemistry and the tailor of the reducing conditions need to be carefully considered. Indeed, reducing species can be easily adsorbed or covalently anchored to the flakes strongly affecting rGO cell toxicity. For this reason, harsh reducing treatments that would remove most of the oxygenated groups should be avoided. Moreover, the designed rGO-based nanocarrier needs to be enough polar to show high stability in cell culture media. For these reasons most of the well-known chemical reducing agents such as hydrazine hydrate,<sup>3</sup> sodium borohydride,<sup>4</sup> and hydroquinone<sup>5</sup> should be avoided both for their toxic and hazardous nature and for their high reduction efficiency. More recently, alternative eco-friendly protocols such as hydrothermal and solvothermal methods, microwave-assisted reactions, biocompatible wet chemistry reductions have been developed.<sup>6</sup>

In the case of thermal reduction, thermal annealing of GO above 450°C affords a higher reducing efficiency than chemical reduction using hydrazine monohydrate at 80°C followed by heating at 200°C.<sup>7</sup> However, such elevated temperature can generate various defects because of the lack of stability of GO. Shivani et al.<sup>8</sup> proposed a green method to reduce GO by heating in water at 100°C under acidic condition for several days. The results of



thermogravimetric analysis (TGA) showed that the labile oxygen moieties are removed around 170-230°C. Moreover, increasing the hydrothermal time leads to stronger reduced effect.

For the solvothermal reduction method, Owen et al.<sup>9</sup> reported that the oxygenated groups on GO can be modulated by the boiling point of the solvent used. Furthermore, increasing the reaction times from 1 to 12 h did not enhance the effect of reduction, meaning that the reduction occurred within the first hours. To understand if the GO reduction was driven by the solvent or by the temperature the group of Owen compared the rGO formation at different temperatures (204°C, 189°C and 153°C) in various organic solvents (NMP, DMSO and DMF). In addition, the presence of oxygenated groups after these reduction treatments was tested via amine ring opening reaction (for epoxides) and isocyanates (for hydroxyl groups) and condensation reactions (for the carboxylic groups). In this study the authors concluded that the thermal reduction of GO is solvent-independent and dependent only on the temperature changes.

In term of alternative energy sources, the reduction of GO was also observed using microwave assisted system. Yanwu et al.<sup>10</sup> described a microwave reduced graphite oxide preparation using a commercial MW-oven starting from graphite oxide powder at 700 W in just one minute. Chen et al.<sup>11</sup> prepared rGO in a mixed solution of N, N-dimethylacetamide and water (DMAc/H<sub>2</sub>O) at 165°C in few minutes under dry nitrogen gas at 800 W.

On the other hand, together with the previously described green reduced processes, natural antioxidants have been also used as an ideal substitute of hydrazine. In particular, vitamin C (L-ascorbic acid) is able to reduce many reactive oxygen species and to avoid the risk of introducing heteroatoms on the sheets. Several methods combining vitamin C with other reducing agents and dispersants, such as ammonia,<sup>12</sup> L-tryptophan,<sup>13</sup> can be found in the literature. Zhang et al.<sup>14</sup> explored the reduction effect of vitamin C alone at room temperature after 48 h, duration time that was shortened only by increasing the concentration of ascorbic acid.

Besides the reduction methods to partially remove the oxygen moieties, we were interested also in increasing the epoxy groups for the reaction with amines (see Chapter 3). In the literature there are available several methods of epoxidation using m-chloroperbenzoic acid (mCPBA), trifluorodimethyldioxirane or ozone applied to single-walled carbon nanotubes (SWCNTs).<sup>15</sup>

## 2.2 Objectives of this chapter

Inspired from these green and easy reduction methods, we tested and tailored different reducing conditions on our graphene oxide materials using two different lateral sizes of starting GO: one from commercial source with small size and one from an academic source with big size. The objective of our study is to prepare amino functionalized rGO materials for a highly efficient siRNA delivery. Therefore, the purpose of the GO reduction described in this chapter was to eliminate a fraction of the oxygenated species (that may hamper siRNA complexation) while keeping most of the epoxide groups in order to subsequently functionalize them with various amines. In this context, different green reducing techniques have been explored: hydrothermal and solvothermal deoxygenation (in water and DMSO), microwave-assisted reduction, and wet chemistry reduction (using vitamin C). After analyzing and comparing these protocols, we performed reepoxidation reaction on the rGO, which was prepared by hydrothermal treatment to further increase the epoxide groups on the reduced GO sheets. Epoxidation process was performed by treating this rGO under ozone.<sup>16</sup> Reduction and reepoxidization were done first on commercial GO before treating GO of academic origin under suitable conditions. The efficiency of these various eco-friendly methods was evaluated and confirmed via TGA and XPS analysis.

## 2.3 Results and discussion

We decide to use two different samples from academic<sup>17</sup> (named GO<sub>L</sub>) and commercial (named GO<sub>S</sub>) sources, both prepared by modified Hummers method. The two GO are prepared by a slightly different process, as they differ in the percentage of oxygenated groups and lateral sizes. The lateral size characterization of the two GO correspond to  $300\pm 200$  nm in the case of GO<sub>S</sub> (Figure 2.1a) and  $3\pm 1$   $\mu\text{m}$  for GO<sub>L</sub> (Figure 2.1b).<sup>18</sup> To understand how the oxygenated groups affect siRNA structure (see further discussion in Chapter 3), we decided to perform a reduction and a subsequent epoxidation of the graphene oxide materials.

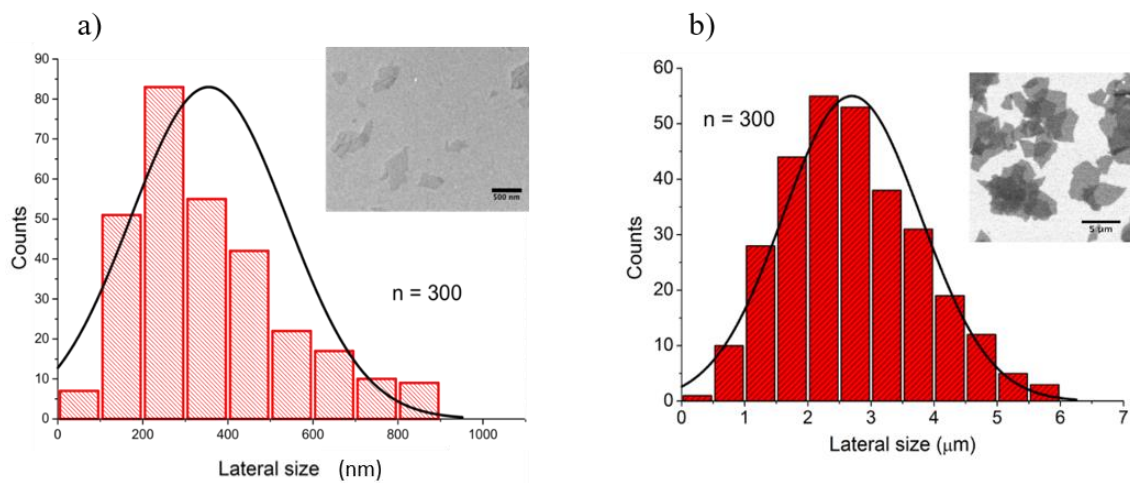


**Figure 2.1:** a) Lateral size distribution of GO<sub>s</sub>. In the inset: TEM image of GO<sub>s</sub>, scale bar corresponds to 500 nm. b) Lateral size distribution of GO<sub>L</sub>. In the inset: SEM image of GO<sub>L</sub>, scale bar corresponds to 5 μm.

First of all, we tried different green reducing methods on GO<sub>s</sub> to evaluate and optimize the condition of reduction. After this screening, we applied the best conditions found on the GO<sub>L</sub> reduction. Hence, we divided the following discussions in two main parts: part A related to the processes on GO<sub>s</sub> and part B related to the specific processes on GO<sub>L</sub>.

### PART A: Reactions on GO<sub>s</sub>

In term of GO<sub>s</sub>, I tried first one of the most eco-friendly and straightforward reducing approach by heating a dispersion of GO in water at 100°C for two days (rGO<sub>s</sub>-2d) and five days (rGO<sub>s</sub>-5d), respectively. This reduction process requires nor chemical reagents neither too high temperatures as in the case of complete annealing.

Since it was studied that the occurrence of reduction on GO is independent on the organic solvents but dependent on the temperature,<sup>9</sup> to increase the reduction efficiency, we decided to use DMSO, which has a higher boiling point than water. The reaction was performed at 155°C with the aim to selectively reduce most of the other oxygen moieties except the epoxy groups.<sup>9</sup> I performed the reaction at two different times: 15 min and in 1 h, affording rGO<sub>s</sub>-D15m and rGO<sub>s</sub>-D1h, respectively.

Furthermore, I explored alternative reduction protocols by using a microwave-assisted machine for reaction at high pressure and high temperature. Normally, the reduction of GO in water at high temperature occurs from hours to days, meanwhile in MW it takes few minutes.<sup>11</sup>

Therefore, by using MW, I tried to reduce GO using two different reaction times to evaluate the efficiency of reduction: 15 min and 2h, affording rGO<sub>S</sub>-MW15m and rGO<sub>S</sub>-MW2h, respectively.

Moreover, as the use of natural products to reduce compounds has become more and more exploited, I decided to treat GO with vitamin C (rGO<sub>S</sub>-C). The reduction was performed by heating the mixture of GO and vitamin C (mass ratio 1:1) at 90°C for 2 h without adding any other reagents.

Finally, I performed the epoxidation of the reduced rGO<sub>S</sub>-5d by fluxing the ozone gas into a dispersion of rGO in water at room temperature for 3 h leading to rGO<sub>S</sub>-5d-O<sub>3</sub>. To diminish the overoxidation effect of ozone,<sup>16</sup> the ozone gas, generated from air source, was fluxed under low rate.

These methods allowed to prepare rGO materials controlling the surface chemistry. In Table 2.1, I reported the list of the different rGO samples.

**Table 2.1:** Examples of reduced GO<sub>S</sub> from small GO.

	Small GO	Hydrothermal		DMSO		Microwave		Vitamin C	Reepoxidation by O <sub>3</sub>
		2 days	5 days	15mins	1h	15mins	2h		
<b>Acronym</b>	GO <sub>S</sub>	rGO <sub>S</sub> -2d	rGO <sub>S</sub> -5d	rGO <sub>S</sub> -D15m	rGO <sub>S</sub> -D1h	rGO <sub>S</sub> -MW15m	rGO <sub>S</sub> -MW2h	rGO <sub>S</sub> -C	rGO <sub>S</sub> -5d-O <sub>3</sub>

The thermal profiles of the starting and reduced GO were assessed by TGA, a routine method to measure the level of functionalization of carbon-based nanomaterials.<sup>19</sup> However, the thermal instability of GO makes it difficult to interpret the weight loss data.<sup>20</sup> Generally GO displays a typical thermogram with degradation in three steps (Figure 2.2, curve a).<sup>3</sup> The significant weight loss below 100°C is ascribed to desorption of water and some unstable oxygen containing functional groups. The main weight loss starting around 200°C is due to the decomposition of other labile oxygenated functionalities. The smaller weight loss occurring over the whole temperature range above 250°C can be referred to the removal of more stable oxygenated functions during the degradation process.

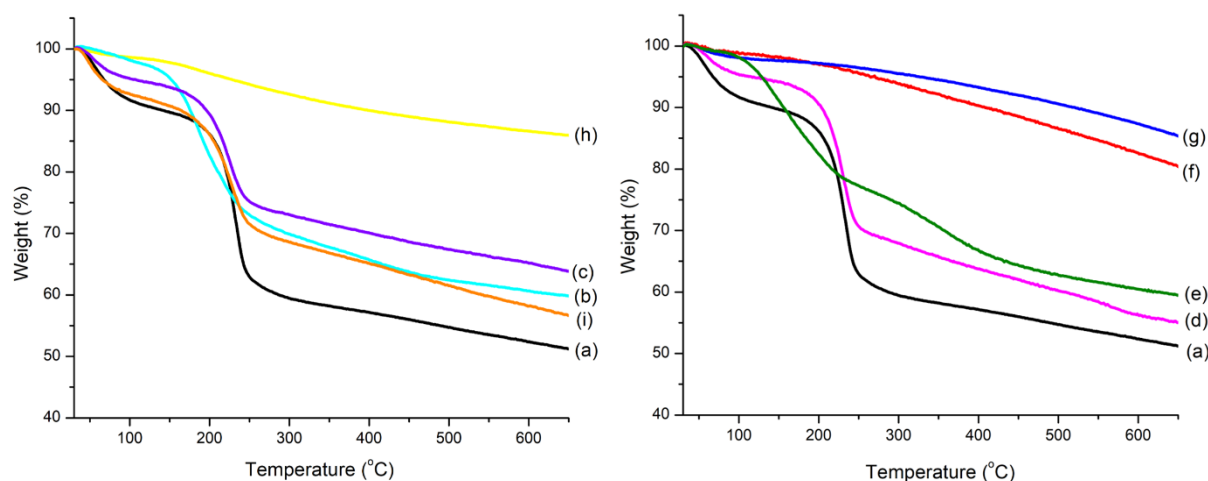


**Figure 2.2:** TGA spectra of the different graphene derivatives. GO<sub>S</sub> in black (a), rGO<sub>S</sub>-2d in cyan (b), rGO<sub>S</sub>-5d in violet (c), rGO<sub>S</sub>-D15m in pink (d), rGO<sub>S</sub>-D1h in green (e), rGO<sub>S</sub>-MW15m in red (f), rGO<sub>S</sub>-MW2h in blue (g), rGO<sub>S</sub>-C in yellow (h), rGO<sub>S</sub>-5d-O<sub>3</sub> in orange (i) The TGA curves are separated in two graphs for clarity.

Except in the case of microwave-assisted (Figure 2.2, curves f and g) and vitamin C (Figure 2.2, curve h) treatments, all the other reduction methods showed a similar three-step thermogram like for starting GO, but with different percentage in mass loss. This loss is associated to a decrease of the functional oxygenated groups due to the reduction process. It should be noticed that the highest weight loss observed corresponds to the highest oxygenated groups present on the rGO surface, meaning a lower efficiency of reduction obtained.

In case of the hydrothermal treatment, the lower weight loss in rGO<sub>S</sub>-5d (Figure 2.2, curve c) than rGO<sub>S</sub>-2d (Figure 2.2, curve b) means that the rGO<sub>S</sub>-5d resulted from a more efficient reduction process than rGO<sub>S</sub>-2d. In the case of solvothermal method using DMSO, the one using 15 min (Figure 2.2, curve d) displayed less reduction than the one using 1h (Figure 2.2, curve e), as indicated by a more significant weight loss in term of rGO<sub>S</sub>-D15m. Comparing the two solvothermal methods there are no evident differences between rGO<sub>S</sub>-5d and rGO<sub>S</sub>-D1h, indicating that the two treatments have similar reducing activity. The microwave-assisted (Figure 2.2, curve f and g) and vitamin C (Figure 2.2, curve h) processes showed the most prominent reduction of the oxygenated groups compared to the other methods, indicated by the lower weight loss in the thermogram curves. Furthermore, there were no remarkable changes between rGO<sub>S</sub>-MW15m (Figure 2.2, curve f) and rGO<sub>S</sub>-MW2h (Figure 2.2, curve g), indicating that the reduction occurred very fast, in few minutes.

To evaluate the effect of ozonation, rGO<sub>S</sub>-5d-O<sub>3</sub> thermogram curve (Figure 2.2, curve i) exhibits a higher weight loss compared to rGO<sub>S</sub>-5d (Figure 2.2, curve c). This would suggest that the ozone treatment of rGO<sub>S</sub>-5d was able to restore some oxygenated groups on the nanosheets. Together with the TGA analysis the reduction of GO was confirmed by X-ray photoelectron spectroscopy (XPS) analysis. The carbon to oxygen ratios are reported in Table 2.2.

**Table 2.2:** C/O ratios obtained by XPS analysis of GOs

Acronym	GO <sub>S</sub>	rGO <sub>S</sub> - 2d	rGO <sub>S</sub> - 5d	rGO <sub>S</sub> - D15m	rGO <sub>S</sub> - D1h	rGO <sub>S</sub> - MW15 m	rGO <sub>S</sub> - MW2h	rGO <sub>S</sub> -C	rGO <sub>S</sub> - 5d-O <sub>3</sub>
C/O ratio	2.2±0.1	2.7±0.1	3.5±0.2	2.7±0.1	4.2±0.2	5.6±0.1	5.8±0.2	8.3±0.3	2.6±0.1

XPS analysis of our starting GO shows a typical C/O ratio of most GO materials.<sup>21</sup> The reduction process is able to decrease the oxygen moieties on the surface of GO, hence increasing the C/O ratio. Indeed, the microwave-assisted (rGO<sub>S</sub>-MW2h and rGO<sub>S</sub>-MW15m) and vitamin C (rGO<sub>S</sub>-C) reduction shows the highest C/O ratio (~6 and ~8, respectively). Similar to the TGA curves, XPS analysis confirmed the strongest reduction in these cases. Besides, the hydrothermal treatment leading to rGO<sub>S</sub>-2d also exhibited a lower value of C/O ratio (2.7) than the treatment affording rGO<sub>S</sub>-5d (3.5), indicating that less oxygen moieties were removed after hydrothermal treatment for 2 days than for 5 days. This is also coherent with the higher weight loss of rGO<sub>S</sub>-2d than rGO<sub>S</sub>-5d in TGA. Furthermore, the solvothermal treatment leading to rGO<sub>S</sub>-D15m showed a lower value of C/O ratio (2.7) than the treatment to form rGO<sub>S</sub>-D1h (4.2), confirming that less oxygen groups remained in rGO<sub>S</sub>-D1h than in rGO<sub>S</sub>-15m. The ozonation process was able to decrease the C/O ratio from 3.5 for rGO<sub>S</sub>-5d to 2.6 for rGO<sub>S</sub>-5d-O<sub>3</sub>, proving the successful introduction of oxygen moieties. The low value of C/O ratio from XPS in case of rGO<sub>S</sub>-D15m and rGO<sub>S</sub>-2d is corresponding to the high weight loss curve obtained by TGA (Figure 2.2, curve d and b, respectively). Thus, these two treatments are not strongly reducing methods for GO.

In addition to XPS survey analyses, a detailed analysis of the C (1s) core level spectra gave us more evidence about the distribution of oxygenated groups. C (1s) peak includes values of the binding energies of different overlapping groups and needs a careful interpretation.<sup>22–25</sup> Therefore, we decided to treat and deconvolute the C (1s) spectra as a sum of the components



assigned to:  $sp^2/sp^3$  carbon atoms (at an interval of 284.4-285.3 eV), the hydroxyl and the epoxide groups (C-O: 286.2-287.2 eV), the carbonyl and the carboxylic groups (C=O: 287.6-289.9 eV) and the p-p\* shake-up satellite<sup>26</sup> (290.5-291 eV).

Generally, the C (1s) spectra of GO showed the presence of high amount of oxygenated groups (Figure 2.3a). Considering the efficiency of the reduction processes, the different intensities of the peaks assigned to the oxygenated groups (286 eV to 290 eV) in the reduced GO were depleted to different degree, as it can be observed in Figure 3.

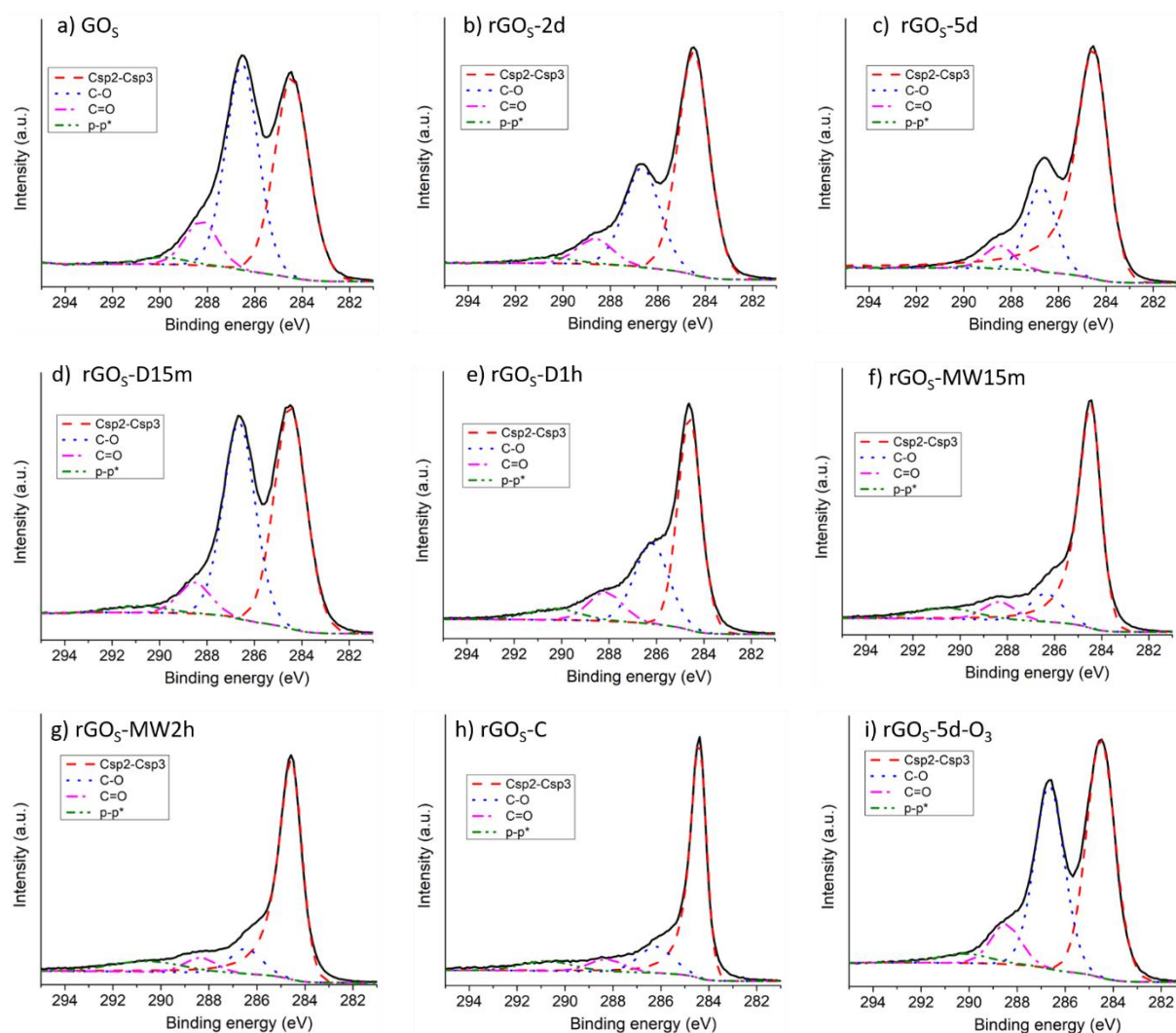


**Figure 2.3:** Deconvolution of the C (1s) peak for GO<sub>5</sub> (a), rGO<sub>5</sub>-2d (b), rGO<sub>5</sub>-5d (c), rGO<sub>5</sub>-D15m (d), rGO<sub>5</sub>-D1h (e), rGO<sub>5</sub>-MW15m (f), rGO<sub>5</sub>-MW2h (g), rGO<sub>5</sub>-C (h), rGO<sub>5</sub>-5d-O<sub>3</sub> (i)

In particular, we could observe the most remarkable decrease of the intensity of the peaks assigned to the oxygenated groups in the case of the microwave-assisted and vitamin C reductions (Figure 2.3f, g and h), concurrent with the most efficient reduction methods. This

observation was in total agreement with the C/O ratio (Table 2.2) and with the TGA thermograms (Figure 2.2 curves f, g and h).

The C (1s) spectra of rGO<sub>S</sub>-D15m and hydrothermal rGO<sub>S</sub>-2d (Figure 2.3d and b, respectively) showed a small reduction in the peak of the oxygenated groups suggesting that the reduction was not strong. In addition, the increase in the intensity of the peaks assigned to oxygenated groups in the rGO<sub>S</sub>-5d-O<sub>3</sub> (Figure 2.3i) compared to the rGO<sub>S</sub>-5d (Figure 2.3c), was coherent with the decreasing of C/O ratio (Table 2.2) and the increase of the TGA curve (Figure 2.2), confirming the success of ozonation on rGO.

Overall, the TGA and XPS analyses confirm the reduction of the GO<sub>S</sub> material and confirm that we were able to prepare rGO materials with different oxidation grades. Besides, from the deconvolution of C (1s) in Figure 2.3, we illustrate the percentages of C-O, C=O, Csp<sup>2</sup>-Csp<sup>3</sup> and  $\pi$ - $\pi^*$  peaks in Figure 2.4.

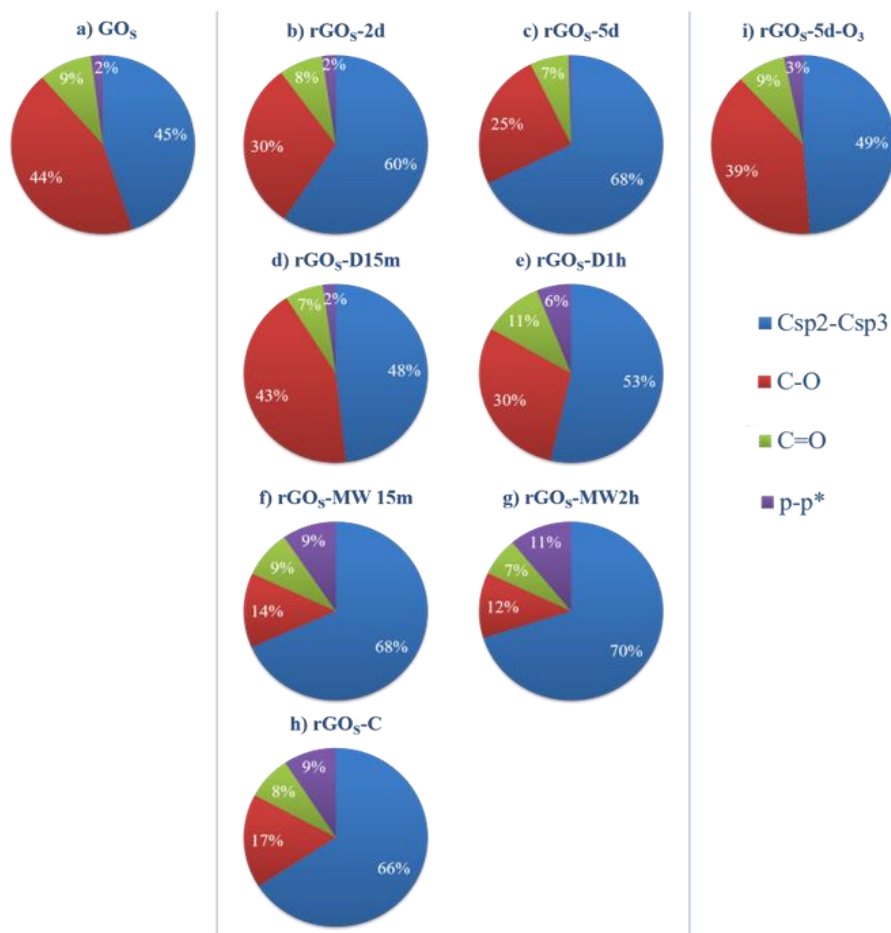


**Figure 2.4:** Comparison the percentages of C-O, C=O, Csp<sup>2</sup>-Csp<sup>3</sup> and  $\pi$ - $\pi^*$  peaks of the different reduced GO<sub>S</sub> based on the deconvolution of the high resolution XPS analysis of C (1s).



First of all, the variation of the percentage of C=O peak in GOs and in the reduced GOs is very small (~1-2%). These values suggest that the carbonyl and carboxyl groups, present on the edges of the nanosheets, are quite stable and are not affected by the reduction processes. Previous studies reported that the carbonyl groups are not removed spontaneously, whereas the carboxyl groups are slowly reduced at high temperature.<sup>9,27</sup> Instead, we can observe that all the reduction treatments affect mainly the C-O bond corresponding to epoxides and alcohols. From these results, we can conclude that all tested reduction methods affect only the in-plane oxygen groups in the GO sheets while the C=O groups present on the edges seem to be resistant to the deoxygenation reactions.

In the case of the hydrothermal treatment, the percentage of C-O bonds was decreased from 44% in GOs to 30% and 25% in rGO<sub>S</sub>-2d and rGO<sub>S</sub>-5d, respectively, confirming the occurrence of GO deoxygenation and the higher efficiency of reduction after 5 days as discussed above. For solvothermal treatment in DMSO, the reaction during 15 min did not provoke significant changes in the percentages of the groups compared to starting GO, while after 1 h of reaction, it appears a sensible decrease in the percentage of C-O groups (down to 30% in rGO<sub>S</sub>-D1h). These data are totally coherent with the C/O ratio and the TGA curves, confirming that the reduction occurred after 1 h of treatment.

In case of microwave-assisted reduction, we obtained the highest decrease of C-O groups, to 14% and 12% for rGO<sub>S</sub>-MW15m and rGO<sub>S</sub>-MW1h, respectively. Thus, this method is useful to reduce most the epoxides and hydroxyl groups. The low percentage of C-O bonds (17%) in case of reduction by vitamin C, together with the data on microwave-assisted reaction emphasizes again that these methods reduce most of the oxygen moieties on the surface of GO. To clarify the effect of ozonation, we measured the percentages of C-O groups between the rGO<sub>S</sub>-5d (Figure 2.4c) and rGO<sub>S</sub>-5d-O<sub>3</sub> (Figure 2.4i). The increase of the percentage of the C-O bonds from 25% (rGO<sub>S</sub>-5d) to 39% (rGO<sub>S</sub>-5d-O<sub>3</sub>) after the reepoxidation treatment was recorded. This XPS change is associated to the ozone ability to epoxidize the carbon-carbon double bond.<sup>15,16</sup>

The morphology of the starting GOs, the highly reduced rGO<sub>S</sub>-MW15m and rGO<sub>S</sub>-5d-O<sub>3</sub> was assessed by transmission electron microscopy (TEM) (Figure 2.5).

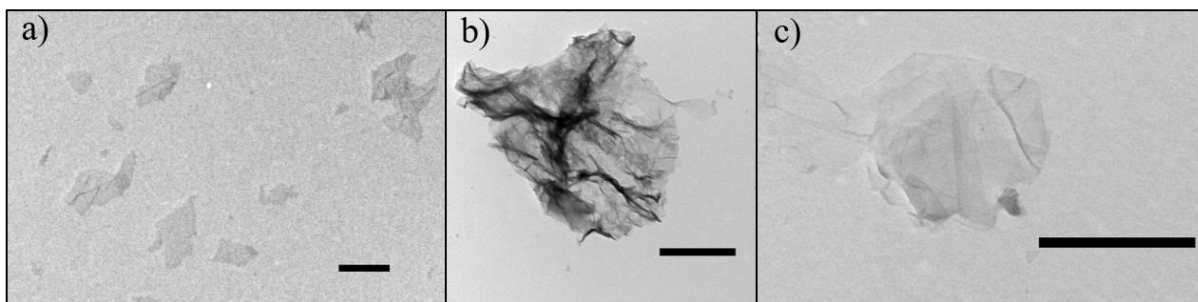


**Figure 2.5:** TEM images of: a) GOs b) rGOs-MW15m c) rGOs-5d-O<sub>3</sub>; scale bar corresponds to 500 nm.

The TEM images of the three samples showed that graphene sheets are highly wrinkled (dark areas). Under the treatment with ozone, it seemed that the structure is still retained, without any apparent size reduction.

In addition, the behavior of the dispersions of GOs at concentration 2 mg/ml in water was analyzed (Figure 2.6). The materials were sonicated for 5 min to obtain an homogenous dispersion. The brownish color of the starting GOs dispersion is typical of the graphene oxide.<sup>28</sup> Furthermore, the blackish color of the other rGOs accompanied by aggregation and precipitation supported the presence of less oxygenated groups on the sheets compared to GOs. We could observe a high aggregation of rGOs-MW15m (sample 6), rGOs-MW2h (sample 7), and rGOs-C (sample 8) right after 5 min. The treatment with DMSO for 1 h (sample 5) also aggregated after 15 min. The poor dispersibility of these rGOs represents a real disadvantage for delivery purposes. The other samples still maintain a good dispersibility after 1 h. It seemed that the dispersibility was correlated with the oxygen functions present on the surface of rGOs. The highest amount of oxygenated groups corresponded (meaning the lower C/O ratio in Table 2) to a better dispersibility of rGO.

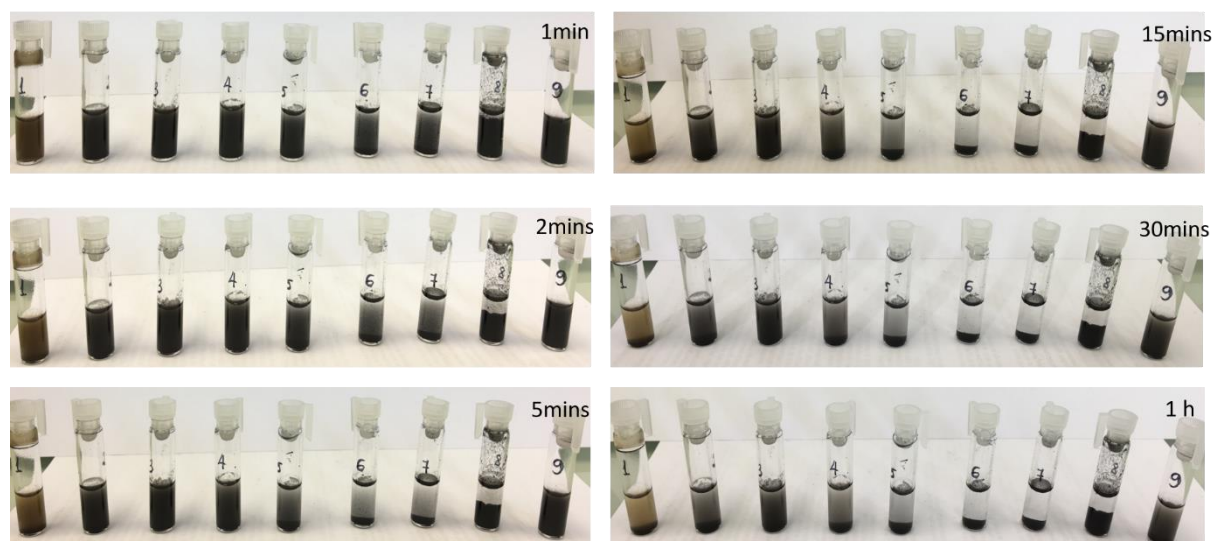


**Figure 2.6:** Dispersion of the different GOs at different time from 1 min to 1 h. The order of the samples is following to the order in Table 2, from left to right: GOs (1), rGOs-2d (2), rGOs-5d (3), rGOs-D15m (4), rGOs-D1h (5), rGOs-MW15m (6), rGOs-MW2h (7), rGOs-C (8), and rGOs-5d-O<sub>3</sub> (9).

The surface charge of the series of GOs was also investigated. Although the oxygen percentages of the series of GOs varied as confirmed by XPS, TGA and the dispersibility test, no significant increase of the  $\zeta$  potential among the reduced GO and the starting GO was recorded. Figure 2.7 reports the  $\zeta$  potential at different pH of three representative samples with a range of oxygenated percentages: the lowest C/O ratio with good dispersibility GOs, the medium C/O ratio with good dispersibility rGOs-5d, and the very high C/O ratio with low dispersibility rGOs-MW2h.

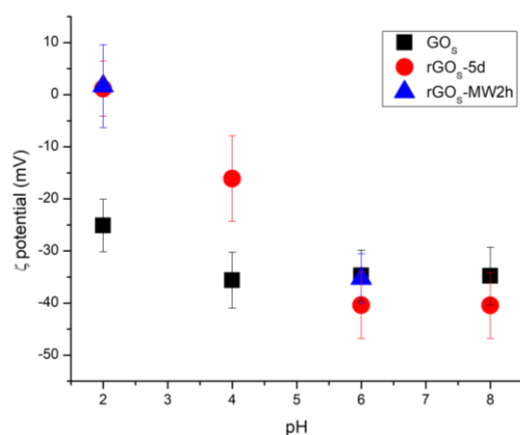


**Figure 2.7:**  $\zeta$  potential at different pH of GOs (black square), rGOs-5d (red circle), and rGOs-MW2h (blue triangle) dispersions in water, at a concentration of 0.05 mg/ml.

Our study showed that the  $\zeta$  potential of all three samples dispersions were pH dependent with a highly negative charge, probably due to the ionization of the carboxylic acid and, possibly, the phenolates on the surface.<sup>29,30</sup> At low pH (2 and 4) we observed a less negative charge surface on the reduced GO in comparison to the GOs. This behavior could be explained by the more oxygenated groups presenting on GO sheets than that of rGO sheets.<sup>31</sup> From pH 6 to 8, no significant difference of charge surface was recorded. The average value of  $\zeta$  potential of these samples at pH 6 was nearly the same and around -40mV. Together with a small variety of percentage of C=O groups from XPS (Figure 2.4) among these samples, it could be assumed that there are still enough carboxylic acid groups remaining leading to a negative charge on the rGOs.

In addition, to better understand the effect of oxygenation/reduction on the morphology of GOs, an X-ray diffraction (XRD) characterization was performed on the GOs, rGOs-5d, and rGOs-5d-O<sub>3</sub> (Figure 2.8 and Table 2.3). Starting GOs shows a peak centered at  $2\theta=11.6^\circ$  corresponding to an interplanar distance of 7.6 Å. This value is typical for GO nanostructures,<sup>17</sup> and is attributed to the [002] interplanar distance in the GO lattice. Reduction and epoxidation processes lead to a shift of the [002] XRD up to  $2\theta=12.9^\circ$  and  $12.8^\circ$  for rGOs-5d and rGOs-5d-O<sub>3</sub>, respectively. The changes detected in the [002] distances can be ascribed to the variation on the oxygen content on the sample surface.<sup>17</sup> Indeed, the hydrothermal hydrogenation depletes oxygen from the GO surface causing a diminution in the average layer to layer distance to 6.8 Å, while rGOs-5d epoxidation causes a small increase up to 6.9 Å.

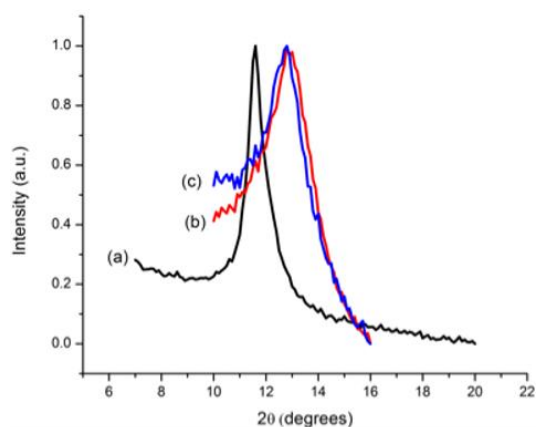


**Figure 2.8:** High resolution XRD spectra of GOs (a, black line), rGOs-5d (b, red line), and rGOs-5d-O<sub>3</sub> (c, blue line).

**Table 2.3:** [002] calculated distance from XRD using Bragg law,  $\lambda = 1.541\text{\AA}$ .

Sample	XRD max. ( $2\theta^\circ$ )	Distance ( $\text{\AA}$ )
GO <sub>S</sub>	11.6	7.6
rGO <sub>S</sub> -5d	12.9	6.8
rGO <sub>S</sub> -5d-O <sub>3</sub>	12.8	6.9

In summary, various green reduction conditions were tested on commercial GO<sub>S</sub>. It should be reminded that we were interested in efficiently reducing partially the oxygenated groups on the surface on GO, but keeping enough polar groups to make rGO stable in cell media. The microwave-assisted reaction, vitamin C method, and solvothermal treatment in DMSO efficiently reduced GO but the formed rGOs were strongly aggregated that limited these techniques for bioapplications. The microwaves-assisted method could be useful in other application with the purpose of obtaining a highly reduced GO in very short time by manipulating the temperature and the pressure of the system. Finally, the hydrothermal method for 5 days seems to efficiently reduce GO while it has preserved its colloidal stability in water. In addition, the ozonation treatment confirmed the introduction of oxygenated groups, especially C-O groups on the surface of reduced GO.

### PART B: Reactions on GO<sub>L</sub>

Based on the efficiency of the reduction of the different methods on GO<sub>S</sub>, I have decided to choose the following conditions for the reduction of GO<sub>L</sub>: the hydrothermal treatment for 5 days and vitamin C, affording rGO<sub>L</sub>-5d and rGO<sub>L</sub>-C, respectively (Table 2.4). Finally, to reintroduce the epoxy groups on the surface of reduced GO, the epoxidation reaction using O<sub>3</sub> was performed on rGO<sub>L</sub>-5d to form rGO<sub>L</sub>-5d-O<sub>3</sub> (Table 2.4).

**Table 2.4:** Examples of reduced GO<sub>L</sub> from large GO.

	Large GO	Hydrothermal 5 days	Vitamin C	Reepoxidation by O <sub>3</sub>
Acronym	GO <sub>L</sub>	rGO <sub>L</sub> -5d	rGO <sub>L</sub> -C	rGO <sub>L</sub> -5d-O <sub>3</sub>

Then, the thermal profiles of the starting GO<sub>L</sub> and reduced GO were assessed by TGA; Figure 2.9 shows the thermograms of the different GO<sub>L</sub>.

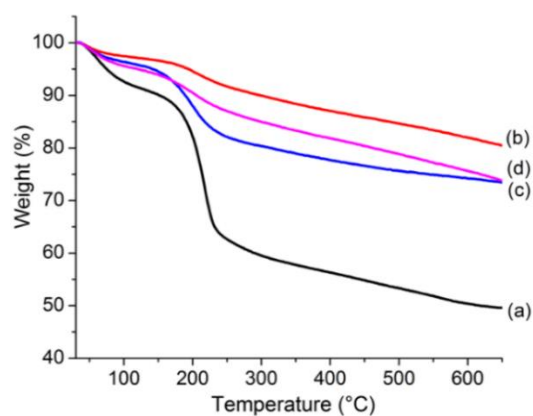


**Figure 2.9:** TGA curves of the different graphene derivatives. GO<sub>L</sub> in black (a), rGO<sub>L</sub>-5d in red (b), rGO<sub>L</sub>-C in blue (c), and rGO<sub>L</sub>-5d-O<sub>3</sub> in pink (d).

The TGA curve of GO<sub>L</sub> (Figure 2.9) shows the typical decomposition features of graphene oxide material with the same trend discussed before for GOs.<sup>18</sup> A similar trend can be seen in the TGA curves of the hydrothermal treatment, vitamin C reduced GO and reoxidized rGO (Figure 2.9 curve b, c, and d, respectively) but with different weight losses. From the TGA characterization, rGO<sub>L</sub>-5d shows the most prominent reduction of the oxygenated groups compared to rGO<sub>L</sub>-C, proving that on GO<sub>L</sub>, the hydrothermal process is a more effective reduction compared to the reduction with vitamin C. Besides, rGO<sub>L</sub>-5d-O<sub>3</sub> curve (Figure 2.9, curve d) exhibits a higher weight loss compared to rGO<sub>L</sub>-5d, which can be associated to the successful introduction of the oxygenated groups after the ozone treatment. The reduction of GO<sub>L</sub> was also confirmed by XPS (Table 2.5).

**Table 2.5:** C/O ratios obtained by XPS analysis.

Samples	C/O ratio
GO <sub>L</sub>	2.6 ± 0.1
rGO <sub>L</sub> -5d	6.1 ± 0.1
rGO <sub>L</sub> -C	4.0 ± 0.1
rGO <sub>L</sub> -5d-O <sub>3</sub>	3.5 ± 0.1

XPS analysis showed that the reduction process was able to sensibly diminish the oxygen content on graphene surface. In particular, rGO<sub>L</sub>-5d and rGO<sub>L</sub>-C displayed the highest values

of 6.1 and 4.0 C/O, respectively. In comparison to the C/O ratio of the starting GO<sub>L</sub> (2.6), the higher C/O ratio in the other rGO supported that the reduction of GO occurred.<sup>32</sup> Similar to TGA, the XPS analysis gave evidences that the hydrothermal process has been a more effective treatment than vitamin C. The ozone reaction was able to decrease the C/O ratio further from 6.1 in rGO<sub>L</sub>-5d to 3.5 in the case of rGO<sub>L</sub>-5d-O<sub>3</sub>, proving the successful reoxidation of the graphene sheets.

Further information can be drawn from the deconvolution of the high-resolution C (1s) peak (Figure 2.10) and the percentages of each peak corresponding to the deconvolution (Figure 2.11).

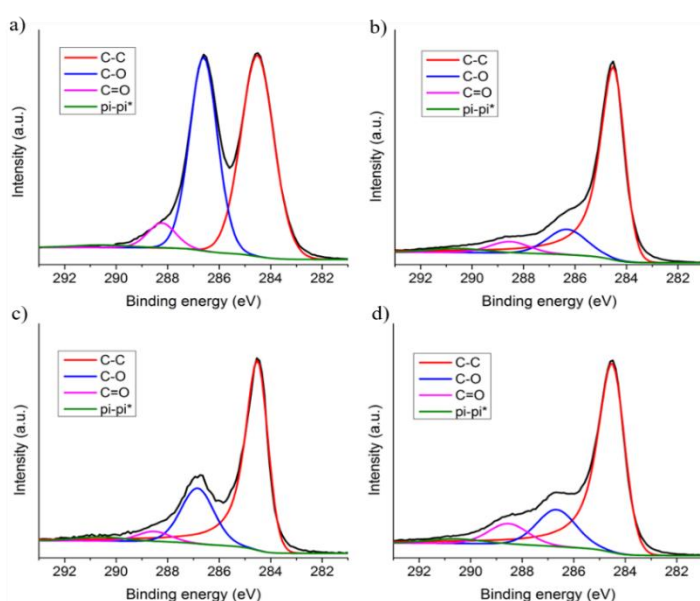


**Figure 2.10:** Deconvolution of the C (1s) peak for GO<sub>L</sub> (a), rGO<sub>L</sub>-5d (b), rGO<sub>L</sub>-C (c), and rGO<sub>L</sub>-5d-O<sub>3</sub> (d).

Generally, in comparison to starting GO<sub>L</sub>, the intensities of the peaks assigned to the oxygenated groups in the two reduced GO were dramatically depleted, as can be directly observed in Figure 2.10b and c. In particular, the rGO<sub>L</sub>-5d displayed a more remarkable decrease of the oxygenated groups compared to rGO<sub>L</sub>-C, indicating that in case of GO<sub>L</sub>, the hydrothermal method was more efficient in the reduction compared to the reduction with vitamin C. This behavior was completely consistent with the C/O ratio (Table 2.5) and with the TGA thermograms (Figure 2.9, curves a, b, and c).

Moreover, I also illustrated the percentages of C-O, C=O, Csp<sup>2</sup>-Csp<sup>3</sup> and  $\pi$ - $\pi^*$  peaks from the deconvolution of C (1s) in Figure 2.10 and Figure 2.11.



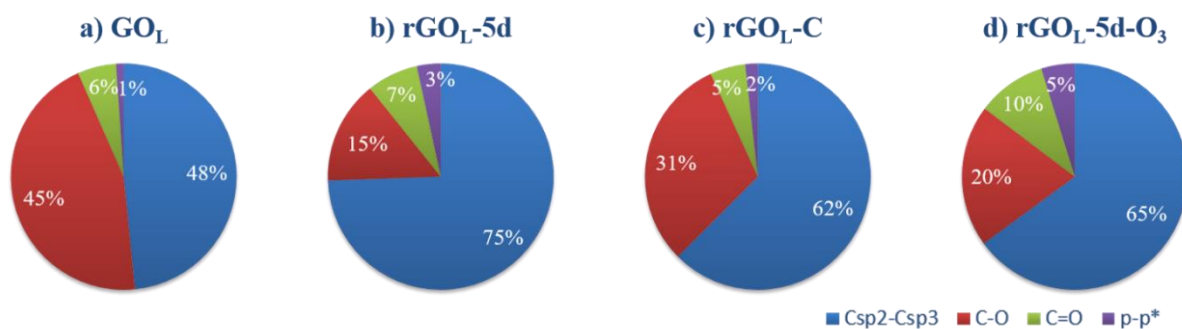


**Figure 2.11:** Comparison of the percentage of C-O, C=O, Csp<sup>2</sup> Csp<sup>3</sup> and p-p\* of various reduced GO based on the deconvolution of the high resolution XPS analysis of C (1s).

Comparing the rGO<sub>L</sub>-5d and rGO<sub>L</sub>-5d-O<sub>3</sub>, we can see an increase of the percentage of C-O bonds from 15% (Figure 2.11b) to 20% (Figure 2.11d) after the epoxidation treatment, corresponding to the enhancement of the peak of C-O in Figure 8b and d. Furthermore, a little increase of the C=O percentage from 7% (Figure 2.11b) to 10% (Figure 2.11d) after reepoxidation of rGO<sub>L</sub>-5d was also observed, which likely derives from a partial etching and formation of pinholes as observed in TEM image (see below in Figure 2.12). This overoxidation of GO under ozonation can increase carboxyl groups on the edge of GO, as well as the carbonyl groups by the oxidation of hydroxyl groups retained in the rGO<sub>L</sub>-5d<sup>33</sup>. The XPS analysis of rGO<sub>L</sub>-5d-O<sub>3</sub> confirmed the increase of C-O bond in rGO<sub>L</sub>-5d-O<sub>3</sub> (Figure 2.10d). This is in total agreement with the increase of C/O ratio by ozonation (Table 2.4), as well as the TGA data (Figure 2.9, curve b and d).

The morphological characterization by TEM of the series of GO<sub>L</sub> was reported in Figure 2.12. In comparison to the TEM of the starting GO<sub>L</sub> (Figure 2.12a), the TEM images of the three other samples exhibited that the graphene sheet structure was still retained after reduction and epoxidation processes without any apparent size reduction. Both hydrothermal (Figure 2.12b) and vitamin C (Figure 2.12c) reduction processes induced a formation of more wrinkly graphene sheets (dark areas). This behavior is well known in the literature and may be due to the dispersibility process and the presence of defects on the rGO structure.<sup>16</sup> The analysis of rGO<sub>L</sub>-5d-O<sub>3</sub> (Figure 2.12d) showed less wrinkled structures and the sheets seemed to be less agglomerated. This behavior is likely due to the reintroduction of oxygenated functional groups that increase the polarity of the surface leading to a stabilization of the single sheets in aqueous media. Besides, the morphological analysis revealed the formation of pinholes and some erosions on the edges of the graphene sheets following the ozone treatment (indicated by red



arrows in Figure 2.12d). As reported previously, these morphological changes could be attributed to the ozonation.<sup>34</sup> Indeed ozone, besides adding oxygen to C sp<sup>2</sup> to form an epoxide, can efficiently decarboxylate and oxidize carbonyl and alcohol groups present at the edges of rGO. This side reaction may alter the morphology and the size of the sheets. For this reason, ozone reaction must be performed avoiding overoxidation. In our case, even working under mild conditions, we observed a little degradation of the sheets that however did not cause a dramatic change in the lateral size of rGO<sub>L</sub>-5d-O<sub>3</sub>.

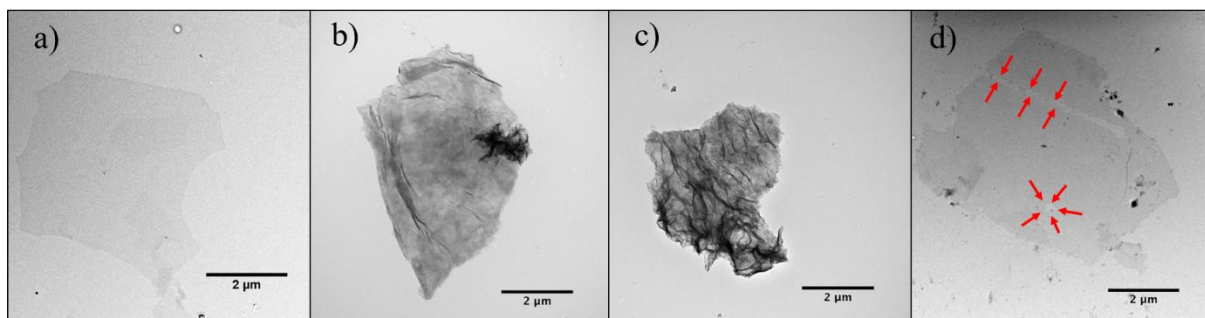


**Figure 2.12:** TEM images of various reduced graphene oxide: a) GO<sub>L</sub> b) rGO<sub>L</sub>-5d c) rGO<sub>L</sub>-C and d) rGO<sub>L</sub>-5d-O<sub>3</sub>. Red arrows indicate pinholes and erosions on the edges of graphene sheets.

The dispersibility of the series of GO<sub>L</sub> is presented in Figure 2.13. I prepared the samples using the same conditions of the series of GO<sub>S</sub>, with the concentration of 2 mg/ml water and sonication for 5 min.

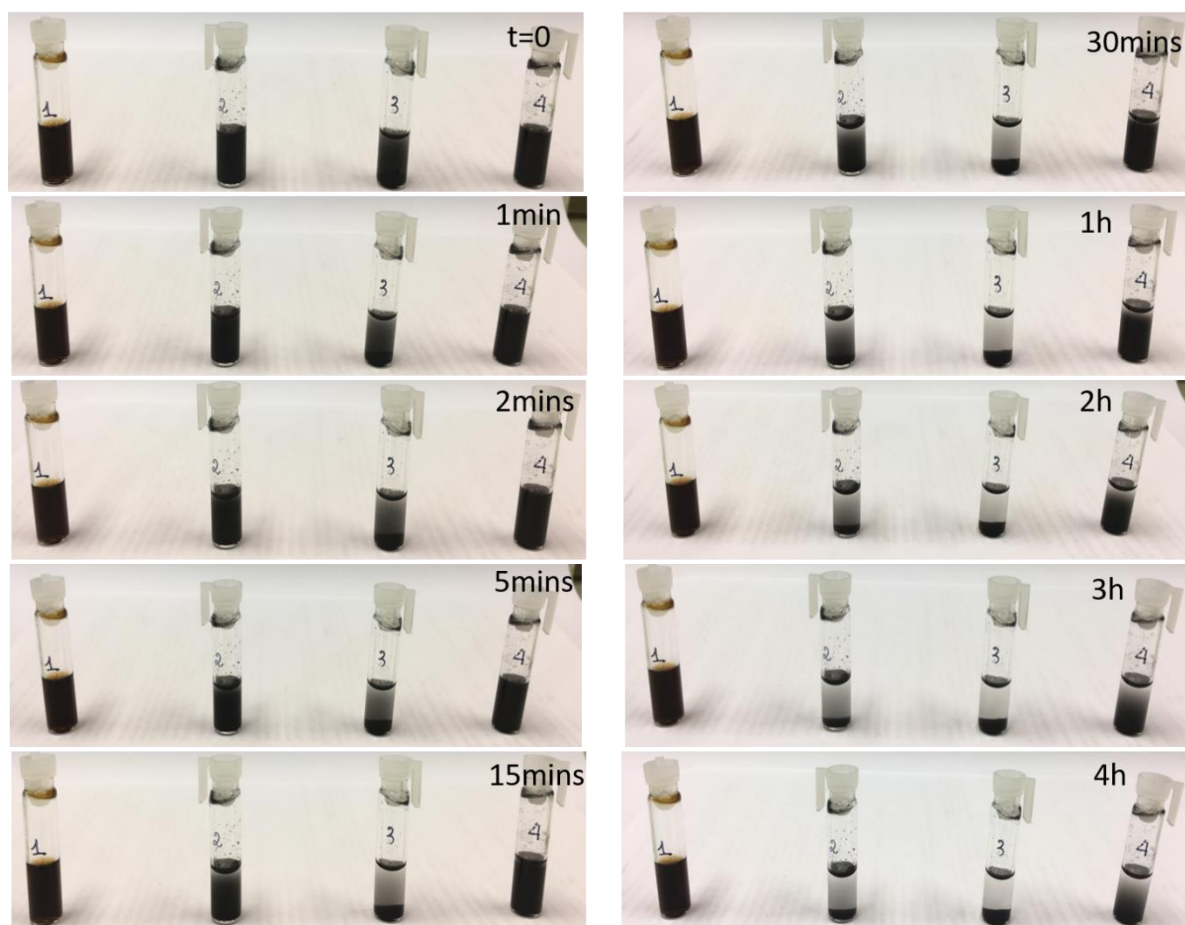


**Figure 2.13:** Dispersion of the different  $GO_L$  at different time from 1 min to 4 h. The order of the samples is following to the order in Table 4, from left to right:  $GO_L$  (1),  $rGO_L$ -5d (2),  $rGO_L$ -C (3),  $rGO_L$ -5d- $O_3$  (4).

Generally, except in the case of the vitamin C treated  $rGO_L$ -C (sample 3), the other samples exhibited a good dispersibility up to 1 h. The dispersibility was enhanced in comparison to the  $rGO_S$  under the same treatments (Figure 2.6). Moreover, the  $GO_L$  and  $rGO_L$ -5d- $O_3$  seemed to be well dispersed up to 4 h. Comparing the two reduced  $rGO_L$ -5d- $O_3$  and  $rGO_L$ -5d, the ozonation method succeeded to increase the dispersibility of the former. Interestingly, even though the C/O ratio of  $rGO_L$ -C is lower than that of  $rGO_L$ -5d (Table 2.5), meaning that more oxygenated groups are present in  $rGO_L$ -C, this conjugate aggregated faster than  $rGO_L$ -5d (after 30 min). This behavior correlated with the TEM images showing more wrinkle graphene sheets in case of  $rGO_L$ -C (Figure 2.12). The  $\zeta$  potential of these samples was also investigated, but again we obtained nearly the same negative value of  $\zeta$  potential around (-40mV) for the different samples at pH 6.

I further analyzed the structure of the series of GO<sub>L</sub> by using solid-state magic angle spinning (MAS) NMR spectroscopy, as shown in Figure 2.14.

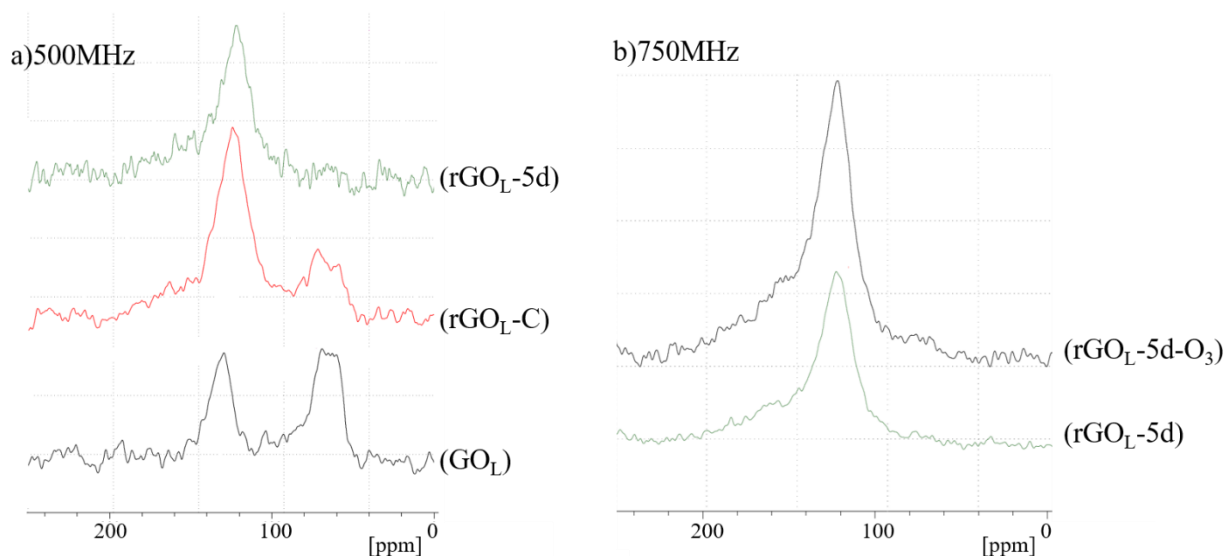


**Figure 2.14:** Direct polarization <sup>13</sup>C ssNMR: a) at 500 MHz of GO<sub>L</sub>, rGO<sub>L</sub>-5d, rGO<sub>L</sub>-C, and b) at 750 MHz of rGO<sub>L</sub>-5d and rGO<sub>L</sub>-5d-O<sub>3</sub>.

The <sup>13</sup>CNMR spectrum of the starting GO<sub>L</sub> is presented in Figure 2.14a. The peak from 60 ppm to 75 ppm was attributed to the epoxides and hydroxyl groups, while the peak at 129.4 ppm corresponded to the C=C conjugated double bonds.<sup>30,35,36</sup> In comparison to the starting GO<sub>L</sub>, I observed in Figure 2.14a a decrease of the intensity of the peak corresponding to the C-O bonds in the two reduced GO. Especially, the rGO-5d displayed a more remarkable decrease of the C-O bonds compared to rGO<sub>L</sub>-C, supporting the same result of the XPS and TGA analyses, and proving that the hydrothermal method efficiently reduced GO<sub>L</sub> compared to the vitamin C method. However, comparing the rGO<sub>L</sub>-5d and rGO<sub>L</sub>-5d-O<sub>3</sub> spectra, even at higher magnetic field for better signal to noise ratio as in Figure 2.14b, we could not confirm the presence of the epoxides. We have still not understood why a direct acquisition of the carbon signals does not allow to detect the C-O groups.

Besides the ozonation, to enhance the epoxy groups, I tried other treatments on rGO<sub>L</sub>-5d using mCPBA,<sup>37</sup> and dimethyldioxirane (DMDO),<sup>38</sup> methods that were reported before to efficiently epoxidize CNTs. However, because of the impurities remained and of the negligible increase of C-O bonds (at position 286.2-287.2 eV in C(1s)), these methods were not explored further. The XPS survey analysis and C(1s) spectra of rGO<sub>L</sub>-5d after treating with mCPBA and DMDO are shown in Figure 2.15.

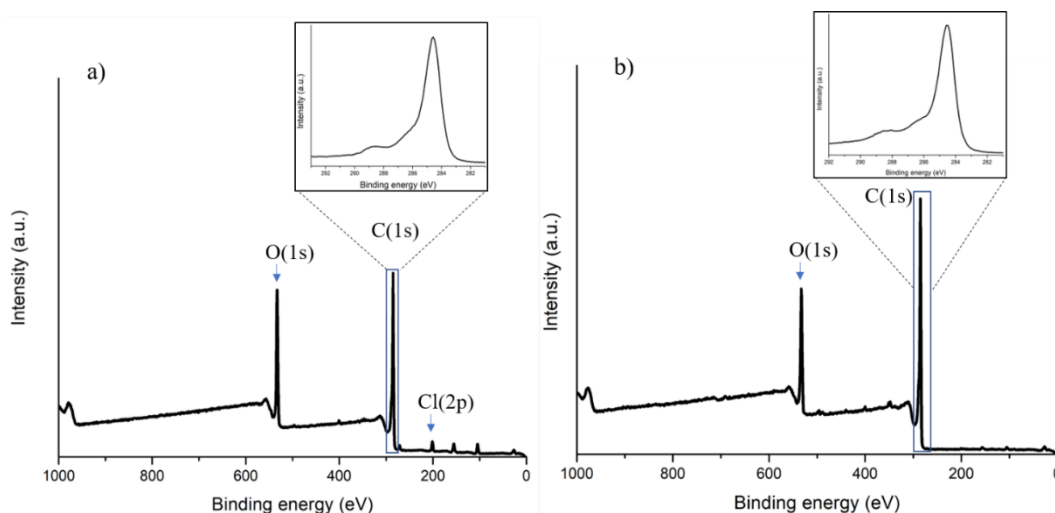


**Figure 2.15:** XPS spectra of rGO<sub>L</sub>-5d after treatment with mCPBA (a) and DMDO (b).

In summary, for GO<sub>L</sub>, we were able to successfully prepare graphene sheets with different oxygen contents. We produced a highly-reduced graphene oxide via hydrothermal treatment and a higher oxygenated graphene via reduction with vitamin C. Epoxidation of hydrothermally treated GO was performed with ozone. The resulting graphene shows an intermediate oxygenation value between non-treated GO and the hydrothermally treated GO.

Comparing the same treatment on the GO of different size and sources, XPS analysis (Table 2.2 and Table 2.5) shows similar values of C/O ratio for both GO<sub>S</sub> and GO<sub>L</sub> (~2.4), which are typical of most of graphene oxide materials.<sup>21</sup> In particular, the hydrothermal treatment, leading to rGO<sub>S</sub>-5d and rGO<sub>L</sub>-5d, afforded materials with C/O ratios of 3.5 and 6.1, respectively. The decrease of O% is more evident in the case of GO<sub>L</sub> than in GO<sub>S</sub>. Meanwhile in term of vitamin C treatment, there is a higher reduction effect on GO<sub>S</sub> than GO<sub>L</sub>, with the higher C/O ratio for rGO<sub>S</sub>-C (~8) than for rGO<sub>L</sub>-C (~4). These observations may be attributed to a different reactivity due to the lateral size and the presence of various oxygenated groups from the starting GO. Ozone treatment causes a decrease of C/O ratio to 3.0 for rGO<sub>S</sub>-5d-O<sub>3</sub> and to 2.5 in the case of rGO<sub>L</sub>-5d-O<sub>3</sub>, proving the successful epoxidation of the graphene sheets. Moreover, the increase of the percentage of C-O band in the case of rGO<sub>S</sub>-5d-O<sub>3</sub> (Figure 2.3d and Figure 2.4d) and rGO<sub>L</sub>-5d-O<sub>3</sub> (Figure 2.10d and Figure 2.11d) proved that the ozone treatments are able to introduce epoxide groups on the GO surface.

## 2.4 Conclusion

In this study, we have applied a variety of green and straightforward methods to reduce GO from different sources and of different sizes to achieve reduced GO with tunable C/O ratio. The surface and morphological characterization of the materials were carried out by diverse techniques. In term of small GO, we observed the highest reduction by using microwave-assisted and vitamin C-base method, confirmed by the significant less weight loss in TGA in comparison to GOs, and the substantial increase of C/O ratio. The hydrothermal reaction also exhibited notable reduction after 5 days of heating at reflux. The solvothermal method using DMSO was reported with a remarkable reduction after 1 h of treatment but suffered of the presence of residual solvent. The reduction under MW irradiation occurred rapidly in few minutes with almost the oxygenated groups removed based on TGA thermograms. Interestingly, we succeeded in the reintroduction of oxygen moieties on reduced GO, as measured by the increase of C-O bond percentage after ozonation.

In the case of large GO<sub>L</sub>, we achieved the reduced GO under the hydrothermal treatment for 5 days and vitamin C method, verified by the lower weight loss from TGA and the higher C/O ratio from XPS in comparison to GO. The ozonation of the hydrothermally reduced GO reintroduced the oxygen moieties, confirmed by the increasing of C-O bond percentage after the reaction. To further determine the efficiency of reduction/oxidation process on GO, the epoxy ring opening reactions with amines and their interaction with siRNA will be discussed in the next chapters.

## 2.5 Experimental part

The large graphene oxide was obtained from the group of Nishina<sup>17</sup> with the form as an aqueous dispersion of GO following the modified Hummers method. The small graphene oxide was obtained from the company Nanoinnova as a powder. Chemicals were purchased from Sigma-Aldrich, Acros and Alfa Aesar, and used as received without any further purification. All solvents used for synthesis were analytical grade. When anhydrous conditions were required, high quality commercial solvents treated with molecular sieves (porosity 4 Å) were used (DMF). Water was purified using a Millipore filter system MilliQ® and endotoxin free Polisseur Biopak®. When stated, suspensions were sonicated in a water bath (20 W, 40 kHz). The filtration and dialysis membranes were purchased from Millipore and Spectrum Laboratories, Inc., respectively.

**Preparation of GO<sub>L</sub>:** Starting from the highly-oxidized graphene oxide (from Prof. Nishina) that has the size higher than 10  $\mu\text{m}$ , an aqueous dispersion of GO with controlled size of  $3\pm 1\ \mu\text{m}$  was obtained using a blender at high speed after 5 cycles (3 min of blender treatment per cycle). The GO, which is strongly acidic, was then dialyzed against milliQ® endotoxin free water (Spectra/Por® dialysis membrane MWCO 12000–14000 Da) for more than 10 days to reach a pH around 4.5.

**Preparation of hydrothermal rGO:** To a suspension of GO<sub>S</sub> or GO<sub>L</sub> in water ( $C = 1\ \text{mg/ml}$ ) sonicated for few min was refluxed at 100°C for 2 days and 5 days with continuous stirring. After centrifugation (4472g, 15 min), the rGO precipitates were dispersed in H<sub>2</sub>O, sonicated in a water bath for few min, and centrifuged. The rGO<sub>S</sub>-2d and rGO<sub>S</sub>-5d were dispersed in milliQ® endotoxin free water then dialyzed against milliQ® endotoxin free water using a Spectra/Por® dialysis membrane (MWCO 12000–14000 Da) for 3 days and then lyophilized.

**Preparation of solvothermal rGO using DMSO:** To a suspension of GO<sub>S</sub> in DMSO ( $C = 0.5\ \text{mg/ml}$ ) was sonicated in a water bath for few min, then it was refluxed for 15 min and 1 h with continuous stirring. The rGO was filtered over a PTFE membrane (0.1  $\mu\text{m}$ ). The solid recovered on the filter was dispersed in DMF, sonicated in a water bath for few min, and filtered again over a PTFE membrane (0.1  $\mu\text{m}$ ). This sequence was repeated twice with DMF, twice with MeOH, twice with DCM, and then rGO was dried under vacuum. The rGO<sub>S</sub>-D1h and rGO<sub>S</sub>-D15m were dispersed in milliQ® endotoxin free water and dialyzed against milliQ® endotoxin free water using a Spectra/Por® dialysis membrane (MWCO 12000–14000 Da) for 3 days and then lyophilized.

**Preparation of microwave-assisted rGO:** To a suspension of GO<sub>S</sub> in water ( $C = 1\ \text{mg/ml}$ ) was sonicated in a water bath for few minutes before moving into the microwave synthesizer (from CEM corporation) with the setting of pressure at 15 bars, the temperature at 150°C and the time from 15 min to 2 h under continuous stirring. After the MW treatment, rGO<sub>S</sub>-MW2h and rGO<sub>S</sub>-MW15m were centrifuged (4472g, 15 min). The rGO precipitates were then redispersed in H<sub>2</sub>O, sonicated for few min and centrifuged. The rGO<sub>S</sub>-MW2h and rGO<sub>S</sub>-MW15m were dispersed in milliQ® endotoxin free water and dialyzed against milliQ® endotoxin free water using a Spectra/Por® dialysis membrane (MWCO 12000–14000 Da) for 3 days and then lyophilized.

**Preparation of vitamin C rGO:** To a suspension of GO<sub>S</sub> or GO<sub>L</sub> in water ( $C = 1\ \text{mg/ml}$ ) was sonicated for few min in a water bath, L-ascorbic acid (mass ratio 1:1) was added. The reaction



mixture was heated at 90 °C for 2 h. The rGO was filtered over a PTFE membrane (0.1 μm). The solid recovered on the filter was dispersed in DMF, sonicated in a water bath for few min, and filtered over a PTFE membrane (0.1 μm). This sequence was repeated twice with DMF, twice with MEOH, twice with DCM and then rGO was dried under vacuum. The rGO was dispersed in milliQ® endotoxin free water then dialyzed against milliQ® endotoxin free water using a Spectra/Por® dialysis membrane (MWCO 12000–14000 Da) for 3 days and then lyophilized.

**Preparation of rGO<sub>S</sub>-5D-O<sub>3</sub> and rGO<sub>L</sub>-5D-O<sub>3</sub>:** To a suspension of rGO<sub>S</sub>-5D or rGO<sub>L</sub>-5D-O<sub>3</sub> in milli-Q® water (C = 1 mg/ml) sonicated for few min in a water bath was fluxed O<sub>3</sub> at room temperature for 3 h (flow rate 2 ml/min), using air as a source of generating ozone gas. After the completion of the reaction, the mixture was filtered over PTFE membrane (0.1 mm). The solid recovered on the filter was dispersed in water, sonicated in a water bath for few min, and filtered over a PTFE membrane (0.1 μm). This sequence was repeated three times with water and twice with methanol. The rGO<sub>S</sub>-5D-O<sub>3</sub> and rGO<sub>L</sub>-5D-O<sub>3</sub> were dispersed in milliQ® endotoxin free water then dialyzed against milliQ® endotoxin free endotoxin free water using a Spectra/Por® dialysis membrane (MWCO 12000–14000 Da) for 3 days and then lyophilized.

**Treatment of rGO<sub>L</sub>-5D with mCPBA:** To a suspension of 90 mg rGO<sub>L</sub>-5d in DCM (50 ml) sonicated for few min in a water bath, a solution of mCPBA (3-chloroperoxybenzoic acid, 1.3 g, 7.5 mmol) in DCM (25 ml) was added every 12 h while as the mixture was refluxed at 50°C for 24 h.<sup>37</sup> After the reaction was complete, the mixture was filtered over PTFE membrane (0.1 μm). The solid recovered on the filter was dispersed in DCM, sonicated in a water bath for few min, and filtered. This sequence was repeated several times with DCM and methanol. The solid obtained was dispersed in milliQ® endotoxin free water then dialyzed against milliQ® endotoxin free water using a Spectra/Por® dialysis membrane (MWCO 12000–14000 Da) for 3 days and then lyophilized.

**Treatment of rGO<sub>L</sub>-5D with DMDO generated in situ:**<sup>38,39</sup> To a suspension of 100 mg of rGO<sub>L</sub>-5d in DCM (50 ml) sonicated for few min in a water bath an aqueous solution (50ml) of NaHCO<sub>3</sub> (5.88g, 0.07 mol) and acetone (75 ml) were added. The resulting solution was stirred and oxone® (6.16 g, 0.01 mol) was added over 2 h. The reaction mixture was stirred at room temperature overnight. The mixture was filtered over PTFE membrane (0.1 μm). The solid recovered on the filter was dispersed in DCM, sonicated in a water bath for few min, and filtered. This sequence was repeated several times with DCM and methanol. The solid obtained

was dispersed in milliQ® endotoxin free water then dialyzed against milliQ® endotoxin free water using a Spectra/Por® dialysis membrane (MWCO 12000–14000 Da) for 3 days and then lyophilized.

### Instruments

TGA was performed on a TGA1 (Mettler Toledo) apparatus from 30 °C to 900 °C with a ramp of 10 °C min<sup>-1</sup> under N<sub>2</sub> using a flow rate of 50 mL·min<sup>-1</sup> and platinum pans.

XPS analyses were performed on a Thermo Scientific K-Alpha X-ray photoelectron spectrometer with a basic chamber pressure of 10<sup>-8</sup>-10<sup>-9</sup> bar with an anode using Al K $\alpha$  radiation ( $h\nu = 1486.6$  eV). The C (1s) photoelectron binding energy was set at  $284.5 \pm 0.2$  eV and used as reference for calibrating the other peak positions. The samples were analyzed as powder. Spot size of 400  $\mu\text{m}$  was used. The survey spectra are average of 10 scans with a pass energy of 200.00 eV and a step size of 1 eV. The high-resolution spectra are an average of 10 scans with a pass energy of 50 eV and a step size of 0.1 eV. An ion gun was turned on during analysis. For each sample, the analysis was repeated three times. For the deconvolution, CasaXPS (Version 2.3.16 PR 1.6) program was used to interpret data based on the Gaussian e Lorentzian line shapes and the Shirley type background.

Solid-state MAS NMR experiments were performed on an AVANCE 750 MHz and 500 MHz wide bore spectrometer (Bruker™) operating at a frequency of 188.5 MHz and 125.7 MHz for <sup>13</sup>C, respectively. Both instruments were equipped with a double resonance MAS probe designed for 2.5 mm o.d. zirconia rotors (closed with Kel-F caps). The samples were spun at the magic angle at a 25 kHz. Due to the rather low amount of protons relative to the other nuclei the direct <sup>13</sup>C polarization method was preferred as any other Cross Polarization experiment would had given poor signal and unreliable quantification. Therefore, owing to the spectral wide lines and in order to get undistorted lineshapes, all quantitative 1D <sup>13</sup>C{<sup>1</sup>H} DP spectra were acquired directly with the original Hahn's echo sequence<sup>40</sup>. This latter echo was synchronized with the MAS rotation and was set equal to 80  $\mu\text{s}$  (two rotation periods for MAS speed = 25kHz). A 10 second recycle delay was chosen to ensure reliable quantification (total experimental time was 48 h per spectrum) and proton decoupling during acquisition was obtained by using SPINAL-64<sup>41</sup> at a 180 kHz RF field. A Lorentzian line broadening of 600 Hz was applied for each spectra prior to Fourier transformation.



X-ray diffraction was measured by PANalytical Co. X' pert PRO using Cu K $\alpha$  radiation ( $\lambda = 1.541\text{\AA}$ ) in the  $2\theta$  range of 5–20°. The operating tube current and voltage were 40mA and 40 kV, respectively.

The ozone treatment was performed using the ozone generator (Ozone Wave Pro, Syoken Co. Ltd).

SEM measurement was performed on a SEM S-5200 (Hitachi High Technologies Corporation, Tokyo, Japan). To prepare the SEM samples, a diluted dispersion of GO was dropped on SiO<sub>2</sub>/Si substrate treated under UV light for few minutes.

TEM analysis were performed with Hitachi 7500 transmission electron microscope (Hitachi High Technologies Corporation, Tokyo, Japan) equipped with an AMT Hamamatsu digital camera (Hamamatsu Photonics, Hamamatsu City, Japan).

$\zeta$  potential was performed using the Zetasizer Nano S (Malvern Instruments) spectrometer operating under 633 nm laser irradiation.

## 2.6 Bibliography

- (1) Compton, O. C.; Nguyen, S. T. Graphene Oxide, Highly Reduced Graphene Oxide, and Graphene: Versatile Building Blocks for Carbon-Based Materials. *Small* **2010**, *6*, 711–723.
- (2) Chua, C. K.; Pumera, M. Chemical Reduction of Graphene Oxide: A Synthetic Chemistry Viewpoint. *Chem. Soc. Rev.* **2014**, *43*, 291–312.
- (3) Stankovich, S.; Dikin, D. A.; Piner, R. D.; Kohlhaas, K. A.; Kleinhammes, A.; Jia, Y.; Wu, Y.; Nguyen, S. T.; Ruoff, R. S. Synthesis of Graphene-Based Nanosheets via Chemical Reduction of Exfoliated Graphite Oxide. *Carbon* **2007**, *45*, 1558–1565.
- (4) Shin, H. J.; Kim, K. K.; Benayad, A.; Yoon, S. M.; Park, H. K.; Jung, I. S.; Jin, M. H.; Jeong, H. K.; Kim, J. M.; Choi, J. Y.; *et al.* Efficient Reduction of Graphite Oxide by Sodium Borohydride and Its Effect on Electrical Conductance. *Adv. Funct. Mater.* **2009**, *19*, 1987–1992.
- (5) Wang, G.; Yang, J.; Park, J.; Gou, X.; Wang, B.; Liu, H.; Yao, J. Facile Synthesis and Characterization of Graphene Nanosheets. *J Phys Chem C* **2008**, *112*, 8192–8195.
- (6) Thakur, S.; Karak, N. Alternative Methods and Nature-Based Reagents for the Reduction of Graphene Oxide: A Review. *Carbon* **2015**, *94*, 224–242.
- (7) Mattevi, C.; Eda, G.; Agnoli, S.; Miller, S.; Mkhoyan, K. A.; Celik, O.; Mastrogiovanni, D.; Granozzi, G.; Carfunkel, E.; Chhowalla, M. Evolution of Electrical, Chemical, and Structural Properties of Transparent and Conducting Chemically Derived Graphene Thin Films. *Adv. Funct. Mater.* **2009**, *19*, 2577–2583.
- (8) Choudhary, S.; Mungse, H. P.; Khatri, O. P. Hydrothermal Deoxygenation of Graphene Oxide: Chemical and Structural Evolution. *Chem. An Asian J.* **2013**, *8*, 2070–2078.
- (9) Compton, O. C.; Jain, B.; Dikin, D. A.; Abouimrane, A.; Amine, K. Chemically Active Reduced Graphene Oxide with Tunable C / O Ratios. *ACS Nano* **2011**, *5*, 4380–4391.
- (10) Zhu, Y.; Murali, S.; Stoller, M. D.; Velamakanni, A.; Piner, R. D.; Ruoff, R. S. Microwave Assisted Exfoliation and Reduction of Graphite Oxide for Ultracapacitors. *Carbon* **2010**, *48*, 2106–2122.
- (11) Chen, W.; Yan, L.; Bangal, P. R. Preparation of Graphene by the Rapid and Mild Thermal Reduction of Graphene Oxide Induced by Microwaves. *Carbon* **2010**, *48*, 1146–1152.
- (12) Fernández-Merino, M. J.; Guardia, L.; Paredes, J. I.; Villar-Rodil, S.; Solís-Fernández, P.; Martínez-Alonso, A.; Tascón, J. M. D. Vitamin C Is an Ideal Substitute for Hydrazine in the Reduction of Graphene Oxide Suspensions. *J. Phys. Chem. C* **2010**, *114*, 6426–6432.
- (13) Gao, J.; Liu, F.; Liu, Y.; Ma, N.; Wang, Z.; Zhang, X. Environment-Friendly Method To Produce Graphene That Employs Vitamin C and Amino Acid. *Chem. Mater.* **2010**, *22*, 2213–2218.
- (14) Zhang, J.; Yang, H.; Shen, G.; Cheng, P.; Zhang, J.; Guo, S. Reduction of Graphene Oxide via L-Ascorbic Acid. *Chem. Commun.* **2009**, *46*, 1112–1114.
- (15) Ogrin, D.; Chattopadhyay, J.; Sadana, A. K.; Billups, W. E.; Barron, A. R. Epoxidation and Deoxygenation of Single-Walled Carbon Nanotubes: Quantification of Epoxide Defects. *J. Am.*

- Chem. Soc.* **2006**, *128*, 11322–11323.
- (16) Xu, Z.; Yue, M.; Chen, L.; Zhou, B.; Shan, M.; Niu, J.; Li, B.; Qian, X. A Facile Preparation of Edge Etching, Porous and Highly Reactive Graphene Nanosheets via Ozone Treatment at a Moderate Temperature. *Chem. Eng. J.* **2014**, *240*, 187–194.
- (17) Morimoto, N.; Kubo, T.; Nishina, Y. Tailoring the Oxygen Content of Graphite and Reduced Graphene Oxide for Specific Applications. *Sci. Rep.* **2016**, *6*, 21715.
- (18) Chau, N. D. Q.; Reina, G.; Raya, J.; Vacchi, I. A.; Ménard-Moyon, C.; Nishina, Y.; Bianco, A. Elucidation of siRNA Complexation Efficiency by Graphene Oxide and Reduced Graphene Oxide. *Carbon* **2017**, *122*, 643–652.
- (19) Singh, P.; Campidelli, S.; Giordani, S.; Bonifazi, D.; Bianco, A.; Prato, M. Organic Functionalisation and Characterisation of Single-Walled Carbon Nanotubes. *Chem. Soc. Rev.* **2009**, *38*, 2214–2230.
- (20) Eigler, S.; Dotzer, C.; Hirsch, A.; Enzelberger, M.; Müller, P. Formation and Decomposition of CO<sub>2</sub> Intercalated Graphene Oxide. *Chem. Mater.* **2012**, *24*, 1276–1282.
- (21) Makharza, S.; Cirillo, G.; Bachmatiuk, A.; Ibrahim, I.; Ioannides, N.; Trzebicka, B.; Hampel, S.; Rummeli, M. H. Graphene Oxide-Based Drug Delivery Vehicles: Functionalization, Characterization, and Cytotoxicity Evaluation. *J. Nanopart. Res.* **2013**, *15*, 2099.
- (22) Vacchi, I. A.; Spinato, C.; Raya, J.; Bianco, A.; Ménard-Moyon, C. Chemical Reactivity of Graphene Oxide towards Amines Elucidated by Solid-State NMR. *Nanoscale* **2016**, *8*, 13714–13721.
- (23) Stobinski, L.; Lesiak, B.; Malolepszy, A.; Mazurkiewicz, M.; Mierzwa, B.; Zemek, J.; Jiricek, P.; Bieloshapka, I. Graphene Oxide and Reduced Graphene Oxide Studied by the XRD, TEM and Electron Spectroscopy Methods. *J. Electron Spectrosc. Relat. Phenom.* **2014**, *195*, 145–154.
- (24) Xue, Y.; Liu, Y.; Lu, F.; Qu, J.; Chen, H.; Dai, L. Functionalization of Graphene Oxide with Polyhedral Oligomeric Silsesquioxane (POSS) for Multifunctional Applications. *J. Phys. Chem. Lett.* **2012**, *3*, 1607–1612.
- (25) Stankovich, S.; Piner, R. D.; Chen, X.; Wu, N.; Nguyen, S. T.; Ruoff, R. S. Stable Aqueous Dispersions of Graphitic Nanoplatelets via the Reduction of Exfoliated Graphite Oxide in the Presence of Poly(sodium 4-Styrenesulfonate). *J. Mater. Chem.* **2006**, *16*, 155–158.
- (26) Estrade-Szwarckopf, H. XPS Photoemission in Carbonaceous Materials: A “defect” peak beside the Graphitic Asymmetric Peak. *Carbon* **2004**, *42*, 1713–1721.
- (27) Gao, X.; Jang, J.; Nagase, S. Hydrazine and Thermal Reduction of Graphene Oxide : Reaction Mechanisms and Design. *J. Phys. Chem. C* **2010**, *114*, 832–842.
- (28) Wilson, N. R.; Pandey, P. A.; Beanland, R.; Young, R. J.; Kinloch, I. A.; Gong, L.; Liu, Z.; Suenaga, K.; Rourke, J. P.; York, S. J.; *et al.* Graphene Oxide: Structural Analysis and Application as a Highly Transparent Support for Electron Microscopy. *ACS Nano* **2009**, *3*, 2547–2556.
- (29) Li, D.; Müller, M. B.; Gilje, S.; Kaner, R. B.; Wallace, G. G. Processable Aqueous Dispersions
-

- of Graphene Nanosheets. *Nat. Nanotechnol.* **2008**, *3*, 101–105.
- (30) Lerf, A.; He, H.; Forster, M.; Klinowski, J. Structure of Graphite Oxide Revisited. *J. Phys. Chem. B* **1998**, *102*, 4477–4482.
- (31) Konkana, B.; Vasudevan, S. Understanding Aqueous Dispersibility of Graphene Oxide and Reduced Graphene Oxide through P K a Measurements. *Journal of Physical Chemistry Letters*, 2012, *3*, 867–872.
- (32) Pei, S.; Cheng, H.-M. The Reduction of Graphene Oxide. *Carbon* **2012**, *50*, 3210–3228.
- (33) Yang, F.; Zhao, M. L.; Wang, Z.; Ji, H. Y.; Zheng, B. Z.; Xiao, D.; Wu, L.; Guo, Y. The Role of Ozone in the Ozonation Process of Graphene Oxide: Oxidation or Decomposition? *Rsc Adv.* **2014**, *4*, 58325–58328.
- (34) Gao, W.; Wu, G.; Janicke, M. T.; Cullen, D. A.; Mukundan, R.; Baldwin, J. K.; Brosha, E. L.; Galande, C.; Ajayan, P. M.; More, K. L.; *et al.* Ozonated Graphene Oxide Film as a Proton-Exchange Membrane. *Angew. Chem. Int. Ed.* **2014**, *53*, 3588–3593.
- (35) Szabó, T.; Berkesi, O.; Forgó, P.; Josepovits, K.; Sanakis, Y.; Dimitris, P.; Imre, D. Evolution of Surface Functional Groups in a Series of Progressively Oxidized Graphite Oxides. *Chem. Mater.* **2006**, *18*, 2740–2749.
- (36) He, H.; Riedl, T.; Lerf, A.; Klinowski, J. Solid-State NMR Studies of the Structure of Graphite Oxide. *J. Phys. Chem* **1996**, *100*, 19954–19958.
- (37) Yuan, W.; Chan-Park, M. B. Covalent Cum Noncovalent Functionalizations of Carbon Nanotubes for Effective Reinforcement of a Solution Cast Composite Film. *ACS Appl. Mater. Interfaces* **2012**, *4*, 2065–2073.
- (38) Markiewicz, K. H.; Wilczewska, A. Z.; Chernyaeva, O.; Winkler, K. Ring-Opening Reactions of Epoxidized SWCNT with Nucleophilic Agents: A Convenient Way for Sidewall Functionalization. *New J. Chem.* **2014**, *38*, 2670–2678.
- (39) Taber, D. F.; DeMatteo, P. W.; A., R.; Hassan. Simplified Preparation of Dimethyldioxirane (DMDO). *Org. Synth.* **2013**, *90*, 350–357.
- (40) Hahn, E. L. Spin Echoes. *Phys. Rev.* **1950**, *80*, 580–594.
- (41) Fung, B. M.; Khitritin, A. K.; Ermolaev, K. An Improved Broadband Decoupling Sequence for Liquid Crystals and Solids. *J. Magn. Reson.* **2000**, *142*, 97–101.



## CHAPTER 3: FUNCTIONALIZATION OF GRAPHENE OXIDE WITH VARIOUS AMINES AND POLYMERS. STUDY THEIR COMPLEXATION WITH siRNA

### 3.1 Introduction

In the field of gene delivery, polycationic molecules are one of the most promising approaches for their ability to efficiently complex and compact genetic materials.<sup>1-3</sup> However, polycationic structures are endowed of an intrinsic toxicity due to their intercalation into cell membranes. To overcome this problem, these polycationic molecules can be grafted onto different nanostructures leading to much less toxic functional materials. Interesting results in gene delivery were achieved using functionalized carbon nanomaterials. Multi-walled carbon nanotubes (MWCNTs) bearing polyamidoamine dendrons of first and second generation showed a good cellular delivery of siRNA and an efficiency of gene silencing.<sup>4</sup> In this pioneer study, CNTs exhibited complexation ability toward siRNA molecules proportional to the increasing of the branches on the dendritic structures. The high efficiency was a consequence of an increase of the positive charges on the surface of conjugated CNTs.<sup>4,5</sup> Our group investigated also the use of MWCNTs functionalized ammonium and guanidinium dendrons for siRNA complexation.<sup>6</sup> It was found that the complexation ability for siRNA was independent of the core dendritic structure, but influenced by the terminal groups. In term of guanidinium dendrons, the higher the generation was, the lower siRNA complexation was observed. Meanwhile the ammonium functionalized dendrons exhibited similar ability of siRNA complexation regardless their size. Interestingly, ammonium dendron modified CNTs showed higher siRNA complexation than the guanidinium counterparts. In another approach, PEI, a polycationic polymer with a high ionic charge density, was commonly used for gene therapy.<sup>7-9</sup> In the last few years, it was demonstrated that the functionalization of GO with PEI can improve the transfection efficiency compared to PEI alone.<sup>10,11</sup>

### 3.2 Objectives of this chapter

In our study, we were interested in the synthesis of amino functionalized GO able to efficiently complex siRNA molecules. Pristine GO is characterized by a high negative surface charge due to the presence of various oxygenated groups. In the previous chapter, we played with the oxygenated groups to tune the oxygenated groups present on GO sheets. In this chapter, the

---

preparation and characterization of amino functionalized GOs will be described. Moreover, we investigated and rationalized the complexation ability of the functionalized materials with siRNA molecules.

First, I investigated the behavior of amino functionalization on GOs and rGOs nanomaterials (see chapter 2 for their preparation). Subsequently, the best strategies found was applied to large GO<sub>L</sub> and large rGO<sub>L</sub> nanomaterials (see chapter 2 for their preparation). In this context, I prepared linear ramified and dendritic amines and I conjugated to GO. I first covalently conjugate the different amines to small GOs via the epoxide ring opening reaction. Then, thanks to gel retardation analyses and an accurate surface GO material characterization, I was able to better understand the principles of the interaction between siRNA and the different prepared materials.

### **3.3 Results and discussion**

This chapter was divided in two main parts: 1) part A related to the small GOs series, and 2) part B related to the GO<sub>L</sub> series. In each part the preparation of the amino functionalized GO materials and their complexation with siRNA will be illustrated. In addition, in part A, an initial section regarding the synthesis and characterization of the different amino moieties will be discussed.

#### **PART A: Functionalization of GOs and reduced GOs materials with the different cationic molecules**

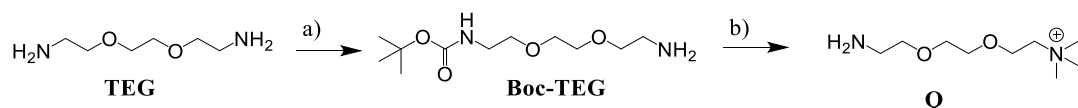
##### **A.1 Synthesis of cationic molecules and dendrons.**

For the preparation of the different amino molecules (Table 3.1) I started from 2,2'-ethylenedioxybisethylamine (named TEG), as precursor to generate a quaternary ammonium derivative and 3,3'-diaminodipropylamine as the zero generation dendritic structure.

**Table 3.1:** List of amines and dendrons

Name	Structure	Name	Structure
TEG		D <sub>2</sub>	
Q			
D <sub>1</sub>			

First, I prepared a quaternary ammonium derivate (termed Q) as illustrated in Scheme 3.1. I first performed the TEG Boc mono-protection, obtaining Boc-TEG. Finally, the quaternary amine of TEG was synthesized by addition of CH<sub>3</sub>I at a ratio 3 to 1 to TEG in THF, followed by the Boc deprotection using trifluoroacetic acid (TFA).



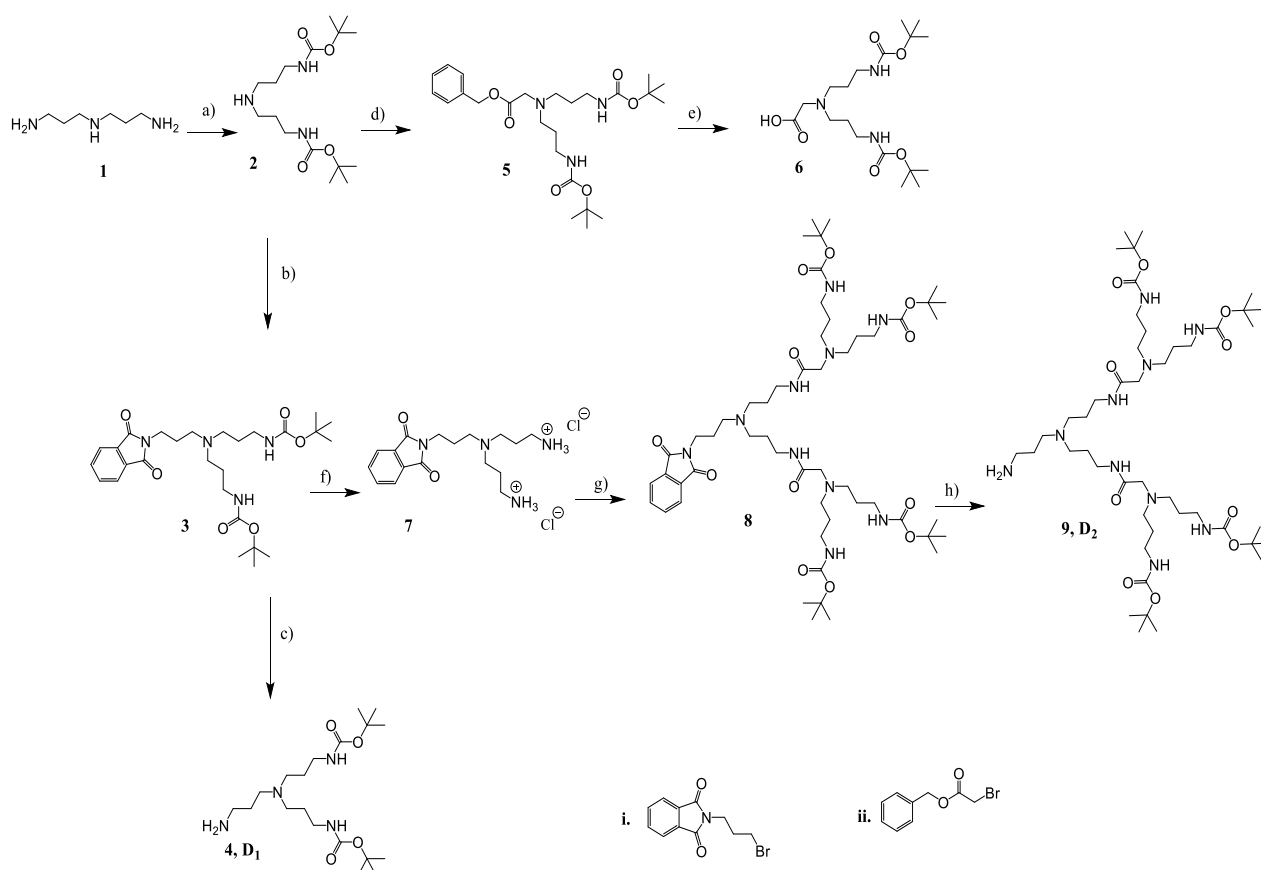
**Scheme 3.1:** Synthesis of quaternary amine. a) Boc<sub>2</sub>O added dropwise in 3h, CH<sub>2</sub>Cl<sub>2</sub>, room T, 24 h; b) 1. CH<sub>3</sub>I, THF, 24 h; 2. TFA/DCM (1:1), 30 mins.

The first generation dendron (D<sub>1</sub> **4**, Scheme 3.2) was started from Boc di-protected compound **2**, which was obtained from the Boc protection of 3,3'-diaminodipropylamine (compound **1**, Scheme 2). Then the phthalimido derivative **3** was formed by adding the N-(3-bromopropyl) phthalimide to the secondary amine group of compound **2** in the presence of Na<sub>2</sub>CO<sub>3</sub> at 75°C. Finally, D<sub>1</sub> dendron (**4**) was obtained via deprotection of the phthalimide group of compound **3** using hydrazine hydrate.

The synthesis of the second generation dendron (D<sub>2</sub> **9**, Scheme 3.2) was achieved starting from addition of benzyl bromoacetate to compound **2** (to form compound **5**) and subsequent cleavage of the benzyl group (compound **6**). After cleavage of the two Boc protecting groups of compound **3** (to form compound **7**), the two free amino groups were coupled with two



equivalents of compound **6**, obtaining compound **8**. Finally, after the deprotection of the phthalimido group via hydrazine treatment compound **9** was obtained.<sup>6</sup> Compound **Q**, TEG, first and second generation dendrons were used for GO functionalization via epoxide opening reaction.

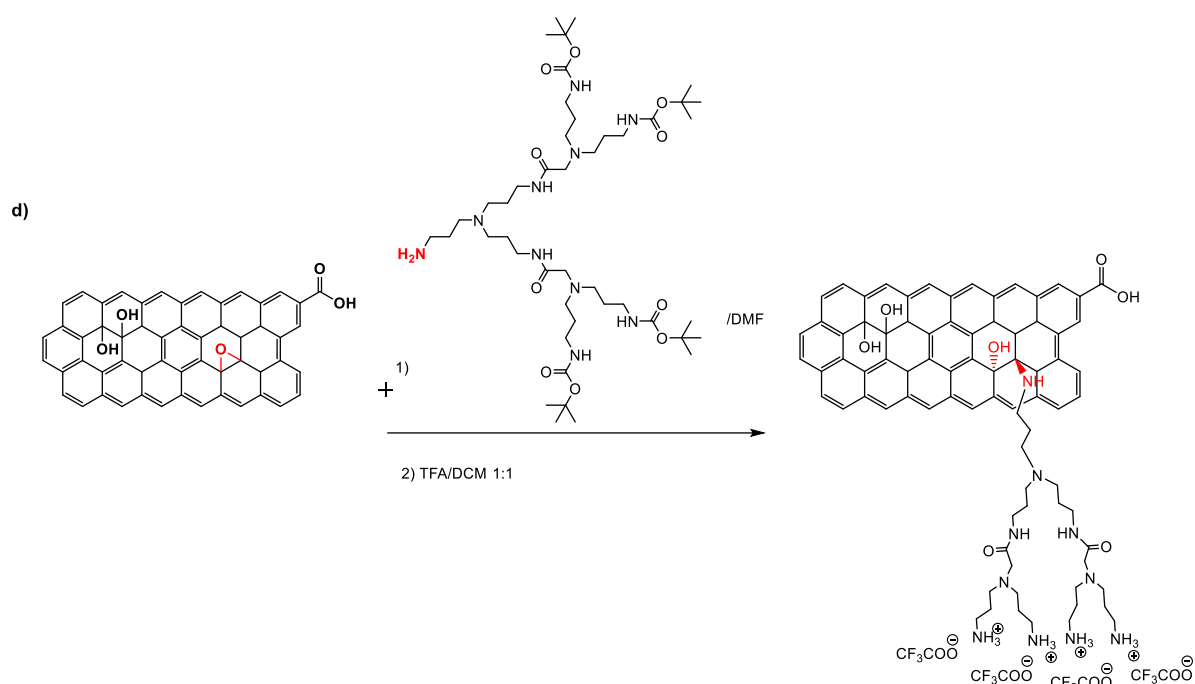


**Scheme 3.2:** Synthesis of the 1<sup>st</sup> and 2<sup>nd</sup> generation dendrons. a) Boc<sub>2</sub>O added dropwise in 3 h, CH<sub>2</sub>Cl<sub>2</sub>, r.t., 48 h; b) **i**, Na<sub>2</sub>CO<sub>3</sub>, CH<sub>3</sub>CN, 75°C, 24 h; c) Hydrazine hydrate, EtOH/Toluene, 50°C, overnight; d) **ii**, DIEA, CH<sub>3</sub>CN, 48 h; e) H<sub>2</sub>, Pd/C, MeOH, 2 h; f) HCl in dioxane, 2 h, quantitative; g) **6**, EDC×HCl, HOBt, DIEA, CH<sub>3</sub>CN, 48 h; h) Hydrazine hydrate, EtOH/Toluene, 50°C, overnight.

### **A.2 Functionalization of the GOs with linear and dendritic amines. Characterization and complexation with siRNA**

To enhance the siRNA complexation abilities, amine derivatization was performed on the prepared GO materials. The different amines (table 3.1) were first used to functionalize GOs.





**Scheme 3.3:** Amino functionalization of GO<sub>s</sub> via nucleophilic epoxy ring opening. For sake of clarity, only one epoxide group is shown. a) Reaction with TEG; b) Reaction with Q; c) Reaction with D<sub>1</sub>; d) Reaction with D<sub>2</sub>

The epoxy opening reaction of GO<sub>s</sub> with TEG was performed in mild conditions, at room temperature and in water. To remove adsorbed TEG, the products were extensively washed with water and centrifuged several times. As a final step, the conjugates were dialyzed. The epoxy ring opening yields 1,2-amino alcohols on the GO sheets, leading to the formation of GO<sub>s</sub>-TEG. (Scheme 3.3a).

In the case of quaternary amine Q, the reaction occurred in DMF in the presence of DIEA (diisopropylethylamine) at room temperature, then the product was thoroughly washed with DMF, methanol, and DCM throughout filtration. After that, the recover sample was suspended in TFA/DCM. This Boc-deprotection was occurred in 2 h, following by the washing with DMF, methanol, and DCM throughout filtration and by dialysis, to form GO<sub>s</sub>-Q. (Scheme 3.3b). Because I want to observe if the thermal stability of GO was affected under these treatments, I also prepared the control samples by treating GO<sub>s</sub> under the same conditions, in the presence of DIEA and without the quaternary amine, named GO<sub>s</sub>-ct1.

In the case of the dendrons D<sub>1</sub> and D<sub>2</sub>, the reactions were performed in DMF at room temperature. After the treatment with TFA in DCM for the Boc-deprotection, the resulting

ammonium derivatives  $\text{GO}_S\text{-D}_1$  and  $\text{GO}_S\text{-D}_2$  were isolated as described above for  $\text{GO}_S\text{-Q}$  (Scheme 3.3c and d). The control sample for these reactions was named  $\text{GO}_S\text{-ct2}$ .

To evaluate the degree of functionalization, the prepared amino functionalized  $\text{GO}_S$  materials were then characterized by TGA and Kaiser test.

The thermal profiles of the different amine functionalized  $\text{GO}_S$ , control  $\text{GO}_S$  and  $\text{GO}_S$  were performed under nitrogen (Figure 3.1).

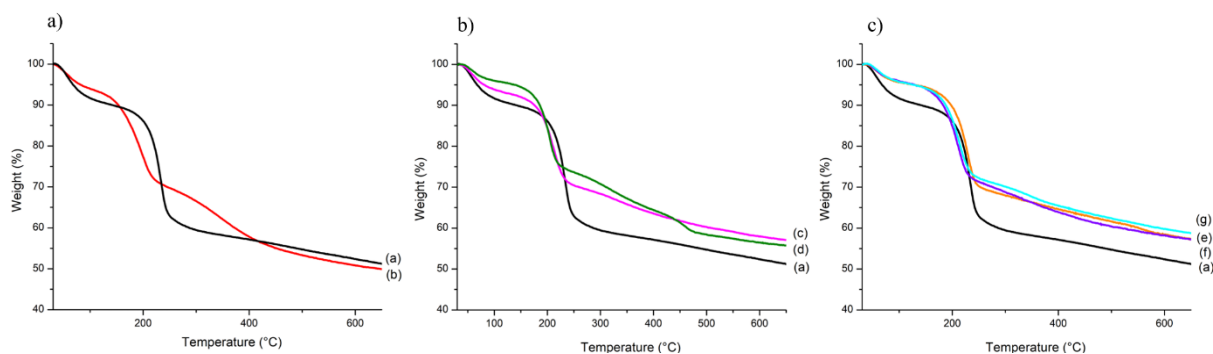


**Figure 3.1:** TGA curves of the different  $\text{GO}$  conjugated. a)  $\text{GO}_S$  in black (a),  $\text{GO}_S\text{-TEG}$  in red (b); b)  $\text{GO}_S$  in black (a),  $\text{GO}_S\text{-ct1}$  in magenta (c),  $\text{GO}_S\text{-Q}$  in green (d); c)  $\text{GO}_S$  in black (a),  $\text{GO}_S\text{-ct2}$  in orange (e),  $\text{GO}_S\text{-D}_1$  in blue (f),  $\text{GO}_S\text{-D}_2$  in cyan (g).

As described before in Chapter 2, the thermogram of  $\text{GO}$  shows a typical degradation in three steps, including the weight loss around  $100^\circ\text{C}$  which related to the desorption of water, the weight loss around  $200^\circ\text{C}$  which ascribed to the decomposition of labile oxygenated groups, and the weight loss around  $250^\circ\text{C}$  which attributed to the removal of more stable oxygen moieties. We observed that both controls  $\text{GO}_S\text{-ct1}$  and  $\text{GO}_S\text{-ct2}$  display a higher thermal stability than  $\text{GO}_S$  indicating that some labile oxygen groups were removed during the solvent treatments from  $\text{GO}_S$ .<sup>12–14</sup> The thermogravimetric profiles of  $\text{GO}_S\text{-Q}$ ,  $\text{GO}_S\text{-D}_1$  and  $\text{GO}_S\text{-D}_2$  do not show any significantly difference from their respective control  $\text{GO}_S$ . Even in the case of  $\text{GO}_S\text{-TEG}$  the thermogram profile recorded was pretty similar to its control reaction ( $\text{GO}_S$ ). As mentioned before, due to the low thermal stability of  $\text{GO}$ , the TGA characterization of  $\text{GO}$  is hard to interpret. Besides,  $\text{GO}$  functionalization shall guarantee a significant mass loss due to the burning of the alkyl chains grafted on the sheets surface. Regrettably, after  $\text{GO}$  functionalization neither small (Q) or big ( $\text{D}_1$  and  $\text{D}_2$ ) molecular weight amines were detected by TGA confirming that this technique is not completely reliable for  $\text{GO}$  surface analysis.

The quantitative Kaiser test<sup>15,16</sup> was also used to estimate the amount of free primary amino groups. Each Kaiser test experiment was repeated at least three times, with a standard error less than 5%. Control reaction showed a negative Kaiser test, while GO<sub>S</sub>-TEG, GO<sub>S</sub>-D1 and GO<sub>S</sub>-D2 gave a functionalization of 299, 207 and 202 μmol/g, respectively (Table 3.2). Surprisingly, there is no enhancement of the Kaiser test values with the increasing of the dendron generation. This may be explained by a decreasing in reactivity of the ninhydrin with the increase of the sterically hindrance of the dendritic structures.<sup>6</sup>

**Table 3.2:** Kaiser test average values of different functionalized GO<sub>S</sub> and rGO<sub>S</sub>.

	<b>Acronym</b>	<b>Kaiser test (μmol/g)</b>
TEG functionalized GO <sub>S</sub>	GO <sub>S</sub> -TEG	299
Q functionalized GO <sub>S</sub>	GO <sub>S</sub> -Q	Not done
D1 functionalized GO <sub>S</sub>	GO <sub>S</sub> -D <sub>1</sub>	207
D2 functionalized GO <sub>S</sub>	GO <sub>S</sub> -D <sub>2</sub>	202
TEG functionalized rGO <sub>S</sub> -5d	rGO <sub>S</sub> -5d-TEG	128
TEG functionalized rGO <sub>S</sub> -D1h	rGO <sub>S</sub> -D1h-TEG	134
TEG functionalized rGO <sub>S</sub> -MW15m	rGO <sub>S</sub> -MW15m-TEG	80

Overall, the higher value of NH<sub>2</sub> loading from the Kaiser test results, the higher amount of amine was loaded on GO. Hence, it seems that the TEG functionalization gave the most efficient GO conjugate. In order to enhance the GO affinity for siRNA molecules, I decided to perform TEG functionalization of the rGO materials described in Chapter 2. For this purpose, I selected the hydrothermal rGO<sub>S</sub>-5d, the solvothermal rGO<sub>S</sub>-D1h and the microwave-assisted rGO<sub>S</sub>-MW15m. The TEG conjugates of these rGO<sub>S</sub> were performed in same condition of GO<sub>S</sub>, and then were isolated and characterized by TGA and Kaiser test.

The thermogravimetric profiles of TEG conjugates and their corresponding starting graphene materials are presented in Figure 3.2.

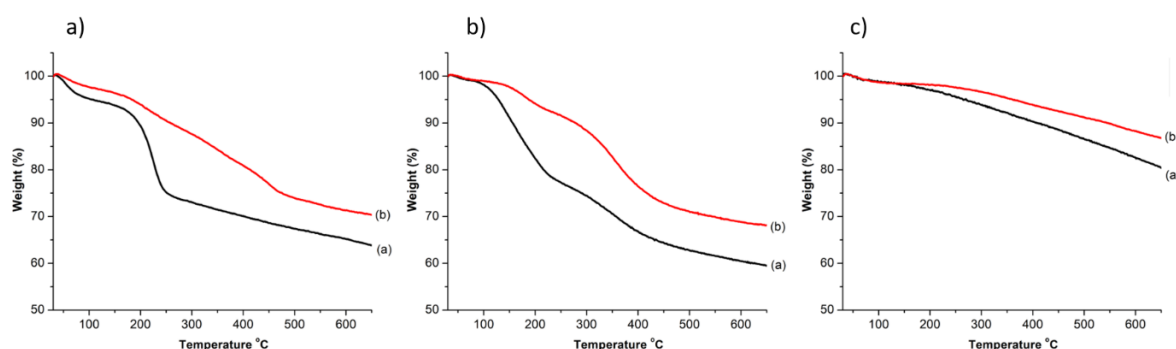


**Figure 3.2:** TGA curves of the different TEG conjugates: a) rGO<sub>S</sub>-5d in black (a), rGO<sub>S</sub>-5d-TEG in red (b); b) rGO<sub>S</sub>-D1h in black (a), rGO<sub>S</sub>-D1h-TEG in red (b); c) rGO<sub>S</sub>-MW15m in black (a), rGO<sub>S</sub>-MW15m-TEG in red (b)

From figure 3.2, it is hard to interpret the TGA characterization of TEG conjugates because of the low thermal stability of GO and the low molecular mass of TEG. Instead of obtaining a significant weight loss in term of TEG conjugates due to the burning of the TEG conjugated on graphene sheets, we observed a less weight loss of these conjugates in comparison to the starting graphene materials. It seems that TGA is not suitable and reliable technique for the analysis of surface of these functionalized graphene materials.

The Kaiser test results (Table 3.2) show that the TEG coupling yields were proportional to the C-O percentages: more C-O groups are present (30% in rGO<sub>S</sub>-D1h, 25% in rGO<sub>S</sub>-5d and 14% in rGO<sub>S</sub>-MW15m from XPS (Figure 2.4 in chapter 2), higher amount of TEG is conjugated (Kaiser test: 134  $\mu\text{mol/g}$  in rGO<sub>S</sub>-D1h-TEG, 128  $\mu\text{mol/g}$  in rGO<sub>S</sub>-5d-TEG, 80  $\mu\text{mol/g}$  in rGO<sub>S</sub>-MW15m-TEG, respectively).

To test if the amino groups were able to change the surface charge, I measured the  $\zeta$  potential of all the conjugates of GO<sub>S</sub> and rGO<sub>S</sub>. Compared to the starting GO and rGO materials ( $\zeta$  potential  $\sim -40\text{mV}$  at pH 6), TEG functionalization was able to increase the  $\zeta$  potential, however never reaching values higher than  $-25\text{mV}$ . Most probably, the TEG functionalization cannot introduce enough positive charges to balance the negative charges of the oxygenated groups present on the GO sheets. Surprisingly, even the other amines and the dendrons were not able to bring the  $\zeta$  potential of functionalized GOs to positive values.

The final aim of this study was to investigate the capacity of the different GOs to interact and complex siRNA. For this purpose, I used a double-strand siRNA that is a small molecule of 19 nucleobases. The ability of amine and dendron functionalized GOs to complex the genetic

materials was evaluated and quantified by gel electrophoresis. Complexation was performed in aqueous solutions without adding any complementary salts or buffer. Each complexation experiment was repeated at least three times. Free siRNA molecules were then estimated comparing the fluorescence signal between the control (GO/siRNA at mass ratio 0) and the other complexation ratios. The complexation ratios were initially calculated via Nitrogen/Phosphate ratios using the amount of amino groups derived from the Kaiser test or the TGA values. Unfortunately, the two techniques showed, between each other, controversial values. Therefore, we decided to perform all the electrophoresis gels considering only the mass ratio between GO and siRNA (Figure 3.3) (see experimental part for more details).

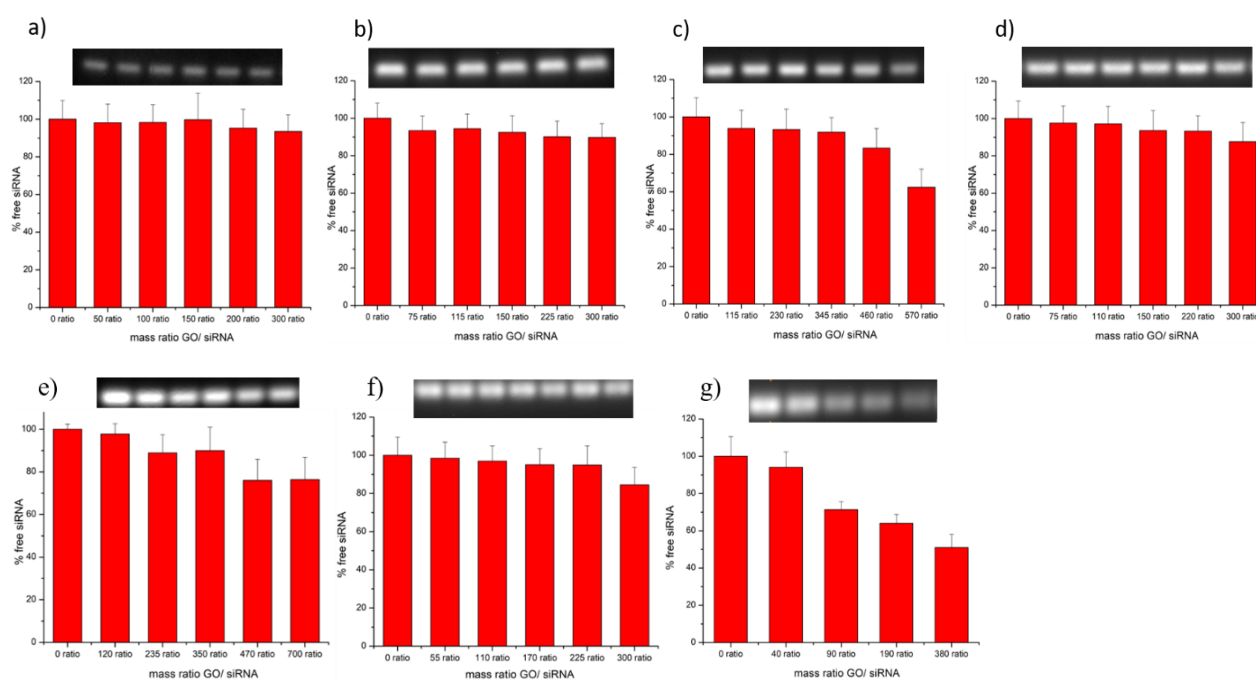


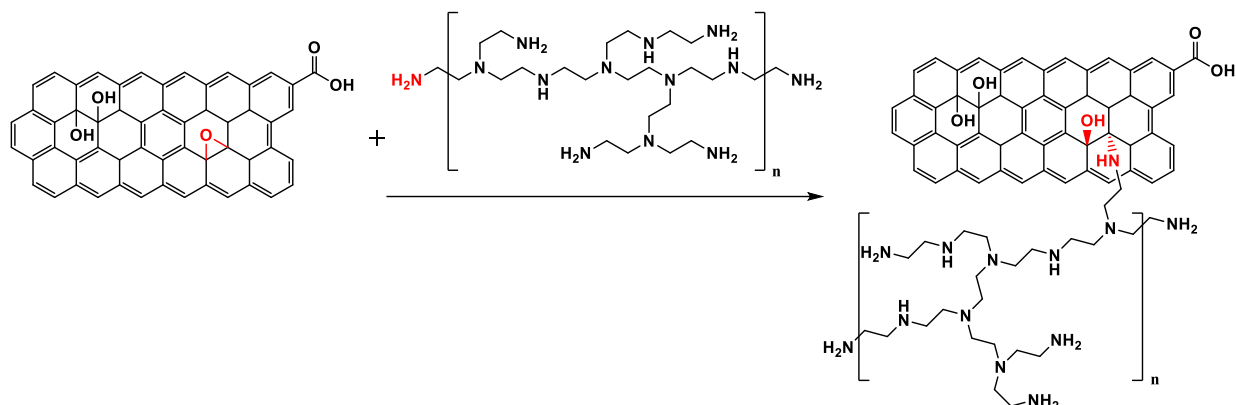
**Figure 3.3:** Complexation of the different amine functionalized GOs: a) GO<sub>S</sub>-TEG, b) GO<sub>S</sub>-Q, c) GO<sub>S</sub>-D<sub>1</sub>, d) GO<sub>S</sub>-D<sub>2</sub>, e) rGO<sub>S</sub>-D1h-TEG, f) rGO<sub>S</sub>-5d-TEG, g) rGO<sub>S</sub>-MW15m-TEG. Top: image of the electrophoresis gel; bottom: histograms showing the free siRNA signal at different GO/siRNA mass ratios.

Surprisingly, none of the conjugated materials displayed a significant complexation ability below 200 mass ratio between GO and siRNA. These disappointing results can be explained considering the negative charge of the functionalized GO surface. Indeed, if we consider a pure electrostatic interaction for complexation of the negatively charged siRNA molecules, a positively charged GO surface is required. Hence, the described functionalizations seem not to

be suitable strategies for the complexation improvement of GO with siRNA. Therefore, we decided to explore a low molecular weight polyethylenimine (MW 800 Da) for the conjugation with our GOs.

### A.3 Preparation of PEI functionalized GOs materials. Characterization and complexation with siRNA

The epoxy ring opening reaction of GOs and PEI is shown in Scheme 3.4.



**Scheme 3.4:** PEI functionalization of GOs via nucleophilic epoxy ring opening (MW 800Da).

We decided to perform the conjugation of GO with PEI on the most promising representative samples from the series of GOs: the starting GOs, the hydrothermal rGOs-5d and its re-epoxide form rGOs-5d-O<sub>3</sub> because of their higher dispersibility in water in comparison to other rGOs. The reactions were performed using the same conditions of TEG conjugation (in water and at room temperature).

The thermal profile of the PEI conjugates after derivatization was assessed by TGA (Figure 3.4).

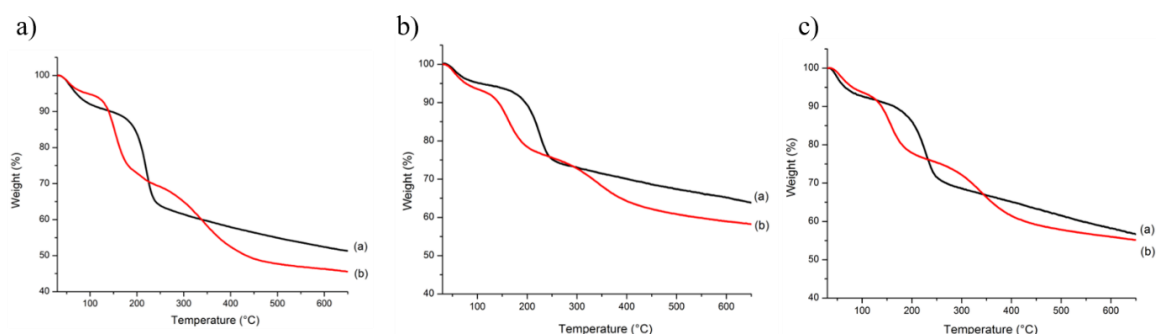


**Figure 3.4.** TGA spectra of PEI functionalized GO: a) GOs in black (a), GOs-PEI in red (b); b) rGOs-5d in black (a), rGOs-5d-PEI in red (b); c) rGOs-5d-O<sub>3</sub> in black (a), rGOs-5d-O<sub>3</sub>-PEI in red (b).



The PEI conjugates showed a similar three-step decomposition process like GO, but with a remarkably greater thermal degradation above 320°C. Most probably the conjugated amino groups start to degrade above this temperature.

In order to better characterize the surface chemistry of PEI functionalized GO materials, I performed XPS analysis. XPS of PEI conjugates showed the appearance of a peak corresponding to the N (1s) moiety at a value close to 400 eV in all samples, confirming the incorporation of nitrogen (Figure 3.5).

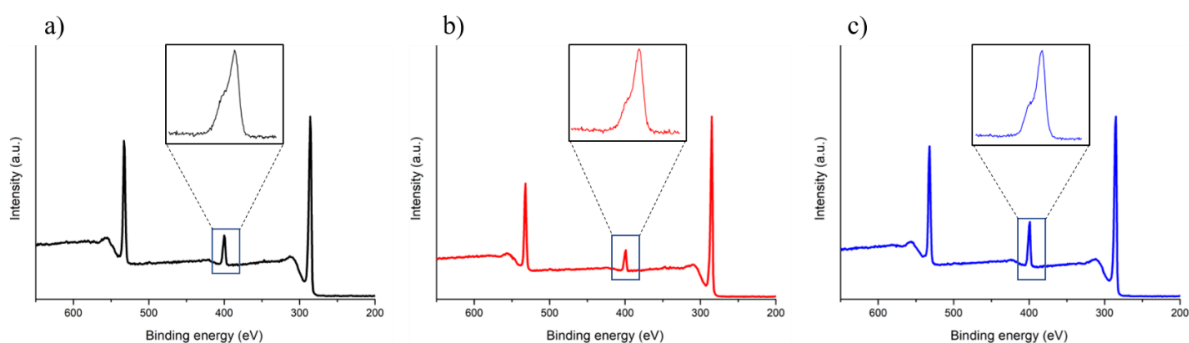


**Figure 3.5:** XPS spectra of different PEI functionalization of GOs with a zoom at N(1s) peak: a) GO<sub>S</sub>-PEI in black, b) rGO<sub>S</sub>-5d-PEI in red, and c) rGO<sub>S</sub>-5d-O<sub>3</sub>-PEI in blue

GO<sub>S</sub>-PEI, rGO<sub>S</sub>-5d-PEI, and rGO<sub>S</sub>-5d-O<sub>3</sub>-PEI contained 7.4, 5.9 and 10.1% of N, respectively (Table 3.3). The hydrothermal reduction method caused a decrease of N% between GO<sub>S</sub> and rGO<sub>S</sub>-5d, while as the epoxidation process favored the amination reaction with a significant increase of N% between rGO<sub>S</sub>-5d and rGO<sub>S</sub>-5d-O<sub>3</sub>. As for the other amines, GO functionalization yield seems to be proportional to the presence of C-O groups estimated by the XPS characterization (see Chapter 2). Interestingly, we obtained a positive value of  $\zeta$  potential (> 30mV at pH 6) for PEI conjugates.

**Table 3.3.** N atomic % of PEI functionalized GO<sub>S</sub> calculated from the XPS peak N1s at 400 eV.

	<b>Small GO</b>		
	Starting	Hydrothermal	Re-epoxidation
PEI-functionalized	GO <sub>S</sub> -PEI	rGO <sub>S</sub> -5d-PEI	rGO <sub>S</sub> -5d-O <sub>3</sub> -PEI
N atomic %	7.4 ± 0.1	5.9 ± 0.1	10.1 ± 0.1

To better characterize PEI functionalized GO, XRD analysis was performed on these PEI conjugates samples (Figure 3.6 and Table 3.4). Although the starting GOs and reduced GOs had different [002] interplanar distance in the GO lattice from XRD results (Table 2.3 in Chapter 2), whenever they were conjugated with PEI, the interplanar distances of the PEI conjugates were the same and enhanced to 9.3 Å (Table 3.4). This increase in the sheet to sheet distance is attributed to the functionalization of the graphene oxides with the polymer chain that, intercalating between the sheets, significantly increases the interplanar distance.

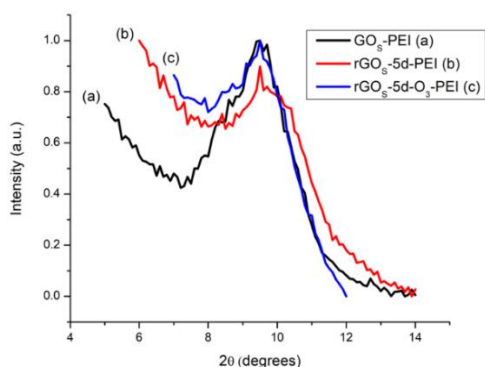


**Figure 3.6.** High resolution XRD spectra of the GOs series. On the left: a) GOs (black line), b) rGOs (red line), c) GOs-O<sub>3</sub> (blue line); on the right: a) GOs-PEI (black line), b) rGOs-5d-PEI (red line), rGOs-O<sub>3</sub>-PEI (blue line).

**Table 3.4.** [002] calculated distance from XRD using Bragg law,  $\lambda = 1.541\text{Å}$ .

Sample	XRD max. (2θ°)	Distance (Å)
GO <sub>S</sub> -PEI	9.5	9.3
rGO <sub>S</sub> -5d-PEI	9.5	9.3
rGO <sub>S</sub> -5d-O <sub>3</sub> -PEI	9.5	9.3

Interestingly, we obtained the  $\zeta$  potential of PEI conjugates with the average value of +33 mV, indicating a potential ability of complexation with siRNA.

I also performed the gel electrophoresis at different mass ratio of PEI functionalized GO<sub>S</sub> with siRNA (Figure 3.7).

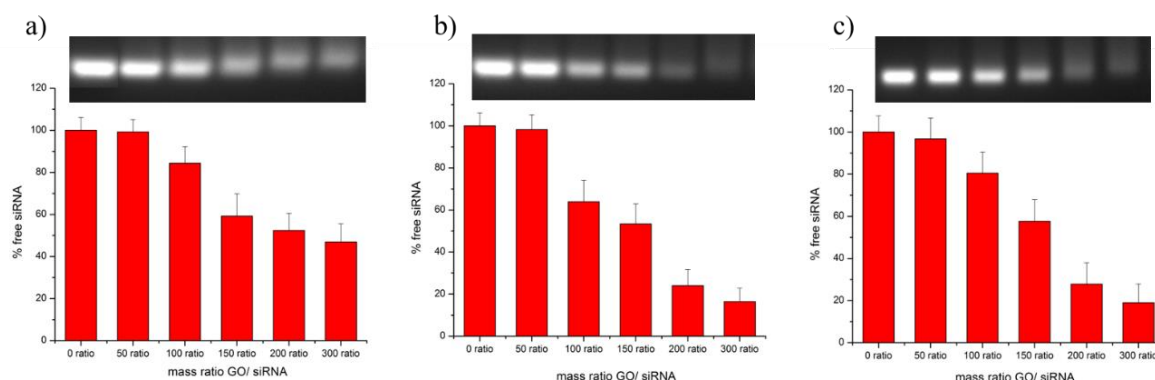


**Figure 3.7.** Complexation of PEI functionalized GOs with siRNA: a) GO<sub>s</sub>-PEI, b) rGO<sub>s</sub>-5d-PEI, c) rGO<sub>s</sub>-5d-O<sub>3</sub>-PEI. Top: image of the electrophoresis gel; bottom: histograms showing the free siRNA signal at different GO/siRNA mass ratios.

The gel retardation analyses presented an efficient complexation of the PEI conjugates with siRNA molecules. At 200 mass ratio GO/siRNA, the PEI derivatives of GOs, rGO<sub>s</sub>-5d, rGO<sub>s</sub>-5d-O<sub>3</sub> showed a value of  $52\pm 8\%$ ,  $24\pm 8\%$ ,  $28\pm 10\%$  of free siRNA, respectively. It should be reminded that the lower amount of free siRNA after interaction with graphene materials corresponded to the higher complexation ability.

To better understand which factor was more influent on the complexation ability, we compared the complexation yield at 200 mass ratio with the O/C ratio of the starting corresponding graphene materials, and the amount loading of PEI based on the N% from XPS, as shown in Figure 3.8.

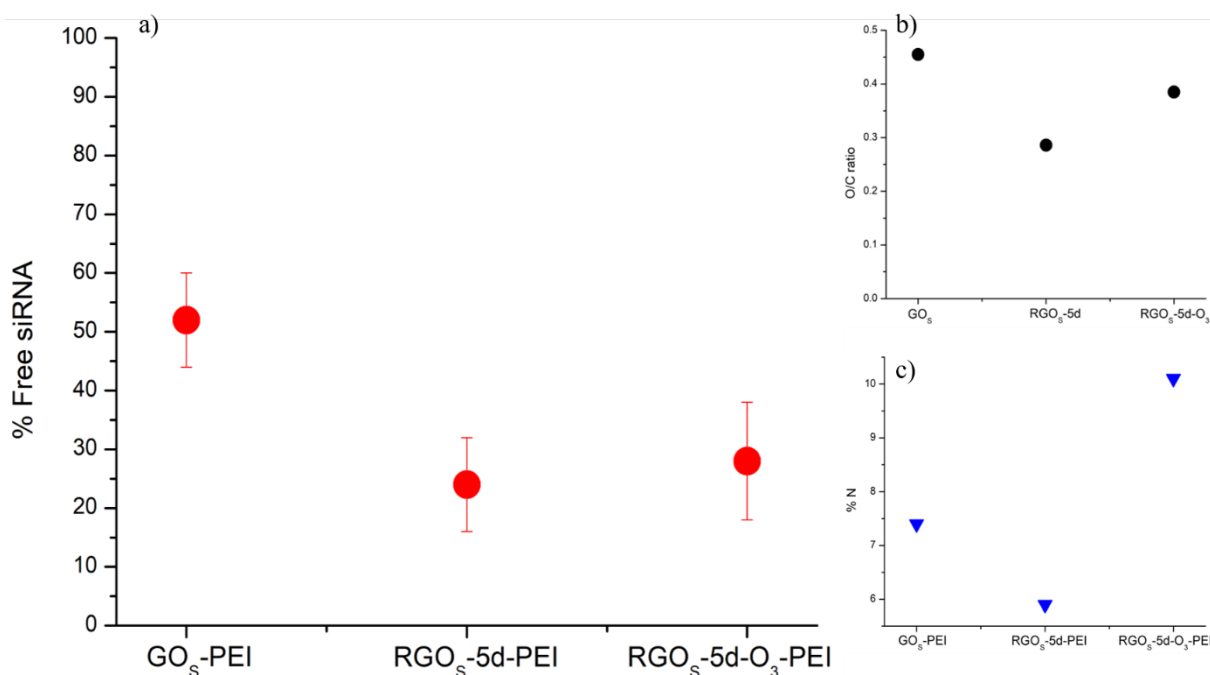


**Figure 3.8.** siRNA complexation at mass ratio GO/siRNA of 200 (a), O/C ratio (b), and N% (c) scattering graph of PEI functionalized graphene materials.

From figure 3.8, it clearly appears that there is not a direct correlation of the complexation ability ( $rGO_s$ -5d-PEI  $\approx$   $rGO_s$ -5d- $O_3$ -PEI  $>$   $GO_s$ -PEI) and the N% ( $rGO_s$ -5d- $O_3$ -PEI  $>$   $GO_s$ -PEI  $>$   $rGO_s$ -5d-PEI), but there is an inverted correlation with the O/C ratios ( $GO_s$   $>$   $rGO_s$ -5d- $O_3$   $>$   $rGO_s$ -5d). PEI can efficiently complex oligonucleotides because this polymer contains many protonable amine and it can interact with siRNA by ionic forces.<sup>17</sup> If we consider a pure electrostatic interaction between siRNA and GO, the residual oxygenated groups would obstacle the complexation due to the columbic repulsions of siRNA molecules. From this model, the complexation yield is ruled by a balance between the repulsive forces due to the oxygenated groups and the attractive electrostatic interactions due to the ammonium groups. In case of  $GO_s$ , the complexation yield seems to be independent from the PEI loading on GO, but mostly related to the oxygenated groups present on the GO surface.

### **PART B: Functionalization of $GO_L$ and reduced $GO_L$ materials with the different cationic molecules**

From the complexation results of  $GO_s$  functionalized with the different amines, the dendrons and PEI, we decided to modified  $GO_L$  only with two different amines: small TEG, and big PEI.

The epoxy ring opening reaction of GO<sub>L</sub> with TEG and PEI in water and at room temperature yielded 1,2-amino alcohols on the GO sheets, leading to the formation of GO<sub>L</sub>-TEG and GO<sub>L</sub>-PEI. We performed the same functionalization of these two compounds on the hydrothermal rGO<sub>L</sub>-5d, the vitamin C rGO<sub>L</sub>-C, and the reepoxidized rGO<sub>L</sub>-5d-O<sub>3</sub> that were presented before in Chapter 2.

The thermal profile of the different GO before and after derivatization was assessed by TGA. The thermograms of all the amino functionalized samples are shown in Figure 3.9.

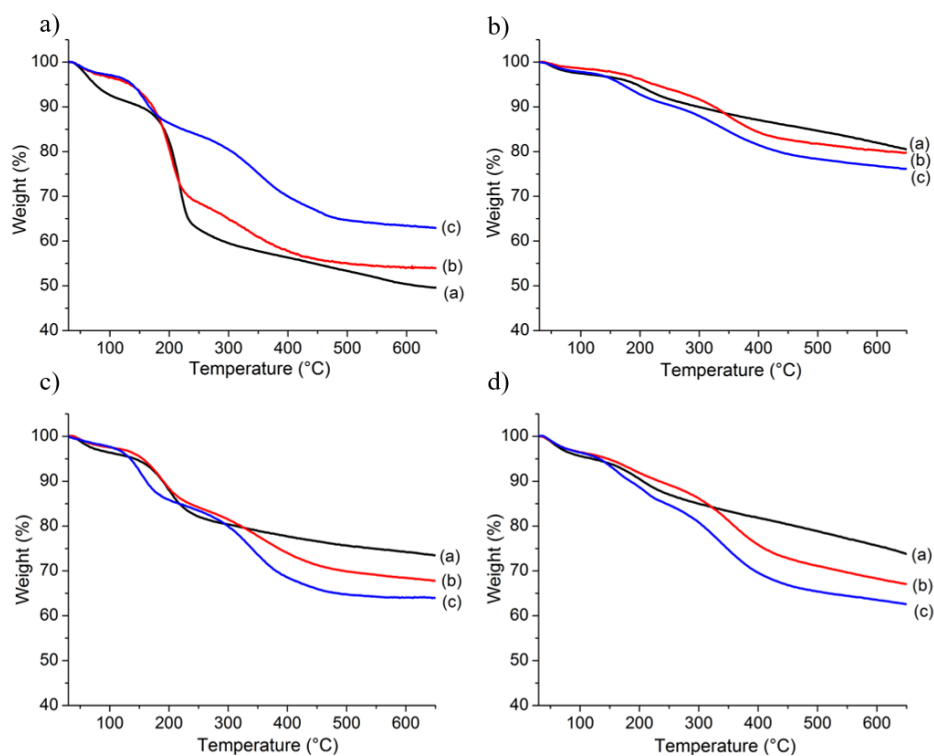


**Figure 3.9.** TGA curves of amino functionalized GO: A) GO<sub>L</sub> in black (a), GO<sub>L</sub>-TEG in red (b), GO<sub>L</sub>-PEI in blue (c); B) rGO<sub>L</sub>-5d in black (a), rGO<sub>L</sub>-5d-TEG in red (b), rGO<sub>L</sub>-5d-PEI in blue (c); C) rGO<sub>L</sub>-C in black (a), rGO<sub>L</sub>-C-TEG in red (b), rGO<sub>L</sub>-C-PEI in blue (c); D) rGO<sub>L</sub>-5d-O<sub>3</sub> in black (a), rGO<sub>L</sub>-5d-O<sub>3</sub>-TEG in red (b), rGO<sub>L</sub>-5d-O<sub>3</sub>-PEI in blue (c).

Similar to starting GO, amino functionalized graphene oxides showed a three-step decomposition process. Compared to non-treated GO<sub>L</sub>, GO<sub>L</sub>-TEG and GO<sub>L</sub>-PEI presented a lower thermal loss (Figure 3.9a). As previously described,<sup>18</sup> this can be caused by the instability of the oxygenated groups present on the GO, making TGA interpretation again not easy. In contrast, the reduction via hydrothermal treatment and vitamin C decreased the number of oxygenated groups rendering the calculation of the weight loss more accurate. Figure 3.9b, c

and d report the TGA spectra of the amino functionalized rGO<sub>L</sub>-5d, rGO<sub>L</sub>-C and rGO<sub>L</sub>-5d-O<sub>3</sub>, in which the weight losses, derived from the functionalization, were clearly distinguished. A general trend can be observed in the degradation profiles. Compared to starting rGO, amination products showed a higher degradation above 320°C. In addition, PEI-functionalized rGOs (blue lines) displayed a remarkably greater thermal degradation than TEG functionalized ones (red lines). This result can be attributed to the big difference between the molecular weight of PEI and TEG that leads to a different degradation profile. In order to better characterize the surface chemistry of aminated GO<sub>L</sub>, XPS analysis was also performed. XPS of all amino functionalized GO<sub>L</sub> show the appearance of a peak corresponding to the N (1s) confirming the amino derivatization of the GO sheets (Figure 3.10).

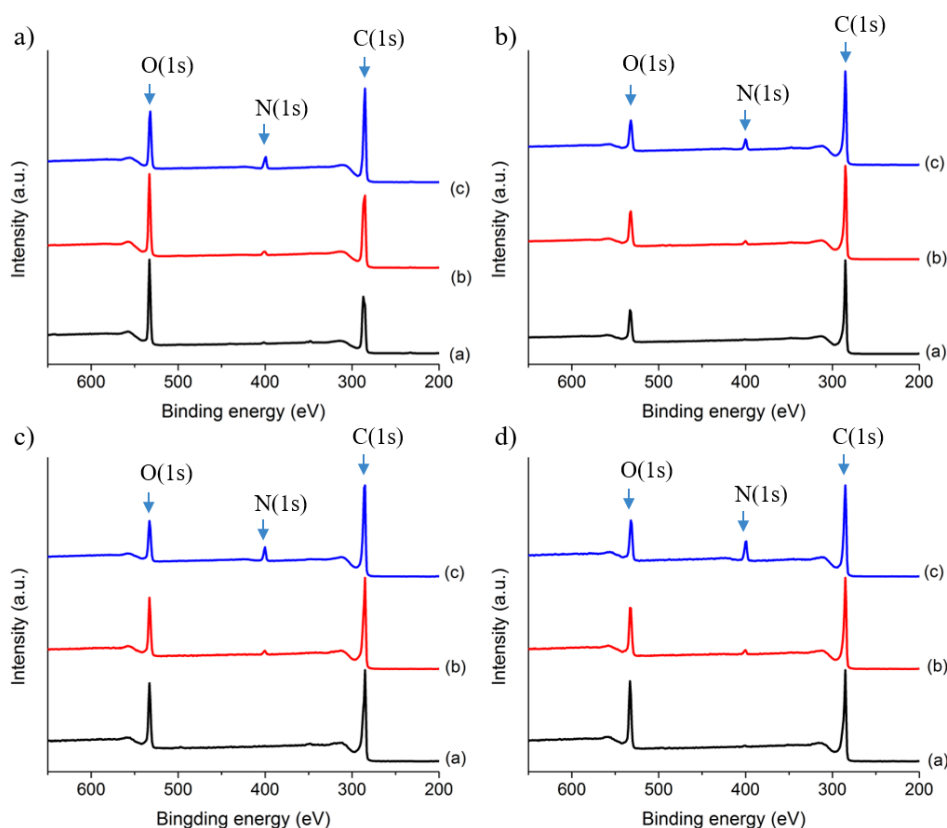


**Figure 3.10.** XPS spectra of amino functionalized GO<sub>L</sub>: a) GO<sub>L</sub> in black (a), GO<sub>L</sub>-TEG in red (b), GO<sub>L</sub>-PEI in blue (c); b) rGO<sub>L</sub>-5d in black (a), rGO<sub>L</sub>-5d-TEG in red (b), rGO<sub>L</sub>-5d-PEI in blue (c); c) rGO<sub>L</sub>-C in black (a), rGO<sub>L</sub>-C-TEG in red (b), rGO<sub>L</sub>-C-PEI in blue (c); d) rGO<sub>L</sub>-5d-O<sub>3</sub> in black (a), rGO<sub>L</sub>-5d-O<sub>3</sub>-TEG in red (b), rGO<sub>L</sub>-5d-O<sub>3</sub>-PEI in blue (c). The C (1s) photoelectron binding energy was set at  $284.5 \pm 0.2$  eV and used as reference for calibrating the other peak positions.

The N atomic % for all the TEG and PEI functionalized samples are reported in Table 3.4.

**Table 3.4.** N atomic % of the various TEG and PEI functionalized GO<sub>L</sub> calculated from the XPS peak N1s at 400 eV.

Sample	TEG	PEI
GO <sub>L</sub>	2.1±0.5	5.8±0.1
rGO <sub>L</sub> -5d	1.9±0.1	5.3±0.1
rGO <sub>L</sub> -C	2.1±0.1	6.3±0.2
rGO <sub>L</sub> -5d-O <sub>3</sub>	2.1±0.1	9.5±0.2

GO<sub>L</sub>-TEG and GO<sub>L</sub>-PEI contain 2.1 and 5.8% of N, respectively. The reduction product rGO<sub>L</sub>-5d-TEG shows a small decrease to 1.9% of N, while rGO<sub>L</sub>-C-TEG shows a similar value of 2.1%. Analogous results were seen in the case of PEI functionalization with a percentage of N for rGO<sub>L</sub>-5d-PEI and rGO<sub>L</sub>-C-PEI of 5.3 and 6.3, respectively. The XPS analysis of amination on rGO<sub>L</sub>-5d-O<sub>3</sub> afforded 2.1 and 9.5% of N for TEG and PEI conjugates, respectively. Among the TEG derivatization, the N% of the various functionalized GO<sub>L</sub> remains similar. A slightly higher change in N% was seen between GO<sub>L</sub>-PEI, rGO<sub>L</sub>-5d-PEI and rGO<sub>L</sub>-C-PEI. GO<sub>L</sub>, rGO<sub>L</sub>-5d and rGO<sub>L</sub>-C functionalized either by TEG or PEI show similar N% values, so each amine seems to exhibit the same reactivity for the three different GO<sub>L</sub>. Most probably the reduction process does not alter the number of epoxide groups on the GO, but affects other oxygenated groups such or alcohols. The value of rGO<sub>L</sub>-5d-O<sub>3</sub>-TEG similar to rGO<sub>L</sub>-5d-TEG is not easy to explain. Indeed, the increase of C-O groups, confirmed by XPS analyses, does not cause a consequent increase of the reactivity of rGO<sub>L</sub>-5d-O<sub>3</sub> with TEG. Besides, in the case of PEI the epoxidation process favors the amination reaction with a significant increase of N% between rGO<sub>L</sub>-5d-O<sub>3</sub> and rGO<sub>L</sub>-5d. Moreover, we obtained a positive value of  $\zeta$  potential (> 30mV at pH 6) for the PEI conjugated GO<sub>L</sub> series as before for the PEI conjugated GO<sub>S</sub> series.

To further clarify the structure of the conjugates after reaction of reduced GO with PEI, we performed a solid-state magic angle spinning (MAS) NMR (ssNMR) analysis on rGO<sub>L</sub>-5d-O<sub>3</sub>, rGO<sub>L</sub>-5d-O<sub>3</sub>-PEI, PEI alone, and the simple mixture (non-covalently conjugated) of rGO<sub>L</sub>-5d-O<sub>3</sub> and PEI. As the low molecular weight PEI, used to functionalize rGOs, is liquid at room temperature, to analyze the ssNMR of PEI alone, we used a solid high molecular weight polyethylenimine hydrochloride (Mn 20 kDa). The amount of LMW PEI on rGO<sub>L</sub>-5d-O<sub>3</sub> was

calculated from the N% average values obtained by XPS (~35%) and the weight loss of the polymer assessed by TGA (~25%). The direct polarization  $^{13}\text{C}$  NMR spectra of these samples are presented in Figure 3.11.

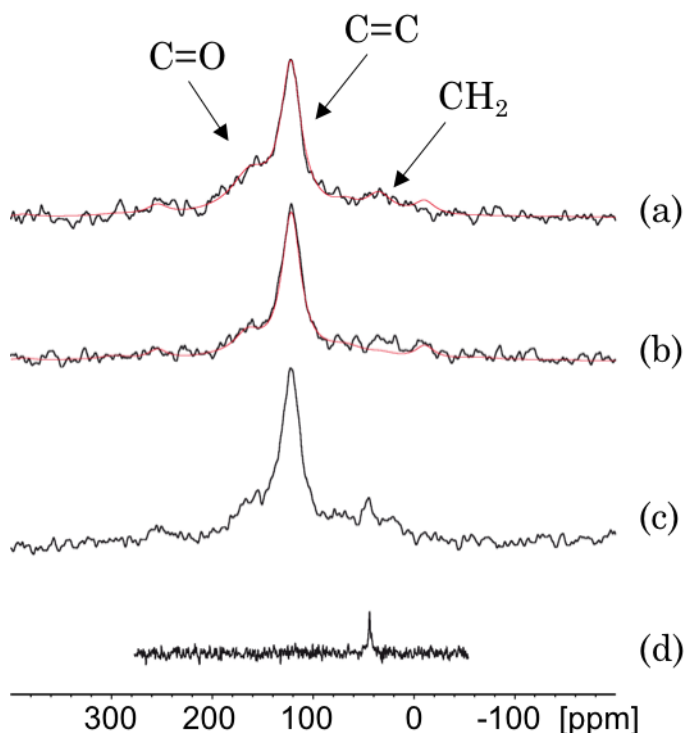


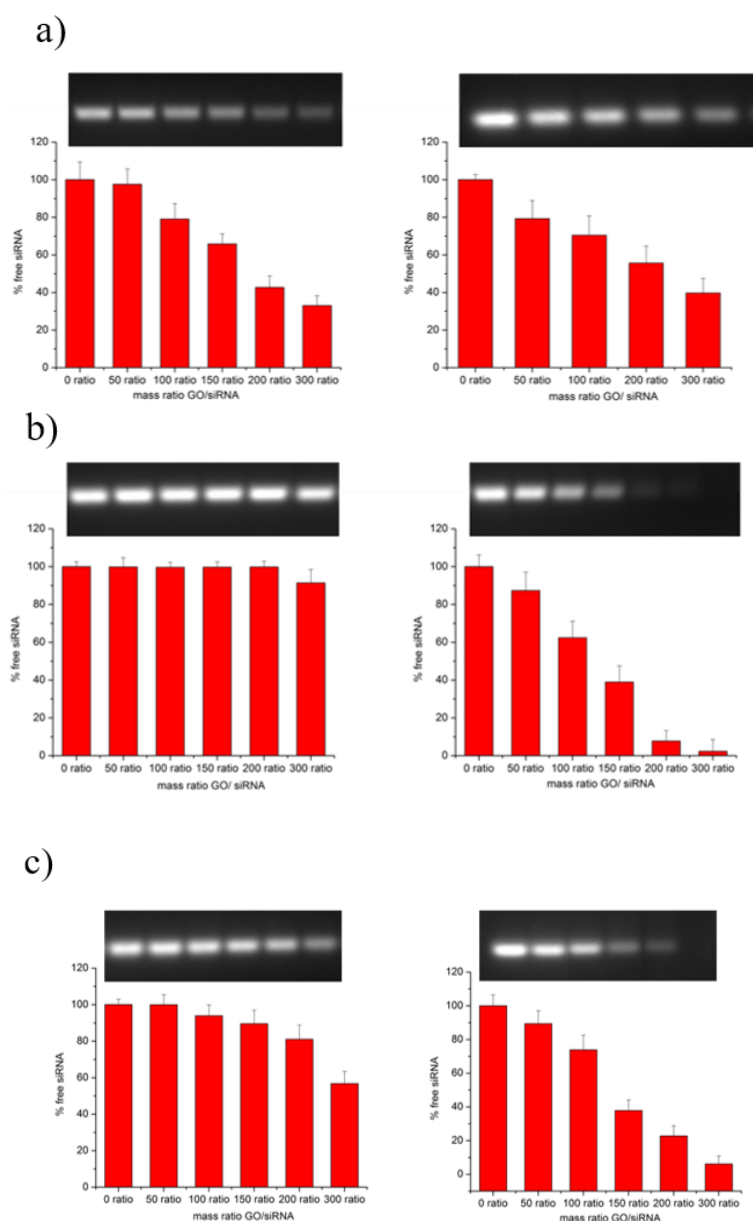
**Figure 3.11.** Direct polarization  $^{13}\text{C}$  ssNMR of rGO<sub>L</sub>-5d-O<sub>3</sub>-PEI (a); rGO<sub>L</sub>-5d-O<sub>3</sub> (b); mechanical mixture of rGO<sub>L</sub>-5d-O<sub>3</sub> and PEI (c); and PEI alone (d). The spectrum of PEI was obtained with a smaller spectral window and processed with a smaller line broadening (150Hz).

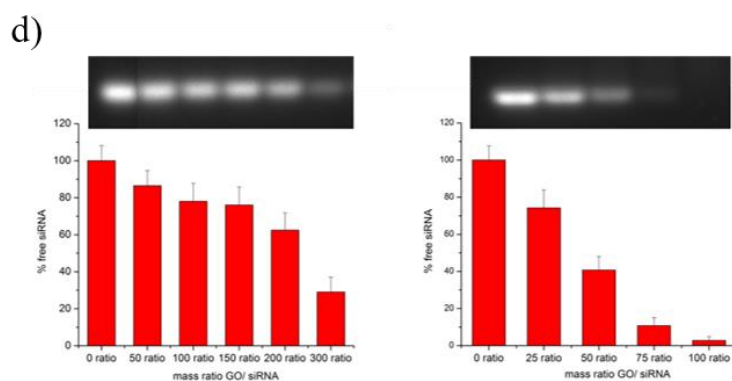
Although the resulting spectra appear rather featureless with broad lines and relatively low S/N ratio, they remain informative as far as we may separate a minimal set of peaks related to chemical functions. Clearest trends may be also extracted from the experimental data by fitting with a pure Chemical Shift Anisotropy model (Figure 3.11, red lines). The NMR spectrum of rGO<sub>L</sub>-5d-O<sub>3</sub> shows two peaks centered at 160 and 121 ppm attributed to C=O and C=C conjugated bonds, respectively (Figure 3.11b).<sup>19</sup> The presence of the C=O peak is in agreement with the XPS data. Comparing this spectrum with that of rGO<sub>L</sub>-5d-O<sub>3</sub>-PEI (Figure 3.11a) we can observe one additional (although weak) peak at 36 ppm assigned to the methylene groups of the PEI chain. To understand if the covalent functionalization with PEI occurred, a simple mechanical mixture of rGO<sub>L</sub>-5d-O<sub>3</sub> and PEI was analyzed by ssNMR (Figure 3.11c). In this case, the methylene PEI groups appear at 45 ppm very closed to the peak obtained from the



polymer alone (Figure 3.11d), although larger (ca. 7 ppm). This peak broadening can be attributed to the highly heterogeneous magnetic susceptibility surrounding due to the aromatic ring currents on the graphene sheets. For rGO<sub>L</sub>-5d-O<sub>3</sub>-PEI the CH<sub>2</sub> signal is rather broad (ca. 30 ppm) and exhibits a 9 ppm upfield shift relative to the equivalent signal (45 ppm) appearing in the physical mixture of PEI and rGO<sub>L</sub>-5d-O<sub>3</sub>. The spectral differences measured among the three samples support further the covalent bonding of PEI to the graphene surface.

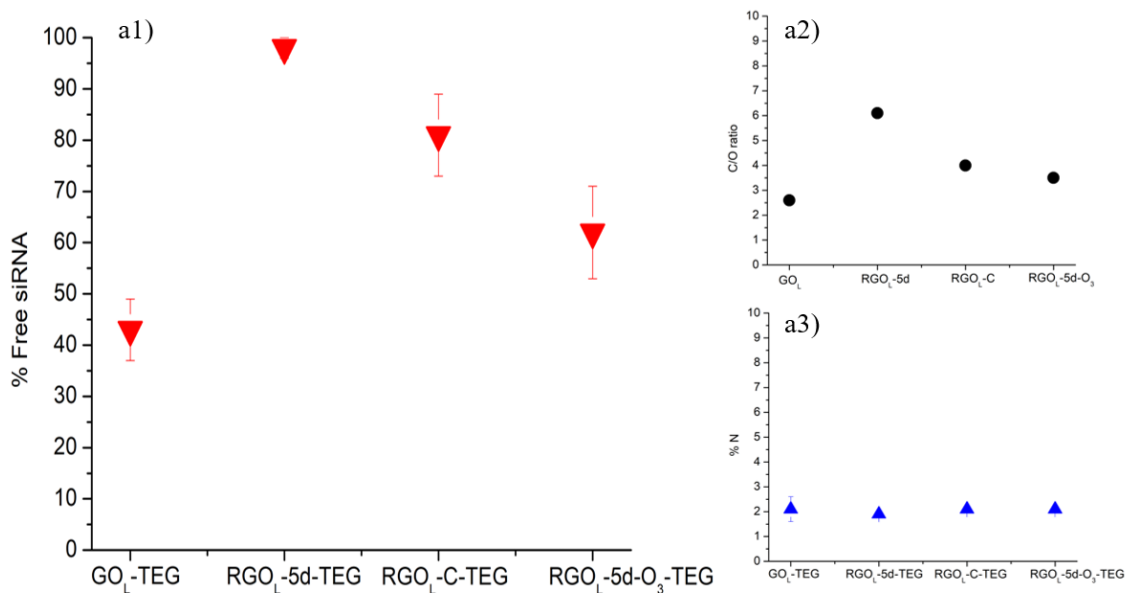
Considering the complexation of these conjugates of series of GO<sub>L</sub> with siRNA, all different electrophoresis gels are shown in Figure 3.12.





**Figure 3.12.** Complexation of TEG functionalized (first column) and PEI functionalized graphene materials (second column): row a)  $GO_L$ , row b)  $rGO_L$ -5d, row c)  $rGO_L$ -C, row d)  $rGO_L$ -5d- $O_3$ . Top: image of the electrophoresis gel; bottom: histograms showing the free siRNA signal at different GO/siRNA mass ratios.

Interestingly, we saw that TEG functionalized  $GO_L$  materials were able to complex siRNA. As for  $GO_S$  series, PEI functionalized  $GO_L$  series evidenced the best complexation yield values. As in the case of  $GO_S$  we wanted to investigate how functionalization of the various  $GO_L$  samples affect their interaction with siRNA molecules (Figure 3.13).



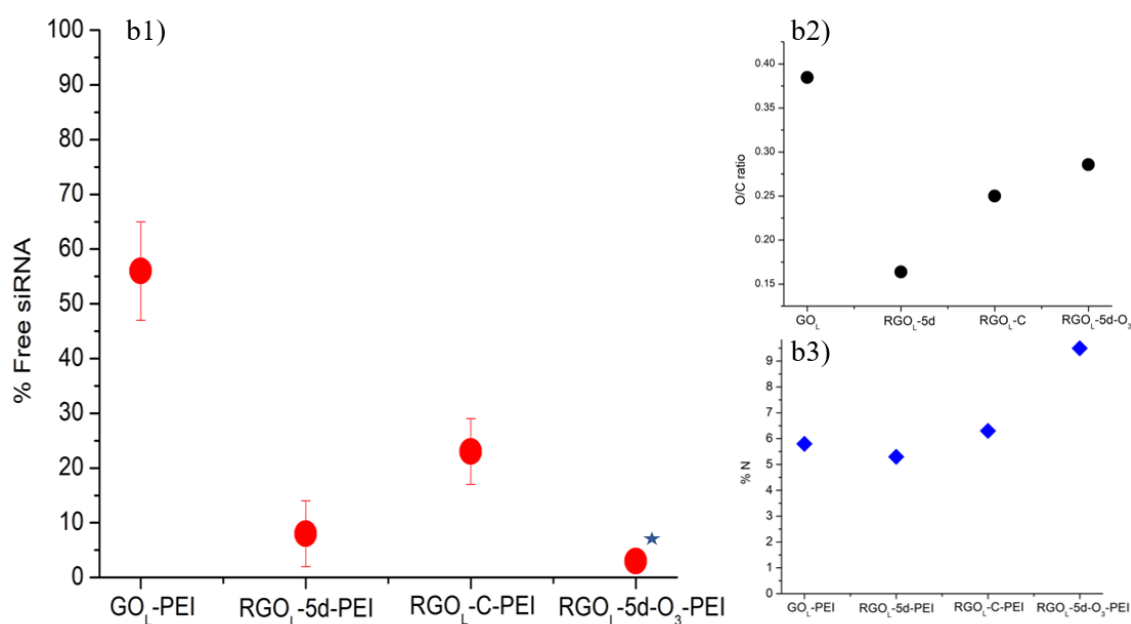


**Figure 3.13.** a) Scattering graphs of TEG functionalized: siRNA complexation at mass ratio GO/siRNA 200 (a1), C/O ratio of starting graphene materials (a2), and N% of TEG conjugates (a3). b) Scattering graphs of PEI functionalized: siRNA complexation at mass ratio GO/siRNA 200 (b1), O/C ratio of starting graphene materials (b2), and N% of PEI conjugates (b3) \* corresponds to a mass ratio rGO<sub>L</sub>-5d-O<sub>3</sub>-PEI/siRNA 100.

First, we were interested in investigating the complexation abilities of TEG conjugates (Figure 3.13a). We observed the most remarkable difference on GO<sub>L</sub>-TEG with a free siRNA of  $43 \pm 6\%$ . Comparing the TEG functionalization of the two reduced GOs, the TEG conjugates with the reduced by vitamin C exerted a higher complexation ability than the TEG functionalized with hydrothermally reduced GO ( $81 \pm 8\%$  and  $98 \pm 2\%$  of free siRNA, respectively). More interestingly, a stronger ability of complexation was observed when rGO underwent the ozone treatment (rGO<sub>L</sub>-5d-O<sub>3</sub>-TEG) ( $62 \pm 9\%$  of free siRNA). GO<sub>L</sub>-TEG exhibited the best complexing ability followed by rGO<sub>L</sub>-5d-O<sub>3</sub>-TEG. The two reduced rGO<sub>L</sub>-5d and rGO<sub>L</sub>-C displayed very low complexation levels. TEG functionalization allowed the introduction of primary amines on GO surface. These protonable groups could bind siRNA via coulombic interactions or simply via H-bond interactions. Moreover, the complexation with the different TEG-modified GOs cannot be attributed to the amount of TEG (Table 3.4). Most probably, the interaction between TEG conjugates and siRNA molecules is driven by the oxygenated groups present on the GO. The trend in the complexation is matching the trend of

C/O ratio. Considering the interaction between graphene oxide and nucleic acids, besides the  $\pi$ - $\pi$  interaction, the siRNA complexation can be triggered by polar interactions between the oxygenated groups of GO and the polar groups on the nucleotide strand.<sup>20</sup> In particular, GO surface is rich in H-bond donors (alcohols and carboxylic acids) and acceptors (epoxides). On the other hand, oxygenated groups are responsible of a negative charge on GO surface<sup>21</sup> that may cause the coulombic repulsion of the negatively charged siRNA, thus hampering the complexation.

PEI functionalized graphene materials exhibit a significant increase in complexation with siRNA molecules, especially in the case of ozone treated rGO<sub>L</sub>-5d-O<sub>3</sub>-PEI, showing a complete complexation even at GO/siRNA mass ratio of 100 (3±2%) ( Figure 3.13b) The PEI derivatives of GO<sub>L</sub>, rGO<sub>L</sub>-5d, rGO<sub>L</sub>-C showed a value of 56±9%, 8±6%, 23±6% of free siRNA, respectively. In the case of PEI functionalized GOs, the trend is rGO<sub>L</sub>-5d-O<sub>3</sub>-PEI > rGO<sub>L</sub>-5d-PEI > rGO<sub>L</sub>-C-PEI > GO<sub>L</sub>-PEI. As for TEG functionalized GO, comparing PEI derivatives of GO<sub>L</sub>, rGO<sub>L</sub>-5d and rGO<sub>L</sub>-C on the basis of XPS data (Table 3.4), there is a small difference on polymer functionalization ratio between the three graphenes that, however, would not directly explain the huge change on GO complexation capacities. The difference in the C/O ratio of these three materials should be attributed to the presence of other oxygenated functions such as hydroxyl or carboxylic groups. These groups may negatively affect the ability of GO in term of complexation with siRNA. Indeed, the presence of proximal negatively charged oxygenated groups on the surface of GO may disfavor the interactions between the different GO-PEI and the negatively charged siRNA molecules. This fact would explain the higher performance in complexation of the two rGO<sub>L</sub>-PEI compared to GO<sub>L</sub>-PEI. In case of the epoxidation, we were able to introduce selectively the epoxy groups onto the rGO<sub>L</sub>-5d. The extremely high complexation capacity of rGO<sub>L</sub>-5d-O<sub>3</sub> for siRNA can be explained by the high amount of PEI functionalization and by the low presence of proximal oxygenated species on the graphene sheets.

### 3.4 Conclusion

In summary, the synthesis and characterization of a series of amines and dendrons bearing positive charges at their termini (i.e. ammonium or quaternary groups) were described. I was able to successfully anchor these amines to different GOs materials through epoxy ring opening. In addition, PEI functionalized GO materials were also prepared. The interaction of

siRNA with these functionalized graphene materials was studied. Unfortunately, I found that the presence of small amines on GO<sub>S</sub> does not show significant improvement in siRNA complexation ability. Nevertheless, by gel electrophoresis, I proved that the low molecular weight PEI conjugates were the most efficient in complexing siRNA molecules. In addition, the interaction between the various PEI functionalized GO<sub>S</sub> and siRNA seems to be driven only by electrostatic interactions.

In addition, I also succeed in functionalizing GO<sub>L</sub> with TEG and PEI. The final products were characterized by complimentary analytical techniques to evaluate the degree of functionalization. The complexation of siRNA with the amino conjugated GO<sub>L</sub> was thoroughly investigated. Interestingly, the capacity in complexation of the amine functionalized GO can be attributed to two main contributions, corresponding to polar interactions by H-bonds and to ionic interactions. H-bond interactions seem to prevail in the case of TEG conjugates, while ionic forces have a major role for PEI conjugates. We believe that the identification and the rationalization of the supramolecular forces that affect the siRNA complexation is the key point for the preparation of efficient GO nanocarriers.

### 3.5 Experimental part

Chemicals were purchased from Sigma-Aldrich, Acros and Alfa Aesar, and used as received without any further purification. All solvents used for synthesis were analytical grade. When anhydrous conditions were required, high quality commercial solvents treated with molecular sieves (porosity 4 Å) were used (DMF). Water was purified using a Millipore filter system MilliQ® and free endotoxin Polisseur Biopak®. When stated, suspensions were sonicated in a water bath (20 W, 40 kHz). The filtration and dialysis membranes were purchased from Millipore and Spectrum Laboratories, Inc., respectively.

#### a) Characterization methods and instruments

TGA, XPS, solid state NMR are already described in Chapter 2.

#### Quantitative Kaiser test protocol:

Three solutions were prepared separately:

- (I): 10 g of phenol in 20 mL of absolute ethanol.
- (II): 2 mL of potassium cyanide 1 mM (aqueous solution) dissolved in 98 mL of pyridine.

- (III): 1 g of ninhydrin in 20 mL of absolute ethanol.

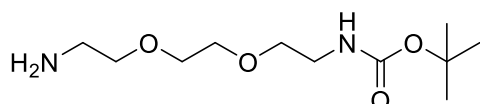
A mass of approximately 200  $\mu\text{g}$  of graphene oxide was carefully weighted in a haemolysis test tube. Then, 75  $\mu\text{L}$  of solution (I) and 100  $\mu\text{L}$  of solution (II). The resulting dispersion was sonicated in a water bath for several minutes until disaggregation of the GO. Then, 75  $\mu\text{L}$  of solution (III) were added to the GO suspension and the dispersion was sonicated again for 1 min. After heating at 110  $^{\circ}\text{C}$  for 5 min in a heating block (Bioblock Scientific), the suspension was immediately diluted with 4750  $\mu\text{L}$  of 60% ethanol. After centrifugation at 15000 rpm, the supernatant was analyzed by UV-Vis spectroscopy. The absorbance at 570 nm was correlated to the amount of free amine functions on the GO surface using the equation:

$$\text{NH}_2 \text{ loading } (\mu\text{mol/g}) = \frac{[\text{Abs}_{\text{sample}} - \text{Abs}_{\text{blank}}] \times \text{dilution (mL)} \times 10^6}{\text{Extinction coefficient} \times \text{sample weight (mg)}}$$

Dilution is 5 mL and extinction coefficient is 15000  $\text{M}^{-1}\text{cm}^{-1}$ . The blank was prepared exactly the same way but without GO. The result is expressed as micromole of amino groups per gram of material. The Kaiser test was repeated at least three times for each sample to ensure reproducibility.

### b) Synthesis of cationic molecules and dendrons

#### Compound **Boc-TEG**



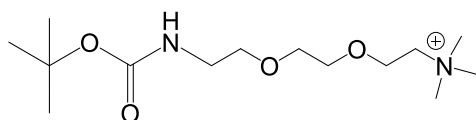
To a solution of 2,2'-(ethylenedioxy)bis(ethylamine) (10 ml, 68.50 mmol) in  $\text{CH}_2\text{Cl}_2$  (50 ml) in an ice bath, a solution of  $\text{Boc}_2\text{O}$  (3.1g, 14.40 mmol) in  $\text{CH}_2\text{Cl}_2$  (30 ml) was added dropwise over a period of 3 hours. The reaction mixture was stirred overnight at room temperature. The solvent was removed under reduced pressure and after dissolving the residue in  $\text{H}_2\text{O}$  (200 ml) the precipitate formed was filtered on celite. The filtrate was extracted with  $\text{CH}_2\text{Cl}_2$  (100 ml x 3) and dried over  $\text{Na}_2\text{SO}_4$ . Evaporation of the solvent afforded **Boc-TEG** as a colorless oil (2.5 g, 10.08 mmol, 70%).  $^1\text{H}$  NMR spectroscopy showed a satisfactory purity; therefore, the crude was used without purification.  $^1\text{H}$ -NMR (400 MHz,  $\text{CDCl}_3$ ):  $\delta$  5.16 (*bs*, 1H), 3.56 (*m*, 4H), 3.43-3.51 (*m*, 4H), 3.25 (*bs*, 2H), 2.84 (*m*, 2H), 2.2 (*s*, 2H), 1.42 (*s*, 9H).  $^{13}\text{C}$ -NMR (125MHz,

CDCl<sub>3</sub>):  $\delta$  155.9, 78.8, 73.1, 70.0, 41.5, 40.2, 28.3. ESI-MS: Found 249.1 [M+H]<sup>+</sup> for C<sub>11</sub>H<sub>25</sub>N<sub>2</sub>O<sub>4</sub>.

All structural assignments were in agreement with the data available from the literature.<sup>22</sup>

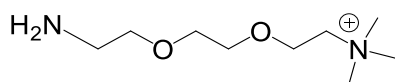
### Synthesis of Compound Q

b1)



To a solution of Boc-TEG (1g, 4.03 mmol) in tetrahydrofuran (6ml), methyl iodide was added (0.8 ml, 12.75 mmol). The reaction was stirred overnight at room temperature under argon. The resulting slurry was filtered to collect the powder. The yellow powder was washed with ethyl acetate and diethyl ether to obtain a light yellow solid (0.2g, 0.7mmol, 18%). <sup>1</sup>H NMR (500 MHz, CDCl<sub>3</sub>)  $\delta$  4.83 (s, 1H), 3.99 – 3.89 (m, 4H), 3.64 (dd, J = 5.4, 3.2 Hz, 2H), 3.57 – 3.52 (m, 2H), 3.50 – 3.38 (m, 11H), 3.23 (d, J = 5.0 Hz, 2H), 1.37 (s, 9H). <sup>13</sup>C NMR (125 MHz, CDCl<sub>3</sub>)  $\delta$  155.9, 79.3, 70.5, 70.2, 69.9, 65.7, 65.1, 55.0, 40.2, 28.4. ESI-MS: Found 291.23, [M]<sup>+</sup> for C<sub>14</sub>H<sub>31</sub>N<sub>2</sub>O<sub>4</sub><sup>+</sup>

b2) Compound Q:



The product was then added in to a solution of TFA/DCM (1:1 volume ratio) to cleave the Boc group. The mixture was stirred in 30 mins at room temperature under argon. The TFA/DCM was then removed by evaporation using a rotavapor. The product was dried under vacuum. <sup>1</sup>H NMR (500 MHz, MeOD)  $\delta$  4.01 – 3.96 (m, 2H), 3.78 – 3.72 (m, 6H), 3.66 – 3.62 (m, 2H), 3.25 (s, 9H), 3.19 – 3.15 (m, 2H). <sup>13</sup>C NMR (125 MHz, MeOD)  $\delta$  71.63, 68.25, 67.21, 66.15, 55.02, 54.99, 54.96, 40.88. ESI-MS: found 191.18, [M]<sup>+</sup> for C<sub>9</sub>H<sub>23</sub>N<sub>2</sub>O<sub>2</sub><sup>+</sup>

All following structural assignments from compound 2 to compound 9 were in agreement with the data available from the literature.<sup>23</sup>

### Compound 2.

To a solution of 3,3'-diaminodipropylamine (20.2 g, 153 mmol) in CH<sub>2</sub>Cl<sub>2</sub> (100 ml) in an ice bath, a solution of Boc<sub>2</sub>O (33.4 g, 153.9 mmol) in CH<sub>2</sub>Cl<sub>2</sub> (100 ml) was added dropwise over a period of 3 hours. The reaction mixture was stirred for 48 hours at room temperature. The solvent was removed under reduced pressure and the white residue obtained was mixed with

H<sub>2</sub>O (150 ml). The product was extracted with CH<sub>2</sub>Cl<sub>2</sub> (150 ml x 5). The combined organic layers were washed with H<sub>2</sub>O (100 ml x 2), brine (200 ml) and dried over by anhydrous Na<sub>2</sub>SO<sub>4</sub>. After evaporation of the solvent, the resulting residue was purified by column chromatography on silica gel (CH<sub>2</sub>Cl<sub>2</sub>/MeOH 95:5, 8:2) afforded compound **2** (5 g, 15.2 mmol, 10%) as a white powder. <sup>1</sup>H NMR (500 MHz, CDCl<sub>3</sub>) of **2**: δ 5.21 (s, 2H), 3.19 (t, *J* = 31.0 Hz, 4H), 2.68 (t, *J* = 6.4 Hz, 4H), 2.01 (d, *J* = 38.2 Hz, 2H), 1.76 – 1.59 (m, 4H), 1.46 (d, *J* = 13.2 Hz, 18H); <sup>13</sup>C NMR (125 MHz, CDCl<sub>3</sub>) δ 156.3, 79.3, 47.2, 38.7, 29.4, 28.4; ESI-MS: [*M* + H]<sup>+</sup> for C<sub>16</sub>H<sub>34</sub>N<sub>3</sub>O<sub>4</sub>, 332.26; found, 332.2.

**Compound 3.** To a solution of compound **2** (1.5 g, 4.5 mmol) in 50 ml of CH<sub>3</sub>CN, Na<sub>2</sub>CO<sub>3</sub> (1 g, 9 mmol) was added and the obtained suspension was stirred at 75°C for 5 minutes. *N*-(3-bromopropyl)phthalimide (1.5 g, 5.6 mmol) was added to the suspension and the reaction was stirred for 24 hours at 75°C. After cooling down the mixture to room temperature, the reaction mixture was firstly filtrated to remove the excess of Na<sub>2</sub>CO<sub>3</sub> and then the solvent was removed under reduced pressure. The resulting residue was purified by column chromatography on silica gel (CH<sub>2</sub>Cl<sub>2</sub>, then CH<sub>2</sub>Cl<sub>2</sub>/MeOH 95:5) afforded compound **3** (1.35 g, 2.6 mmol, 58%) as a white solid; <sup>1</sup>H NMR (400 MHz, CDCl<sub>3</sub>) δ 7.84 (m, 2H), 7.72 (m, 2H), 5.19 (s, 2H), 3.75 (s, 2H), 3.20 (m, 4H), 2.47 (m, 4H), 1.84 (m, 2H), 1.56 (s, 4H), 1.43 (s, 18H); <sup>13</sup>C NMR (125 MHz, CDCl<sub>3</sub>) δ 168.3, 156.2, 134.0, 132.1, 123.2, 78.9, 51.8, 50.8, 39.1, 36.3, 28.5, 27.0, 26.1; ESI-MS: [*M* + H]<sup>+</sup> for C<sub>27</sub>H<sub>43</sub>N<sub>4</sub>O<sub>6</sub>, 519.32; found, 519.3.

**Compound 4:** obtaining the compound from our previous project,<sup>6</sup> with the procedure of synthesis: To a solution of compound **3** (1.5 g, 3 mmol) in a mixture of EtOH/toluene 2:1 (12 ml + 6 ml), hydrazine hydrate (0.3 ml, 5.6 mmol) was added. The reaction mixture was stirred overnight at 50°C. After removing the solvent under reduced pressure, the residue was suspended in CH<sub>2</sub>Cl<sub>2</sub> (100 ml) and washed with a 40% aqueous solution of KOH (50 ml per 10), brine (100 ml) and dried over Na<sub>2</sub>SO<sub>4</sub>. The final product was a yellow oil. <sup>1</sup>H NMR (300 MHz, CDCl<sub>3</sub>) δ 5.32 (s, 2H), 3.12 (q, *J* = 6.2 Hz, 4H), 2.71 (t, *J* = 6.9 Hz, 2H), 2.39 (t, *J* = 6.7 Hz, 6H), 1.59 (m, 6H), 1.41 (s, 18H); <sup>13</sup>C NMR (75 MHz, CDCl<sub>3</sub>) δ 156.1, 79.0, 52.4, 51.8, 40.5, 39.2, 29.7, 28.4, 27.0; ESI-MS: [*M* + H]<sup>+</sup> for C<sub>19</sub>H<sub>41</sub>N<sub>4</sub>O<sub>4</sub>, 389.31; found, 389.40.

**Compound 5.** To a solution of compound **2** (3.5 g, 10.5 mmol) and DIEA (3.5 ml, 21 mmol) in CH<sub>3</sub>CN (50 ml) in an ice bath, a solution of benzyl bromoacetate (2.1 ml, 12.6 mmol) in CH<sub>3</sub>CN (50 ml) was added dropwise over a period of 2 hours. The reaction mixture was stirred



for 48 hours at room temperature. The solvent was removed under reduced pressure and the residue obtained was mixed with AcOEt (50 ml). The organic phase was washed with H<sub>2</sub>O (50 ml x 3) and brine (50 ml) and the organic layer was dried over Na<sub>2</sub>SO<sub>4</sub>. After evaporation of the solvent, the resulting residue was purified by column chromatography on silica gel (AcOEt/Cyclohexane 1:4 to 2:3) afforded compound **5** (3.46 g, 7.2 mmol, 69%) as a white powder. <sup>1</sup>H NMR (300 MHz, CDCl<sub>3</sub>) δ 7.42 – 7.32 (m, 5H), 5.33 – 5.20 (m, 2H), 5.18 – 5.10 (m, 2H), 3.36 – 3.28 (m, 2H), 3.23 – 3.11 (m, 4H), 2.65 – 2.52 (m, 4H), 1.68 – 1.56 (m, 4H), 1.48 – 1.43 (m, 18H); <sup>13</sup>C NMR (125 MHz, CDCl<sub>3</sub>) δ 171.5, 156.1, 135.6, 128.6, 128.42, 128.40, 78.9, 66.4, 52.1, 38.8, 28.4, 27.2, 26.9; ESI-MS: [*M* + H]<sup>+</sup> for C<sub>25</sub>H<sub>42</sub>N<sub>3</sub>O<sub>6</sub>, 480.31; found, 480.2.

**Compound 6.** To a solution of compound **5** (3 g, 6.3 mmol) in methanol (75 ml), 200 mg of Pd/C (10%) were added. The suspension was placed under H<sub>2</sub> atmosphere and the reaction mixture was stirred for two hours at room temperature. The solution was filtered through a celite pad and the solvent was evaporated under reduced pressure, obtaining the compound **6** (2.4 g, 6.2 mmol, quantitative) as a white solid; <sup>1</sup>H NMR (400 MHz, MeOD) δ 3.62 (s, 2H), 3.17 (dt, *J* = 8.3, 7.2 Hz, 8H), 1.92 – 1.83 (m, 4H), 1.44 (s, 18H); <sup>13</sup>C NMR (125 MHz, CDCl<sub>3</sub>) δ 168.7, 156.8, 79.6, 56.1, 52.9, 37.7, 28.7, 24.0; ESI-MS: [*M* + H]<sup>+</sup> for C<sub>18</sub>H<sub>36</sub>N<sub>3</sub>O<sub>6</sub>, 390.26; found, 390.20.

**Compound 7.** Compound **3** (1.35 g, 2.6 mmol) was dissolved in a 4N HCl solution in dioxane (20 ml) and the reaction mixture was stirred for two hours at room temperature. The solvent was then evaporated under pressure affording compound **7** without further purification as a white powder (0.8 g, 2.5 mmol, quantitative). <sup>1</sup>H NMR (300 MHz, D<sub>2</sub>O) δ 7.88 (t, *J* = 6.2 Hz, 4H), 3.80 (t, *J* = 6.6 Hz, 2H), 3.33 (dd, *J* = 10.2, 6.0 Hz, 6H), 3.13 (t, *J* = 7.7 Hz, 4H), 2.23 – 2.09 (m, 6H); <sup>13</sup>C NMR (125 MHz, D<sub>2</sub>O) δ 170.5, 134.8, 131.2, 123.4, 50.8, 50.0, 36.5, 34.7, 22.8, 21.6.; ESI-MS: [*M* + H]<sup>+</sup> for C<sub>17</sub>H<sub>27</sub>N<sub>4</sub>O<sub>2</sub>, 319.23; found, 319.4.

**Compound 8.** To a solution of compound **7** (0.75 g, 2.35 mmol), compound **6** (2 g, 5.13 mmol), DIEA (7.9 ml, 45 mmol) and HOBT (0.88 g, 6.8 mmol) in CH<sub>3</sub>CN (44 ml) in an ice bath, EDC×HCl (1.76 g, 9.1 mmol) was added. The reaction mixture was stirred for 48 hours at room temperature. The solvent was removed under reduced pressure and the residue obtained was mixed with AcOEt (80 ml). The organic phase was washed with saturated aqueous NaHCO<sub>3</sub> solution (50 ml per 4), H<sub>2</sub>O (50 ml) and brine (50 ml). The organic layer was dried over Na<sub>2</sub>SO<sub>4</sub>

and the solvent evaporated under reduced pressure. The resulting material was purified by column chromatography (CH<sub>2</sub>Cl<sub>2</sub>/MeOH 9:1) yielding compound **8** as a yellow oil (1.16 g, 1.09 mmol, 47%). <sup>1</sup>H NMR (400 MHz, CDCl<sub>3</sub>) δ 7.84 (m, 2H), 7.71 (m, 2H), 7.50 (br s, 2H), 5.08 (br s, 4H), 3.72 (t, *J* = 7.1 Hz, 2H), 3.30 (q, *J* = 6.2 Hz, 4H), 3.14 (br q, 8H), 3.03 (s, 4H), 2.50 (m, 14 H), 1.95-1.65 (br, 4H), 1.62 (m, 10H), 1.42 (s, 36H); <sup>13</sup>C NMR (125 MHz, CDCl<sub>3</sub>) δ 171.7, 168.6, 156.4, 134.3, 132.3, 123.5, 79.4, 58.6, 52.8, 51.7, 51.0, 38.6, 37.5, 36.5, 28.6, 27.8, 27.6 ; ESI-MS: [*M* + H]<sup>+</sup> for C<sub>53</sub>H<sub>93</sub>N<sub>10</sub>O<sub>12</sub>, 1061.70; found, 1061.7.

**Compound 9.** To a solution of compound **8** (0.92 g, 0.87 mmol) in a mixture of EtOH/toluene 2:1 (30 ml + 15 ml), hydrazine hydrate (340 μl, 7 mmol) was added. The reaction mixture was stirred overnight at 50°C. After removing the solvent under reduced pressure, the residue was suspended in CH<sub>2</sub>Cl<sub>2</sub> (100 ml) and washed with a 40% aqueous solution of KOH (100 ml per 10), brine (50 ml) and dried over Na<sub>2</sub>SO<sub>4</sub>. After evaporation of the solvent, compound **9** was afforded as a yellow oil (0.51 g, 0.55 mmol, 63%). <sup>1</sup>H NMR (400 MHz, CDCl<sub>3</sub>) δ 7.50 (br s, 2H), 5.21 (br s, 4H), 3.29 (q, *J* = 6.4 Hz, 4H), 3.14 (q, 8H), 3.02 (s, 4H), 2.77 (t, 2H), 2.47 (m, 14H), 1.97 (br s, 2H), 1.63 (m, 14H), 1.43 (s, 36H). <sup>13</sup>C NMR (125 MHz, CDCl<sub>3</sub>) δ 171.6, 156.2, 79.1, 58.5, 53.4, 52.6, 51.6, 40.6, 38.4, 37.4, 28.4, 27.6, 27.2; ESI-MS: [*M* + H]<sup>+</sup> for C<sub>45</sub>H<sub>91</sub>N<sub>10</sub>O<sub>10</sub>, 931.69; found, 931.9.

### c) Functionalization of GO

**General procedure for preparation of TEG conjugates:** To a suspension of GO (20 mg) in MilliQ® endotoxin free water (20 mL) sonicated for 5 min in a water bath, 2,2'-(ethylenedioxy)bis(ethylamine) (TEG) (20 mg, 0.135 mmol) was added. The reaction mixture was stirred for 3 days. After centrifugation (5000 rpm, 25 min), the precipitate was dispersed in H<sub>2</sub>O, sonicated in a water bath for a few minutes, and centrifuged. This sequence was repeated until the pH of the supernatant was neutral. The functionalized GO was dialyzed against milliQ® endotoxin free water (Spectra/Por® dialysis membrane MWCO 12000–14000 Da) for 3 days and then lyophilized.

**General procedure for preparation of GOs-Q:** To a suspension of GO (10 mg) in dry DMF (10 ml) sonicated in a water bath for 10 min, quaternary amine Q (10 mg, 0.05 mmol) and DIPEA (0.3 ml) were added. The reaction mixture was stirred for 3 days. GO was separated from the solvent through filtration (0.1 μm PTFE membrane). The recovered sample was

dispersed in DMF, sonicated in a water bath for a few minutes and filtrated. This work-up sequence was repeated twice with DMF, twice with MeOH, and twice with DCM. The functionalized GO was then followed the Boc deprotection procedure.

**General procedure for preparation of GOs-D<sub>1</sub> and GOs-D<sub>2</sub>:** To a suspension of GO (10 mg) in dry DMF (10 ml) sonicated in a water bath for 10 min, dendrons D<sub>1</sub> or D<sub>2</sub> (10 mg) was added. The reaction mixture was stirred for 3 days. GO was separated from the solvent through filtration (0.1 μm PTFE membrane). The recovered sample was dispersed in DMF, sonicated in a water bath for a few minutes and filtrated. This work-up sequence was repeated twice with DMF, twice with MeOH, and twice with DCM. The functionalized GO was then followed the Boc deprotection procedure.

**General procedure for preparation of GOs-ct<sub>1</sub> and GOs-ct<sub>2</sub>:** A suspension of GO (10 mg) in dry DMF (10 ml) sonicated in a water bath for 10 min and stirred for 3 days (in case of GOs-ct<sub>1</sub>, 0.3 ml of DIPEA was added to hance the same condition as the preparation of GOs-Q). GO was then separated from the solvent through filtration (0.1 μm PTFE membrane). The recovered sample was dispersed in DMF, sonicated in a water bath for a few minutes and filtrated. This work-up sequence was repeated twice with DMF, twice with MeOH, and twice with DCM. The control GOs was then followed the Boc deprotection procedure.

**General procedure for Boc deprotection:** GO possessing Boc protecting groups (10 mg) were suspended in 3 ml of trifluoroacetic acid in 3 ml of dichloromethane and sonicated in a water bath for 5 min. The reaction mixture was stirred 2 h at room temperature. GO were filtered on a PTFE membrane (0.1 μm). The solid recovered on the filter was dispersed in DMF, sonicated in a water bath for few min, and filtered on a PTFE membrane (0.1 μm). This sequence was repeated twice with DMF, twice with MEOH, twice with DCM and then GO was dried under vacuum. After that, GO was dispersed in milliQ® endotoxin free water and dialyzed against milliQ® endotoxin free water using a Spectra/Por® dialysis membrane (MWCO 12000–14000 Da) for 3 days and then lyophilized.

**General procedure for preparation of PEI conjugates:** To a suspension of GO (20 mg) in milliQ® endotoxin free water (20 mL) sonicated for 5 min in a water bath, PEI (20 mg, 0.025 mmol) was added. The reaction mixture was stirred for 3 days. After centrifugation (5000 rpm, 25 min), the precipitate was dispersed in H<sub>2</sub>O, sonicated in a water bath for a few minutes, and

centrifuged. This sequence was repeated until the pH of the supernatant was neutral. The functionalized GO was dispersed in MilliQ® endotoxin free water and dialyzed against milliQ® endotoxin free water (Spectra/Por® dialysis membrane MWCO 12000–14000 Da) for 3 days and then lyophilized.

#### **Evaluation of siRNA/GOs complexation by agarose gel electrophoresis mobility assay**

Double-stranded Yakima-labeled siRNA (Eurogentec, MW=12285.7 g/mol) was diluted in RNase-free water in order to have a final concentration of 0.1 mg of siRNA in 1 ml of solution. siRNA amount is kept constant at 2 µl in every mass ratio. The suspensions of GOs, aminated GOs in MilliQ® RNase-free water were prepared in corresponding to each mass ratio GO/siRNA required for the complexation with siRNA. The suspensions were left at room temperature for 30 min to allow the formation of the complexes. After staining with Orange DNA loading dye (6X, Thermo Fisher Scientific) (total loading sample volume = 30 µL), the suspensions were added to 2% agarose containing GelRed (Biotium, USA) followed by electrophoresis in Tris-Acetate-EDTA (TAE) buffer at 100 mV for 30 min. The gels were then visualized under UV light using the Gel Doc™ EZ Imager - Bio-Rad and Image lab software. The signal of each experiment was normalized to the signal of the free siRNA as a control and subtracted by the background signal by using ImageJ program. Each experiment was repeated at least three times.

### 3.6 Bibliography

- (1) Goldman, C.; Soroceanu, L.; Smith, N.; Gillespie, G.; Shaw, W.; Burgess, S.; Bilbao, G.; Curiel, D. In Vitro and in Vivo Gene Delivery Mediated by a Synthetic Polycationic Amino Polymer. *Nat. Biotechnol.* **1997**, *15*, 462–466.
- (2) Putnam, D.; Gentry, C. A.; Pack, D. W.; Langer, R. Polymer-Based Gene Delivery with Low Cytotoxicity by a Unique Balance of Side-Chain Termini. *Proc. Natl. Acad. Sci. USA* **2001**, *98*, 1200–1205.
- (3) Xiang, Y.-Z.; Feng, Z.-H.; Zhang, J.; Liao, Y.-L.; Yu, C.-J.; Yi, W.-J.; Zhu, W.; Yu, X.-Q. Linear Cyclen-Based Polyamine as a Novel and Efficient Reagent in Gene Delivery. *Org. Biomol. Chem.* **2009**, *8*, 640–647.
- (4) Antonia Herrero, M.; Toma, F. M.; Al-Jamal, K. T.; Kostarelos, K.; Bianco, A.; Da Ros, T.; Bano, F.; Casalis, L.; Scoles, G.; Prato, M. Synthesis and Characterization of a Carbon Nanotube-Dendron Series for Efficient siRNA Delivery. *J. Am. Chem. Soc.* **2009**, *131*, 9843–9848.
- (5) Al-Jamal, K. T.; Toma, F. M.; Yilmazer, A.; Ali-Boucetta, H.; Nunes, A.; Herrero, M.-A.; Tian, B.; Eddaoudi, A.; Eddaoui, A.; Al-Jamal, W. T.; *et al.* Enhanced Cellular Internalization and Gene Silencing with a Series of Cationic Dendron-Multiwalled Carbon nanotube:siRNA Complexes. *FASEB J.* **2010**, *24*, 4354–4365.
- (6) Battigelli, A.; Wang, J. T. W.; Russier, J.; Da Ros, T.; Kostarelos, K.; Al-Jamal, K. T.; Prato, M.; Bianco, A. Ammonium and Guanidinium Dendron-Carbon Nanotubes by Amidation and Click Chemistry and Their Use for siRNA Delivery. *Small* **2013**, *9*, 3610–3619.
- (7) Wiseman, J. W.; Goddard, C. a; McLelland, D.; Colledge, W. H. A Comparison of Linear and Branched Polyethylenimine (PEI) with DCChol/DOPE Liposomes for Gene Delivery to Epithelial Cells in Vitro and in Vivo. *Gene Ther.* **2003**, *10*, 1654–1662.
- (8) Godbey, W. T.; Wu, K. K.; Mikos, A. G. Tracking the Intracellular Path of poly(ethylenimine)/DNA Complexes for Gene Delivery. *Proc. Natl. Acad. Sci. U. S. A.* **1999**, *96*, 5177–5181.
- (9) Godbey, W. T.; Wu, K. K.; Mikos, A. G. Poly(ethylenimine) and Its Role in Gene Delivery. *J. Control. Release* **1999**, *60*, 149–160.
- (10) Zhang, L.; Lu, Z.; Zhao, Q.; Huang, J.; Shen, H.; Zhang, Z. Enhanced Chemotherapy Efficacy by Sequential Delivery of siRNA and Anticancer Drugs Using PEI-Grafted Graphene Oxide. *Small* **2011**, *7*, 460–464.
- (11) Zhang, Y.; Hu, Z.; Qin, H.; Wei, X.; Cheng, K.; Liu, F.; Wu, R.; Zou, H. Highly Efficient Extraction of Cellular Nucleic Acid Associated Proteins in Vitro with Magnetic Oxidized Carbon Nanotubes. *Anal. Chem.* **2012**, *84*, 10454–10462.
- (12) Kim, S.; Zhou, S.; Hu, Y.; Acik, M.; Chabal, Y. J.; Berger, C.; de Heer, W.; Bongiorno, A.; Riedo, E. Room-Temperature Metastability of Multilayer Graphene Oxide Films. *Nat. Mater.* **2012**, *11*, 544–549.

- (13) Paci, J. T.; Belytschko, T.; Schatz, G. C. Computational Studies of the Structure, Behavior upon Heating, and Mechanical Properties of Graphite Oxide. *J Phys Chem C* **2007**, *111*, 18099–18111.
- (14) Kumar, P. V.; Bardhan, N. M.; Tongay, S.; Wu, J.; Belcher, A. M.; Grossman, J. C. Scalable Enhancement of Graphene Oxide Properties by Thermally Driven Phase Transformation. *Nat. Chem.* **2013**, *6*, 151–158.
- (15) E.Kaiser; R.L.Colescott; C.D.Bossinger; P.I.Cook. Color Test for Detection of Free Terminal Amino Groups in the Solid-Phase Synthesis of Peptides. *Anal. Biochem.* **1970**, *34*, 595–598.
- (16) Virender, K. S.; H.Kent, S. B.; P.Tam, J.; R.B.Merrifield. Quantitative Monitoring of Solid-Phase Peptide Synthesis by the Ninhydrin Reaction. *Anal. Biochem.* **1981**, *117*, 147–157.
- (17) Rheiner, S.; Bae, Y. Increased Poly(ethylene Glycol) Density Decreases Transfection Efficacy of siRNA/poly(ethylene Imine) Complexes. *AIMS Bioeng.* **2016**, *3*, 454–467.
- (18) Vacchi, I. A.; Spinato, C.; Raya, J.; Bianco, A.; Ménard-Moyon, C. Chemical Reactivity of Graphene Oxide towards Amines Elucidated by Solid-State NMR. *Nanoscale* **2016**, *8*, 13714–13721.
- (19) Szabó, T.; Berkesi, O.; Forgó, P.; Josepovits, K.; Sanakis, Y.; Dimitris, P.; Imre, D. Evolution of Surface Functional Groups in a Series of Progressively Oxidized Graphite Oxides. *Chem. Mater.* **2006**, *18*, 2740–2749.
- (20) Park, J. S.; Na, H.-K.; Min, D.-H.; Kim, D.-E. Desorption of Single-Stranded Nucleic Acids from Graphene Oxide by Disruption of Hydrogen Bonding. *Analyst* **2013**, *138*, 1745–1749.
- (21) Makharza, S.; Cirillo, G.; Bachmatiuk, A.; Ibrahim, I.; Ioannides, N.; Trzebicka, B.; Hampel, S.; Rummeli, M. H. Graphene Oxide-Based Drug Delivery Vehicles: Functionalization, Characterization, and Cytotoxicity Evaluation. *J. Nanopart. Res.* **2013**, *15*, 2099.
- (22) Pastorin, G.; Wu, W.; Wieckowski, S.; Briand, J.-P.; Kostarelos, K.; Prato, M.; Bianco, A. Double Functionalisation of Carbon Nanotubes for Multimodal Drug Delivery. *Chem. Commun.* **2006**, 1182–1184.
- (23) Battigelli, A.; Ménard-Moyon, C.; Bianco, A. Carbon Nanomaterials as New Tools for Immunotherapeutic Applications. *J. Mater. Chem. B* **2014**, *2*, 6144–6156.



## CHAPTER 4: GRAPHENE OXIDE SIZE AND OXIDATION DEGREE GOVERN ITS SUPRAMOLECULAR INTERACTIONS WITH siRNA

### 4.1 Introduction

In gene therapy, especially gene silencing, the development of effective and non-toxic delivery systems is crucial to overcome the barrier between siRNA promises and its therapeutic applications. Graphene and its derivatives have attracted increasing interest as a prominent potential vector in gene delivery.<sup>1</sup> The study of the interactions of GO with nucleic acids has been substantially enhanced over the past few years for the application in biosensing, diagnostics and biomedicine.<sup>2</sup> Generally, the binding between GO and single strand DNA or single strand RNA is ascribed either to the  $\pi$ - $\pi$  stacking or the hydrogen bonding and van der Waals forces. However, understanding deeply how the conformation of double strand siRNA is affected by GO remains ambiguous. A thorough comprehension of the mechanism of interaction between graphene materials and siRNA is crucial for design a novel platform with an efficient capacity of delivery of nucleic acids.

### 4.2 Objectives of this chapter

For these reasons, we performed various spectroscopic investigations demonstrating that non-functionalized GO significantly alters the double strand native structure. We focused on how GO size, oxygenated groups present on the surface and chemical functionalization affect the double helix siRNA structure, using gel electrophoresis, UV-Vis spectroscopy, fluorescence resonance energy transfer (FRET) and circular dichroism (CD). In particular, small GO flakes seem to intercalate inside the double strand, breaking some of the base-to-base hydrogen bonds (H-bonds). On the other side, large GO flakes alter mainly the secondary structure geometry interacting mostly with the helix groove and causing the winding angle relaxation. Interestingly, PEI functionalized GO is able to avoid siRNA double strand structural modifications and to sensibly enhance siRNA adsorption onto GO sheets. Finally, the *in vitro* test on delivery of siRNA into HeLa cells using both non-functionalized and PEI functionalized graphene materials as a vehicle will be discussed.

### 4.3 Results and discussion

This chapter is divided in two main parts: part A investigates on the interaction of our materials and siRNA, while part B presents preliminary biological test *in vitro*.



## PART A: Investigations on the interaction of graphene materials with siRNA: complexation or denaturation?

The aim of this part was to elucidate the mechanism of interaction between siRNA molecules and GO flakes. For this purpose, lateral size, oxygenated groups and functionalization effects were taken into consideration. From the series of prepared samples presented in Chapter 2 and Chapter 3, I decided to use the two starting GO<sub>S</sub> and GO<sub>L</sub>, the two hydrothermal reduced rGO<sub>S</sub>-5d and rGO<sub>L</sub>-5d, the two reepoxidized reduced rGO<sub>S</sub>-5d-O<sub>3</sub> and rGO<sub>L</sub>-5d-O<sub>3</sub>, and their PEI functionalized conjugates. Table 4.1 reports the list of the different samples (with their corresponding C/O ratio and N% that were presented in previous chapters) tested for siRNA binding.

**Table 4.1.** Different GO materials used in this study, and C/O ratio of non-functionalized GO obtained by XPS analysis.

	Small GO			Large GO		
	Starting material	Hydrothermal reduction	Epoxidation	Starting material	Hydrothermal reduction	Epoxidation
Non-functionalized (C/O ratio)	GO <sub>S</sub> (2.2 ± 0.1)	rGO <sub>S</sub> -5d (3.5 ± 0.2)	rGO <sub>S</sub> -5d-O <sub>3</sub> (2.6 ± 0.1)	GO <sub>L</sub> (2.6 ± 0.1)	rGO <sub>L</sub> -5d (6.1 ± 0.1)	rGO <sub>L</sub> -5d-O <sub>3</sub> (3.5 ± 0.1)
PEI conjugates (N%)	GO <sub>S</sub> -PEI (7.4 N%)	rGO <sub>S</sub> -5d-PEI (5.9 N%)	rGO <sub>S</sub> -5d-O <sub>3</sub> -PEI (10.1 N%)	GO <sub>L</sub> -PEI (5.8 N%)	rGO <sub>L</sub> -5d-PEI (6.3 N%)	rGO <sub>L</sub> -5d-O <sub>3</sub> -PEI (9.5 N%)

### A1. Complexation of starting GO materials with siRNA

In Chapter 3, I showed that, when GO was functionalized with PEI, the interaction was guided by the polymer chains while the residual oxygenated groups rather acted to hamper the siRNA complexation. In this chapter, I investigated the interaction of the starting non-functionalized graphene materials with siRNA. Does the electrostatic charge play an essential role as the main driving force of the interaction of graphene materials with siRNA? Hence, the complexation of siRNA with the non-functionalized GO<sub>S</sub> and GO<sub>L</sub> series was analyzed using again the method of gel retardation assay. The complexation of the non-functionalized graphene materials possessing different size and oxygen degree with siRNA at different mass ratio is presented in Figure 4.1. A lower amount of free siRNA, measured after interaction with graphene materials, corresponded to a higher complexation ability.

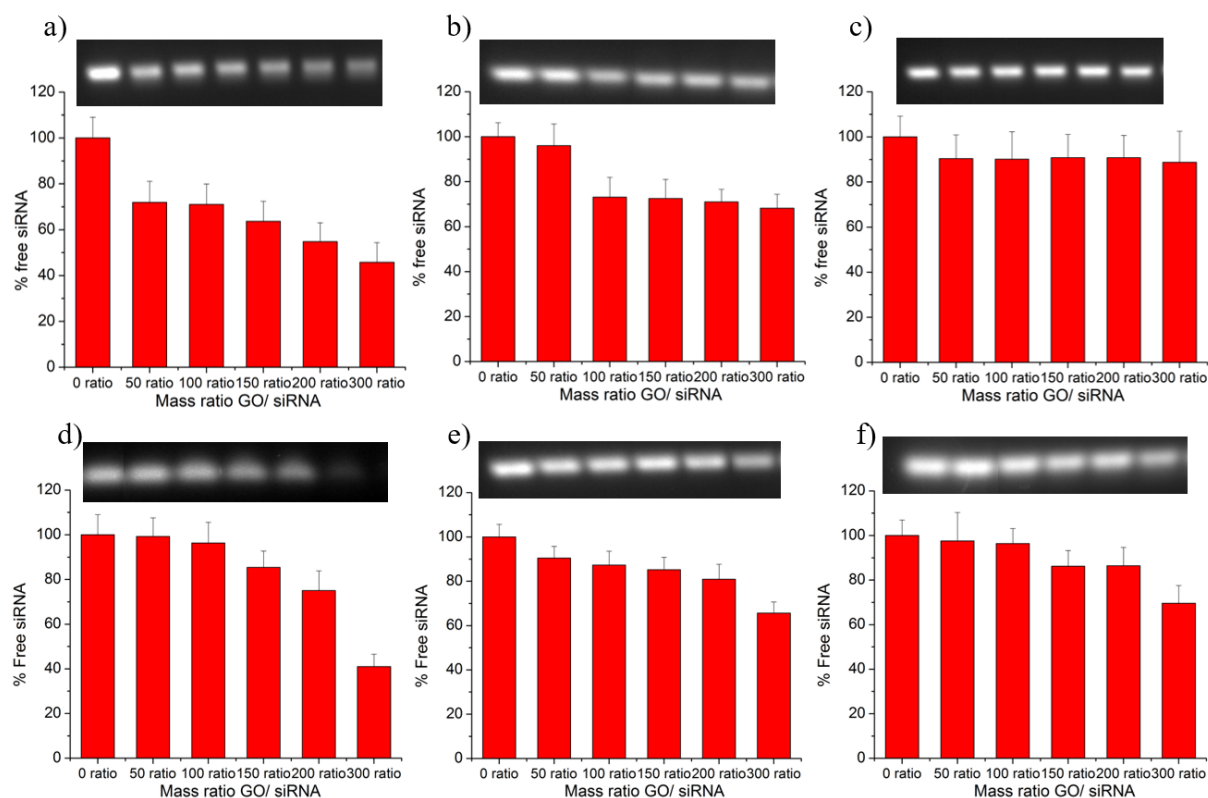


**Figure 4.1:** Complexation of GO<sub>S</sub> and GO<sub>L</sub> with siRNA:(a) GO<sub>S</sub>, b) rGO<sub>S</sub>-5d, c) rGO<sub>S</sub>-5d-O<sub>3</sub>, (d) GO<sub>L</sub>, e) rGO<sub>L</sub>-5d, f) rGO<sub>L</sub>-5d-O<sub>3</sub>) at different GO/siRNA mass ratios. Top: image of the electrophoresis gel; bottom: histograms showing the free siRNA signal at different GO/siRNA mass ratios.

Considering a mass ratio of 200, among the GO<sub>S</sub> series, the GO<sub>S</sub> exhibits the highest complexation ability with  $55 \pm 8\%$  of free siRNA detected, while the hydrothermally (rGO<sub>S</sub>-5d) and ozone treated (rGO<sub>S</sub>-5d-O<sub>3</sub>) have a lower interaction capacity, with  $71 \pm 5\%$  and  $90 \pm 9\%$  of free siRNA measured, respectively. Among the GO<sub>L</sub> series, the GO<sub>L</sub>, rGO<sub>L</sub>-5d, and rGO<sub>L</sub>-5d-O<sub>3</sub> show  $67 \pm 9\%$ ,  $81 \pm 7\%$ , and  $86 \pm 8\%$  of free siRNA, respectively. It is interesting that an increasing trend of complexation ability follow:  $GO > rGO-5d > rGO-5d-O_3$ , independent of their size.

Since reduction and epoxidation treatments mainly affect the graphene surface, the complexation trend may be explained by comparing the amount of oxygenated groups present on each GO sheet. As mentioned in Chapter 3, the interaction between GO and siRNA can be governed by  $\pi$ - $\pi$  stacking or by polar interaction between the oxygen moieties on GO and the polar groups on the nucleotide strands. Moreover, GO surface has many H-bond donors (alcohols and carboxylic acids) and acceptors (epoxides). Hence, when some oxygenated

groups on the surface of GO were removed after the hydrothermal treatment, rGO-5d exerted a lower complexation ability than GO. For this reason, the interaction between GO and siRNA strands is likely driven mostly by the H-bond interactions. The re-epoxidation of rGO-5d is not able to restore the affinity of the complexation ability of GO. Most probably, the introduced epoxy groups than can act only as H-bond acceptors are not able to efficiently increase the binding of siRNA molecules. Interestingly, no smears were detected in any gel electrophoresis test of any non-functionalized and functionalized materials, even at high mass ratios, suggesting that no double strand cleavage was occurring.

## **A2. Spectroscopic investigations on the interaction of graphene materials with siRNA**

Following these results, we aimed to clarify the supramolecular interaction of GO with siRNA molecules, and in particular to understand if GO can alter the conformation of the native siRNA. For this purpose, we had to overcome some spectroscopic characteristics of GO: for instance, GO displays a high absorbance below 300 nm in UV-Vis spectra.<sup>3</sup> In addition, GO is a good acceptor that can efficiently quench many dyes and therefore may interfere with many optical spectroscopies. Such interferences make the study of the interaction between GO and other molecules complicate. For these reasons, we decided to investigate the siRNA conformational changes after removing the GO from the solution. More precisely, after performing the incubation of siRNA with GO, we filtered the GO complex and collected the free siRNA molecules after the interaction with GO. Initially, we optimized the conditions in order to avoid the passage of the non-functionalized and functionalized graphene materials through the filters, confirmed by the absence of absorbance at 230 nm. In addition, we demonstrated that siRNA molecules are able to easily pass the filters by measuring their absorbance at 260 nm before and after filtration. Filtered siRNA solutions have been also used as a reference for all the experiments to avoid any effect of this treatment on the siRNA conformational stability. The GO/siRNA mass ratio was another crucial parameter to take into consideration. Indeed, a low mass ratio may not induce significant changes in siRNA structure, while a too high mass ratio would favor the complexation leaving a low amount of free siRNA passing the filter, likely not detectable by UV-Vis spectroscopy. Generally, the GO/siRNA mass ratio used for *in vitro* experiments is between 10 and 50.<sup>4</sup> We decided to perform our experiments at mass ratio of 20. This value reflects a good compromise between the complexing ratios found in the literature and the scope of our study. Only GO<sub>L</sub>-PEI was used at mass ratio of 5 because of its high siRNA complexation ability.

Considering all these parameters, we initially analyzed the UV-Vis spectra of free siRNA after complexation with the different GO. The absorbance bands of dsRNA are very sensitive to intramolecular H-bonding cleavage.<sup>5</sup> In particular, it was reported that the nucleotide unpairing in dsRNA nucleobases induces a hyperchromic effect of the band centered at 260 nm that can be easily detected by UV-Vis spectroscopy. To study if our GO materials were able to induce unpairing of nucleobases, we used siRNA labeled with the Yakima Yellow (YY) dye. The calibration curve of siRNA was performed using the YY absorbance at 522 nm and the nucleobase absorbance at 260 nm (Figure 4.2a and b). The YY absorbance is proportional to the real concentration of siRNA molecules in solution while the siRNA absorbance at 260 nm may be affected by the base unpairing.<sup>5</sup> After interaction with the different GO, the free siRNA was collected and analyzed by UV-Vis. The concentration of free siRNA was measured using the YY absorbance. The hyperchromicity was calculated considering the percentage of increase of the siRNA absorbance at 260 nm after contact with GO and the siRNA absorbance, at the same concentration, estimated from the YY calibration curve. Figure 4.2c clearly shows the hyperchromic effect occurring when siRNA is in contact with GO<sub>S</sub>, while the functionalization with PEI does not affect the intensity of the maximum at 260 nm. A similar trend was also observed for the GO<sub>L</sub> series.

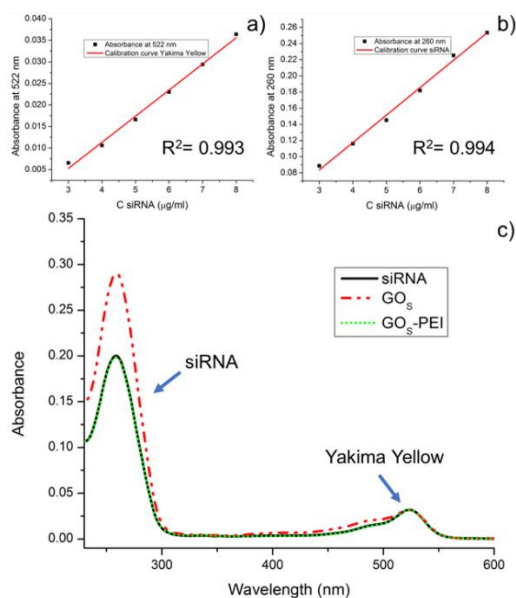


**Figure 4.2.** UV-Vis analyses of siRNA. a) Calibration curve of Yakima Yellow signal at 522 nm; b) calibration curve of siRNA signal at 260 nm; c) UV-Vis spectra at the same concentration (corresponding to same absorbance intensity at 522 nm) of the starting siRNA (black line), siRNA after incubation with GO<sub>S</sub> (dash-dot red line) and siRNA after incubation with GO<sub>S</sub>-PEI (dot green line).

The data, obtained from the UV-Vis analysis, for the different GO are summarized in Figure 4.3. Non-functionalized small GO series ( $GO_S$ ,  $rGO_S$ -5d and  $rGO_S$ -5d- $O_3$ ) induced a high hyperchromicity reaching intensities higher than 55%, without an appreciable difference among the different GO (Figure 4.3a). PEI functionalization of small GO samples was able to instead remarkably reduce the hyperchromic effect. Similar results were found for the large GO samples. Non-functionalized  $GO_L$ ,  $rGO_L$ -5d and  $rGO_L$ -5d- $O_3$  afforded hyperchromic effect higher than 25%. Even in this case, hyperchromic effect was almost completely suppressed after PEI functionalization. Comparing the non-functionalized  $GO_S$  and  $GO_L$  samples, we can see that small GO destabilizes the double strands of siRNA more than large GO. This behavior can be attributed mainly to an effect of size. Indeed, it has been already demonstrated that small GO can intercalate into DNA breaking the H-bonds inside the double strands.<sup>6,7</sup> Most probably, smaller GO flakes can intercalate more easily into DNA nucleobases than larger GO, thus inducing more damages on the double strand structure. There are no evident trends comparing the amount of oxygenated groups on the GO surface. Intercalation seems instead driven by the GO size.

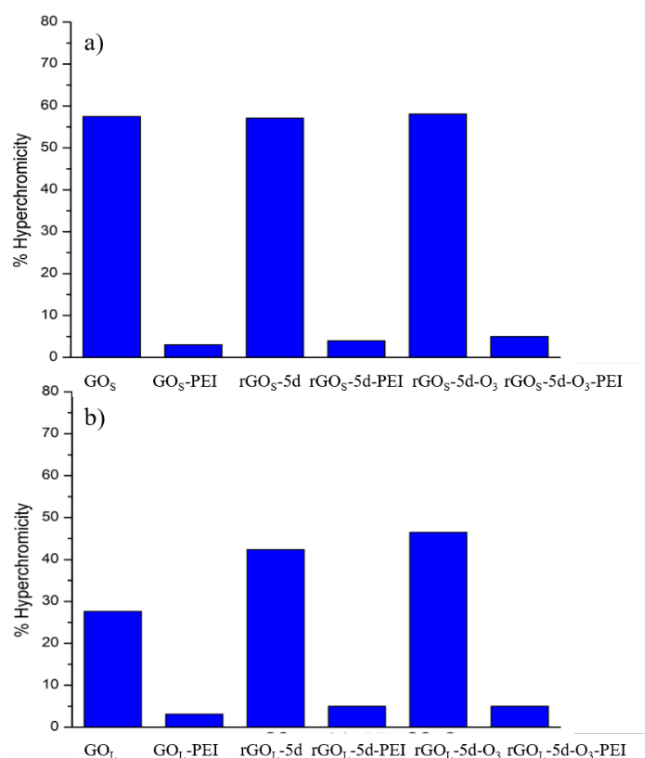


**Figure 4.3.** Hyperchromicity values of siRNA at 260 nm after incubation with the different GO and PEI conjugates. The reported data are obtained from two sets of measurements.





Interestingly, PEI functionalized GO samples exert a negligible H-bonding cleavage with a hyperchromic percentage lower than 5%. This effect is likely due to the direct interaction of PEI chains that protect the integrity of siRNA double strand.<sup>8</sup>

To better elucidate the mechanism of interaction between the small and large GO, in the next step, we tested the integrity of free siRNA using FRET. For this study, we decided to use a double strand siRNA (termed AA) with one strand labeled in 5' position with Alexa Fluor<sup>®</sup>546 (donor) and the other strand labeled in 5' position with Alexa Fluor<sup>®</sup>647 (acceptor), respectively. As a donor alone, we used a siRNA functionalized in 5' position with Alexa Fluor<sup>®</sup>546. With this donor/acceptor pair we were able to estimate the 5'-5' distance (longitudinal distance) of the siRNA chain (Table 4.2). Another important information was to understand if the strand to strand distance may be affected by the GO interaction. For this set of experiments, we decided to use a second double strand siRNA (termed CC) labeled in 5' position with Cy<sup>®</sup>3 (donor) and the other strand marked in 3' position with Cy<sup>®</sup>5 (acceptor), respectively. As a donor alone, we used a dsRNA functionalized in 5' position with Cy<sup>®</sup>3 (Table 4.2). Each FRET pair and solution of donor alone have been incubated with GO at GO/siRNA mass ratio of 20. After 30 min, the solutions were filtered and analyzed by UV-Vis and fluorescence spectroscopies. FRET efficiency (E) was calculated following the equation (1):<sup>9</sup>

$$E = 1 - \frac{A_D}{A_{DA}} \frac{I_{DA}}{I_D} \quad (1) \quad E = \frac{R_0^6}{R^6 + R_0^6} \quad (2)$$

where  $A_D$  and  $A_{DA}$  are the UV absorbance at the excitation wavelength of the donor (535 nm) alone and of the donor in the presence of the acceptor, respectively, while  $I_D$  and  $I_{DA}$  are the fluorescence intensities of the solution of the donor alone and the donor in the presence of the acceptor at the maximum (570 nm for Alexa Fluor<sup>®</sup>546, and 565 nm for Cy<sup>®</sup>3). The FRET distances (R) have been calculated following equation (2), where R is the distance between the donor and the acceptor, and  $R_0$  is the Förster radius distance that was assumed 3.8 nm for the couple Cy<sup>®</sup>3/Cy<sup>®</sup>5<sup>9</sup> and 7.4 nm for the Alexa Fluor<sup>®</sup>546/Alexa Fluor<sup>®</sup>647 as reported from the provider.<sup>10</sup> Since the FRET efficiency is inversely proportional to the sixth power of the distance R between the donor and the acceptor, the two fluorescent molecules should be in close proximity to allow significant energy transfer. The measured distances are reported in Table 4.2.

**Table 4.2.** Distances measured via FRET on siRNA after interaction with the different GO at mass ratio GO/siRNA of 20: AA and CC distance corresponds to the distance between Alexa Fluor<sup>®</sup>546/Alexa Fluor<sup>®</sup>647 and Cy<sup>®</sup>3/Cy<sup>®</sup>5 labeled siRNA pairs, respectively.

Small GO			Large GO		
	AA distance (nm)	CC distance (nm)		AA distance (nm)	CC distance (nm)
siRNA	8.2±0.1	2.7±0.1	siRNA	8.2±0.1	2.7±0.1
GO <sub>S</sub>	11.0±0.3	5.5±0.7	GO <sub>L</sub>	6.9±0.5	2.9±0.1
GO <sub>S</sub> -PEI	7.6±0.1	2.5±0.1	GO <sub>L</sub> -PEI*	7.5±0.1	2.6±0.1
rGO <sub>S</sub> -5d	10±1	4±1	rGO <sub>L</sub> -5d	8.0±0.3	2.7±0.2
rGO <sub>S</sub> -5d-PEI	7.4±0.3	2.7±0.1	rGO <sub>L</sub> -5d-PEI	7.6±0.1	2.6±0.1
rGO <sub>S</sub> -5d-O <sub>3</sub>	9±1	3.0±0.3	rGO <sub>L</sub> -5d-O <sub>3</sub>	7.6±0.2	2.7±0.1
rGO <sub>S</sub> -5d-O <sub>3</sub> -PEI	7.5±0.1	2.6±0.1	rGO <sub>L</sub> -5d-O <sub>3</sub> -PEI	7.5±0.1	2.6±0.1

\* GO/siRNA mass ratio corresponding to 5

A siRNA molecule can be represented as a nanometric rod with an average size below 10 nm in length and approximately 2 nm in diameter.<sup>11</sup> FRET measurement of native siRNA used in our experiments displayed a longitudinal distance of 8.2±0.1 nm (measuring the AA distance) and a strand to strand distance of 2.7±0.1 nm (measuring the CC distance) (Table 4.2). These values are in full agreement with those found in the literature.<sup>11</sup> The non-functionalized small GO samples display a general enhancement of both lateral and longitudinal distances. In particular, AA distance resulted 11.0±0.3, 10±1 and 9±1 nm for GO<sub>S</sub>, rGO<sub>S</sub>-5d and rGO<sub>S</sub>-5d-O<sub>3</sub>, respectively. The CC distance also increased to 5.5±0.7 nm for GO<sub>S</sub>, and to 4±1 and 3.0±0.3 nm for rGO<sub>S</sub>-5d and rGO<sub>S</sub>-5d-O<sub>3</sub>. No significant differences were instead observed for PEI functionalized small GO<sub>S</sub> in the CC distance, meanwhile the AA distance appears a bit shorter (i.e. 0.6-0.8 nm) (Table 4.2). In the case of large GO<sub>L</sub>, less evident changes in the strand-to-



strand and the longitudinal distances could be observed. The data for  $\text{GO}_L$ ,  $\text{rGO}_L\text{-5d}$  and  $\text{rGO}_L\text{-5d-O}_3$  correspond to  $6.9\pm 0.5$ ,  $8.0\pm 0.3$  and  $7.6\pm 0.2$  nm for AA distances, and to  $2.9\pm 0.1$ ,  $2.7\pm 0.2$  and  $2.7\pm 0.1$  nm for CC distances, respectively. Even in the case of large  $\text{GO}_L$  flakes functionalized with PEI, the interaction with siRNA did not affect the lateral distances, but slightly decreases the longitudinal distance ( $7.5\pm 0.1$  nm for  $\text{GO}_L\text{-PEI}$  and  $\text{rGO}_L\text{-5d-O}_3\text{-PEI}$ , and  $7.6\pm 0.1$  nm for  $\text{rGO}_L\text{-5d-PEI}$ ).

As mentioned before, hyperchromicity analysis gave us some information about the H-bond breaking, while FRET helped to understand the displacement of the RNA strands after interaction with GO. However, neither FRET nor UV allow to describe the secondary structure of the siRNA. To deeply understand the nature of the structural modifications induced by GO, we decided to characterize the siRNA conformation after incubating with GO using circular dichroism. In Figure 4.4, I reported the CD spectra of the siRNA after the process of incubation with GO and filtration.

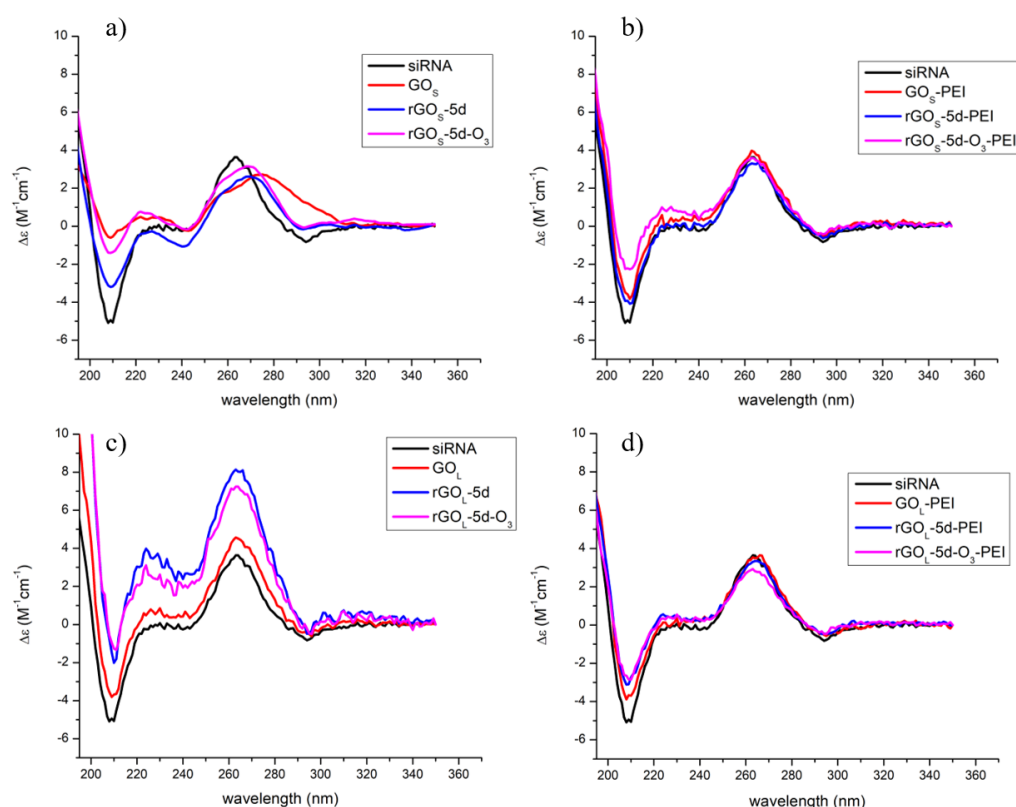


**Figure 4.4.** CD spectra of siRNA after incubation with: a)  $\text{GO}_S$ , b)  $\text{GO}_S\text{-PEI}$ , c)  $\text{GO}_L$ , and d)  $\text{GO}_L\text{-PEI}$ .

Native siRNA CD spectrum (Figure 4.4, black lines) shows a positive band at 264 nm and a negative band at 210 nm, which are typical for the A-helix conformation.<sup>12,13</sup> In particular, the positive band at 264 nm is associated to the stacking interactions between the planar base pairs



and the helical structure of the RNA that induces a chiral environment on the nucleobases, while the negative band centered at 210 nm is related to the A-helix backbone conformation.<sup>14</sup> After contact with small GO<sub>S</sub> flakes, several changes in the CD spectra can be observed (Figure 4.4a). The positive band at 264 nm decreases in intensity with a bathochromic shift of the maximum, while the negative band centered at 210 nm is remarkably reduced in intensity. Comparing the shifts of the positive band, siRNA signal undergoes a shift of  $\approx 15$  nm after interaction with GO<sub>S</sub>, while with rGO<sub>S</sub>-5d and rGO<sub>S</sub>-5d-O<sub>3</sub> the shifts are about 7 nm. This behavior is typically related to the siRNA unfolding and denaturation.<sup>12,15</sup> Instead, the interaction of siRNA with PEI functionalized small GO<sub>S</sub> does not alter the polynucleotide secondary structure (Figure 4.4b) showing only a small decrease of the band at 210 nm. In the case of non-functionalized large GO<sub>L</sub> samples, the CD spectra appear different (Figure 4.4c). Once again, siRNA secondary structure is affected. We measured an enhancement of the band at 264 nm without any significant shift and a little decrease of the negative band at 210 nm. It has been reported before that in duplex RNA, the CD intensity near 260 nm is inversely correlated with the helical winding angle.<sup>16</sup> Similarly, the increasing in the CD intensity induced by the interaction of GO<sub>L</sub> series can be associated with a reduction of the winding angle of the siRNA helix, leading to a modification of the structure in close relation with the FRET analysis. PEI functionalized GO<sub>L</sub> present only small modifications in the 210 nm CD band like in the case of the PEI functionalized GO<sub>S</sub> (Figure 4.4d). All data on siRNA conformation from CD spectroscopy confirmed siRNA strong conformational changes due to the interaction with the different non-functionalized GO.

Combining the results from hyperchromicity, FRET and CD, we can conclude that siRNA presents clear structural modifications after interaction with GO, induced by both small and large size nanosheets. The nature and the type of interactions are however dependent on the GO size. Comparing the two series of non-functionalized small and large GO, the small GO<sub>S</sub> series show a higher hyperchromicity with an enhancement of the lateral and the longitudinal distance. The changes on these parameters demonstrate unambiguously that smaller GO is able to induce more damages in the siRNA structure than the larger one. It has been already reported that GO can intercalate easily into DNA double strands<sup>6</sup> and can cause the cleavage of the duplex. In our study, from electrophoresis we did not observe any smears of the siRNA band (from our previous chapters and in Figure 4.1) indicating that the two RNA strands are still intramolecularly stabilized. In addition, the CD analysis showed that the interaction with small GO<sub>S</sub> samples sensibly decreases the helicity suggesting that double strand denaturation may

occur.<sup>12,15</sup> In this case, there is probably a high intercalation of the small GO<sub>S</sub> flakes leading to a strong unpairing (confirmed by high hyperchromicity) that causes a moderate displacement of the two strands (confirmed by higher FRET distances), and induces the partial transition from A-helix to random coil (lower and shifted helicity at 264 nm) (Figure 4.5a).

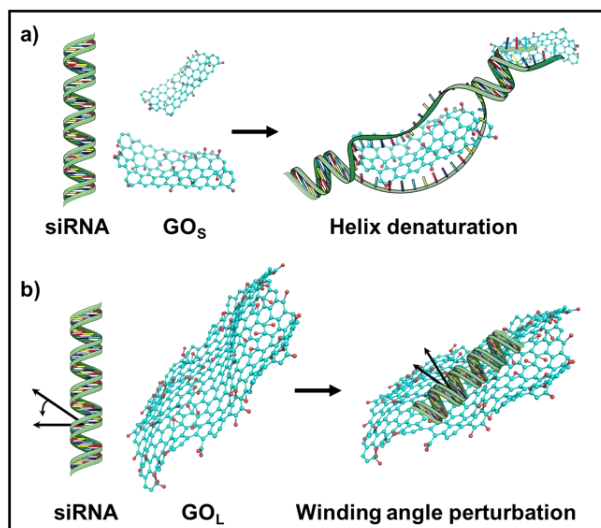


**Figure 4.5** Cartoon of the possible interactions and conformational changes of siRNA molecules in contact with a) GO<sub>S</sub> and b) GO<sub>L</sub>

Within the three small GO specimens, GO<sub>S</sub> shows the highest siRNA destabilization ability, while rGO<sub>S</sub>-5d-O<sub>3</sub> induces more alterations in the native structure than rGO<sub>S</sub>-5d (GO<sub>S</sub> > rGO<sub>S</sub>-5d-O<sub>3</sub> > rGO<sub>S</sub>-5d). This trend can be explained if we consider the functional groups present on the GO surface. In particular, this seems to be correlated to the C/O ratio obtained from XPS (Table 4.1). Destabilization of siRNA with small GO may be triggered by the oxygenated groups. Most probably, these electronegative groups are able to form polar bonds with the nitrogen nucleobases, destabilizing the H-bond between the double strands. In the case of large GO, there is a lower destabilization of the interstrand H-bonds (supported by low hyperchromicity) and a general reduction of the AA distance proved by FRET. On the other hand, CD spectra show an enhancement of the helicity at 264 nm due to a clear interaction with the GO<sub>L</sub> flakes. Most probably, large GO<sub>L</sub> is too big to intercalate between the nucleotides, but it interacts with the RNA groove causing a decrease of the winding angle, thus altering the structure of the double A-helix (Figure 4.5b). The reduction of the winding angle allows the increasing of the number of bases per turn in the helix. This conformational change causes the enhancement of the base to base stacking (increasing the CD band at 264 nm), alters the helix backbone structure (decrease of the CD band at 210 nm), and provokes a helical length shrinking (as shown by FRET analysis). In the case of protein interaction with RNA, it has been proven, by

solving the crystal structure of the complex, that the distortion from the ideal RNA A-helix is due to an interaction on the major groove without any contact with the nucleotides.<sup>17</sup> For the large GO, there is a destabilization of some H-bond between the strands (Figure 4.5), but it is not clear if this behavior is due to a direct interaction of GO with the nucleobases or only with the helix groove. Comparing the differently oxygenated large GO specimens, it appears clear that the rGO<sub>L</sub>-O<sub>3</sub> and rGO<sub>L</sub> induce more changes on the native siRNA conformation than GO<sub>L</sub>. The latter tendency may be again correlated with the amount of oxygenated groups (Table 4.1). In particular, it seems that the oxygenated species avoid the siRNA conformational change. Most probably, the siRNA secondary structure alteration induced by large GO flakes is mediated by non-polar interactions such as  $\pi$ - $\pi$  stacking.

More interestingly, PEI functionalization of both large and small GO does not induce significant changes on the siRNA structure. Only small backbone conformational alterations (slight decrease of 210 nm CD band) were evidenced, most probably due to the interaction between the positively charged PEI chains and the negative phosphate groups in the siRNA skeletal structure.<sup>18</sup> However, these small changes are not yet clear. We hypothesized that the ionic interaction of PEI chains with the phosphate groups partially alter the siRNA backbone geometry causing a small A-helix bending that provoke the decrease of the band at 210 nm in the CD spectra and the small shortening of the 5'-5' distance seen by FRET. Nevertheless, these siRNA small secondary structure modification have been already described in the literature and should not alter the siRNA biological activity *in vitro* or *in vivo*.<sup>18</sup>

In the next step, I will describe the preliminary biological tests *in vitro* to evaluate the ability of both non-functionalized and PEI-functionalized graphene materials as a platform for siRNA delivery.

### **PART B: Internalization and release of siRNA into HeLa cells**

As previously discussed, functionalized GO has become a prominent vector for the shuttling of genetic material into cells. However, the interaction between GO and siRNA molecules have been less explored. Our spectroscopic investigations in part A demonstrated that there is a perturbation of the siRNA secondary structure which was induced by the contact between non-functionalized GO, mainly dependent on the size of flakes. In particular, small sized GO could induce partially A-helix denaturation. In contrast, PEI functionalization not only enhances siRNA molecules adsorption on GO but also protects the double strand RNA from damages.

Our next goal was to assess if the prepared GO materials were able to efficiently internalize and release siRNA into cells.

For this study, we focused our attention on GO produced in the group of Prof. Y. Nishina that shows a remarkable dispersibility in cell culture media, hence being a better candidate for our *in vitro* studies. Indeed, as previously described, the small commercial GOs shows a sensible damage on siRNA structure most probably via intercalation. For this reason, in addition to GO<sub>L</sub> ( $3 \pm 1 \mu\text{m}$ ), which was described above, we decided to prepare a GO with a smaller size than GO<sub>L</sub>, named GO<sub>M</sub> ( $600 \pm 300 \text{ nm}$ ) to evaluate the size effect on the ability of siRNA delivery. This GO<sub>M</sub> has a bigger size than the commercial GOs in order to decrease the damages on the helix structure of siRNA as seen in part A. The lateral size distribution and SEM characterization of GO<sub>M</sub> are presented in Figure 4.6.

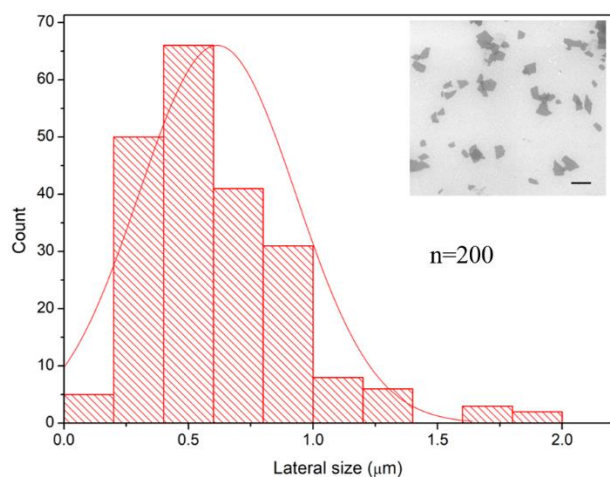


**Figure 4.6:** Lateral size distribution of GO<sub>M</sub>. In the inset: SEM image of GO<sub>M</sub>, scale bar corresponds to 1  $\mu\text{m}$ .

PEI functionalization of GO<sub>M</sub> was also performed and confirmed by XPS (functionalization with 5.4% of N). The complexation of GO<sub>M</sub>-PEI with siRNA was evaluated via gel electrophoresis (Figure 4.7). Again, GO<sub>M</sub>-PEI functionalization is able to complex with siRNA molecules showing a complete complexation at mass ration of 50.

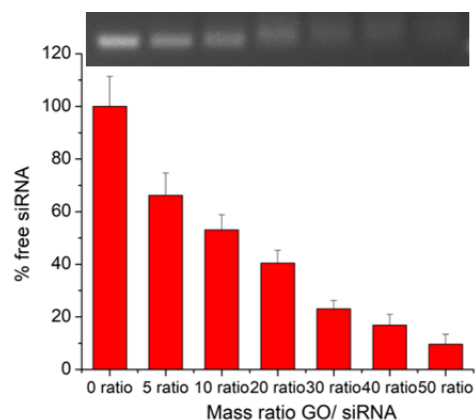


**Figure 4.7:** Complexation with siRNA of GOM-PEI at different mass ratio. Top: image of the electrophoresis gel; bottom: histograms showing the free siRNA signal at different GO/siRNA mass ratios.

The four samples used to assess the efficiency of siRNA delivery into cells are presented in Table 4.3.

**Table 4.3:** List of samples of GO will be used in the following biological test

	Medium GO	Large GO
Size	600±300 nm	3±1 μm
Non-functionalized (C/O ratio)	GO <sub>M</sub> (2.7 ± 0.1)	GO <sub>L</sub> (2.6 ± 0.1)
PEI conjugates (N%)	GO <sub>M</sub> -PEI (5.4 ± 0.1)	GO <sub>L</sub> -PEI (5.8 ± 0.1)

The biological tests were performed *in vitro*, using HeLa as a cellular model for transfection. We aimed to visualize the siRNA uptake and release *via* confocal microscopy using a fluorescently labeled siRNA. When siRNA is complexed to the GO materials, the fluorescence is quenched by the proximity with the nanosheets, but once the genetic material is released the fluorescence is restored. For this set of experiments, we used a concentration of graphene oxides of 50 μg/ml with a siRNA mass ratio corresponding to 20 (meaning 2.5 μg/ml of siRNA). The siRNA was labeled with Cy3 dye as previously described in part A. A kinetic study of 4, 8 and 24 hours was performed and was followed by a staining of the cells with cell mask and DAPI to mark the cell membrane and the nucleus, respectively. After incubation, the cells were analyzed by confocal microscopy. Control experiments are reported in Figure 4.8.

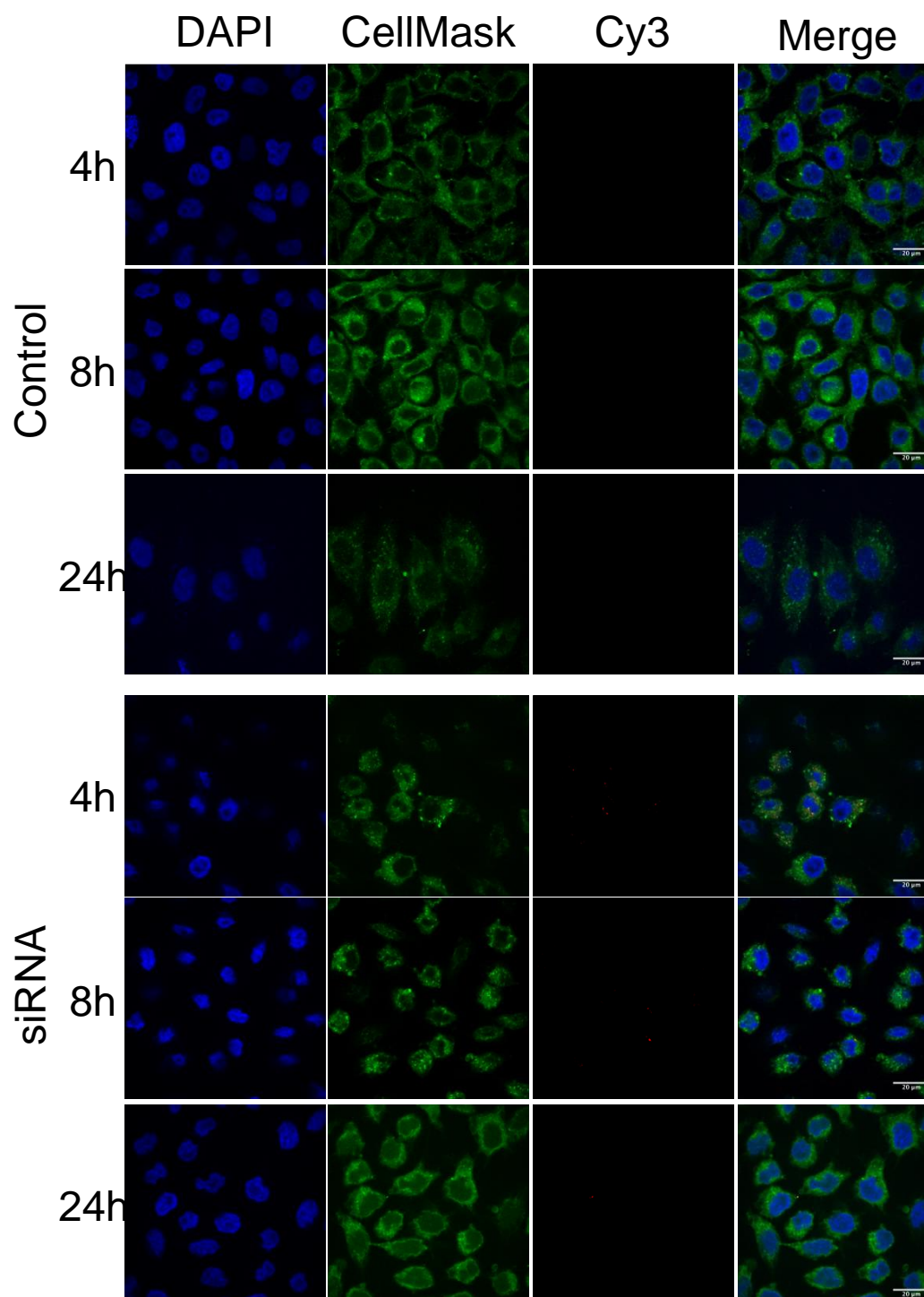


**Figure 4.8:** Confocal images of HeLa cells: on the top control panel; bottom panel of siRNA treated cells. Blue nuclear DAPI staining; green CellMask™ Green Plasma Membrane Stain; red Cy3-siRNA.

As expected, siRNA alone is not able to penetrate inside cell compartments. Some agglomerates can however be visualized, after 4 and 8 h, outside of cell membranes.



The non-functionalized and PEI-functionalized GO materials were also tested, as shown in Figure 4.9. As expected, no detectable luminescence in the red channel (Cy<sub>3</sub>) was recorded for all the GO materials tested. Interestingly, it appears that there is a morphological alteration of the membranes when HeLa cells are incubated with GO<sub>M</sub>-PEI and GO<sub>L</sub>-PEI. This effect can be attributed to the cationic charged polymer chains that can intercalate with the negatively charged membranes.

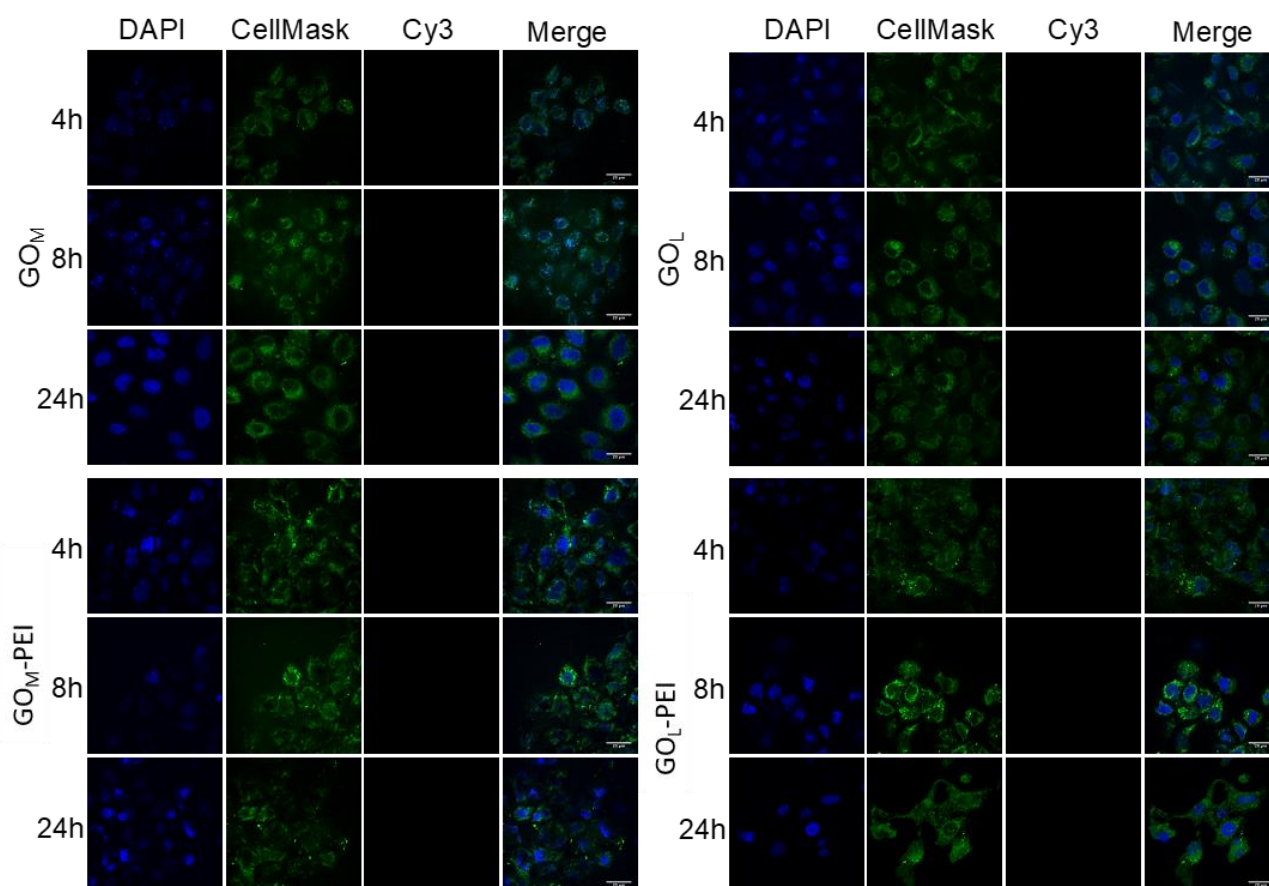


**Figure 4.9:** Confocal image of GO-treated HeLa cells: top left panel GO<sub>M</sub>; top right panel GO<sub>L</sub>, bottom left panel GO<sub>M</sub>-PEI, bottom right panel GO<sub>L</sub>-PEI. Blue nuclear DAPI staining; green CellMask™ Green Plasma Membrane Stain; red Cy<sub>3</sub>-siRNA.

After performing all control and reference samples, the cell treated with GO/siRNA complexes were tested (Figure 4.10).

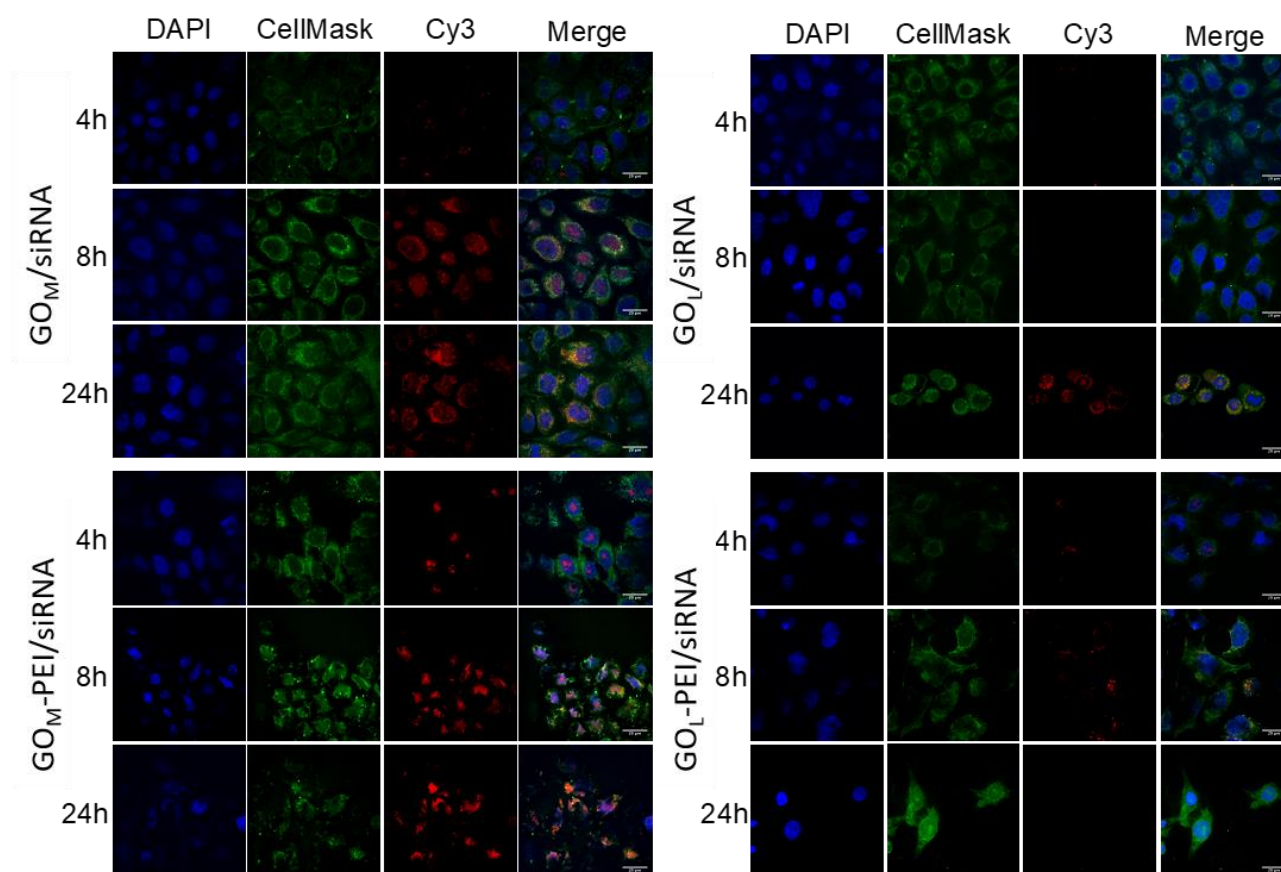


**Figure 4.10:** Confocal image of different GO/siRNA treated HeLa cells: top left panel  $GO_M$ /siRNA; top right panel  $GO_L$ /siRNA, bottom left panel  $GO_M$ -PEI/siRNA, bottom right panel  $GO_L$ -PEI/siRNA. Blue nuclear DAPI staining; green CellMask™ Green Plasma Membrane Stain; red Cy3-siRNA.

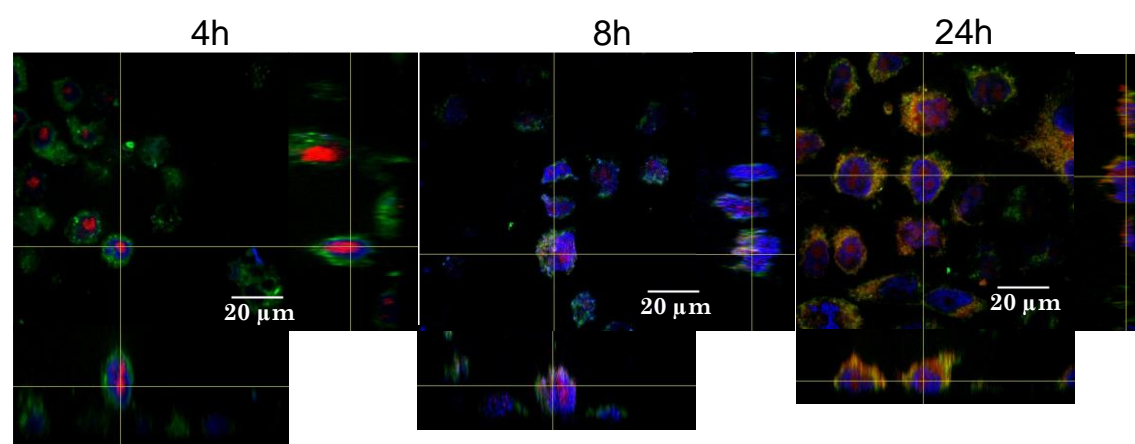
Interestingly, the appearance of a red fluorescence signal confirms the uptake and release of siRNA molecules from all graphene materials. Indeed, in case of  $GO_M$ , there is a modest release already after the first 4 h. Moreover, the co-staining of siRNA and the plasma (orange signal) is observable after 8 h of incubation. After 24 h, the siRNA molecules remain in the cytoplasm as confirmed by the strong red signal detected inside the cells. On the other hand,  $GO_L$  shows a release of siRNA only after 24 h. The red signal corresponding to siRNA desorption from GO is not detected at 4 and 8 h time points. PEI functionalization enhances and accelerates the release of the siRNA. In the case of  $GO_M$ -PEI, there is a strong delivery after the first 4 h and the siRNA seems to be totally released at 8 h.  $GO_L$ -PEI can release siRNA already at 4 h while after 24 h we are not able to detect any red signal.

This kinetic study conveys the idea that the siRNA releasing features are strongly dependent on GO size and functionalization. Indeed,  $GO_M$  is able to deliver siRNA faster than  $GO_L$ . A

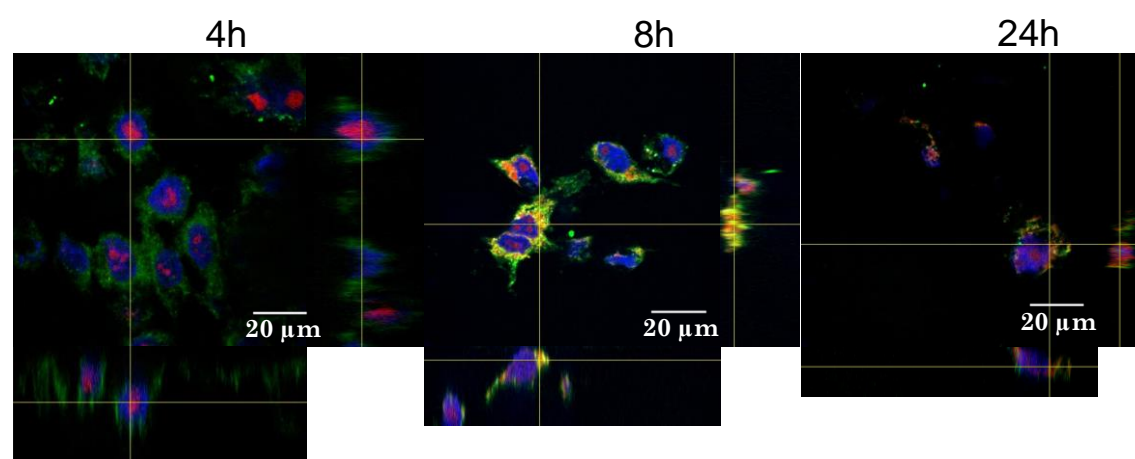


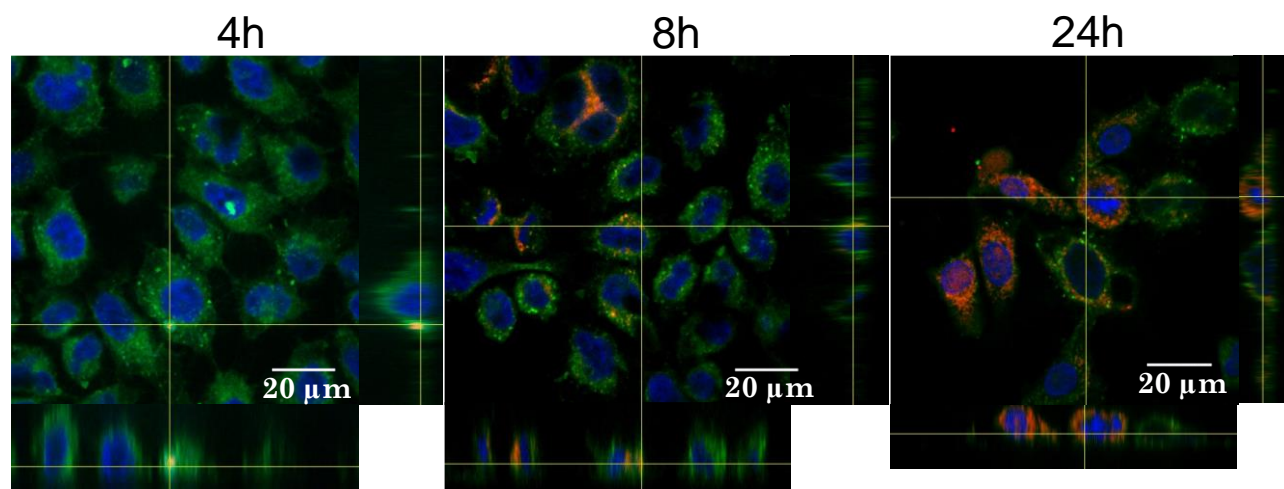
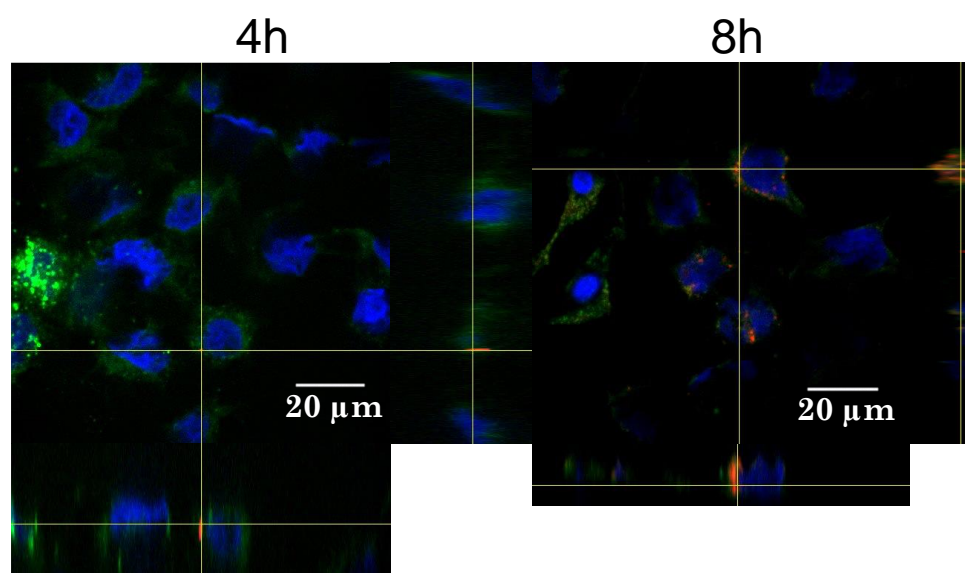
similar trend was also observed in case of PEI-functionalized GO, where we noticed again that the releasing time of GO<sub>L</sub>-PEI is clearly slower than that of GO<sub>M</sub>-PEI. One of the most challenging problem in gene silencing is the delivery of the siRNA into the cytoplasm. In fact, a cell contains different protection systems to avoid the interaction with exogenous genetic material. One of these self-protected systems is the lysosomal degradation pathway.<sup>19</sup> In this case, the siRNA molecules are first compartmentalized into lysosomes where RNases, which are activated at low pH, digest the nucleotide sequence. It is well known that PEI is able to bypass this RNA lysosomal degradation using the proton sponge effect.<sup>20,21</sup> Indeed, PEI, containing many protonatable amine groups, can condense the nucleic acids and resist the acidification of endosome, hence escaping the endosomal vesicles.<sup>21</sup> In our case, we were interested to understand the fate of siRNA in cells: whether siRNA localization is free in the cytoplasm or it is into vesicles. For this reason, z-stacking at the described time points was performed, as shown in Figure 4.11.

#### GO<sub>M</sub>/siRNA



#### GO<sub>M</sub>-PEI/siRNA



**GO<sub>L</sub>/siRNA****GO<sub>L</sub>-PEI/siRNA**

**Figure 4.11:** Confocal image and the z-stacking of different GO/siRNA treated HeLa cells: GO<sub>M</sub>/siRNA, GO<sub>L</sub>/siRNA, GO<sub>M</sub>-PEI/siRNA, and GO<sub>L</sub>-PEI/siRNA at different time points.

In the case of non-functionalized materials GO<sub>M</sub>/siRNA and GO<sub>L</sub>/siRNA, we observe that the siRNA molecules are delivered first into the nucleolus (as highlighted in Figure 4.12) before being diffused freely in the cytoplasm.

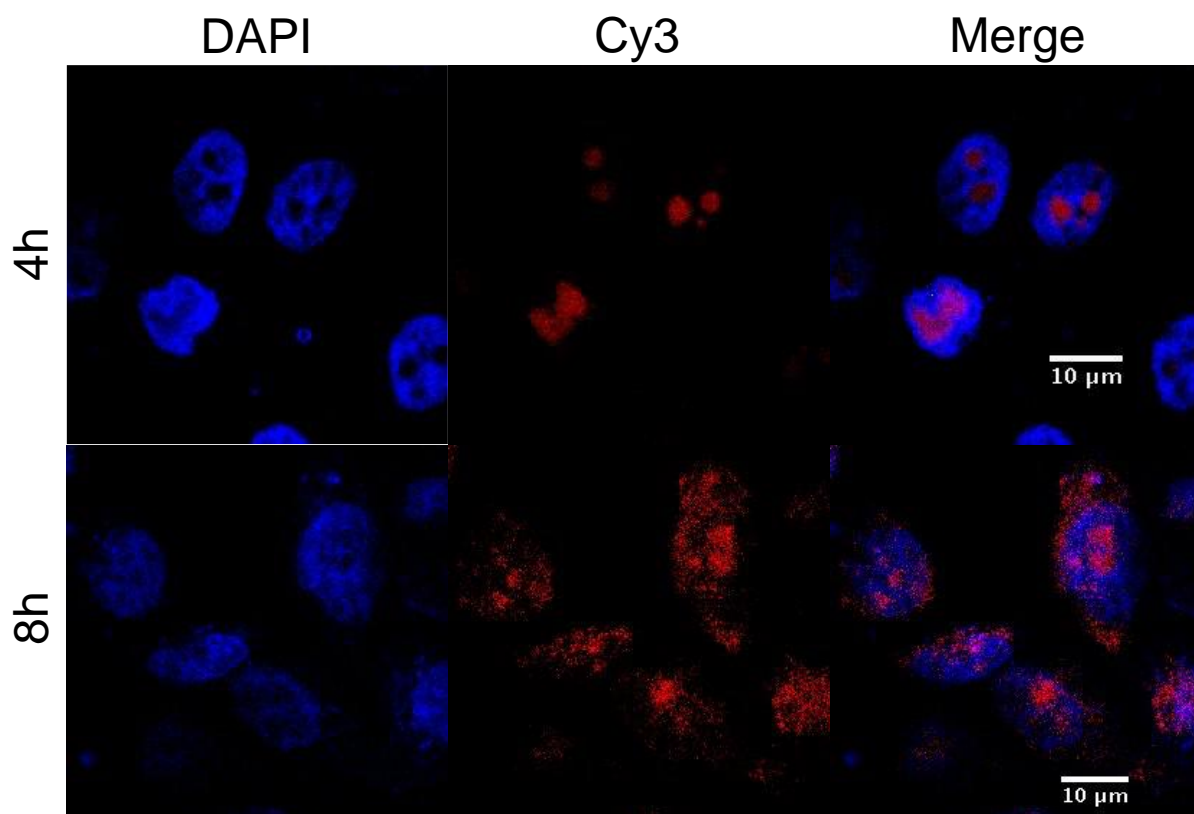


**Figure 4.12:** Confocal image of  $GO_M$ /siRNA treated HeLa cells after 4(top) and 8 (bottom) hours incubation.

Indeed, an intense red siRNA fluorescence was observed only within the nucleolus, which is the region inside the nucleus unstained by DAPI. It has been already proven that nanoparticles are able to modulate the siRNA localization in HeLa cells. In particular, it was found that a high nanomaterial concentration favor the siRNA localization in the nucleoli and in the nucleus after 16 h incubation. This fact is not still well understood but was unambiguously correlated to a decrement of RNAi activity.<sup>22</sup> My results show that the  $GO_M$  series deliver siRNA first in the nucleolar region but then after only 8 h and 24 h the siRNA is mostly present in the perinuclear regions where it can be then sequestered by RISC (RNA induced silencing complex). In case of  $GO_L$ /siRNA, it seems that after 24 h, despite a good distribution of siRNA into the cytoplasm, some siRNA molecules still appear to have a co-localization with the plasma membrane (orange part). For  $GO_M$ -PEI/siRNA, we observe a good cytoplasmic distribution of siRNA right after 4 h. Moreover, we do not see any compartmentalization, indicating that the siRNA molecules are free into the cytoplasm.<sup>23</sup> With  $GO_L$ -PEI/siRNA, the siRNA seems to be released at 4 h, while it occurs at 8 h with  $GO_L$ /siRNA.

In conclusion, in these preliminary cellular tests, we used a random sequence of siRNA to evidence its delivery into the cells. From the *in vitro* test, we succeeded in observing that the siRNA molecules indeed are internalized and released into HeLa cells, in the presence of GO and GO-PEI as a platform for delivery. More interestingly, the siRNA molecules are well-distributed in the nuclear periphery where they can be activated and transformed into active RNAi species. In the next step, a specific sequence of siRNA should be used for testing the efficiency of targeted gene silencing in a specific cell line.

#### 4.4 Conclusions

In summary, we discover that depending on the size and the amount of oxygenated groups, GO can efficiently unwind, displace and partially denature the double siRNA strands. On the other hand, our results also demonstrate that PEI-functionalized GO can overcome a partial denaturation effect of GO after interaction with siRNA, and retain the native polynucleotide conformation. This protecting activity together with its high siRNA complexing capacity makes GO-PEI a promising material for gene delivery and silencing applications. Moreover, we succeeded in figuring out that graphene materials is a suitable platform for delivery of siRNA into cells, with a very good distribution of siRNA into the cytoplasm, by carefully modulating various factors that could affect this process including size and surface functionalization of GO. The mechanism of how siRNA is delivered and if it could exhibit the ability in gene silencing need to be attentively studied in the future.

#### 4.5 Experimental part

##### Materials

GO<sub>M</sub> was prepared by using Jet Milling machine (Star Burst mini) to reduce the size of the GO<sub>L</sub>. siRNA (sUGC-GCU-ACG-AUC-GACGAU-G55) labeled Yakima Yellow; siRNA with one strand labeled in 5' position with Alexa Fluor<sup>®</sup>546; siRNA with one strand labeled in 5' position with Alexa Fluor<sup>®</sup>546 (donor) and the other strand marked in 5' position with Alexa Fluor<sup>®</sup>647 (acceptor); siRNA labeled in 5' position with Cy<sup>®</sup>3; siRNA labeled in 5' position with Cy<sup>®</sup>3 (donor) and the other strand marked in 3' position with Cy<sup>®</sup>5 (acceptor) were purchased from Eurogentec.

**Instruments**

The UV-Vis absorption spectra were recorded on a Cary 5000 UV-Vis-NIR spectrophotometer and were corrected for the baseline and the solvent. Steady-state luminescence experiments were performed with a Fluoromax-4 spectrofluorometer (Horiba-Jobin-Yvon Inc.). The emission spectra were corrected for monochromator and detector efficiency and for the light source intensity (450 W xenon arc lamp), employing standard correction files and recording the reference signal. Circular dichroism spectra have been recorded with J-810 Jasco spectropolarimeter. Each spectrum was recorded at 1 nm resolution after 16 accumulations from 190 to 350 nm. In all measurements using UV, CD or fluorimetry, the temperature of the samples is maintaining at 25°C. Filtration was performed using Sterile Millex® (13mm) filter unit with Durapore® membrane and pore size 0.22 µm.

**Preparation of the solutions for the spectroscopic analyses**

For CD and UV, to 180 µl of siRNA labeled with Yakima Yellow ( $C=0.1 \mu\text{g}/\mu\text{l}$ ,  $m=180 \mu\text{g}$ ), 270 µl of Milli-Q® RNase-free water was added to obtain 450 µl of siRNA solution ( $C'=40 \mu\text{g}/\text{ml}$ ) as a control. A calibration of siRNA signal in UV with concentration from 10 µg/ml to 50 µg/ml was also performed. At mass ratio GO/siRNA equal 20, to 180 µl of siRNA ( $C=0.1 \mu\text{g}/\mu\text{l}$ ,  $m=180 \mu\text{g}$ ), a suspension of 72 µl of GO ( $C=5 \mu\text{g}/\mu\text{l}$ ,  $m=360 \mu\text{g}$ ) and 198 µl of Milli-Q® RNase-free water were added to obtain a solution of siRNA at the same concentration of the control. After the interaction of GO with siRNA, the helicity was calculated normalizing the signal to the cuvette length (0.2 cm) and the molar concentration obtained from the Yakima Yellow signal at 523 nm in the UV.

For the FRET analysis, to 60 µl of each siRNA (siRNA labeled Cy<sub>3</sub>, siRNA labeled Cy<sub>3</sub>/Cy<sub>5</sub>, siRNA labeled Alexa Fluor®546, siRNA labeled Alexa Fluor®546/Alexa Fluor®647,  $C=0.1 \mu\text{g}/\mu\text{l}$ ,  $m=60 \mu\text{g}$ ), 90 µl of Milli-Q® RNase-free water was added to obtain 150 µl of separated siRNA solution ( $C'=40 \mu\text{g}/\text{ml}$ ) as a control. At mass ratio GO/siRNA equal 20, to 60 µl of siRNA ( $C=0.1 \mu\text{g}/\mu\text{l}$ ,  $m=60 \mu\text{g}$ ), a suspension of 24 µl of GO ( $C=5 \mu\text{g}/\mu\text{l}$ ,  $m=120 \mu\text{g}$ ) and 66 µl of Milli-Q® RNase-free water were added to obtain a solution of siRNA at the same concentration of the control. After interaction of siRNA with GO, the filtered siRNA solutions were excited at 535 nm and the maximum was recorded at 570 and 575 nm for Alexa 546 and Cy<sub>3</sub>, respectively. The FRET efficiency was calculated normalizing for the absorbance of each solution at 535 nm (measured by UV-Vis).

**Cell culture**

HeLa cells were seeded in an 8-chamber culture slide (Falcon, Boulogne-Billancourt, France, C354118) at a density of  $1 \times 10^5$  cells/well and incubated over night at 37°C, with 5% CO<sub>2</sub> in culture medium (DMEM (Lonza, Verviers, Belgium, BE12-604F/U1) supplemented with 10% (v/v) fetal bovine serum (Dutscher, Brumath, France), 10mM Hepes (Lonza), 10µg/mL gentamycine (Lonza), 0,05mM β-mercaptoethanol (Invitrogen, Oslo, Norway)) to favor their adherence. Then the medium was removed and GO, GO-PEI, GO/siRNA or GO-PEI/siRNA were added at a concentration of 50 µg/mL in a final volume of 500 µL of the same medium for 4h, 8h or 24h.

**Cell staining and imaging**

After the different incubation time points (4h, 8h, and 24h), the cells were washed twice with tris-buffered saline (TBS) (1×) (50 mM Tris-Cl, pH 7.5. 150 mM NaCl). Then the cells were stained with CellMask™ Green Plasma Membrane Stain (Thermo Fisher Scientific, Illkirch, France, C37608) (diluted 2000× in TBS 1×) for 5 min at 37°C. The cell mask staining solution was then removed and the wells were washed twice with TBS 1× before their fixation with 4% paraformaldehyde buffer and incubated 1 h at 4°C. The cells were once again washed twice after the fixation solution was removed and then stained with DAPI for 10 min at room temperature. In the following step, the cells were washed twice with TBS 1× and the chamber of the slide was removed and after adding Dako Fluorescence Mounting Medium (Glostrup, Denmark, S3023) over each cell preparation, a coverslip was mounted on the slide. The slides were imaged at least 2h later using a spinning disk confocal microscope (Zeiss, Oberkochen, Germany) with an A-Plan 60×/0.8 Zeiss ×60 objective. For z-stacking experiments, the 3D reconstruction of the cells using a z-stack of 0.5 µm, were collected.



#### 4.6 Bibliography

- (1) Cheng, G.; Liu, Y.-L.; Wang, Z.-G.; Zhang, J.-L.; Sun, D.-H.; Ni, J.-Z. The GO/rGO-Fe<sub>3</sub>O<sub>4</sub> Composites with Good Water-Dispersibility and Fast Magnetic Response for Effective Immobilization and Enrichment of Biomolecules. *J. Mater. Chem.* **2012**, *22*, 21998.
- (2) Yang, Y.; Asiri, A. M.; Tang, Z.; Du, D.; Lin, Y. Graphene Based Materials for Biomedical Applications. *Mater. Today* **2013**, *16*, 365–373.
- (3) Shang, J.; Ma, L.; Li, J.; Ai, W.; Yu, T.; Gurzadyan, G. G. The Origin of Fluorescence from Graphene Oxide. *Sci. Rep.* **2012**, *2*, 792.
- (4) Shim, G.; Kim, M.-G.; Park, J. Y. Graphene-Based Nanosheets for Delivery of Chemotherapeutics and Biological Drugs. *Adv. Drug Deliv. Rev.* **2016**, *105*, 205–227.
- (5) Draper, D. E.; Xing, Y.; Laing, L. G. Thermodynamics of RNA Unfolding: Stabilization of a Ribosomal RNA Tertiary Structure by Thiostrepton and Ammonium Ion. *J. Mol. Biol.* **1995**, *249*, 231–238.
- (6) Ren, H.; Wang, C.; Zhang, J. J.; Zhou, X.; Xu, D.; Zheng, J.; Guo, S.; Zhang, J. J. DNA Cleavage System of Nanosized Graphene Oxide Sheets and Copper Ions. *ACS Nano* **2010**, *4*, 7169–7174.
- (7) Zheng, B.; Wang, C.; Wu, C.; Zhou, X.; Lin, M.; Wu, X.; Xin, X.; Chen, X.; Xu, L.; Liu, H.; *et al.* Nuclease Activity and Cytotoxicity Enhancement of the DNA Intercalators via Graphene Oxide. *J. Phys. Chem. C* **2012**, *116*, 15839–15846.
- (8) Chau, N. D. Q.; Reina, G.; Raya, J.; Vacchi, I. A.; Ménard-Moyon, C.; Nishina, Y.; Bianco, A. Elucidation of siRNA Complexation Efficiency by Graphene Oxide and Reduced Graphene Oxide. *Carbon* **2017**, *122*, 643–652.
- (9) Massey, M.; Algar, W. R.; Krull, U. J. Fluorescence Resonance Energy Transfer (FRET) for DNA Biosensors: FRET Pairs and Förster Distances for Various dye–DNA Conjugates. *Anal. Chim. Acta* **2006**, *568*, 181–189.
- (10) <https://www.thermofisher.com/fr/fr/home/references/molecular-probes-the-handbook/tables/r0-values-for-some-alex-fluordyes.html>  
<https://www.thermofisher.com/fr/fr/home/references/molecular-probes-the-handbook/tables/r0-values-for-some-alex-fluor-dyes.htm>. Access August 2017
- (11) Barichello, J. M.; Kizuki, S.; Tagami, T.; Soares, L. A. L.; Ishida, T.; Kikuchi, H.; Kiwada, H. Agitation during Lipoplex Formation Harmonizes the Interaction of siRNA to Cationic Liposomes. *Int. J. Pharm.* **2012**, *430*, 359–365.
- (12) Kypr, J.; Kejnovská, I.; Renciuk, D.; Vorlícková, M. Circular Dichroism and Conformational Polymorphism of DNA. *Nucleic Acids Res.* **2009**, *37*, 1713–1725.
- (13) Cho, I. S.; Kim, J.; Lim, D. H.; Ahn, H.-C.; Kim, H.; Lee, K.-B.; Lee, Y. S. Improved Serum Stability and Biophysical Properties of siRNAs Following Chemical Modifications. *Biotechnol. Lett.* **2008**, *30*, 1901–1908.
- (14) Woody, R. W. Circular Dichroism. *Methods Enzymol.* **1995**, *246*, 34–71.
- (15) Phillips, D. J.; Bobst, A. M. Circular Dichroism Melting Studies on R17 Phage RNA. *Biochem. Biophys. Res. Commun.* **1972**, *47*, 150–156.
- (16) Ucci, J. W.; Kobayashi, Y.; Choi, G.; Alexandrescu, A. T.; Cole, J. L. Mechanism of Interaction of the Double-Stranded RNA (dsRNA) Binding Domain of Protein Kinase R with Short dsRNA Sequences. *Biochemistry* **2007**, *46*, 55–65.
- (17) Ryter, J. M.; Schultz, S. C. Molecular Basis of Double-Stranded RNA-Protein Interactions:

- Structure of a dsRNA-Binding Domain Complexed with dsRNA. *EMBO J.* **1998**, *17*, 7505–7513.
- (18) Merkel, O. M.; Beyerle, A.; Librizzi, D.; Pfestroff, A.; Behr, T. M.; Sproat, B.; Barth, P. J.; Kissel, T. Nonviral siRNA Delivery to the Lung: Investigation of PEG–PEI Polyplexes and Their In Vivo Performance. *Mol. Pharm.* **2009**, *6*, 1246–1260.
- (19) Liang, W.; Lam, J. K. W. Endosomal Escape Pathways for Non-Viral Nucleic Acid Delivery Systems. In *Molecular Regulation of Endocytosis*; InTech, 2012; pp. 429–456.
- (20) Putnam, D.; Gentry, C. A.; Pack, D. W.; Langer, R. Polymer-Based Gene Delivery with Low Cytotoxicity by a Unique Balance of Side-Chain Termini. *Proc. Natl. Acad. Sci. USA* **2001**, *98*, 1200–1205.
- (21) Mccallion, C.; Burthem, J.; Rees-Unwin, K.; Golovanov, A.; Pluen, A. Graphene in Therapeutics Delivery: Problems, Solutions and Future Opportunities. *Eur. J. Pharm. Biopharm.* **2016**, *104*, 235–250.
- (22) Chiu, Y.-L.; Ali, A.; Chu, C.; Hong Cao; M., R. T. Visualizing a Correlation between siRNA Localization, Cellular Uptake, and RNAi in Living Cells. *Chem. Biol.* **2004**, *11*, 1165–1175.
- (23) Pontes, O.; Pikaard, C. S. siRNA and miRNA Processing: New Functions for Cajal Bodies. *Curr. Opin. Genet. Dev.* **2008**, *18*, 197–203.





## CHAPTER 5: CONCLUSIONS AND PERSPECTIVES

Graphene oxide is showing lot of potential in biomedicine, especially in gene delivery, by virtue of its wide surface area that offers the opportunity to load a large amount of various therapeutic molecules. In ongoing RNAi research, delivery of nucleic acids inside cells and into the cytoplasm, where siRNA based gene silencing occurs, is one of the major goals. In this context, I focused my interest in developing a novel platform complexing siRNA by control covalent functionalization of graphene oxide with various amines. We aim to clarify the supramolecular interactions between GO surface and the double strand siRNA that could affect the ability to deliver this type of biomolecules into human cancer cells or other types of cells.

In the first part of my Thesis (Chapter 2), various facile and green reduction methods have been investigated on two types GO from difference sources characterized by a different lateral size. I was able to achieve reduced GO possessing a range of C/O ratio, different percentages of oxygenated groups, thus endowed of varied dispersibility. After testing the reduction processes on the commercial small GO<sub>s</sub>, we needed to consider several factors for the decision on the method of modification applied to the academic large GO<sub>L</sub>. In addition to the dispersibility, which is important for further biological test, the percentage of oxygenated groups remaining after reduction is also essential for the efficiency of reaction with the amines and the complexation with siRNA. Therefore, even though a high reduced efficiency on GO<sub>s</sub> was obtained using microwave-assisted, vitamin C-base method, and solvothermal method using DMSO, the low dispersibility of these prepared rGO is a disadvantage. Interestingly, the hydrothermal reaction possessed not only a notable reduction with enough remained epoxides, but also a good dispersibility. More interestingly, the ozonation process can reintroduce the oxygen moieties on reduced GO and enhance the dispersibility of the reduced GO<sub>s</sub>. In the case of large GO<sub>L</sub>, we achieved the reduced GO with various C/O ratio, good dispersibility using the hydrothermal treatment during 5 days and vitamin C-based method. The ozonation of the hydrothermally reduced GO once again can reintroduce the oxygen moieties and improve the dispersibility. Hence, in this study, with the surface and morphology characterization of the materials via various techniques, it was evident that the oxygenated moieties groups present on the surface of GO could be modulated by using different straightforward and non-toxic reduction processes. The efficiency of

reduction/oxidation process on GO were also confirmed further in Chapter 3 via the reactions with amines and the ability of complexation with siRNA.

In Chapter 3, I succeeded to synthesize and characterize cationic molecules and dendrons for the conjugation with GO<sub>S</sub> via epoxy ring opening reaction. In addition, the functionalization of GO materials with low molecular weight PEI was also obtained. By gel electrophoresis, I can conclude that small amine conjugated GO<sub>S</sub> do not show a significant complexation with siRNA, meanwhile PEI conjugates give a high efficiency in complexing siRNA. I also found that the driving force of this complexation ability of PEI functionalized GO<sub>S</sub> and siRNA is likely due to electrostatic interactions. In comparison to GO<sub>L</sub>, I performed the functionalization on a series of GO<sub>L</sub> with TEG and PEI. Interestingly, I figured out that while the H-bonds contributed in the ability of complexing of TEG conjugates with siRNA, the ionic forces play the main role in the case of PEI containing conjugates.

In summary, from the study in Chapter 2 and 3, I could identify and rationalize the supramolecular forces that affect the complexation with siRNA of a series of amino functionalized graphene oxide possessing various oxygen moieties.

The last part of the work, described in Chapter 4, was dedicated to the analysis of the siRNA structure alterations induced by GO. A deep understanding of the interaction of siRNA and GO is crucial for its future applications. I performed a systematic study varying the size and the oxidation level of GO. In addition, to see the effect of amino groups, I tested the different GO materials after PEI functionalization, and complexed to siRNA molecules. Using a mild filtration protocol, I was able to separate free siRNA molecules from GO flakes after their incubation and to assess the conformational damages via UV-Vis, fluorescence and CD spectra. My results indicate that the alteration of siRNA structure is strongly mediated by the GO size. Indeed, small GO<sub>S</sub> seems to intercalate between the double strands and induce severe damages on RNA conformation. Large GO<sub>L</sub> instead seems to basically reduce the A-helix pitch of the double strand siRNA structure. The most interesting part is that all PEI functionalized GO not only enhance the complexation ability with siRNA but also protect denaturation effect of GO. Lastly, the *in vitro* assay suggested that both non-functionalized GO and PEI conjugates are potential carriers for delivery of siRNA into cancer cells. Indeed, we observed for the first time an efficient internalization and a good distribution of siRNA into the cytoplasm.

To conclude, I have explored various methodologies for adjusting the oxygenated groups present on the surface of graphene oxide. I succeeded in functionalization of these graphene materials with various amines and polymers to obtain a high complexation ability with siRNA. My study helped to elucidate the driving forces and the crucial impacts that affect the interaction between graphene materials and nucleic acids. I believe that the full comprehension of the supramolecular interactions between GO and siRNA is essential for an effective GO application in biomedicine. The current biological tests with very interesting results in the ability of GO as a platform of delivery of siRNA into cancer cells open a wide access for the experiments using different types of cells. Moreover, besides GO and PEI-GO, the ozonated GO samples possessing a high dispersibility and high complexity with siRNA are also potential samples for biological experiments in future. Specific sequences of siRNA will be carefully designed for a gene silencing investigation on specific cells to avoid the unwanted side effect of siRNA including off-target effect or the activation of innate immune system. The study of cytotoxicity of our graphene derivatives will be also further explored.



# LIST OF PUBLICATIONS AND COMMUNICATIONS

## PUBLICATIONS

- “Carbon nanomaterial-nucleic acid conjugates and their applications” Book chapter, under preparation.
- G. Reina<sup>#</sup>, **N.D.Q. Chau**<sup>#</sup>, Y. Nishina, A. Bianco “Graphene oxide size and oxidation degree govern its supramolecular interactions with siRNA”, submitted to *Adv. Funct. Mater.*, <sup>#</sup>: co-first authors
- **N.D.Q. Chau**, G. Reina, J. Raya, C. Ménard-Moyon, I. Anna-Vacchi, Y. Nishina, A. Bianco. “Elucidation of siRNA complexation efficiency by graphene oxide and reduced graphene oxide”, *Carbon*, 2017, 122, 643-652.
- A. Kermagoret, **N.D.Q. Chau**, B. Grignard, D. Cordella, A. Debuigne, C. Jérôme, C. Detrembleur. “Cobalt-Mediated Radical Polymerization of Vinyl Acetate and Acrylonitrile in Supercritical Carbon Dioxide” *Macromol. Rapid Commun.* 2016, 37, 539–544.
- **N.D.Q. Chau**, C. Ménard-Moyon, K. Kostarelos, A. Bianco. “Multifunctional carbon nanomaterial hybrids for magnetic manipulation and targeting”. *Biochemical and Biophysical Research Communications* 468, 2015, 454–462.
- T. Duffar, C.T. Nwosu, I.M. Asuo, J. Muzy, **N.D.Q. Chau**, Y. Du Terrail-Couvat, F. Robaut “Experimental study of grain boundary orientations in multi-crystalline silicon”, *Journal of Crystal Growth*, 401, 2014, 404–408.
- P.T.S. Nam, L.V. Ha, **N.D.Q. Chau**. “Microwave – assisted synthesis of pravastatin in ionic liquids as green solvents”. *Journal of Chemistry Vietnam*, 2011, 497-503.

## COMMUNICATIONS

- **N.D.Q. Chau**, G. Reina, I. Anna-Vacchi, C. Ménard-Moyon, Y. Nishina, A. Bianco. “Interaction of graphene oxide and functionalized graphene oxide with small interference RNA for application in gene silencing”. Chem2DMat, 2017, Strasbourg, France (**Poster**)
- **N.D.Q. Chau**, G. Reina, C. Ménard-Moyon, Y. Nishina, A. Bianco. “Polyethyleneimine-functionalized graphene oxide, a novel platform for efficient siRNA complexation”. European Polymer Federation Congress, 2017, Lyon, France (**Poster**)
- **N.D.Q. Chau**, G. Reina, J. Raya, C. Ménard-Moyon, Y. Nishina, A. Bianco. “Synthesis of

- graphene oxide with different degrees of oxidation for applications in gene silencing”. Graphene 2017, Barcelona, Spain (**Oral**)
- V. Bordoni, **N.D.Q. Chau**, P. Nicolussi, F. Sgarella, A. Bianco, L.G. Delogu. “The application of swine model for immune characterization of graphene nanomaterials”. Nanobiomed, 2017, Sardinia, Italy. (Poster)
  - **N.D.Q. Chau**, C. Ménard-Moyon, A. Bianco. “Controlled covalent functionalization of graphene oxide: towards the development of an amino functionalized platform for complexation of nucleic acids”. Graphene Study 2016, Les Houches, France (**Poster**)
  - **N.D.Q. Chau**, A. Kermagoret, B. Grignard, C. Detrembleur. “Implementation of Cobalt-Mediated Radical Polymerization (CMRP) of Vinyl Acetate in supercritical CO<sub>2</sub>”, FAME Master Workshop, 2014, Bordeaux, France (**Oral**)
  - **N.D.Q. Chau**, T. Duffar, F. Robault, M. Cablea, K. Zaidat, “Study of the zig-zag grain boundary in multicrystalline Si”, International Conference Crystal Growth, 2013, Warsaw, Poland (**Poster**)





## L'oxyde de graphène peut-il devenir une plateforme appropriée pour la complexation d'acides nucléiques ?

### Résumé

L'oxyde de graphène (GO) a attiré un intérêt croissant comme vecteur potentiel pour la délivrance de gènes, en particulier pour l'inhibition de gènes spécifiques. Le but principal de ce travail est le développement de nouvelles plateformes complexant de petits ARN interférents (siRNA) et la rationalisation des interactions supramoléculaires entre la surface du GO et l'ARN double brin. L'étude s'est concentrée d'abord sur la synthèse de GO avec divers groupes oxygénés, puis sur la fonctionnalisation covalente du GO avec des amines et des polymères. De plus, j'ai étudié les facteurs qui pourraient affecter la structure double hélice du siRNA. Enfin, la question que je me suis posé: « l'oxyde de graphène peut-il devenir une plateforme appropriée pour la complexation d'acides nucléiques ? » a été résolue à l'aide d'expériences biologiques prouvant la capacité du GO à délivrer du siRNA dans les cellules.

Mots clés : graphène, siRNA, complexes supramoléculaires, dénaturation, délivrance de gènes

### Résumé en Anglais

Graphene oxide (GO) has attracted increasing interest as a prominent potential vector in gene delivery and in particular in gene silencing. The main goal of this work is to develop novel platforms to complex small interfering RNA (siRNA) molecules and to rationalize the supramolecular interactions between GO surface and the double strand RNA. The study focused first on the synthesis of GO with various oxygenated groups, subsequently chemically covalently modified with amines and polymers. Moreover, I investigated on the factors that could affect the double helix siRNA structure. Finally, the question of the thesis, « Can graphene oxide be a suitable platform for complexation of nucleic acids? » could be answered from the biological tests proving the ability of graphene derivatives as a carrier of siRNA into the cells.

Key words: Graphene, siRNA, supramolecular complex, denaturation, gene delivery